ADVERTIMENT. La consulta d'aquesta tesi queda condicionada a l'acceptació de les següents condicions d'ús: La difusió d'aquesta tesi per mitjà del servei TDX (www.tesisenxarxa.net) ha estat autoritzada pels titulars dels drets de propietat intel·lectual únicament per a usos privats emmarcats en activitats d'investigació i docència. No s'autoritza la seva reproducció amb finalitats de lucre ni la seva difusió i posada a disposició des d'un lloc aliè al servei TDX. No s'autoritza la presentació del seu contingut en una finestra o marc aliè a TDX (framing). Aquesta reserva de drets afecta tant al resum de presentació de la tesi com als seus continguts. En la utilització o cita de parts de la tesi és obligat indicar el nom de la persona autora.

ADVERTENCIA. La consulta de esta tesis queda condicionada a la aceptación de las siguientes condiciones de uso: La difusión de esta tesis por medio del servicio TDR (www.tesisenred.net) ha sido autorizada por los titulares de los derechos de propiedad intelectual únicamente para usos privados enmarcados en actividades de investigación y docencia. No se autoriza su reproducción con finalidades de lucro ni su difusión y puesta a disposición desde un sitio ajeno al servicio TDR. No se autoriza la presentación de su contenido en una ventana o marco ajeno a TDR (framing). Esta reserva de derechos afecta tanto al resumen de presentación de la tesis como a sus contenidos. En la utilización o cita de partes de la tesis es obligado indicar el nombre de la persona autora.

WARNING. On having consulted this thesis you're accepting the following use conditions: Spreading this thesis by the TDX (www.tesisenxarxa.net) service has been authorized by the titular of the intellectual property rights only for private uses placed in investigation and teaching activities. Reproduction with lucrative aims is not authorized neither its spreading and availability from a site foreign to the TDX service. Introducing its content in a window or frame foreign to the TDX service is not authorized (framing). This rights affect to the presentation summary of the thesis as well as to its contents. In the using or citation of parts of the thesis it's obliged to indicate the name of the author

“Study of Nanocomposites Prepared from Polyamides and Biodegradable Polyesters and Poly(ester amide)s”

Laura Teresa Morales Gámez

Advisors:

Dr. Jordi Puiggalí Bellalta

Dra. Mª Lourdes Franco García

DEPARTAMENT D’ENGINYERIA QUÍMICA
UNIVERSITAT POLITÈCNICA DE CATALUNYA
2011

Once you make a decision, the universe conspires to make it happen

Ralph Waldo Emerson

Abstract

Polymer clay nanocomposites of polyamides and biodegradable polymers with three kinds of organomodified clays were prepared by different techniques (*in situ* polymerization, solution casting, and melt mixing). The polymers used in this research were nylons 56, 65 and 47 and the biodegradable polymers: poly (glycolic acid-*alt*-6-hydrohexanoic acid) and poly(glycolic acid-*alt*-6-aminohexanoic acid). The development of biodegradable nanocomposites with improved or modified material properties is an interesting topic since these new materials are expected to replace already existing biodegradable and non-biodegradable commodity plastics in some specific applications. This project aims to study the influence of clay particles incorporated in a polymer matrix on the crystallization processes, the study of the in situ polymerization kinetics of mixtures of clays and monomers of biodegradable polymers, as well as the influence of nanoparticles on the thermal behavior and morphologic parameters.

Even-odd, and odd-even polyamides were chosen to study the Brill transition and to prepare nanocomposites with organomodified clays. These polyamides have a peculiar structure where hydrogen bonds are established along two different directions. X-ray diffraction as well as SAXS-WAXD synchrotron experiments were employed to study the structural changes induced by temperature, during heating and cooling. Different organomodified clays were used to prepare nanocomposites, which final structure was found to be dependent on the preparation method.

Nanocomposites derived from biodegradable polymers were characterized by means of X-ray diffraction and transmission electron microscopy. Morphological studies showed that the extent of clay dispersion depended on the clay type and on the preparation technique. Hence, exfoliated and intercalated nanocomposites could be obtained. The final nanocomposite structure was found to have a great influence on both cold and hot crystallization processes. Hence, the crystallization rate increased and decreased with respect to the neat polymer when intercalated and exfoliated structures were respectively obtained. The kinetics of the polymerization process was also studied by means of FTIR and SAXS-WAXD. The results indicate that the presence of the organomodified clay had a remarkable effect on the kinetic parameters.

Acknowledgements

I would like to start by thanking the research group that received me at the *Universitat Politècnica de Catalunya*, especially Dr. Jordi Puiggalí for his support and guidance throughout these years, whose dedications have made this work possible and who has not just only helped me to complete my research work but also to overcome all kinds of problems that arise during this time. I would also like to express my gratitude to Dr. Lourdes Franco for her help, especially in the experimental part at the beginning of my research. To all the members of the research group professors and students, for all the support, help and friendly words including Drs. Teresa Casas, Alfonso Rodriguez, Luis Javier del Valle, Meritxel Martinez and to my PhD colleague Elena Diaz. I also want to thank our "neighbors": MACROM research group for their help and friendship, particularly to Francisco Acosta and Drs. Juan Antonio Subirana, Lourdes Campos and Daniela de Luchi.

I also want to acknowledge to the National Council for Science and Technology CONACYT, from whom I received the first funding for this PhD, for the excellent job they perform supporting young Mexicans that want to start a scientific career.

I would also like to thank to the Leibniz Institute of Polymer Research in Dresden, for the opportunity to do a research stay, specially Dr. Manfred Stamm who accepted my application and Dr. Leonid Ionov for receiving me in his group, for all the help and all the kind people I met, I am thankful to all the members of the research group specially Georgi Stoychev for his time and explanations, and to my office colleagues Anja, Ksenia, Alexander and Falk for all the good moments and friendship.

I am grateful to Dr. François Fauth, for all the help during the performance of synchrotron experiments that was always beyond the expected, for his quick and efficient answers to my e-mail question.

Finally thanks most of all to my beloved Family, for their support and company no mattering the distance. To my mother and my brother Luis Fernando for the almost everyday conversations that kept me close to them all these years, and to my friends that either in Mexico, Dallas or even here in Spain always sent me their best wishes. You all made my time away from my homeland easier and better, I am especially thankful to my dearest friends Veronica and Alejandra and to Arturo for all the nice moments we spent together.

Publications

Work from this thesis has been published by the author:

1. **Morales, L**., Franco, L., Casas, M.T. & Puiggalí, J. Crystallization behavior of clay nanocomposites prepared from a degradable alternating copolyester constituted by glycolic acid and 6-hydroxyhexanoic acid. *Journal of Polymer Science Part B: Polymer Physics* **48**, 33-46 (2010).

2. **Morales, L**., Franco, L., Casas, M.T. & Puiggalí, J. Poly(ester amide)/clay nanocomposites prepared by in situ polymerization of the sodium salt of N - chloroacetyl-6-aminohexanoic acid. *Journal of Polymer Science Part A: Polymer Chemistry* **47**, 3616-3629 (2009).

3. **Morales-Gámez, L**. Jones, I., Franco, L. & Puiggalí, J. Poly(ester amide) nanocomposites by in situ polymerization: Kinetic studies on polycondensation and crystallization. *Express Polymer Letters* **5**, 717-731 (2011).

4. **Morales-Gámez, L**., Franco, L., Casas, M.T. & Puiggalí, J. Crystallization studies on a clay nanocomposite prepared from a degradable poly(ester amide) constituted by glycolic acid and 6-aminohexanoic acid. *Polymer Engineering & Science* **51**, 1650-1661 (2011).

5. **Morales-Gámez, L**., Franco, L. & Puiggalí, J. Thermal stability studies on clay nanocomposites prepared from a degradable poly(ester amide) constituted by glycolic acid and 6-aminohexanoic acid. *Thermochimica Acta* **512**, 142-149 (2011).

6. **Morales-Gámez, L.**, Ricart, A., Franco, L. & Puiggalí, J. Study on the brill transition and melt crystallization of nylon 65: A polymer able to adopt a structure with two hydrogen-bonding directions. *European Polymer Journal* **46**, 2063-2077 (2010).

7. **Morales-Gámez, L.**, Soto, D., Franco, L. & Puiggalí, J. Brill transition and melt crystallization of nylon 56: An odd–even polyamide with two hydrogen-bonding directions. *Polymer* **51**, 5788-5798 (2010).

8. **Morales-Gámez, L**., Casas, M.T. Artigas, A. Franco, L. Puiggalí, J. Crystallization studies on clay nanocomposites of nylon 47 having exfoliated or intercalated structures. *Submitted Papper*

9. Puiggalí, J. **Morales-Gamez, L.** Franco, L. Casas, M. del Valle, luis J.; Rodriguez-Galan, A. *Society of Plastics Engineers. Plastics Research Online* **2011**, 10-12 (2011).doi:10.1002/spepro.003598

10. Ricart, a, Soto, D., Franco, **L., Morales,** L.T. & Puiggalí, J. Synchrotron Radiation Studies on Even-Odd and Odd-Even Nylons. *IOP Conference Series: Materials Science and Engineering* **14**, 012006 (2010).

11. **Morales-Gámez, L.,** Rodríguez-Galán, Alfonso Franco, L. & Puiggalí, J. Aliphatic Polyester and Poly(ester amide) Clay Nanocomposites by In-situ Polymerization. In-situ Synthesis of Polymer Nanocomposites Polymer Nano-, Micro and Macrocomposites V. Edited by V. Mittal. John Wiley & Sons 367-384 (2011).

Table of contents

1

INTRODUCTION

1.1

Biodegradable Polymers

Nowadays, biodegradable polymers are becoming an important research focus due to the increasing demand of biodegradable materials for novel biomedical technologies including tissue engineering, regenerative medicine, gene therapy, controlled drug delivery, biothecnology [1] and also for applications in which plastics are used for short time periods and then disposed [2]. These so called biodegradable polymers can be degraded by bioactive environments (such as those containing bacteria, fungi, or algae), or by hydrolysis in water or even in buffered solutions [3]. For this reason, biodegradable polymers can be used as attractive substitutes for many synthetic materials, thereby alleviating problems associated with solid waste disposal.

Biodegradable polymers can be classified into tree major categories: (1) polyesters produced by microorganisms, (2) natural polysaccharides or other biopolymers, (3) synthetic polymers, particularly aliphatic polyesters. In this last category, industrially produced polymers can be found, such as poly(ε-caprolactone), poly(L-lactide), poly(butylene succinate), besides these aliphatic polyesters, various types of synthetic biodegradable polymers have been designated and tested for practical applications. For example, polyesters containing aromatic rings or cyclic ether moieties, poly(ester amide)s, poly(ester carbonate)s, poly(ester urethanes)s etc. Some attempts have been made to introduce ester groups into vinyl polymer chains, to make vinyl polymers biodegradable, but not effective and practical method have been developed yet [4]. **Scheme 1.1.1** shows the classification of more important biodegradable polymers.

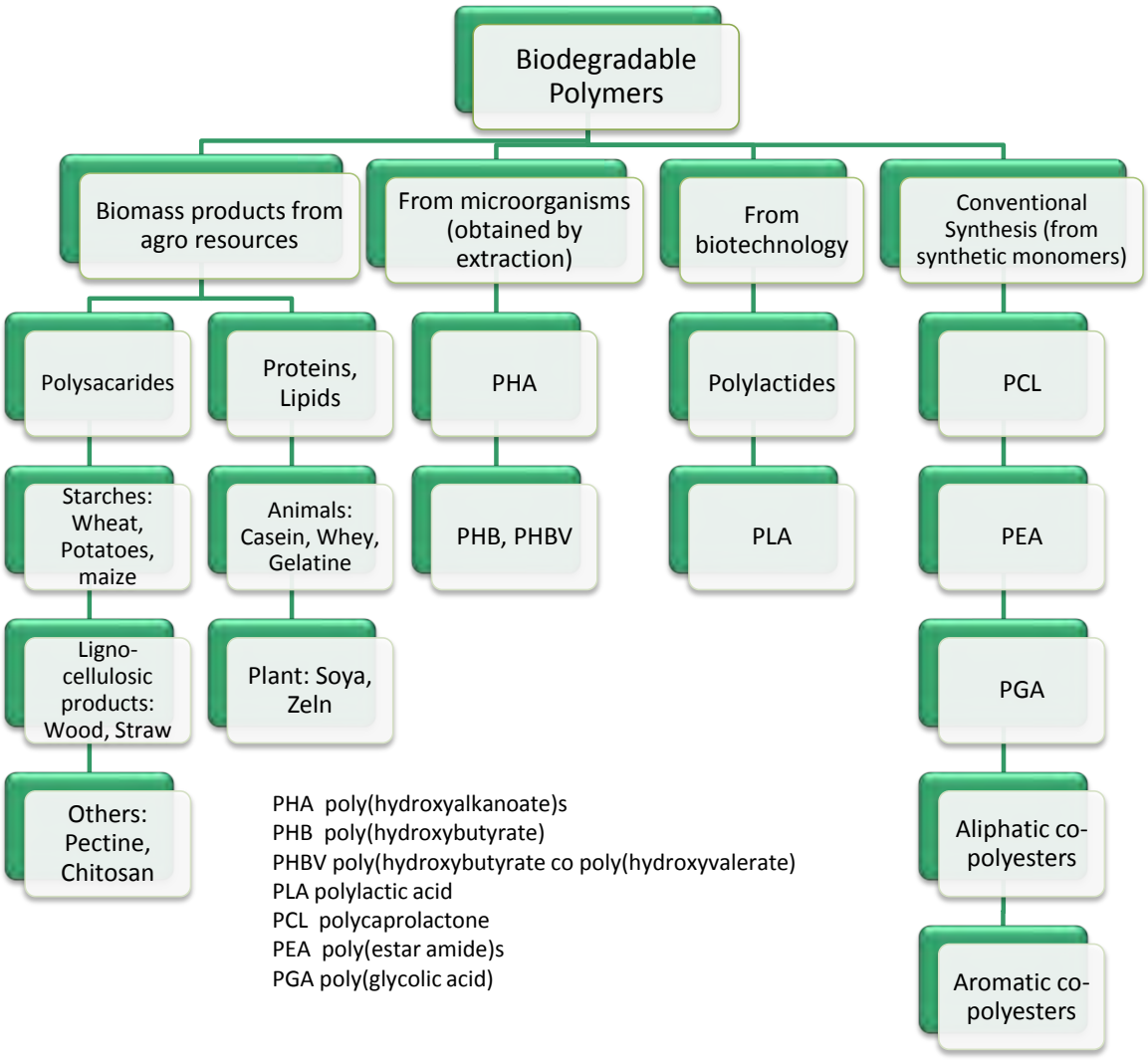

Scheme 1.1.1 Biodegradable Polymers Classification [5].

Biodegradable polymers can be defined as the polymers that can undergo microbial induced chain scission leading to mineralization. Some of them have comparable properties as the petroleum based polymers, and the clear advantage of being biodegradable. However, in general, it seems necessary to improve properties in order to increase both the number of disposable polymers and the range of applications. In this sense, efforts are nowadays focused to prepare nanocomposites by addition of different types of organomodified clays and other nanoparticles; moreover development of new biodegradable and bioabsorbable polymers with temporary function is also of great interest in the field of biomedical materials [5]. For these applications some specific properties are required. The polymer has not just only be biocompatible-nontoxic and not rejected by the intended organism but also it must have the ability to maintain mechanical properties for certain period of time, flexibility and an adequate

absorption rate. In this sense, the study of how the performance of these materials can be modified by incorporation of nanoparticles becomes again an interesting topic.

Polyesters constitute the main family of biodegradable polymers due to their high degradation rate. In general, the derivatives of Poly(glycolic-acid) are the most commonly used for biomedical applications including drug delivery systems, wound treatment applications and implants [6]. Poly(ester amide)s constitute a new promising family of materials which has some advantages associated to the hydrophilic character of their amide groups and the capability to establish strong hydrogen bond interactions that influence on both thermal and mechanical properties. Furthermore, the presence of ester groups should ensure degradability, although in this case the hydrolysis proceeds at a lower rate than in parent polyesters which have a higher rate of hydrolyzable ester bonds.

Our group has recently developed a synthesis procedure that allows to get polyesters and poly(ester amide)s constituted by glycolic acid units and ω-amino acid or ω-hydroxy acid units with a regular sequence distribution. This kind of polymers can be obtained by a classical methodology based on a selective protection of reactive groups. However in this case, the process is highly more complicated and have lower yields respect to the proposed one. The new synthesis is based on a thermal polycondensation reaction where the formation of a metal halide salt becomes the driving force of the process. The high simplicity of this method opens again the interest towards these families of polymers characterized by a semicrystalline character that contrasts with the irregular sequence distribution of commercial copolymers prepared by ring opening polymerization.

In the present work, we have selected a representative polyester derived from glycolic acid and 6-hydroxyhexanoic acid, and a representative poly(ester amide) derived from glycolic acid and 6-aminohexanoic acid, which will be thereafter named as poly(glc-*alt*-6HH) and poly(glc-*alt*-amh), respectively. Their chemical repeat units are consequently similar since only differ in the substitution of an ester group by an amide group (**Scheme 1.1.2**).

-[OCH_2CO-$O(CH_2)_5CO$]-	Poly(glc-*alt*-6HH)
-[OCH_2CO-$NH(CH_2)_5CO$]-	Poly(glc-*alt*-amh)

Scheme 1.1.2 polyester derived from glycolic acid and 6-hydroxyhexanoic acid, and a representative poly(ester amide) derived from glycolic acid and 6-aminohexanoic acid.

1.2

Nanocomposites

Nanocomposites have emerged in the last two decades as an efficient strategy to upgrade the structural and functional properties of synthetic polymers. Aliphatic polyesters such as polylactide (PLA), polyglycolide (PGL) and poly (ε-caprolactone) (PCL) have attracted wide attention for their biodegradability and biocompatibility in the human body. The incorporation of nanofillers (organic and inorganic) into biodegradable polymers has been a consequence of the willing to prepare new biomaterials with enhanced properties [7].

Nanocomposites are hybrid materials consisting of a polymer matrix in which nano-sized particles are homogeneously dispersed. In fact, to be called nanocomposite at least one dimension of the added particle must be in the nanometer scale [8]. Due to their small size, dispersed structures in the polymer matrix, have relatively huge surface areas per unit weight, and often these surface areas dominate the behavior of these materials. Some important nanostructures include, carbon nanotubes, biomolecules such as proteins, silica nanoparticles and montmorillonite type clays [9].

Considering the nano-sized particles that can be added to the polymer matrix, phyllosilicates are of particular interest, especially montmorillonite due to their abundance, low cost and geometrical features [10]. The indicated clay is present typically at concentrations less than 5% [11-22]. The resulting interactions with the polymer matrix can improve substantially many physical properties such as mechanical performance [23], barrier resistance [24] and flammability [25]. In the case of biodegradable polymers, biodegradability could indeed be improved [26] .

The natural montmorillonite clays consist of several hundred individual plate-like particles of dimensions 1μm ·1μm ·1nm, held together by electrostatic forces with a gap of approximately

0.3 nm between two adjacent particles. **Figure 1.2.1** shows the structure of this clay at atomic level.

In a such layered material, the bonds between the atoms in the layer are very strong, but the bonds between the layers become weaker. This feature allows an easy separation of the constitutive layers. This clay consists of three subunits: an octahedral center layer consisting of aluminum cations (Al^{+3}); two tetrahedral layers consisting mainly of silica (Si) and oxygen (O) atoms. In the octahedral layer some of the Al^{3+} cations are substituted by Mg^{2+} cations which gives rise to a net negative charge on the layer. Similarly, some of the Si^{4+} cations may be substituted by Al^{3+} cations resulting again in a net negative charge in the tetrahedral layer. In natural clays the charge balancing cations in the gap between the silicate layers are mainly Na^{+}, K^{+} and Ca^{+2} [27]. The gap between the silicate leyers is widely known as a gallery or an interlayer.

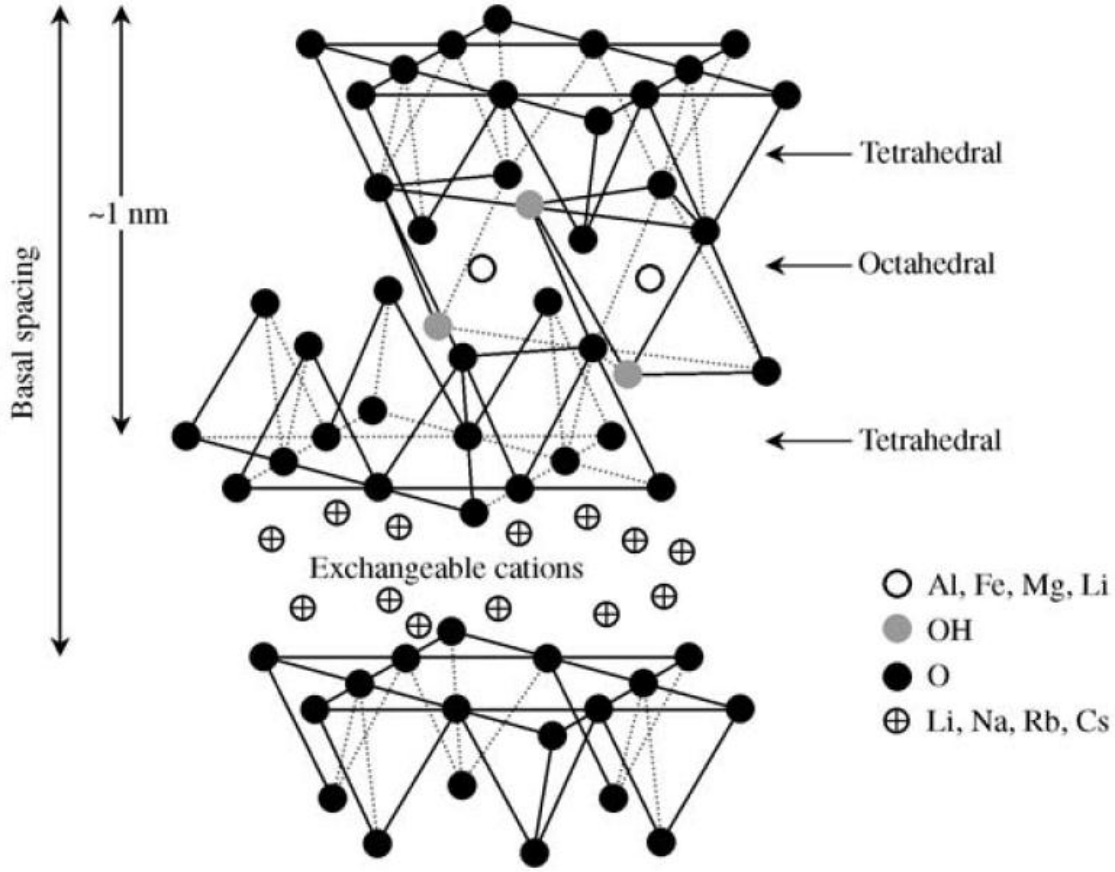

Figure 1.2.1. Typical clay layer structure: octahedral center layer consisting of aluminium (Al^{+3}) cations; two tetrahedral layers consisting mainly of silica (Si) and oxygen (O) atoms [28].

Natural clays mixed with polymers lead to the formation of nanocomposites very rarely. Homogeneous dispersion in the organic polymer phase is hindered by the hydrophilic nature of the clay. **Figure 1.2.2** shows a general procedure to increase compatibility: the cations present

in nature like Na^+, Ca^{++}, or K^+ are exchanged with cationic surfactants such as alkylammonium or alkylphosphonium.

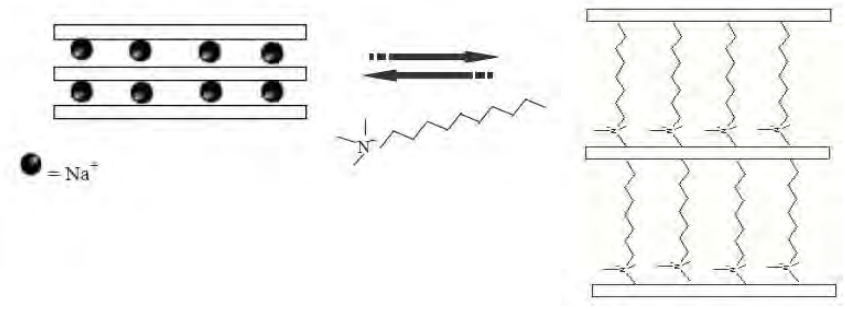

Figure 1.2.2. Ionic exchange between Na^+ and alkylammonium cations to increase matrix – clay compatibility and to achieve a homogeneous dispersion.

1.2.1 Preparation Techniques

Nanocomposites can be prepared by many different methods, such as, in situ polymerization, solution casting and melt mixing [28].

In situ polymerization is a very versatile technique, as it makes possible to adjust the chemistry to optimize the affinity between the clay and the polymer. Many different types of polymerization techniques can be used to prepare nanocomposites, such as bulk, solution, suspension or emulsion free radical polymerization, among others. This flexibility in the preparation of nanocomposites by in situ polymerization leads to materials with a very good clay dispersion. However, this technique has some disadvantages. It is not always simple to synthesize the materials, so that the processes may be quite expensive, what makes them not very suitable for large scale production and industrial applications. This technique has been important for this research work and it is explained further in **Appendix A**.

When preparing nanocomposites by melt mixing, less reactive clay surfactants must be used, because the most reactive ones are more thermally unstable and decompose during the preparation of the material. With this technique it is possible to use common polymer processing equipment to produce the material, such as extrusion and internal mixers what makes this technique easier to use. The shear provided by processing may also help to increase the clay dispersion, although may be not enough to break big clay aggregates. The resulting dispersion is usually poorer than in a material prepared by in situ polymerization.

The third alternative method is to prepare the nanocomposite using a solvent that dissolves the polymer and disperses the clay at the same time. After the evaporation of the solvent the structure of the material is usually rearranged, so that the clay usually forms an intercalated

morphology, rather than a exfoliated one [29]. However, the clay dispersion is usually better than in materials prepared by melt mixing. A disadvantage of this technique is the need to use an organic solvent, what is not very desirable, especially to environmental issues [30].

- **Nanocomposites of Biodegradable Polymers.**

Biodegradable polymers are considered as an alternative to the existing petroleum-based plastics. To improve their properties, the incorporation of layered silicates (organically modified or not) into the polymer matrices has recently been widely studied [31]. The resulting biodegradable nanocomposites possess several advantages generally attained at low silicate content (5 wt%)[11-22]. Although, biodegradable nanocomposites have very strong future prospects, the present low level of production and high costs restrict them for a wide range of applications.

- **Structure of Nanocomposites.**

From a structural point of view there are two main possible arrangements of the clay into the polymer matrix: the intercalated and exfoliated structures. In most cases, it is usual to find a mixture of both structures [12] if enough care is not taken. In the intercalated system the silicate layer stacking is preserved, but the polymer is inserted between the layers. In the exfoliated system the silicate layers are fully separated and randomly dispersed. The nanostructure effect is more pronounced in the exfoliated nanocomposite than in the intercalated one due to the improved dispersion and consequently properties are enhanced in the former structure.

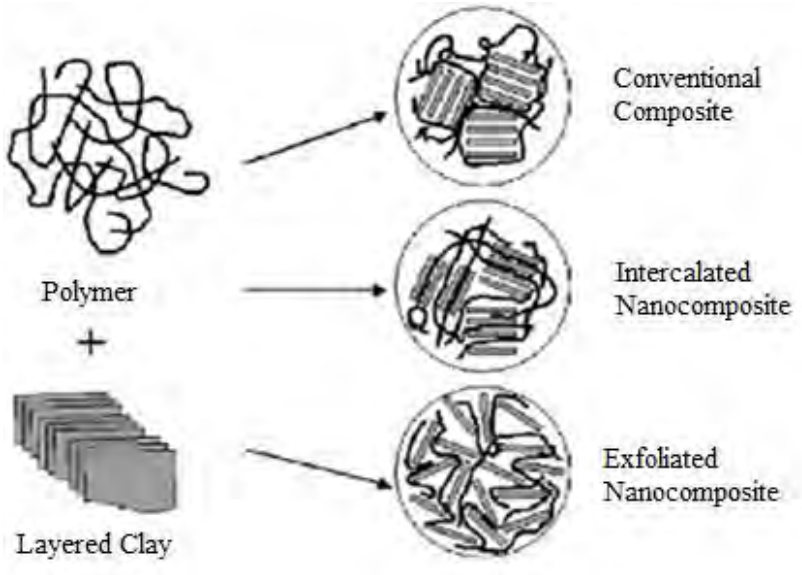

Figure 1.2.3 Schematic illustration of different types of thermodynamically achievable polymer/layered silicate nanocomposites [33]

1.3

Polymer Structure

The size and shape of polymer are intimately connected to their properties.

Natural and synthetic polymers are usually described for their levels of structures. The primary structure describes the precise sequence of the individual atoms that compose the polymer chain. The secondary structure describes the molecular shape or the conformation of the polymer chain (the most linear polymers shape approaches a helical or plated skirt (or sheet) arrangements). The tertiary structure describes the shaping or folding of the polymer. Quaternary structure represents the overall shape of groups of the tertiary structures where the tertiary structures may be similar or different.

It is well known that a linear polymer possess a combination of amorphous and crystalline structures, that varies with the structure of the polymer and the precise conditions that have been imposed on the material. The reason why linear ordered polymers fail to be almost totally crystalline is largely kinetic, resulting from an inability of the long chains to totally disentangle and perfectly align themselves during the time that the polymer chain is cooling and mobile.

Mixtures of amorphous and mini – crystalline structures or regions may consist of somewhat random chains containing some chains that are parallel to one another forming short-range mini crystalline regions. Crystalline regions may be formed from large range ordered platelet-like structures, including polymer single crystals, or they may form even larger organizations such as spherulites. Short and longer range ordered structures can act as physical cross-links.

The kind, amount, and distribution of polymer chain order/disorder (crystalline/amorphous) is driven by the processing (including pre- and post-) conditions and thus it is possible to vary the polymer properties through a knowledge of and ability to control the molecular-level structures. Some polymer properties can be manipulated by altering the crystallinity [32]. When polymer crystallinity is increased the following properties increase as well: abrasion resistance, chemical resistances, hardness, T_g tensile strength and yield while other properties decrease such as brittleness solubility and toughness [33]; furthermore, crystallinity can be favored by some factors like interchain forces, regular structure, high symmetry, decrease in volume, increased stress, slow cooling from melt, and homogenous chain length. Consequently many polymeric materials contain both crystalline an amorphous regions giving them a balance between strength and flexibility. Hence the final properties of a polymer are then dependent on the molecular structure of that material [33].

1.3.1 Polymer Crystallization

While it is impossible to cover polymer crystallization in a dissertation of this size, it is important to review some fundamental features that are essential to the study this topic, since this is a central matter for a part of this research work. Polymer crystallization can be broadly classified in three categories a) crystallization during polymerization b) crystallization induced by orientation and c) crystallization under quiescent condition. This last one is important for this research and it is further explained.

It can be said that crystallization under quiescent condition is divided in two types i) crystallization from diluted solutions and ii) crystallization from the melt. While the first one can lead to form lamellar –shaped single crystals, which exhibit a folded-chain habit that are of the order of 100 to 200 Å [9]. Crystallization from the melt of many polymers result in the formation of so the called spherulites that are large enough to be seen in the optical microscope [34] (¡Error! No se encuentra el origen de la referencia. a).

Polarized optical microscopy allows detecting spherulites as (ideally) circular birefingent areas presenting a dark Maltese cross pattern. Birefringence effects are associated with molecular orientation resulting from the characteristic lamellar morphology recognized in spherulites. The spherulite textures show positive and negative spherulites with the direction of the ellipsoid shown in **Figure 1.3.1**. From the optical sign of the spherulite, information of the orientation for the molecular chain in the spherulite can be obtained [35]. In some spherulites, another type of extinction patterns, which consists in radial banding, are observed under the same conditions. These are called “ringed” spherulites. ¡Error! No se encuentra el origen de la referencia. b shows a ringed spherulite of nylon 47 under polarized microscope with a sensitive tint plate. It is commonly believed that the periodic extinction of ringed spherulites is led by lamellar

twisting along the radial direction during crystal growth. **Figure 1.3.1** c shows a schematic representation of the lamella twisting and the periodic extinction in polymer ringed spherulite.

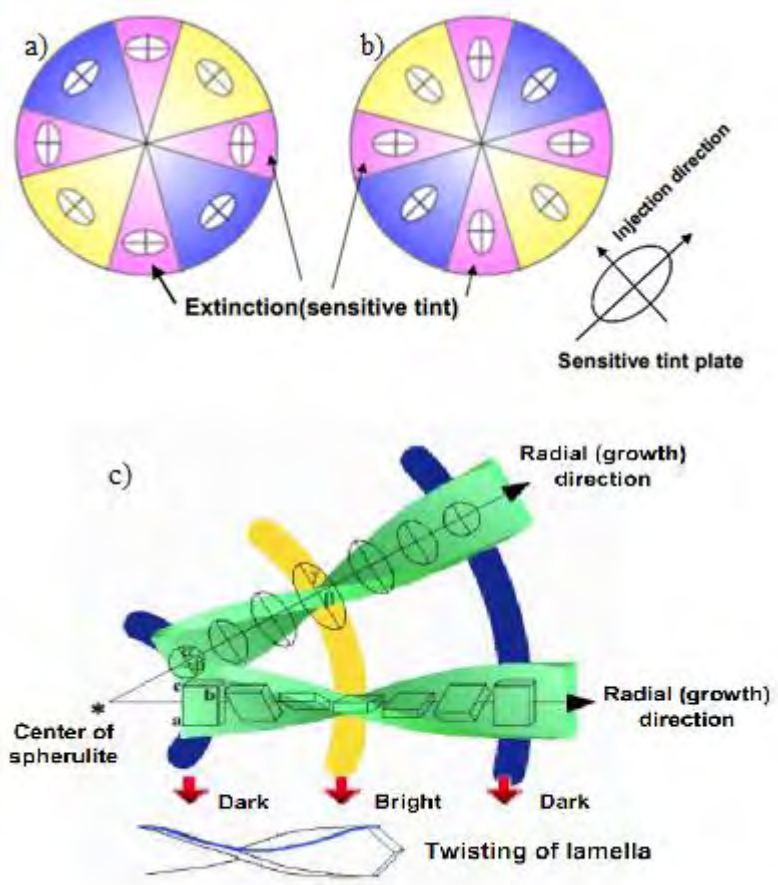

Figure 1.3.1 Optical sign of the spherulite using a sensitive tint plate, (a) negative sherulite, (b) positive spherulite. (c) schematic representation of the lamella twisting and the periodic extinction in polymer ringed spherulite [35] .

The existence of spherulites is an evidence of structural organization at the level of several micrometers [36]. Interestingly, the amorphous regions within the spherulites confer onto the material some flexibility while crystalline platelets give the material strength, just as in the case with largely amorphous materials. Thus relation between amorphous flexibility and crystalline strength (and brittleness) is a central idea in polymer structure-property relationships.

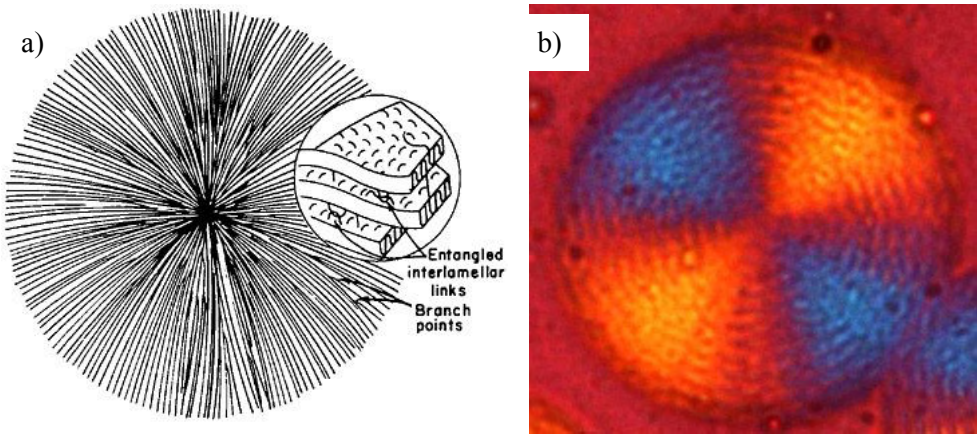

Figure 1.3.2 (a) Schematic diagram of polymer spherulite with chain-folded lamellae. The spherulite consists of chain-folded lamellae radiating from a central point. The polymer chain axes in lamellae are more or less perpendicular to the radius of the spherulite. Branching causes the spherulite to become spherical in shape after sufficient growth. Noncrystallizable material (not shown) when present accumulates between lamellae and at the outer boundary [38] . (b) Optical micrograph of Nylon 4 7 using a sensitive tint plate. The spherulite shows the Maltese Cross, that according to the extinction patterns, it is a negative ringed spherulite.

Lamellar Model

It is a proved fact that lamellar crystal is the fundamental form from which many semicrystalline polymers crystallize. Many studies have been conducted [37] which showed that single crystals grown from dilute solution had a similar appearance that consist of thin lamella [38]. This structural mode is dominant of crystallization for a large number of polymers, and different models were proposed to explain their nature:

Random re-entry or switchboard folded model

It was proposed by Flory [39], [40] and consists of chains randomly folding back into the same lamella or even participating in adjoining lamellae. The upper and lower surfaces consist of loops of varying sizes. The upper and lower surfaces may consist of transitional regions that constitute a diffuse phase boundary – their density being intermediate between the crystal and purely amorphous regions [34].

Figure 1.3.3 Random re-entry or "switchboard" lamellar polymer crystals model [41].

- **Adjacent re-entry chain-folded models (regular folding)**

Two possibilities have been considered:

The smooth surface model which is a very idealized visualization of the chain folding process and tries to be consistent with the highly ordered molecular arrangement expected for a crystal.

The rough surface model the reentry of the chain is still in the nearest growth plane, though large variations in the fold length may exist on a local scale. Multiple nucleation and chain-end defects will further contribute to a rough surface [42] [43].

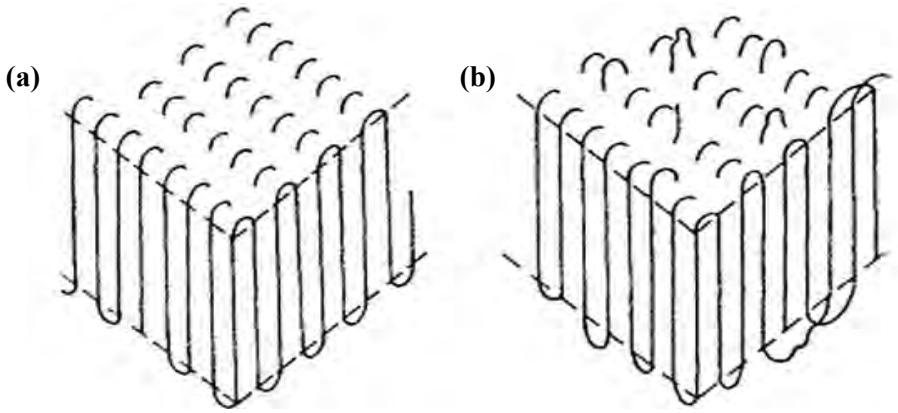

Figure 1.3.4 (a) Adjacent reentry model with smooth, regular chain folds b) Adjacent reentry model with rough fold surface [40] .

- **Solidification model**

This model explain the constancy of the radios of gyration in crystalline state, as detected by small angle neutron scattering [37]. The model is visualized in terms of an alignment of chains without a long-range diffusion process to give rise to a lamellar morphology. The chain sequences in proper conformations are incorporated into the crystal without significant reorganization of the chain conformation.

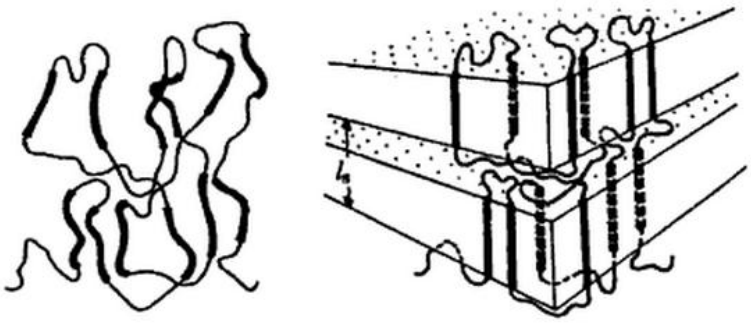

Figure 1.3.5 Solidification model of crystallization process, showing how a chain can be incorporated into a lamellar structure without significant change of overall shape [43]

Isothermal Crystallization

Crystallization in polymers can be described by the process of nucleation and crystal growth. Primary nucleation can be heterogeneous, when the nucleation sites are foreign substances (dust, impurities, nucleating agents, residual catalyst and any existing surfaces). Homogeneous nucleation involves the aggregation of polymer chains, chain segments of parent material to certain size and order. Nucleation is a time-dependent process and takes place as a rate even under isothermal conditions [38].

Thermodynamically, crystallization will be favored if the entropy penalty is outweighed by the enthalpy change. Crystallization is an exothermic process whereas melting is endothermic as energy is required to overcome the intermolecular interactions established in the crystal. T_m is usually higher than T_c due to the high viscosity of molten polymers. Crystallization is therefore determined by kinetics as well as thermodynamics. The crystal growth process is explained by two theories: surface nucleation theory by Hoffman and Lauritzen [44-46] and the surface roughing theory by Sandler and Gimler [47-49]

Surface Nucleation

This theory and its modifications is the most widely used methodology to interpret and model the crystallization behavior of a large number of polymers. It describes the process of crystal growth by surface nucleation events: primary, secondary and tertiary nucleation. Primary nucleation can be seen as a process of crystal formation of six new surfaces, secondary and tertiary nucleation events, involve the formation of four and two new surfaces, respectively, see **Scheme 1.3.1**. The model describes the crystal growth process as a combination of secondary nucleation rate "i" and the substrate completion rate "*g*" . In the classical secondary nucleation theory, the nucleation rate is taken as a rate determining step for crystal growth where "*g*" is very fast compared to "*i*"[50].

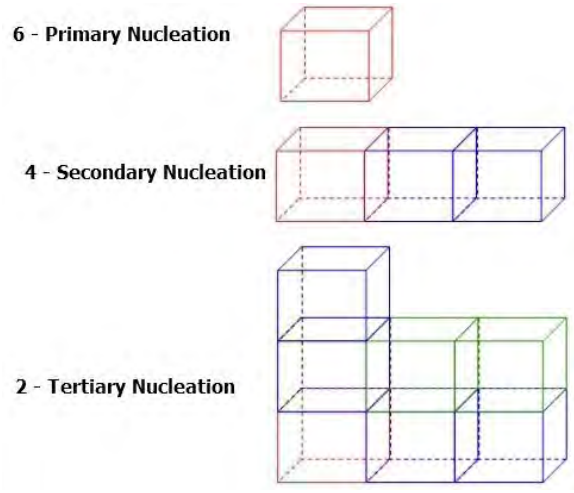

Scheme 1.3.1 Primary , secondary and tertiary nuecleation events [51].

In the Hoffman and Lauritzen theory for polymers the crystal growth process is described via three regimes so far depending on the relative values of the nucleation (*i*) and the substrate completion (*g*) rates [42]. **Figure 1.3.6** shows schematically three regimes of crystal growth. Regime I is from classical secondary nucleation theory where the rate of spreading (*g*) is much faster than rate of secondary nucleation (*i*). In regime II, both the rates are comparable and in regime III, the rate of secondary nucleation (*i*) is very high compared to rate of spreading (*g*). This model also assumes the single stem nucleation, i.e. deposition of a single stem on a surface (a primary nucleus) starts the crystal growth process.

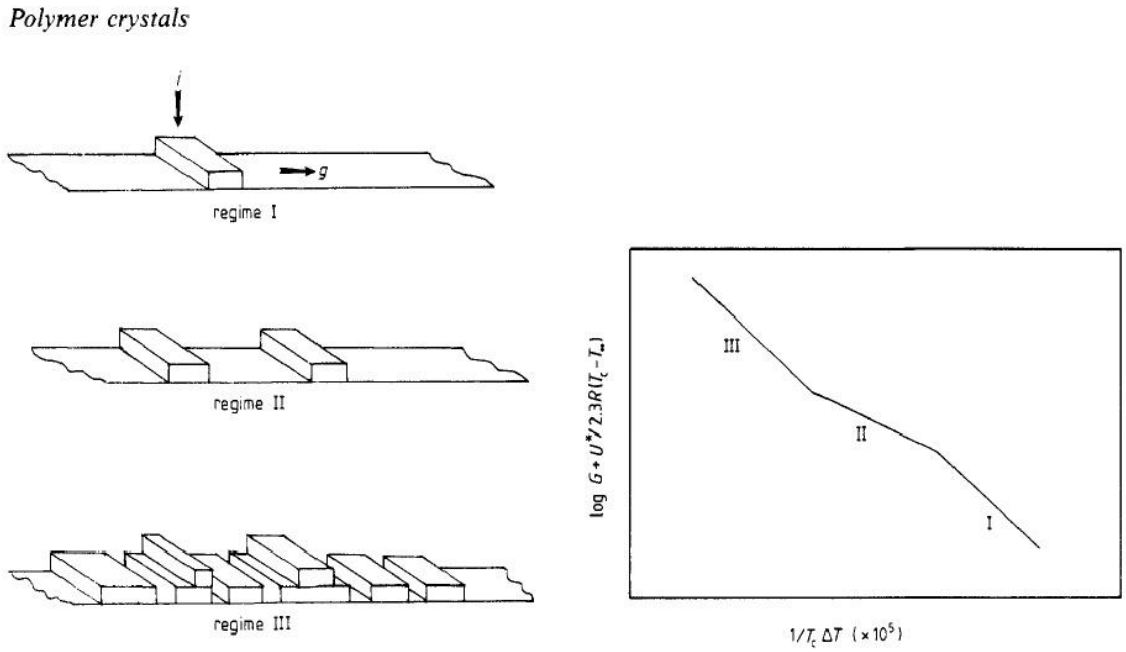

Figure 1.3.6 a) Schematic for crystal growth regimes for polymers according to Lauritzen and Hofmman, *i* is the rate of secondary nucleation and *g* is the substrate completion rate. b) Schematic showing the dependence of crystal growth rate with temperature for three regimes [42]

Surface Roughening Theory

Sandler and Gilmer developed a theory that is based in roughening at atomic length scales [47-49], due to the observation of curved surfaces for the solution grown single crystals, this is different from the Hoffman and Lauritzen assumption of the presence of a flat grown facet. The theory is able to predict regime transition as well as the curved grown surfaces of crystals. A secondary nucleation step is not required according to this theory, nevertheless surface roughening can lead to secondary nucleation.

1.4

Polyamides

Aliphatic polyamides also called nylons are important industrial materials, valued for their good physical properties and processability. They belong to the wide family of synthetic polymer materials containing-amide linkages in their backbones [52]. Nylons are used both, as plastics and as fibres. These polymers generally exhibit high impact strength, toughness, good flexibility, and abrasion resistance [53]. Phenols, cresols and formic acid dissolve the polyamides at room temperature.

Nomenclature

Nylons can be synthesized by ring opening polymerization of lactams, by condensation of ω-amino acids, and also by condensation of diamines and dicarboxylic acids. The polymers formed by the two former methods, are called nylon *n*, where *n* is the number of carbon atoms in the repeating unit, (e.g polycaprolactam is nylon 6). Nylons from diamines and dibasic acids are designated as nylons *m n* where *m* represents the number of carbon atoms in the diamine and *n* is the number of carbon atoms in the dicarboxylic acid [53], (e.g. poly(hexamethylene adipamide) is named nylon 6 6)

Structure

Crystallinity and orientation are the most important features of polyamides affecting the final properties. One determining factor for the their structure is the ability of the NH group to form strong hydrogen bonds (H-bonds) with the CO group [54]. Thus, molecular chains must be oriented in such a way that hydrogen bonding becomes maximized. Intermolecular H-bonds connect neighboring chains or chain segments and form extended planar sheets that contain these H-bonds. Formation of extended sheets usually characterizes the structure of aliphatic

polyamides, and depends on the directionality of the molecular chain and the parity (odd/even) of the involved monomers [54].

In nylons *n*, all the amide groups lie in the same direction whereas in nylons *m n* two consecutive amide groups are in opposite directions. Thus, in the former case, packing is established between directional molecular chains whereas in the second case implies non-directional chains. Carbonyl as well as amine groups can point out to the same side of the molecular chain or in opposite sides depending on the number of carbon atoms (even or odd) of the repeat unit, which clearly influences the hydrogen bonding geometry. The more energetically favorable structure should be obtained when NH and C=O groups of neighboring chains face each other, allowing to attain an ideal H-bond geometry.

Nylons are divided in two main types of stable crystal structures, the α and γ structures [54]. The most important features related to the *α* structure are the formation of planar sheets of hydrogen bonded molecules with a fully extended (planar zig-zag) conformation. These sheets are stacked upon one another giving rise to the three-dimensional unit cell arrangement. Thus, nylon 66 was characterized by triclinic unit cell and a $P\bar{1}$space group defined by center of symmetry in both the diamine and diacid moieties (**Figure 1.4.1**).

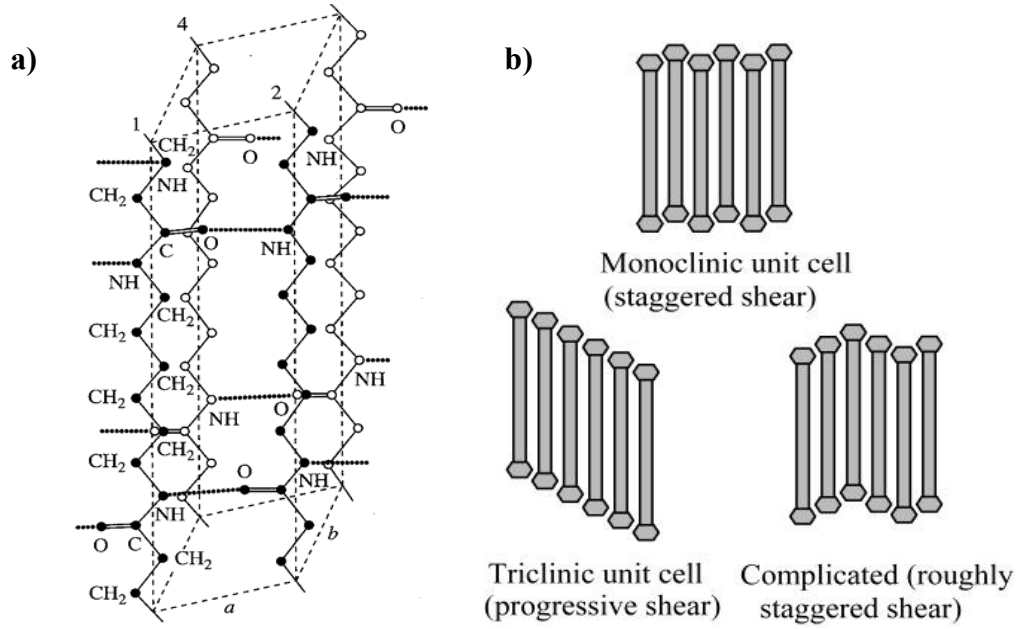

Figure 1.4.1 a) Packing of nylon 66 molecules in the triclinic unit cell [55], b) Various stacking schemes of H-bonded sheets [56].

The γ – form corresponds to a pseudohexagonal arrangement, which is favoured when the amide groups are tilted ca. 60º off the sheet plane. As a consequence, a characteristic shortening in the chain axis repeat is noticed when compared with the values of the extended conformation.

However, hydrogen bonds remain in a single direction. The γ -structure is considered to be a less ordered phase than the α -form. It is characteristic of nylons with a high methylene content in their chemical repeat units (nylons 11 or 12) or nylons for which linear hydrogen bonds between adjacent chains cannot be established when an extended conformation is considered.

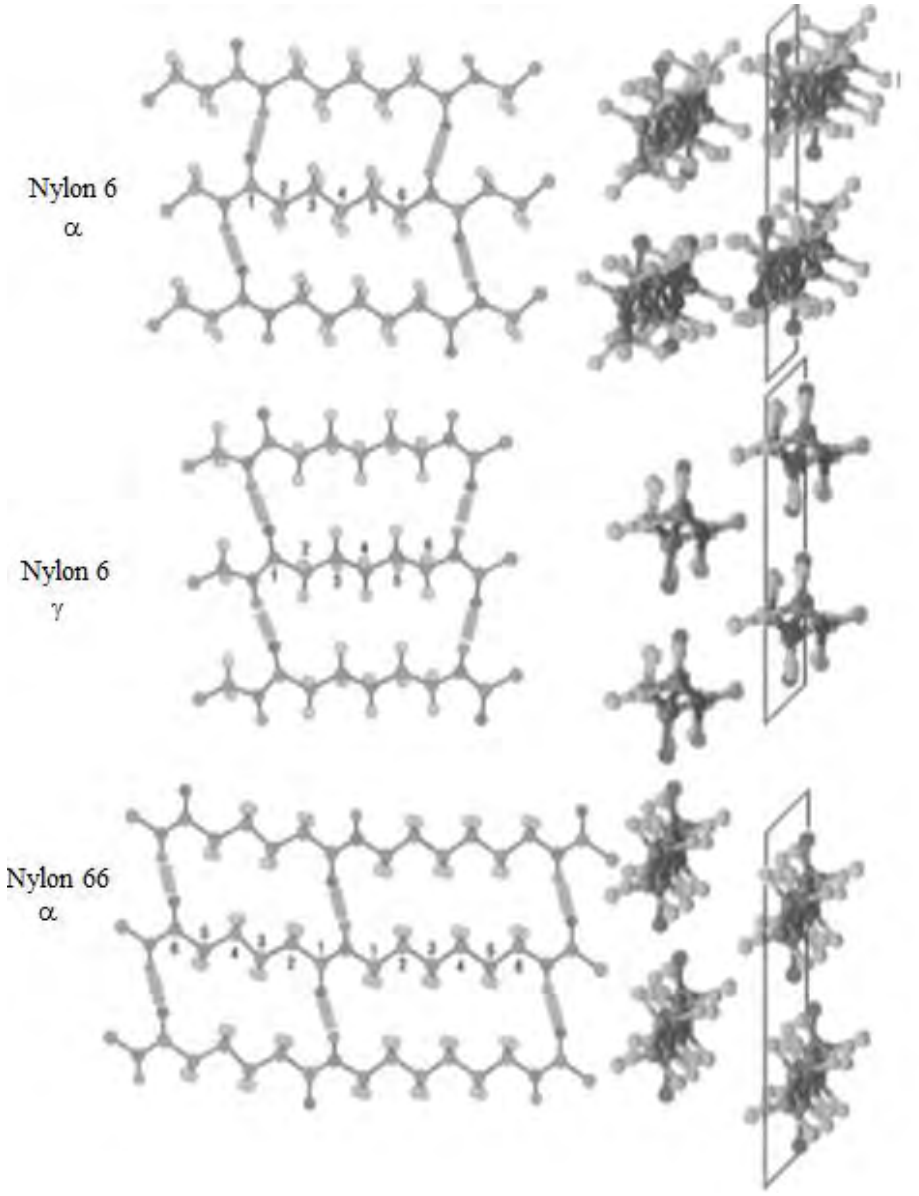

Figure 1.4.2 Structures of the α and γ forms of nylon 6 and nylon 6 6. The left side shows the view of the hydrogen-bonding planes, and the right side shows the view down the chain axis. For the α form of nylon 6, the adjacent chains are antiparallel and the hydrogen bonding is between adjacent chains within the same sheet (bisecting the CH_2 angles). For the γ form of nylon 6, the chains are parallel and the hydrogen-bonding is between chains in adjacent sheets. In nylon 6 6, the chains have no directionality [57]

Brill Transition

The Brill Transition was reported in 1942 by R. Brill, who first observed from X-ray diffraction patterns, that as nylon 6 6 crystals were heated, the two characteristic reflections move together and meet [58][59] (see figure **Figure 1.4.3** b and c). This behavior is due to the structural changes in the lattice parameters during heating, in which basically the two basic equatorial spacings characteristic of the α-form (i.e. those corresponding to intrasheet and intersheet spacings at 0.440 and 0.380 nm, respectively), merge into a single one indicative of a pseudohexagonal modification, which is presumably related to a γ-form [60]. This feature is usually observed in even-even nylons with the logical variations caused by the differences on melting points and density of amide groups along the polymer chain. The structural change is often called "transition", but it is not certain that it has ~~is~~ a themodynamic explanation. Brill transition occurs in a wide temperature range and is not detected in the calorimetric scans. Usually, is assigned as the lowest temperature for which the spacings of the two characteristic equatorial reflections are identical, above the Brill temperature the single spacing increases slightly as a consequence of thermal expansion. Therefore, the crystal structure at equilibrium below this temperature is triclinic and pseudohexagonal above it. Although different theories have been postulated to explain the Brill transition, nowadays it is assumed that it is only the consequence of the conformational motion of methylene groups (i.e. amide interactions remain unaltered) due to the temperature increase that gives rise to a packing change within the crystal [61], The pseudohexagonal structure is actually a special class of triclinic structures in which the projection on a plane normal to the chain axis is metrically hexagonal (see **Figure 1.4.3** a)

The Brill transition is most clearly displayed in X-ray diffration studies, as the two strongest reflections of for example nylon 6 6, the 100 and 010/110 reflections, merge into a single reflection at the transition, as it si shown in **Figure 1.4.3** b and c. Other techniques such as DSC are less sensitive, and in general do not show the Brill transition by way of a distinct endothermic peak [61]. Some explanations for this phenomenon have been given [60]: a) anisotropy of the thermal expansion, b) the development of a tree dimensional network of hydrogen bonds between the chains induced by rotational molecular jumps of 60º at elevated temperatures, c) a transition involving a greater mobility of the methylene groups, while hydrogen bonds remain arranged in a single direction.

A complete understanding of the Brill transition does not yet exist, some features need to be further explained like, the transition temperature to pseudohexagonal phase is not constant for a specific polyamide since it clearly depends on the thermal history of the sample. A pseudohexagonal phase can also be observed for some even nylons in quenched samples, and it has been interpreted as a frozen state arising from the high temperature modification, however , such state is not stable since it reverts quickly to the α-modification when crystals are heated

above their T_g [60], in the present research work some studies were performed in order to understand better this phenomenon.

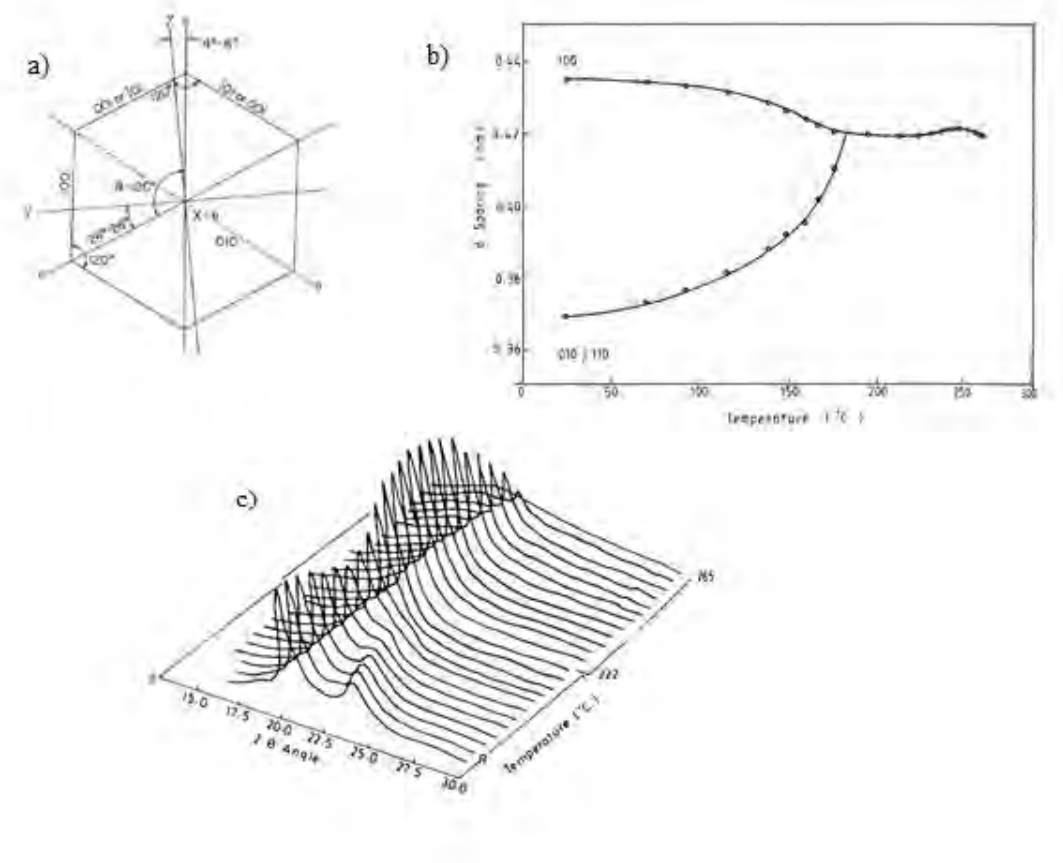

Figure 1.4.3 a) Example of pseudohexagonal structure [62] b) Variation of d_{100} and $d_{010/110}$ spacings with temperature on heating nylon 66 from room temperature to melting [61] c) Thee-dimensional view of the X-ray diffraction patterns of nylon 66 on heating from room temperature to melting [61].

1.4.1 References

[1] L. S. Nair and C. T. Laurencin, "Biodegradable polymers as biomaterials," *Progress in Polymer Science*, vol. 32, no. 8-9, pp. 762-798, Aug. 2007.

[2] R. a Gross and B. Kalra, "Biodegradable polymers for the environment.," *Science (New York, N.Y.)*, vol. 297, no. 5582, pp. 803-7, Aug. 2002.

[3] R. J. Müller, "Biodegradability of polymers: regulations and methods for testing," in *Biopolymers Online*, Wiley Online Library, 2003, pp. 365-374.

[4] M. Okada, "Chemical syntheses of biodegradable polymers," *Synthesis*, vol. 27, pp. 87-133, 2002.

[5] M. Vera, L. Franco, and J. Puiggalí, "Synthesis and Characterization of Poly(glycolic acid-alt-6-aminohexanoic acid) and Poly(glycolic acid-alt-11-aminoundecanoic acid)," *Macromolecular Chemistry and Physics*, vol. 205, no. 13, pp. 1782-1792, Aug. 2004.

[6] E. S. Stevens, *Green plastics: an introduction to the new science of biodegradable plastics*. Princeton University Press, 2002.

[7] I. Armentano, M. Dottori, E. Fortunati, S. Mattioli, and J. M. Kenny, "Biodegradable polymer matrix nanocomposites for tissue engineering: A review," *Polymer Degradation and Stability*, vol. 95, no. 11, pp. 2126-2146, Jun. 2010.

[8] M. Alexandre, "Polymer-layered silicate nanocomposites: preparation, properties and uses of a new class of materials," *Materials Science and Engineering: R: Reports*, vol. 28, no. 1-2, pp. 1-63, Jun. 2000.

[9] L. H. Sperling, *Introduction to Physical Polymer Science*. Hoboken, NJ, USA: John Wiley & Sons, Inc., 2005.

[10] S. Marras, I. Zuburtikudis, and C. Panayiotou, "Nanostructure vs. microstructure: Morphological and thermomechanical characterization of poly(l-lactic acid)/layered silicate hybrids," *European Polymer Journal*, vol. 43, no. 6, pp. 2191-2206, Jun. 2007.

[11] H. Yang et al., "Largely improved toughness of PP/EPDM blends by adding nano-SiO2 particles," *Polymer*, vol. 48, no. 3, pp. 860-869, Jan. 2007.

[12] A. Vermogen, K. Masenelli-Varlot, R. Séguéla, J. Duchet-Rumeau, S. Boucard, and P. Prele, "Evaluation of the Structure and Dispersion in Polymer-Layered Silicate Nanocomposites," *Macromolecules*, vol. 38, no. 23, pp. 9661-9669, Nov. 2005.

[13] M. Zanetti, S. Lomakin, and G. Camino, "Polymer layered silicate nanocomposites," *Most*, vol. 9, pp. 1-9, 2000.

[14] B. Lepoittevin, N. Pantoustier, M. Alexandre, C. Calberg, R. J??r??me, and P. Dubois, "Polyester layered silicate nanohybrids by controlled grafting polymerization," *Journal of Materials Chemistry*, vol. 12, no. 12, pp. 3528-3532, Nov. 2002.

[15] P. Bordes, E. Pollet, and L. Averous, "Nano-biocomposites: Biodegradable polyester/nanoclay systems," *Progress in Polymer Science*, vol. 34, no. 2, pp. 125-155, Feb. 2009.

[16] S. Y. Hwang, E. S. Yoo, and S. S. Im, "Effect of the urethane group on treated clay surfaces for high-performance poly(butylene succinate)/montmorillonite nanocomposites," *Polymer Degradation and Stability*, vol. 94, no. 12, pp. 2163-2169, Dec. 2009.

[17] D. Lincoln, R. Vaia, Z. G. Wang, and B. Hsiao, "Secondary structure and elevated temperature crystallite morphology of nylon-6/layered silicate nanocomposites," *Polymer*, vol. 42, no. 4, pp. 1621–1631, 2001.

[18] J. H. Chang, B. S. Seo, and D. H. Hwang, "An exfoliation of organoclay in thermotropic liquid crystalline polyester nanocomposites," *Polymer*, vol. 43, no. 10, pp. 2969–2974, 2002.

[19] R. K. Shah and D. R. Paul, "Organoclay degradation in melt processed polyethylene nanocomposites," *Polymer*, vol. 47, no. 11, pp. 4075-4084, May. 2006.

[20] C. J. G. Plummer, L. Garamszegi, Y. Leterrier, M. Rodlert, and J.-A. E. Månson, "Hyperbranched Polymer Layered Silicate Nanocomposites," *Chemistry of Materials*, vol. 14, no. 2, pp. 486-488, Feb. 2002.

[21] M. Shibata, Y. Someya, M. Orihara, and M. Miyoshi, "Thermal and mechanical properties of plasticized poly(L-lactide) nanocomposites with organo-modified montmorillonites," *Journal of Applied Polymer Science*, vol. 99, no. 5, pp. 2594-2602, Mar. 2006.

[22] E. Pollet, C. Delcourt, M. Alexandre, and P. Dubois, "Transesterification catalysts to improve clay exfoliation in synthetic biodegradable polyester nanocomposites," *European Polymer Journal*, vol. 42, no. 6, pp. 1330-1341, 2006.

[23] J. W. Cho and D. R. Paul, "Nylon 6 nanocomposites by melt compounding," *Polymer*, vol. 42, no. 3, pp. 1083-1094, Feb. 2001.

[24] C. Lu and Y.-W. Mai, "Influence of Aspect Ratio on Barrier Properties of Polymer-Clay Nanocomposites," *Physical Review Letters*, vol. 95, no. 8, pp. 1-4, Aug. 2005.

[25] J. W. Gilman et al., "Flammability Properties of Polymer−Layered-Silicate Nanocomposites. Polypropylene and Polystyrene Nanocomposites †," *Chemistry of Materials*, vol. 12, no. 7, pp. 1866-1873, Jul. 2000.

[26] B. Jang and C. Wilkie, “The effect of clay on the thermal degradation of polyamide 6 in polyamide 6/clay nanocomposites,” *Polymer*, vol. 46, no. 10, pp. 3264-3274, Apr. 2005.

[27] S. Sinha Ray, “Polymer/layered silicate nanocomposites: a review from preparation to processing,” *Progress in Polymer Science*, vol. 28, no. 11, pp. 1539-1641, Nov. 2003.

[28] M. Okamoto, “Biodegradable polymer/layered silicate nanocomposites: a review,” *J. Ind. Eng. Chem*, vol. 10, pp. 1156–1181, 2004.

[29] T. H. Kim, S. T. Lim, C. H. Lee, H. J. Choi, and M. S. Jhon, “Preparation and rheological characterization of intercalated polystyrene/organophilic montmorillonite nanocomposite,” *Journal of Applied Polymer Science*, vol. 87, no. 13, pp. 2106-2112, Mar. 2003.

[30] S. Sinharay and M. Bousmina, “Biodegradable polymers and their layered silicate nanocomposites: In greening the 21st century materials world,” *Progress in Materials Science*, vol. 50, no. 8, pp. 962-1079, Nov. 2005.

[31] S. Sinharay and M. Bousmina, “Biodegradable polymers and their layered silicate nanocomposites: In greening the 21st century materials world,” *Progress in Materials Science*, vol. 50, no. 8, pp. 962-1079, Nov. 2005.

[32] S. Pavlidou and C. Papaspyrides, “A review on polymer–layered silicate nanocomposites,” *Progress in Polymer Science*, vol. 33, no. 12, pp. 1119-1198, Dec. 2008.

[33] G. G. Odian, *Principles of polymerization*. Wiley-Interscience, 2004.

[34] C. E. J. Carraher, *Introduction to Polymer Chemistry, Second Edition*. Boca Raton , Fl 33487-2742: CRC Press, 2010, p. 534.

[35] P. C. Painter and M. M. Coleman, *Fundamentals of Polymer Science: An Introductory Text, Second Edition*. Lancaster, Pennsylvania 17064 U.S.A: Technomic , 1994, p. 433.

[36] E. MURAYAMA, “Optical Properties of Ringed Spherulites,” *Polym. Prepr. Jpn*, vol. 51, p. 460, 2002.

[37] L. Mandelkern, “Crystallization of polymers,” in *Journal of Polymer Science*, Second., Cambridge, New York, Melbourne, Madrid, Cape Town, Singapore, Sao Paulo: Cambridge University Press, 2002.

[38] J. D. H. HOFFMAN and R. L. MILLER, “Organic Polymers,” in *Advancing Materials Research*, s P. A. Psara and D. H. Langford, Eds. National Academy of Engineering, 1987, p. 251.

[39] M. Stamm, E. W. Fischer, M. Dettenmaier, and P. Convert, “Chain conformation in the crystalline state by means of neutron scattering methods,” *Faraday Discussions of the Chemical Society*, vol. 68, p. 263, 1979.

[40] P. H. Geil, *Polymer single crystals*. Krieger, 1973.

[41] P. J. Flory and D. Y. Yoon, “Molecular morphology in semicrystalline polymers,” *Nature*, vol. 272, no. 5650, pp. 226-229, Mar. 1978.

[42] P. Flory, “On the morphology of the crystalline state in polymers,” *Journal of the American Chemical Society*, vol. 721, no. 1959, 1962.

[43] A. N. Wilkinson and A. J. Ryan, *Polymer processing and structure development*. Kluwer Academic Publishers, 1998.

[44] J. D. Hoffman and R. L. Miller, “Kinetic of crystallization from the melt and chain folding in polyethylene fractions revisited: theory and experiment,” *Polymer*, vol. 38, no. 13, pp. 3151-3212, Jan. 1997.

[45] D. I. Bower, *An introduction to polymer physics*. Cambridge University Press, 2002, p. 124.

[46] J. Lauritzen and J. Hoffman, “Theory of formation of polymer crystals with folded chains in dilute solution,” *Journal of Research of the National Bureau of Standards Section a- Physics and Chemistry*, vol. 64, pp. 73-102, 1960.

[47] J. D. Hoffman, “Polymer Single Crystals. Philip H. Geil. Interscience (Wiley), New York, 1963. xii + 560 pp. Illus. $16,” *Science*, vol. 143, no. 3602, pp. 121-121, Jan. 1964.

[48] J. Hoffman and J. Lauritzen, “Crystallization of bulk polymers with chain folding theory of growth of lamellar spherulites,” *Journal of Research of the National Bureau of Standards A*, vol. 65, pp. 297-336, 1961.

[49] D. M. Sadler and G. H. Gilmer, “A model for chain folding in polymer crystals: rough growth faces are consistent with the observed growth rates,” *Polymer*, vol. 25, no. 10, pp. 1446-1452, 1984.

[50] D. M. Sadler, “Roughness of growth faces of polymer crystals: Evidence from morphology and implications for growth mechanisms and types of folding,” *Polymer*, vol. 24, no. 11, pp. 1401-1409, Nov. 1983.

[51] D. Sadler and G. Gilmer, “Rate-Theory Model of Polymer Crystallization,” *Physical Review Letters*, vol. 56, no. 25, pp. 2708-2711, Jun. 1986.

[52] B. Wunderlich, *Macromolecular physics*, no. 3. Academic Press, 1980.

[53] A. Ravve, *Principles of polymer chemistry*, no. 1. Kluwer Academic/Plenum Publishers, 2000.

[54] A. Rudin, *The elements of polymer science and engineering: an introductory text and reference for engineers and chemists*. Academic Press, 1999.

[55] X. Alex and C. Edward S, “Nylon Plastics Handbook,” M. I. Kohan, Ed. Hanser Publishers: Munich, Vienna and New York, 1995, pp. 108-137.

[56] C. W. Bunn and E. V. Garner, “The Crystal Structures of Two Polyamides (’Nylons'),” *Proceedings of the Royal Society A: Mathematical, Physical and Engineering Sciences*, vol. 189, no. 1016, pp. 39-68, Mar. 1947.

[57] Y. Li and W. a Goddard, “Nylon 6 Crystal Structures, Folds, and Lamellae from Theory,” *Macromolecules*, vol. 35, no. 22, pp. 8440-8455, Oct. 2002.

[58] S. Dasgupta, W. B. Hammond, and W. a Goddard, “Crystal Structures and Properties of Nylon Polymers from Theory,” *Journal of the American Chemical Society*, vol. 118, no. 49, pp. 12291-12301, Jan. 1996.

[59] N. a Jones, S. J. Cooper, E. D. T. Atkins, M. J. Hill, and L. Franco, “Temperature-induced changes in chain-folded lamellar crystals of aliphatic polyamides. Investigation of nylons 2 6, 2 8, 2 10, and 2 12,” *Journal of Polymer Science Part B: Polymer Physics*, vol. 35, no. 4, pp. 675-688, Mar. 1997.

[60] N. a Jones, E. D. T. Atkins, M. J. Hill, S. J. Cooper, and L. Franco, “Chain-Folded Lamellar Crystals of Aliphatic Polyamides. Comparisons between Nylons 4 4, 6 4, 8 4, 10 4, and 12 4,” *Macromolecules*, vol. 29, no. 18, pp. 6011-6018, Jan. 1996.

[61] E. Navarro, L. Franco, J. a Subirana, and J. Puiggali, “Nylon 65 has a Unique Structure with Two Directions of Hydrogen Bonds,” *Macromolecules*, vol. 28, no. 26, pp. 8742-8750, Dec. 1995.

[62] C. Ramesh, A. Keller, and S. J. E. A. Eltink, “Studies on the crystallization and melting of nylon-6,6: 1. The dependence of the Brill transition on the crystallization temperature,” *Polymer*, vol. 35, no. 12, pp. 2483-2487, Jun. 1994.

[63] C. Sclar and L. Carrison, “Optical crystallography of coesite,” *Am. Mineral*, vol. 47, pp. 1292-1302, 1962.

[64] D. K. Platt and R. T. Limited, *Biodegradable polymers: market report*. Rapra Technology, 2006.

2

OBJECTIVES

The present study is part of a larger project with the main objective of developing new polyesters and poly(ester amide)s with improved properties for biomedical and even commodity applications. The incorporation of organically modified silicate clays plays a significant role in improving gas barrier properties, mechanical, thermal, rheological and processability of polymers. The development of biodegradable nanocomposites with improved or modified material properties is an interesting topic since these new materials are expected to replace already existing biodegradable and non-biodegradable commodity plastics in some specific applications.

This project aims to study the influence of clay particles incorporated in a polymer matrix on the crystallization processes, the study of the in situ polymerization kinetics of mixtures of clays and monomers of biodegradable polymers, as well as the influence of nanoparticles on the thermal behavior and morphologic parameters.

The work developed for this doctoral Thesis can be structured in two main sections involving: a) polyamides and b) biodegradable polyesters and poly(ester amide)s. The general objectives have been applied as described below.

2.1.1 Polyamides

We are interested in even-odd and odd-even nylons, which are characterized by a recently postulated structure where hydrogen bonds were established along two different directions. The proposed work implies the following points:

- Choice of representative odd-even and even-odd polyamides with the indicated peculiar hydrogen-bonding scheme.
- Structural characterization of the chosen polyamides (i.e. nylons 56, 65 and 47)
- Gain insight into the structural transition induced by temperature for representative even-odd polyamides as well as for odd-even polyamides having the new structure with two hydrogen-bonding directions.
- To obtain new data on the crystallization behaviour of composites based on polyamides having different intermolecular interactions from those of conventional nylons.
- Preparation of nanocomposites based on nylons with the different structures from at least one representative polyamide.

- Evaluation of the influence of the incorporation of clay particles on the crystallization behaviour of nylons having the peculiar structure with two hydrogen bonding directions.

2.1.2 Biodegradable polyesters and poly(ester amide)s

Polyesters

- Preparation of exfoliated nanocomposites from a new biodegradable polyester constituted by an alternating distribution of glycolic acid and 6-hydroxyhexanoic acid units.
- Study of the influence of clay particles on the isothermal crystallization process
- Evaluation for the pristine and the nanocomposite of the overall crystallization rate, crystal growth rate, and change of morphological parameters during crystallization by means of FTIR spectroscopy, optical microscopy and combined SAXS/WAXD diffraction data.

Poly(ester amide)s

- Choice of a representative polymer of a new family of biodegradable polymers which composition is based on the most usual units existing in polyesters employed for biomedical applications and the commercial polyamides.
- Preparation of nanocomposites of the chosen polymer: an alternating poly(ester amide) constituted by glycolic and 6-aminohexanoic acid units via in situ intercalation polymerization.
- Determination of the effect of different types of montmorillonites, based on three different surfactants (Cloisites 25A, 30B and 20A) on the polymerization kinetics of the monomer salt. In this sense, calorimetric, spectroscopic and diffraction techniques will be combined to gain further insight.
- Study of the crystallization processes (cold and hot crystallizations) of nanocomposites having different structures to get insight into the influence of the clay arrangement on nucleation and crystal growth rate.
- Study of the influence of the incorporation of clay particles on the thermal stability and degradation kinetics of the selected poly(ester amide).

3

EXPERIMENTAL

3.1

Characterization Techniques

3.1.1 Transmission Electron Microscopy (TEM)

- **Method**

In this technique an electron beam is passed through a very thin section of the sample and an image is obtained due to the differences in electron density of the materials. Since there is sufficient difference in electron density between the polymer and the clay to provide a contrast between the two materials it is possible to see the clay dispersion. TEM was carried out with a Philips TECNAI 10 at an accelerating voltage of 100 kV. The specimens were prepared by embedding in a low viscosity modified Spurr epoxy resin and curing them at 40 ºC for a few days and then at 60 ºC for some hours. Ultrathin sections (less than 100nm) were cut at room temperature using Sorvall Porter-Blum microtome equipped with a diamond knife. Finally, the sections were collected in a though filled with water and lifted onto carbon coated copper grids. To prevent diffusion of the epoxy resin into the polymer film, a thin layer of carbon was evaporated over the film surface.

3.1.2 X-ray Scattering

- **Experimental Technique**

X-rays are electromagnetic waves of very short wavelength; The X-rays used in polymer characterization have wavelengths of about 0.1-0.2 nm. Two types of X-ray scattering are used in the study of polymers, *wide-angle X-ray diffraction* (WAXD) and *small-angle X-ray scattering* (SAXS) depending on scale of the features studied. SAXS studies are performed on polymers for the investigation on structures on a much larger scale than the separations of crystal planes, which implies scattering angles much smaller than those used in WAXD.

Scattering from structures of any size takes place at well-defined angles. The scattering is usually called *diffraction* only when the structures are periodic. The most important periodic structures suitable for WAXD investigations are crystals, which are periodic in three dimensions [43] .

X-rays are produced by bombarding a metal target with a beam or high voltage electrons. This is done inside a vacuum tube. The target metal as well as the applied voltage determines the wavelength of X-rays produced. The diffracted X-rays may be detected by their action on photographic films or plates, or by means of radiation counter and electronic equipment feeding data to a computer [63]. It is possible to obtain X-ray reflections from a series of planes inside the crystal. The orientation and interplanar spacings of these planes are defined by the three integers *h, k, l* called Miller indices of a plane or a face [64]. A given set of planes with indices *h*, *k*, *l* cut the *a*-axis of the unit cell in *h* sections, the *b* axis in *k* sections and the *c* axis in *l* sections. A zero indicates that the planes are parallel to the corresponding axis e. g. **Figure 3.1.1** shows the 2 0 0 planes which cut the *a* axis in half but are parallel to *b* and *c* axes.

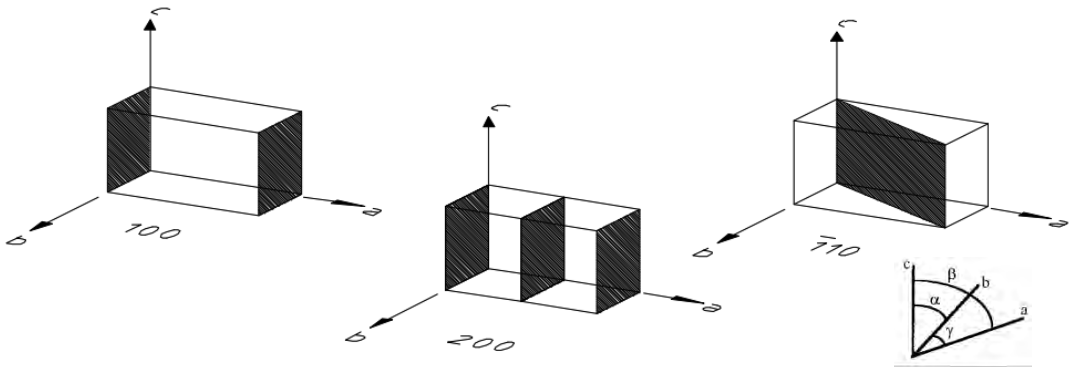

Figure 3.1.1 Example of three dimensional diffraction, where three indices *hkl* become the order of diffraction along the unit cell axes *a*, *b* and *c* respectively.

Diffraction can easily be understood in terms of the reflection of the incident beam by the different crystallographic planes. Thus, the intensity of rays reflected by a pair of planes with an interplanar spacing *d* (**Figure 3.1.2**) is maximum when the waves are in phase. Equation 3.1 corresponds to the Bragg's law, which relates the angle of the incident beam, the interplanar spacing and the wavelength of the radiation. The geometric derivation is shown in **Figure 3.1.2**.

(3.1)

$$n\lambda = 2d\sin\theta$$

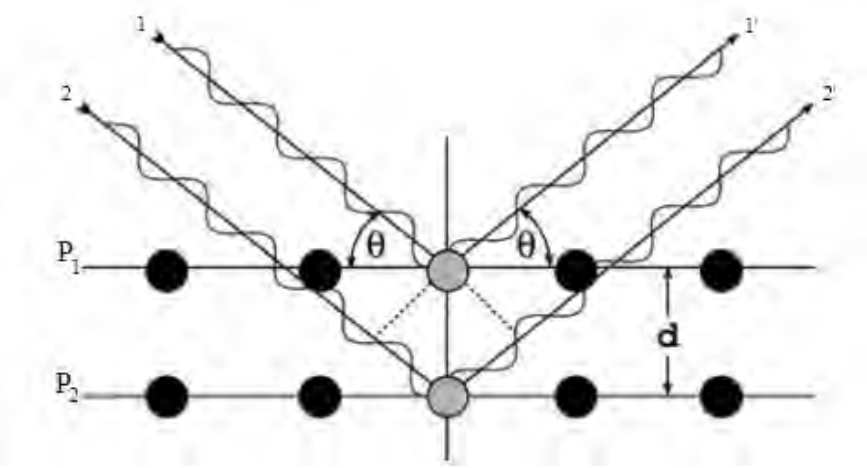

Figure 3.1.2 Geometric derivation of Bragg's law: Constructive interference occurs when the delay between waves scattered from adjacent lattice planes given by 1 + 1' and 2 + 2' is an integer multiple of the wavelenght λ [64].

The process of reflection is described here in terms of incident and diffracted rays, each making an angle θ with a fixed crystal plane. Reflections occur from planes set at angle θ with respect to the incident beam and generates a reflected beam at an angle 2θ from incident beam. The possible *d* spacing defined by the indices *hkl* (d_{hkl}) are determined by the shape of the unit cell. Rewriting Bragg's law:

(3.2)

$$2d_{hkl}\sin\theta = \lambda$$

The spacing d_{hkl} is easily calculated for a given measured value of θ and with a set of experimental spacings is possible to determine the dimensions of the unit cell (*a*, *b*, *c*, α, β and γ) through the indexing process. For example, the following equation relates indices, cell parameters and spacings for an orthorhombic unit cell (α, β and γ are 90º): $\frac{1}{d_{hkl}} = \sqrt{\frac{h^2}{a^2} + \frac{k^2}{b^2} + \frac{l^2}{c^2}}$

Figure 3.1.3 shows some important planes for the special case of a lattice with a rectangular projection on a plane perpendicular to the *c*-axis. Integers *hkl* label the points of intersection of three sets of equally spaced parallel planes. These planes can be chosen so that this new lattice (called reciprocal lattice) has the next property: for all values of *h*, *k* and *l* the line joining the origin of the reciprocal lattice to the point *hkl* is of length 1/ d_{hkl} and is normal to the *hkl* planes of the real lattice. The reciprocal-lattice plane for a given value of *l* and all values of *h* and *k* is perpendicular to the *c*-axis and is distant *l/c* from the origin of the reciprocal lattice.

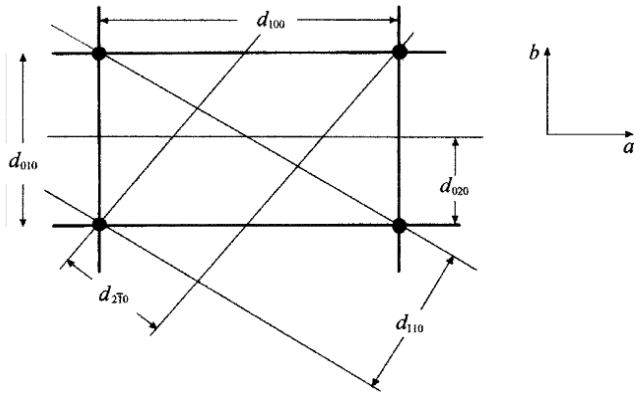

Figure 3.1.3 Planes for a lattice with a rectangular projection on a plane perpendicular to the *c*-axis [43].

However, the intensities of the reflections are determined by the distribution of the electrons in the cell. The highest electron density are found around atoms. Therefore, the intensities depend on what kind of atoms are present and where in the unit cell they are located. Planes going through areas with high electron density will reflect strongly, planes with low electron density will give weak intensities.

Method

In X-ray polymer diffraction it is normally distinguish among single crystal, polycrystalline or powder applications and fiber pattern diffraction. The single crystal sample is a perfect (all unit cells aligned in a perfect extended pattern) crystal with a cross section of about 0.3 mm. The single crystal diffractometer and associated computer package is used mainly to elucidate the molecular structure of novel compounds, either natural products or synthetic molecules [65]. However this kind of samples are very difficult to obtain for polymers.

Powder diffraction is mainly used for "finger print identification" of various solid materials, e.g. asbestos, quartz. In powder or polycrystalline diffraction it is important to have a sample with a smooth plane surface. The ideal sample has a random distribution of all possible *hkl* planes. Only crystallites having reflecting planes (*hkl*) parallel to the specimen surface will contribute to the reflected intensities. If a sample is truly random, each possible reflection from a given set of h, k, l planes will have an equal number of crystallites contributing to it. The specimen must be rocked through the glancing angle θ in order to produce all possible reflections.

Fiber diffraction patterns are good option to analyze structure of polymer crystallites since a fiber pattern contains information about the crystal structure of the polymer. It also contains information about the size of the crystallites and about their degree of alignment [66]. Crystalline polymers fibers must be stretched to be oriented in order to obtain a fiber diffraction

pattern. Thus highly oriented fiber consists of a very large number of crystallites, which all have one particular crystallographic direction oriented almost parallel to the fiber axis (usually the chain axis, the *c*-axis) and the remaining directions are oriented randomly around this direction. Assuming that the axis of the fiber is normal to the incident X-ray beam, the scattering expected is therefore almost exactly the same as that which would be observed from a single crystal with its *c*-axis parallel to the fiber axis if this crystal were rotated continuously around the c-axis during the exposure of the X-rays.

Highly oriented polymer fiber diffraction pattern shows the same features that a rotating crystal, when planes are parallel to fiber axis: only four diffraction spots lying at particular points on the imaginary circle of the corresponding powder-pattern would be observed. These points are symmetrically placed with respect to the plane that contains the incident X-ray beam and normal to the rotation axis at it is shown in **Figure 3.1.4**. The radius of the (imaginary) powder circle and the positions of the four spots on it for a particular type of crystal plane depend on the indices of the planes.

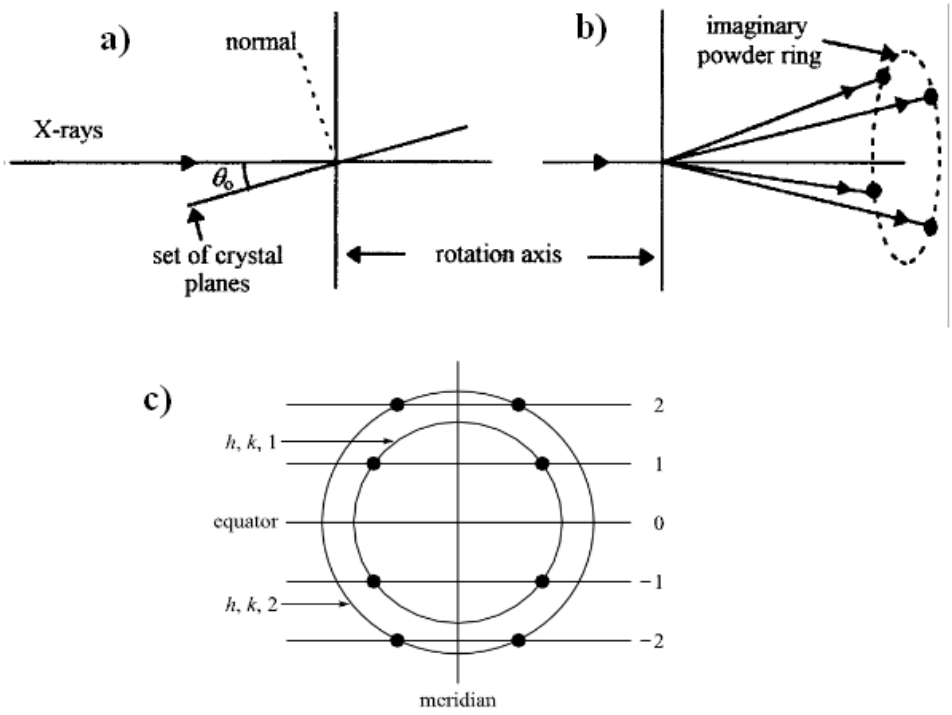

Figure 3.1.4 (a) and (b) show the production of four diffraction spots corresponding to a given set of planes for a rotation pattern: (a) the starting position, where θ0 is greater than the Bragg angle; and (b) the location of the four diffraction spots corresponding to a given set of planes. c) is a schematic diagram showing the relationship among layer lines, powder rings and diffraction spots in a fiber diagram. For simplicity the layer lines are shown straight and the powder rings as circles [43].

Powder ring corresponds to a particular set of values *h*, *k* and *l* and it follows that diffraction spots can be seen only at those places where the l^{th} layer line crosses the position where a powder circle corresponding to the same value of *l* would have been seen, as shown

schematically in **Figure 3.1.4** c. Each circle and pair of layer lines (i.e. for ±*l*) gives rise to the four spots previously shown to arise from any particular set of planes. Because there can be various sets of planes with different values of *h* and *k* but the same value of *l* there will be several pairs of spots on each layer line. The layer line for $l = 0$ is called the equator and the normal to this through the point where the incident X-ray beam would strike the film is called the meridian. **Figure 3.1.5** shows, as an example, the X-ray scattering pattern obtained for an oriented fiber of syndiotactic propylene.

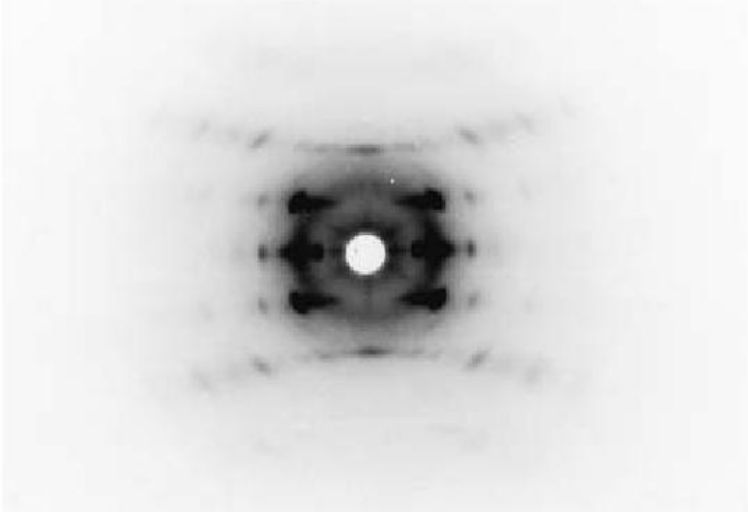

Figure 3.1.5 Fibre pattern from oriented syndiotactic polypropylene, drawn to a draw ratio of about 5 at 109ºC [43].

X-ray diffraction (XRD) is useful to characterize the morphology of the polymer nanocomposites as it enables the average basal spacing (distance between two clay platelets) to be calculated. This spacing is often referred as the d_{001} spacing where *d* refers to the spacing between the planes in a lattice and *001* refers to the indics of the involved reflection. An increase in the spacing indicates an increase in the extent of intercalation and the point where the XRD peak can no longer be observed. The clay is through to become fully exfoliated within the polymer matrix, since in an exfoliated nanocomposite the clay platelets will be at larger distances from each other with random orientation. This means that there will be no average distance between the platelets and therefore no XRD peak will be observed.

Figure 3.1.6 shows an example of intercalated nanocomposite, and an exfoliated one. The XRD patterns that have to be corroborated with TEM analysis (**Figure 3.1.6** b) to draw a conclusion about nanocomposite structure.

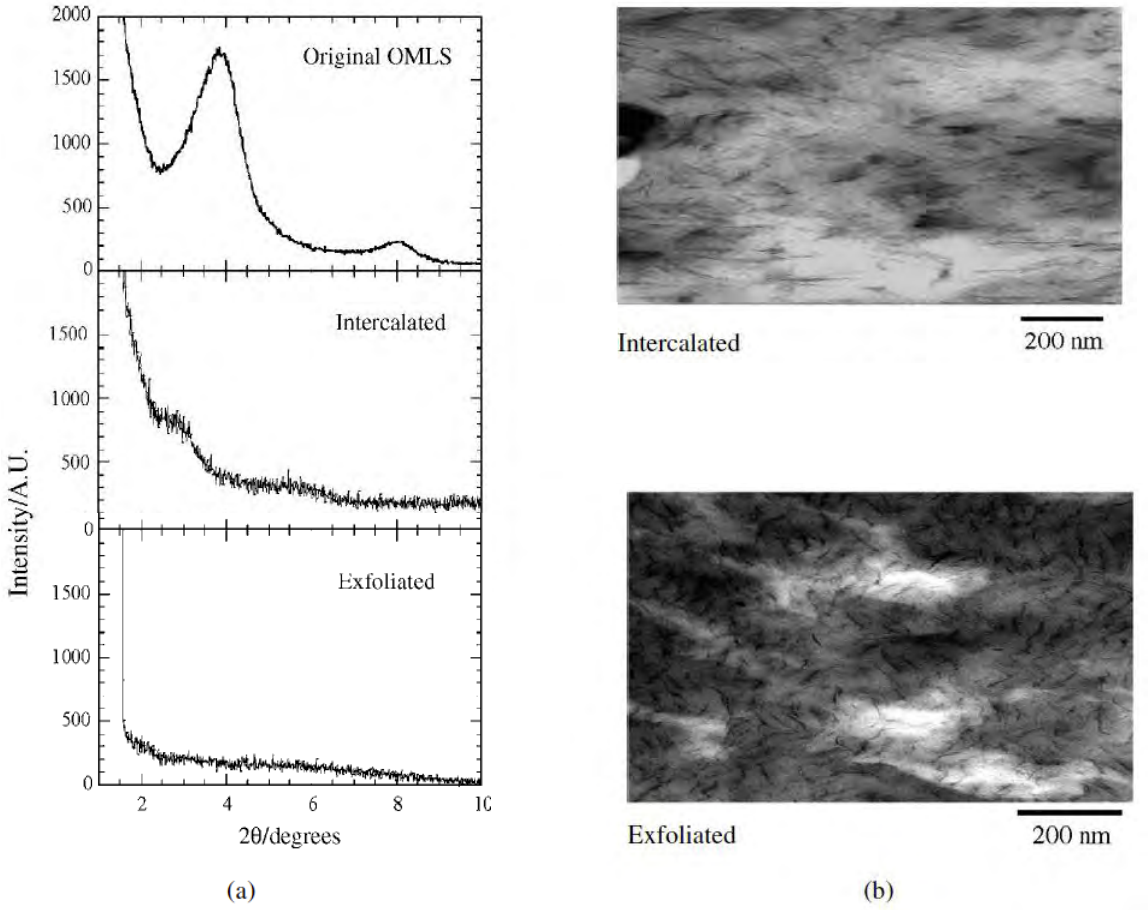

Figure 3.1.6 (a) WAXD patterns and (b) TEM images of three different types of nanocomposites .

3.1.3 Synchrotron Radiation

Experimental Technique

Synchrotron radiation is the electromagnetic radiation emitted by high-speed electrons spiraling along the lines of force of a magnetic field. Depending on the electron's energy and the strength of the magnetic field, the maximum intensity will occur as radio waves, visible light or X-rays, the radiation is highly polarized and the intensity greatly exceed other sources (**Figure 3.1.7** shows the large spectral region covered by the synchrotron radiation). These properties make synchrotron radiation a recognized and powerful research tool for all scientific areas.

In this research work simultaneous small and wide angle X-ray diffraction (SAXS-WAXD) techniques were used. These techniques allow to investigate at different length scales the structure and dynamics of the material of interest. Simultaneous SAXS/WAXD permits studding structural and morphological changes in real time. During the experiment, two position-sensitive detectors are placed in different locations covering a wide angular range, of about four orders of magnitude of scattering angle. The scheme of the experimental setup for

simultaneous SAXS-WAXD it is shown in **Figure 3.1.8.** The WAXD provides information about the molecular and atomic ordering of materials, while SAXS is sensitive to heterogeneities in the electron density on a larger scale (1-10^2 nm).

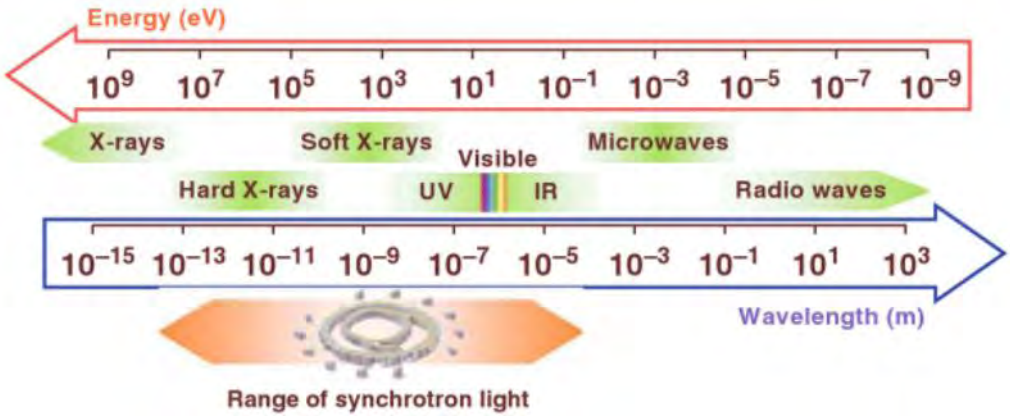

Figure 3.1.7 Energy and wavelength scales for a very large range of the electromagnetic wave field. Showing the large spectral region covered by the synchrotron radiation [67] .

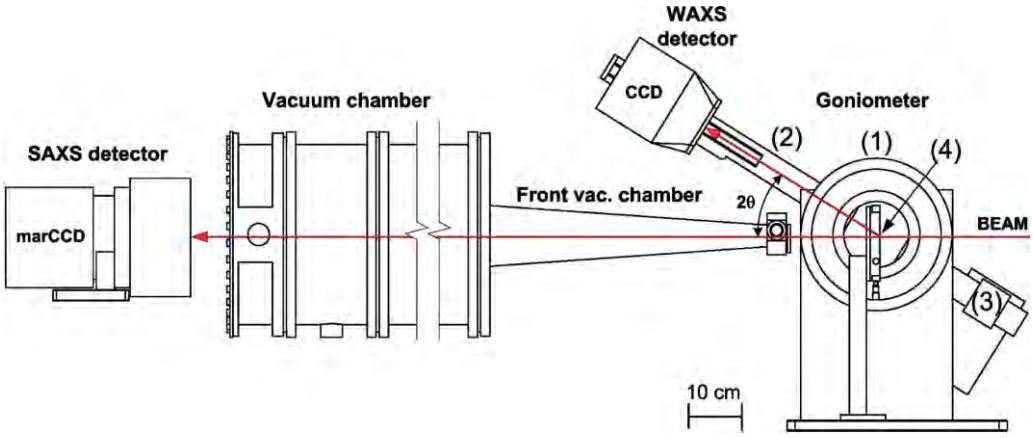

Figure 3.1.8 Scheme of the experimental setup for simultaneous SAXS-WAXS experiments at the BM16 beam line. The main parts of the goniometer are rotation unit (1), arm (2), counterweight (3), and hot stage (4). The vacuum chamber is made of cylindrical parts of different lengths and a square based truncated pyramid at the front [68].

Method

The collected data was then treated with different scientific software. For WAXD experiments, deconvolution was performed and the overall crystallinity of the samples as well as morphology were evaluated. On the other hand for SAXS experiments the correlation function analysis was

made using CORFUNC software, that obtains the Fourier transform of the scattering curve to get structural parameters describing the sample[69].

3.1.4 Differential Scanning Calorimetry

- **Experimental Technique**

Differential scanning calorimetry (DSC) can detect changes in the heat capacity caused by chemical or physical transitions. In the case of polymer materials, transitions such as glass transition (T_g), melting points (T_m), crystallization and rate of cure can be detected. These transitions generally depend on the polymer architecture, molecular weight, chemical composition and thermal history. DSC works by measuring the heat flow (the supplier per unit time) required to either heat the sample at a constant rate (non – isothermal studies) or to maintain a sample at a constant temperature (isothermal, this is useful for example in some crystallization or polymerization experiments). The signal in a DSC experiment is related to the difference between the thermal response of the sample and reference cells as the two are heated or cooled at the same rate or maintained at a constant temperature[70]. **Figure 3.1.9** shows the main features that can be observed in DSC polymer thermograms.

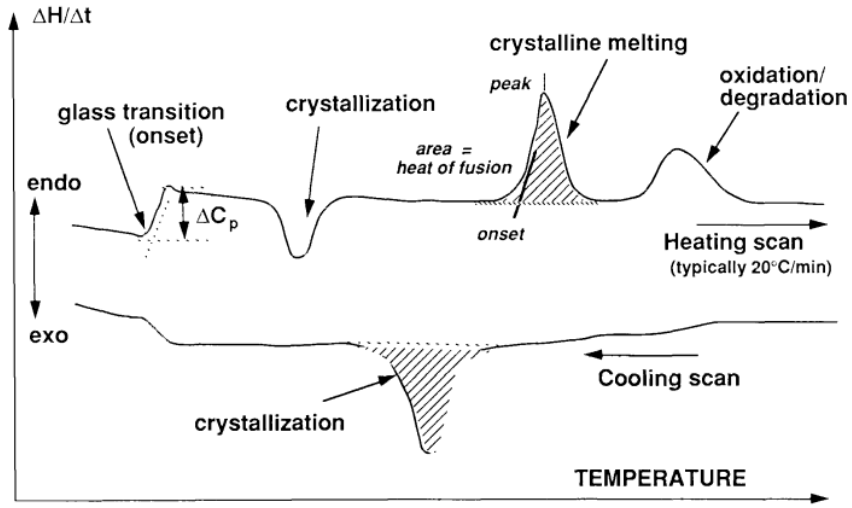

Figure 3.1.9. Typical polymer DSC thermograms [71].

3.1.5 Thermogravimetric Analysis (TGA)

- **Experimental Technique**

Thermogravimetric analysis measures the amount and rate of change in the weight of a material as a function of temperature or time in a controlled atmosphere. TGA is particularly useful for

the following measurements: thermal stability, degradation kinetics, composition etc. It makes continuous weighing of a small sample as the temperature is increased at a programmed linear rate. The thermograms obtained illustrate weight losses due to desorption of gasses or decomposition. **Figure 3.1.10** shows a typical thermogram of an elastomer compound. The kinetics of degradation process may be characterized to model and predict cure, thermal stability an aging due to thermal and thermo-oxidative processes [72]. In this way kinetic information is crucial for evaluating the times and temperatures associated with the processing, service lifetimes, and storage of materials. It is also of value for understanding the mechanisms of thermal processes. In a pragmatic sense the objective of kinetics is often to provide a mathematical relationship between time, temperature and conversion. In this research work TGA experiences were conducted to perform kinetic studies.

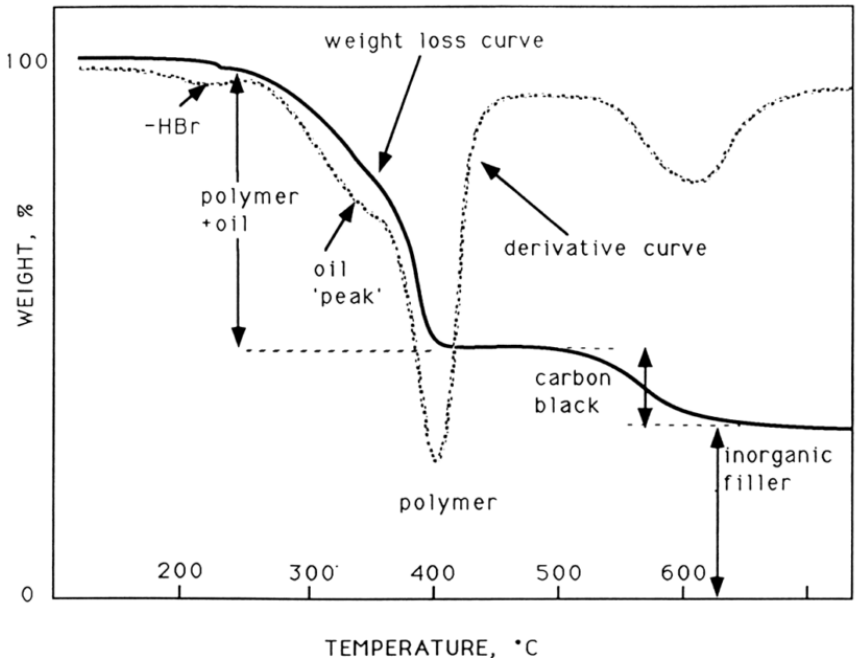

Figure 3.1.10 Thermogram showing the mass los curves of an elastomer compound [72]

Method

Kinetics studies in TGA polymer analysis are based in *solid-state kinetics* theory. Some mathematical methods have been developed to evaluate *solid-state kinetics*. They generally fall into two categories: model-fitting and model-free (isoconversional) methods. Model-fitting methods determine the kinetic triplet: model ($f(\alpha)$), frequency factor (A) and activation energy (E) whereas isoconversional methods generate the activation energy as a function of reaction progress without modelistic assumptions. The assumptions of solid-state kinetics as the methods used in this research work are explained here.

To perform *solid-state kinetics* analysis with thermal analytical methods. Weight loss data are converted to a normalized form called conversion fraction (α). This conversion fraction ranges from 0 and 1 and is a measure of reaction progress as a function of time or temperature.

There are many types of solid-state reactions but in TGA the focus is on reactions that involve single solid reactant. A simple reaction is one which follows the reaction scheme below.

$$A_{(s)s} \rightarrow B_{(s)} + C_{(g)}$$

Where *A* decomposes thermally to produce a solid *B* and a gas *C*. The conversion rate law for an elementary solid – state reaction depend on factors such as rate of nuclei formation, interface advance, diffusion and/or geometrical shape of solid particles. These factors lead to several decomposition models that are summarized in **Table 3.1.1**.

- **Isothermal analyses**

In an isothermal degradation test, the experimental data must fit the standard kinetic equation:

(3.3)

$$\frac{d\alpha}{dt} = k(T)f(\alpha)$$

where $k(T)$ is the kinetic rate constant, t is time, a is the normalized degree of degradation or conversion, and $f(\alpha)$ is the differential conversion function.

The conversion is calculated in terms of mass loss as:

(3.4)

$$\alpha = \frac{W_0 - W}{W_0 - W_\infty}$$

where W_0, W, and W_∞ are, respectively, the initial polymer weight, the actual weight at each point of the degradation curve, and the final weight at the end of the degradation process.

The temperature dependence of the kinetic rate constant is assumed to follow an Arrhenius form:

(3.5)

$$K = Ae^{-\frac{E_a}{RT}}$$

where *T* is the absolute temperature, R is the gas constant, and *A* and *E* are the preexponential and the activation energy for the decomposition reaction, respectively.

The major disadvantage of this approach is that complete degradation may require significant amounts of time. However, the simplicity of analysis and the fact that no approximations are needed must be pointed out. For predictive purposes, it is possible to create an isothermal

master curve by simply scaling the raw data with time. This is accomplished by dividing the time on the abscissa axis by the time required for a conversion of 0.5 ($t_{1/2}$). In this way, degradation curves obtained at different temperatures collapse onto a single one.

- **Dynamic Methods**

According to the nonisothermal *solid-state kinetic* theory, thermal degradation of a polymer can be expressed by the following function:

$$\frac{d\alpha}{dT} = \frac{A}{\beta} e^{-\frac{E_a}{RT}} f(\alpha) \tag{3.6}$$

where β is the heating rate and the other terms have the above indicated meaning.

The integration of $f(\alpha)$ leads to:

$$g(\alpha) = \frac{A}{\beta} \int_0^T e^{-\frac{E_a}{RT}} dT \tag{3.7}$$

The differential ($f(\alpha)$) and the integral ($g(\alpha)$) conversión functions may take different forms according to the solid state reaction mechanism. These are summarized in **Table 3.1.1**.

The most probable mechanism can be determined by using the Coats–Redfern approximation [73] to solve eq. (3.7) and considering that $2RT/E \ll 1$, this equation may be rewritten as:

$$\ln \frac{g(\alpha)}{T^2} = \ln \left(\frac{AR}{\beta E} \right) - \frac{E}{RT} \tag{3.8}$$

For a given kinetic model, the linear representation of $\ln[g(\alpha)/T^2]$ versus $1/T$ makes it possible to determine E and A from the slope and the ordinate at the origin, respectively. The model can be selected taking into account the linear regression coefficient (r) and the agreement of the activation energy with that estimated by isoconversional methods such as the Kissinger–Akahira–Sunose (KAS) [74], Friedman [75], Kissinger [74] and Flynn–Wall–Ozawa (FWO) methods [76], [77]. The KAS method is based on eq.(3.9) which is obtained by reordering the above-indicated equation of the integral conversion function:

$$\ln \frac{\beta}{T^2} = \ln \left(\frac{AR}{g(\alpha)E} \right) - \frac{E}{RT} \tag{3.9}$$

For each degree of conversion the activation energy can be obtained from the slope of linear representation of $\ln(\beta/T^2)$ versus $1/T$.

The Friedman method is based on eq. (3.10), which in this case derives from the logarithmic form of the rate eq. (3.6):

$$\ln\left(\beta\frac{d\alpha}{dT}\right) = \ln A + \ln f(\alpha) - \frac{E}{RT} \tag{3.10}$$

For each degree of conversion, the plot of ln $\beta\ d\alpha/dT$ versus *1/T*, obtained from thermograms recorded at several heating rates, should be a straight line whose slope allows the evaluation of the activation energy.

The Kissinger equation can be considered a particular case of eq. (3.9) applied for $\alpha = \alpha_{max}$ (the conversión at the maximum weight loss rate) and assuming $f(\alpha) = (1-\alpha)^n$:

$$\ln\frac{\beta}{T_{max}^2} = \ln\frac{AR}{E} + ln[n(1-\alpha_{max})^{n-1}] - \frac{E}{RT} \tag{3.11}$$

where T_{max} is the temperature at the inflection point of the thermodegradation curves, which corresponds to the maximum reaction rate. In this case, the activation energy can be determined from the slope of the linear plot of ln (β/T_{max}^2) versus ln $1/T_{max}$. It is now well-known that this method may also be applied when *f*(α) correspond to other kinetic models [78].

The Flynn–Wall–Ozawa eq. (3.12) is one of the integral methods by which the activation energy can be determined without knowing the reaction order: [76], [77]

$$\ln\beta = \ln\frac{0.0048AE}{g(\alpha)R} - 1.0516\frac{E}{RT} \tag{3.12}$$

The activation energy can be calculated for different conversions from the slopes of the linear plots of ln β versus 1/*T*.

Another method used to evaluate the kinetic parameters is the IKP (invariant kinetic parameters) Method [79], [80] . According to this procedure, the values of the activation parameters, obtained from various forms of *f*(α), are correlated through an apparent compensation effect:

$$\ln g(\alpha) = \alpha^*\beta^*E \tag{3.13}$$

Where α^* and β^* are constants (the compensation effect parameters).

To apply this method, the values of ln A_i versus E_i at each heating rate (β_i) were plotted. These parameters were obtained using the Coats–Redfern methodology for the different kinetic models studied (**Table 3.1.1**) The plot allowed the α_i^* and β_i^* constants to be determined from the intersection at the origin and the slope, respectively. Furthermore, the straight lines ln A_i versus

E_i for each heating rate should intersect at a point, which corresponds to the true values of A and E. These are called the invariant activation parameters (A_{inv}, E_{inv}). Certain variations of the experimental conditions actually determine a region of intersection in the ln A, E space. For this reason, the evaluation of the invariant activation parameters is performed using the following relation:

(3.14)

$$\ln A_{inv} = \alpha_i^* + \beta_i^* E_{inv}$$

Thus, a plot of α_i^* versus β_i^* is actually a straight line whose parameters allow evaluation of the invariant activation parameters.

Table 3.1.1 solid-state rate expressions for different reaction models [72].

Model	Differential form $f(\alpha)=1/k\ d\alpha/dt$	Integral forma $g(\alpha)=kt$
Nucleation models		
Power law (P2)	$2\ \alpha^{(1/2)}$	$\alpha^{(1/2)}$
Power law (P3)	$3\ \alpha^{(2/3)}$	$\alpha^{(1/3)}$
Power law (P4)	$4\ \alpha^{(3/4)}$	$\alpha^{(1/4)}$
Avarami-Erofeyev (A2)	$2(1-\alpha)[-\ln(1-\alpha)]^{1/2}$	$[-\ln(1-\alpha)\ ]^{1/2}$
Avarami-Erofeyev (A3)	$3(1-\alpha)[-\ln(1-\alpha)]^{2/3}$	$[-\ln(1-\alpha)\ ]^{1/3}$
Avarami-Erofeyev (A4)	$4(1-\alpha)[-\ln(1-\alpha)]^{3/4}$	$[-\ln(1-\alpha)\ ]^{1/4}$
Prout-Tompkins (B1)	$\alpha\ (1-\alpha)$	$\ln[\alpha/(1-\alpha)]+c^b$
Geometrical contraction models		
Contracting area (R2)	$2(1-\alpha)^{1/2}$	$[1-(1-\alpha)^{1/2}]$
Contracting volume (R3)	$3(1-\alpha)^{2/3}$	$[1-(1-\alpha)^{1/3}]$
Diffusion models		
1-D Diffusion (D1)	$1/(2\alpha)$	α^2
2-D Diffusion (D2)	$[-\ln(1-\alpha)]^{-1}$	$[(1-\alpha)\ln(1-\alpha)]+\alpha$
3-D Diffusion-Jander (D3)	$[3(1-\alpha)^{2/3}] / [2(1-(1-\alpha)^{1/3})]$	$[1-(1-\alpha)^{1/3}]^2$
Ginstling-Brounshtein (D4)	$3/[2((1-\alpha)^{-1/3}-1)]$	$1-(2\alpha/3)-(1-\alpha)^{2/3}$
Reaction-order models		
Zero-order (F0/R1)	1	α
First-order (F1)	$(1-\alpha)$	$-\ln(1-\alpha)$
Second-order (F2)	$(1-\alpha)^2$	$(1-\alpha)^{-1}-1$
Third-order (F3)	$(1-\alpha)^3$	$0.5\ [(1-\alpha)^{-2}-1]$

[a] In some references $f(\alpha)$ and $g(\alpha)$ have opposite designations.

[b] constant of integration.

3.1.6 Fourier Transform Infrared Spectroscopy (FTIR)

- **Experimental Technique**

Infrared spectroscopy is a technique based on the vibration of the atoms of a molecule. An infrared spectrum is obtained by passing infrared radiation though a sample and determining what fraction of the incident radiation is absorbed at a particular energy. This energy of absorption corresponds to the frequency of a vibration of a part of a sample molecule [81].

For a molecule to show infrared absorption it must possess a specific feature, an electric dipole moment of the molecule must change during the vibration. A molecule containing N atoms has 3N normal vibration modes, including rotational and transitional motions of the entire molecule. In polymers the infrared absorption spectrum are of the very simple due to the occurrence of normal vibrations at almost same frequency.

The main type of molecular vibrations are stretching (symmetrical and asymmetrical) and bending (scissoring, wagging, twisting and rocking). As different kinds of bonds, and thus different functional groups absorbed infrared radiation of different wave length, analysis of absorption reveals details about the molecular structure of the sample.

- **Method**

This technique was used to perform crystallization and polymerization dynamic studies, identifying functional groups that appear while temperature was varied, the methodology developed to treat the data obtained during this experiments allowed to evaluate polymerization and crystallization kinetics.

3.1.7 Nuclear Magnetic Resonance Spectroscopy (NMR)

- **Experimental Technique**

Nuclear Magnetic Resonance (NMR) spectroscopy can be used to study chain configuration, sequence distribution, and microstructure in polymers. It utilizes the property of spin (angular momentum and its associated magnetic moment) possessed by nuclei whose atomic number and mass number are not both even, such as isotopes of hydrogen and ^{13}C, ^{15}N, ^{17}O and ^{19}F. When a strong magnetic field is applied to the material containing such nuclei, the energy level splits into two, representing states with spin parallel and antiparallel to the field. Transitions between the states lead to absorption or emission of an energy [63]

The most common nuclei examined by NMR ^{1}H and ^{13}C, since these are the most abundant NMR sensitive nuclei [71]. The resonant frequencies can be used to determine molecular structures. ^{1}H resonances are fairly specific for the types of carbon they are attached to, these

resonances may be split into multiples. The magnitude of splittings, and the multiplicity, can be used to better determine the chemical structure in the vicinity of hydrogen. Since only hydrogen is observed, any feature in the molecule without attached hydrogen can only be inferred, and this turns out impossible to resolve complex structures or molecules. ^{13}C resonance can be used to determine skeleton of an organic molecule.

NMR is a very powerful tool, to characterize compound structure, and may provide a general characterization by functional groups. In this research work NMR was often used to verify purity and non – degradation of sample material.

3.1.8 References

[1] L. S. Nair and C. T. Laurencin, "Biodegradable polymers as biomaterials," *Progress in Polymer Science*, vol. 32, no. 8-9, pp. 762-798, Aug. 2007.

[2] R. a Gross and B. Kalra, "Biodegradable polymers for the environment.," *Science (New York, N.Y.)*, vol. 297, no. 5582, pp. 803-7, Aug. 2002.

[3] R. J. Müller, "Biodegradability of polymers: regulations and methods for testing," in *Biopolymers Online*, Wiley Online Library, 2003, pp. 365-374.

[4] M. Okada, "Chemical syntheses of biodegradable polymers," *Synthesis*, vol. 27, pp. 87-133, 2002.

[5] M. Vera, L. Franco, and J. Puiggalí, "Synthesis and Characterization of Poly(glycolic acid-alt-6-aminohexanoic acid) and Poly(glycolic acid-alt-11-aminoundecanoic acid)," *Macromolecular Chemistry and Physics*, vol. 205, no. 13, pp. 1782-1792, Aug. 2004.

[6] E. S. Stevens, *Green plastics: an introduction to the new science of biodegradable plastics*. Princeton University Press, 2002.

[7] I. Armentano, M. Dottori, E. Fortunati, S. Mattioli, and J. M. Kenny, "Biodegradable polymer matrix nanocomposites for tissue engineering: A review," *Polymer Degradation and Stability*, vol. 95, no. 11, pp. 2126-2146, Jun. 2010.

[8] M. Alexandre, "Polymer-layered silicate nanocomposites: preparation, properties and uses of a new class of materials," *Materials Science and Engineering: R: Reports*, vol. 28, no. 1-2, pp. 1-63, Jun. 2000.

[9] L. H. Sperling, *Introduction to Physical Polymer Science*. Hoboken, NJ, USA: John Wiley & Sons, Inc., 2005.

[10] S. Marras, I. Zuburtikudis, and C. Panayiotou, "Nanostructure vs. microstructure: Morphological and thermomechanical characterization of poly(l-lactic acid)/layered silicate hybrids," *European Polymer Journal*, vol. 43, no. 6, pp. 2191-2206, Jun. 2007.

[11] H. Yang et al., "Largely improved toughness of PP/EPDM blends by adding nano-SiO2 particles," *Polymer*, vol. 48, no. 3, pp. 860-869, Jan. 2007.

[12] A. Vermogen, K. Masenelli-Varlot, R. Séguéla, J. Duchet-Rumeau, S. Boucard, and P. Prele, "Evaluation of the Structure and Dispersion in Polymer-Layered Silicate Nanocomposites," *Macromolecules*, vol. 38, no. 23, pp. 9661-9669, Nov. 2005.

[13] M. Zanetti, S. Lomakin, and G. Camino, "Polymer layered silicate nanocomposites," *Most*, vol. 9, pp. 1-9, 2000.

[14] B. Lepoittevin, N. Pantoustier, M. Alexandre, C. Calberg, R. J??r??me, and P. Dubois, "Polyester layered silicate nanohybrids by controlled grafting polymerization," *Journal of Materials Chemistry*, vol. 12, no. 12, pp. 3528-3532, Nov. 2002.

[15] P. Bordes, E. Pollet, and L. Averous, "Nano-biocomposites: Biodegradable polyester/nanoclay systems," *Progress in Polymer Science*, vol. 34, no. 2, pp. 125-155, Feb. 2009.

[16] S. Y. Hwang, E. S. Yoo, and S. S. Im, "Effect of the urethane group on treated clay surfaces for high-performance poly(butylene succinate)/montmorillonite nanocomposites," *Polymer Degradation and Stability*, vol. 94, no. 12, pp. 2163-2169, Dec. 2009.

[17] D. Lincoln, R. Vaia, Z. G. Wang, and B. Hsiao, "Secondary structure and elevated temperature crystallite morphology of nylon-6/layered silicate nanocomposites," *Polymer*, vol. 42, no. 4, pp. 1621–1631, 2001.

[18] J. H. Chang, B. S. Seo, and D. H. Hwang, "An exfoliation of organoclay in thermotropic liquid crystalline polyester nanocomposites," *Polymer*, vol. 43, no. 10, pp. 2969–2974, 2002.

[19] R. K. Shah and D. R. Paul, "Organoclay degradation in melt processed polyethylene nanocomposites," *Polymer*, vol. 47, no. 11, pp. 4075-4084, May. 2006.

[20] C. J. G. Plummer, L. Garamszegi, Y. Leterrier, M. Rodlert, and J.-A. E. Månson, "Hyperbranched Polymer Layered Silicate Nanocomposites," *Chemistry of Materials*, vol. 14, no. 2, pp. 486-488, Feb. 2002.

[21] M. Shibata, Y. Someya, M. Orihara, and M. Miyoshi, “Thermal and mechanical properties of plasticized poly(L-lactide) nanocomposites with organo-modified montmorillonites,” *Journal of Applied Polymer Science*, vol. 99, no. 5, pp. 2594-2602, Mar. 2006.

[22] E. Pollet, C. Delcourt, M. Alexandre, and P. Dubois, “Transesterification catalysts to improve clay exfoliation in synthetic biodegradable polyester nanocomposites,” *European Polymer Journal*, vol. 42, no. 6, pp. 1330-1341, 2006.

[23] J. W. Cho and D. R. Paul, “Nylon 6 nanocomposites by melt compounding,” *Polymer*, vol. 42, no. 3, pp. 1083-1094, Feb. 2001.

[24] C. Lu and Y.-W. Mai, “Influence of Aspect Ratio on Barrier Properties of Polymer-Clay Nanocomposites,” *Physical Review Letters*, vol. 95, no. 8, pp. 1-4, Aug. 2005.

[25] J. W. Gilman et al., “Flammability Properties of Polymer−Layered-Silicate Nanocomposites. Polypropylene and Polystyrene Nanocomposites †,” *Chemistry of Materials*, vol. 12, no. 7, pp. 1866-1873, Jul. 2000.

[26] B. Jang and C. Wilkie, “The effect of clay on the thermal degradation of polyamide 6 in polyamide 6/clay nanocomposites,” *Polymer*, vol. 46, no. 10, pp. 3264-3274, Apr. 2005.

[27] S. Sinha Ray, “Polymer/layered silicate nanocomposites: a review from preparation to processing,” *Progress in Polymer Science*, vol. 28, no. 11, pp. 1539-1641, Nov. 2003.

[28] M. Okamoto, “Biodegradable polymer/layered silicate nanocomposites: a review,” *J. Ind. Eng. Chem*, vol. 10, pp. 1156–1181, 2004.

[29] T. H. Kim, S. T. Lim, C. H. Lee, H. J. Choi, and M. S. Jhon, “Preparation and rheological characterization of intercalated polystyrene/organophilic montmorillonite nanocomposite,” *Journal of Applied Polymer Science*, vol. 87, no. 13, pp. 2106-2112, Mar. 2003.

[30] S. Sinharay and M. Bousmina, “Biodegradable polymers and their layered silicate nanocomposites: In greening the 21st century materials world,” *Progress in Materials Science*, vol. 50, no. 8, pp. 962-1079, Nov. 2005.

[31] S. Sinharay and M. Bousmina, “Biodegradable polymers and their layered silicate nanocomposites: In greening the 21st century materials world,” *Progress in Materials Science*, vol. 50, no. 8, pp. 962-1079, Nov. 2005.

[32] G. G. Odian, *Principles of polymerization*. Wiley-Interscience, 2004.

[33] C. E. J. Carraher, *Introduction to Polymer Chemistry, Second Edition*. Boca Raton , Fl 33487-2742: CRC Press, 2010, p. 534.

[34] P. C. Painter and M. M. Coleman, *Fundamentals of Polymer Science: An Introductory Text, Second Edition*. Lancaster, Pennsylvania 17064 U.S.A: Technomic , 1994, p. 433.

[35] E. MURAYAMA, “Optical Properties of Ringed Spherulites,” *Polym. Prepr. Jpn*, vol. 51, p. 460, 2002.

[36] L. Mandelkern, “Crystallization of polymers,” in *Journal of Polymer Science*, Second., Cambridge, New York, Melbourne, Madrid, Cape Town, Singapore, Sao Paulo: Cambridge University Press, 2002.

[37] M. Stamm, E. W. Fischer, M. Dettenmaier, and P. Convert, “Chain conformation in the crystalline state by means of neutron scattering methods,” *Faraday Discussions of the Chemical Society*, vol. 68, p. 263, 1979.

[38] P. H. Geil, *Polymer single crystals*. Krieger, 1973.

[39] P. J. Flory and D. Y. Yoon, “Molecular morphology in semicrystalline polymers,” *Nature*, vol. 272, no. 5650, pp. 226-229, Mar. 1978.

[40] P. Flory, “On the morphology of the crystalline state in polymers,” *Journal of the American Chemical Society*, vol. 721, no. 1959, 1962.

[41] A. N. Wilkinson and A. J. Ryan, *Polymer processing and structure development*. Kluwer Academic Publishers, 1998.

[42] J. D. Hoffman and R. L. Miller, “Kinetic of crystallization from the melt and chain folding in polyethylene fractions revisited: theory and experiment,” *Polymer*, vol. 38, no. 13, pp. 3151-3212, Jan. 1997.

[43] D. I. Bower, *An introduction to polymer physics*. Cambridge University Press, 2002, p. 124.

[44] J. Lauritzen and J. Hoffman, "Theory of formation of polymer crystals with folded chains in dilute solution," *Journal of Research of the National Bureau of Standards Section a- Physics and Chemistry*, vol. 64, pp. 73-102, 1960.

[45] J. D. Hoffman, "Polymer Single Crystals. Philip H. Geil. Interscience (Wiley), New York, 1963. xii + 560 pp. Illus. $16," *Science*, vol. 143, no. 3602, pp. 121-121, Jan. 1964.

[46] J. Hoffman and J. Lauritzen, "Crystallization of bulk polymers with chain folding theory of growth of lamellar spherulites," *Journal of Research of the National Bureau of Standards A*, vol. 65, pp. 297-336, 1961.

[47] D. M. Sadler and G. H. Gilmer, "A model for chain folding in polymer crystals: rough growth faces are consistent with the observed growth rates," *Polymer*, vol. 25, no. 10, pp. 1446-1452, 1984.

[48] D. M. Sadler, "Roughness of growth faces of polymer crystals: Evidence from morphology and implications for growth mechanisms and types of folding," *Polymer*, vol. 24, no. 11, pp. 1401-1409, Nov. 1983.

[49] D. Sadler and G. Gilmer, "Rate-Theory Model of Polymer Crystallization," *Physical Review Letters*, vol. 56, no. 25, pp. 2708-2711, Jun. 1986.

[50] B. Wunderlich, *Macromolecular physics*, no. 3. Academic Press, 1980.

[51] J. D. H. HOFFMAN and R. L. MILLER, "Organic Polymers," in *Advancing Materials Research*, s P. A. Psara and D. H. Langford, Eds. National Academy of Engineering, 1987, p. 251.

[52] A. Ravve, *Principles of polymer chemistry*, no. 1. Kluwer Academic/Plenum Publishers, 2000.

[53] A. Rudin, *The elements of polymer science and engineering: an introductory text and reference for engineers and chemists*. Academic Press, 1999.

[54] X. Alex and C. Edward S, "Nylon Plastics Handbook," M. I. Kohan, Ed. Hanser Publishers: Munich, Vienna and New York, 1995, pp. 108-137.

[55] C. W. Bunn and E. V. Garner, "The Crystal Structures of Two Polyamides ('Nylons')," *Proceedings of the Royal Society A: Mathematical, Physical and Engineering Sciences*, vol. 189, no. 1016, pp. 39-68, Mar. 1947.

[56] Y. Li and W. a Goddard, "Nylon 6 Crystal Structures, Folds, and Lamellae from Theory," *Macromolecules*, vol. 35, no. 22, pp. 8440-8455, Oct. 2002.

[57] S. Dasgupta, W. B. Hammond, and W. a Goddard, "Crystal Structures and Properties of Nylon Polymers from Theory," *Journal of the American Chemical Society*, vol. 118, no. 49, pp. 12291-12301, Jan. 1996.

[58] N. a Jones, S. J. Cooper, E. D. T. Atkins, M. J. Hill, and L. Franco, "Temperature-induced changes in chain-folded lamellar crystals of aliphatic polyamides. Investigation of nylons 2 6, 2 8, 2 10, and 2 12," *Journal of Polymer Science Part B: Polymer Physics*, vol. 35, no. 4, pp. 675-688, Mar. 1997.

[59] N. a Jones, E. D. T. Atkins, M. J. Hill, S. J. Cooper, and L. Franco, "Chain-Folded Lamellar Crystals of Aliphatic Polyamides. Comparisons between Nylons 4 4, 6 4, 8 4, 10 4, and 12 4," *Macromolecules*, vol. 29, no. 18, pp. 6011-6018, Jan. 1996.

[60] E. Navarro, L. Franco, J. a Subirana, and J. Puiggali, "Nylon 65 has a Unique Structure with Two Directions of Hydrogen Bonds," *Macromolecules*, vol. 28, no. 26, pp. 8742-8750, Dec. 1995.

[61] C. Ramesh, A. Keller, and S. J. E. A. Eltink, "Studies on the crystallization and melting of nylon-6,6: 1. The dependence of the Brill transition on the crystallization temperature," *Polymer*, vol. 35, no. 12, pp. 2483-2487, Jun. 1994.

[62] C. Sclar and L. Carrison, "Optical crystallography of coesite," *Am. Mineral*, vol. 47, pp. 1292-1302, 1962.

[63] F. W. Billmeyer, *Textbook of polymer science*. Wiley, 1984, p. 578.

[64] H. Stanjek and W. Häusler, "Basics of X-ray Diffraction," *Hyperfine Interactions*, vol. 154, no. 1-4, pp. 107-119, 2004.

[65] U. W. Gedde, *Polymer physics*. Chapman & Hall, 1995.

[66] G. R. Strobl, *The physics of polymers: concepts for understanding their structures and behavior*. Springer, 1997.

[67] M. García-Gutierrez and D. Rueda, "Bases of Synchrotron Radiation, Light Sources, and Features of X-Ray Scattering Beamlines," in *Applications of Synchrotron Light to Scattering and Diffraction in Materials*, Springer, 2009, p. 2.

[68] D. R. Rueda et al., "Versatile wide angle diffraction setup for simultaneous wide and small angle x-ray scattering measurements with synchrotron radiation," *Review of Scientific Instruments*, vol. 77, no. 3, p. 033904, 2006.

[69] "Software for small angle scattering," *Light, Source Source Diamond Neutron, AND the STFC ISI*, 2004. [Online]. Available: http://www.small-angle.ac.uk/small-angle/Software/CORFUNC.html.

[70] V. B. F. Mathot and L. Benoist, *Calorimetry and thermal analysis of polymers*. Hanser Publishers, 1994.

[71] N. P. P. Cheremisinoff, *Polymer characterization: laboratory techniques and analysis*. Noyes Publications, 1996.

[72] J. D. Menczel and R. B. Prime, *Thermal analysis of polymers: fundamentals and applications*. John Wiley, 2009.

[73] A. W. Coats and J. P. Redfern, "Kinetic Parameters from Thermogravimetric Data," *Nature*, vol. 201, no. 4914, pp. 68-69, 1964.

[74] H. E. Kissinger, "Reaction Kinetics in Differential Thermal Analysis," *Analytical Chemistry*, vol. 29, no. 11, pp. 1702-1706, 1957.

[75] H. L. Friedman, "Kinetics of thermal degradation of char-forming plastics from thermogravimetry. Application to a phenolic plastic," *Journal of Polymer Science Part C*, vol. 6, no. 1, pp. 183-195, 1964.

[76] T. Ozawa, "A New Method of Analyzing Thermogravimetric Data," *Bulletin of the Chemical Society of Japan*, vol. 38, no. 11, pp. 1881–1886, 1965.

[77] J. H. Flynn and L. A. Wall, "A quick, direct method for the determination of activation energy from thermogravimetric data," *Journal Of Polymer Science Part B Polymer Letters*, vol. 4, no. 5, pp. 323-328, 1966.

[78] A. Mianowski, "The kissinger law and isokinetic effect," *Journal of Thermal Analysis and Calorimetry*, vol. 74, no. 3, pp. 953-973, Dec. 2003.

[79] A. I. Lesnikovich and S. V. Levchik, "A method of finding invariant values of kinetic parameters," *Journal of Thermal Analysis*, vol. 27, no. 1, pp. 89-93, May. 1983.

[80] A. I. Lesnikovich and S. V. Levchik, "Isoparametric kinetic relations for chemical transformations in condensed substances (analytical survey). I," *Journal of Thermal Analysis*, vol. 30, no. 1, pp. 237-262, Jan. 1985.

[81] S. Barbara, "Infrared spectroscopy: fundamentals and applications," *Analytical Techniques in the Science*, 2004.

[82] D. K. Platt and R. T. Limited, *Biodegradable polymers: market report*. Rapra Technology, 2006.

[83] S. Pavlidou and C. Papaspyrides, "A review on polymer–layered silicate nanocomposites," *Progress in Polymer Science*, vol. 33, no. 12, pp. 1119-1198, Dec. 2008.

4

ODD-EVEN AND EVEN-ODD POLYAMIDES:STRUCTURE AND NANOCOMPOSITES

The work described in this chapter previously appeared in:

[1] Morales-Gámez, L. Ricart, A. Franco, L.; Puiggalí, J. *European Polymer Journal* **2010**, *46*, 2063-2077.

[2] Morales-Gámez, L. Soto, D. Franco, L.; Puiggalí, J. *Polymer* **2010**, *51*, 5788-5798.

[3] Morales-Gámez, L., Casas, M.T. Artigas, A. Franco, L. Puiggalí, J. *Submitted Papper*

[4] Ricart, A, Soto, D. Franco, L. Morales, L. T.; Puiggalí, J. *IOP Conference Series: Materials Science and Engineering* **2010**, *14*, 012006.

4.1

Brill transition and melt crystallization of nylon 56: an odd-even polyamide with two hydrogen bonding directions

Brill transition and crystallization behaviour of nylon 56, a representative polymer of odd-even polyamides, was investigated by simultaneous WAXD and SAXS synchrotron radiation. Nylon 56 crystallized from solution into a peculiar structure where hydrogen bonds were established along two direction. Nylon 56 experimented on heating a Brill transition that lead to a pseudohexagonal packing and lately to a monoclinic unit cell where neighbouring molecular segments were shifted along the chain axis direction. In disagreement with conventional polyamides, the Brill transition of nylon 56 was not reversible since on cooling the pseudohexagonal arrangement was mainly attained.

Optical microscopy studies performed under both isothermal and non-isothermal conditions demonstrated that nylon 56 spherulites had different optical properties than even-even nylons having conventional sheet structures. The birefringence sign changed in the sequence positive-negative-positive when crystallization temperature was decreased.

4.1.1 Introduction

Aliphatic polyamides derived from odd diamines and even dicarboxylic acids (i.e. odd-even nylons) cannot establish all possible intermolecular hydrogen-bonding interactions when molecular chains have an all trans conformation (**Figure 4.1.1**a). In this way, the conventional α/β forms usually found in commercial even-even nylons [1,2] (e.g. nylon 66) cannot be expected considering the minimization of the packing energy. These conventional structures are based on a stacking of sheets composed of hydrogen-bonded molecular chains with a planar zig-zag conformation. The corresponding fiber diffraction patterns are mainly characterized by two strong equatorial reflections at approximately 0.44 and 0.38 nm which are related to interchain distances within and between sheets, respectively.

A pseudohexagonal structure, which fiber diffraction pattern is characterized by a single strong equatorial reflection at approximately 0.415 nm, has been postulated for polyamides derived from an odd diamine and/or an odd dicarboxylic acid [1,3] (e.g. nylon 77). In this case, the torsional angles of the bonds adjacent to the amide groups tend to ± 120 ºC, causing a tilt of the amide plane by approximately 60º, a shortening of the chain length and the establishment of good hydrogen-bonding interactions along a single direction.

However, it has recently been demonstrated that typical spacings of the α/β forms can surprisingly be found in nylons derived from odd diamines (e.g. nylons 56 [4], 92 [5] and 5-10 [6]) or odd dicarboxylic acids (e.g. nylons 65 [7] and 69 [8]). These structures were observed in both stretched fibers and single crystals obtained from diluted solutions. Structural studies on this kind of polyamides revealed a peculiar arrangement characterized by the establishment of intermolecular hydrogen bonds along two different directions. Basically, the molecular conformation was close to the all trans since only a slight deviation towards 150º (or -150º) for the two torsional angles vicinal to the odd diamide unit was necessary to face all NH and CO groups of neighbouring chains. The two amide groups of the odd unit rotated in opposite senses from the plane defined by the methylene carbon atoms allowing the establishment of good hydrogen bonding interactions when neighbouring chains became conveniently shifted along the chain axis direction (**Figure 4.1.1**b). In this way, a monoclinic unit cell containing two molecular segments was derived and the chain axis projection corresponded to a rectangular unit cell.

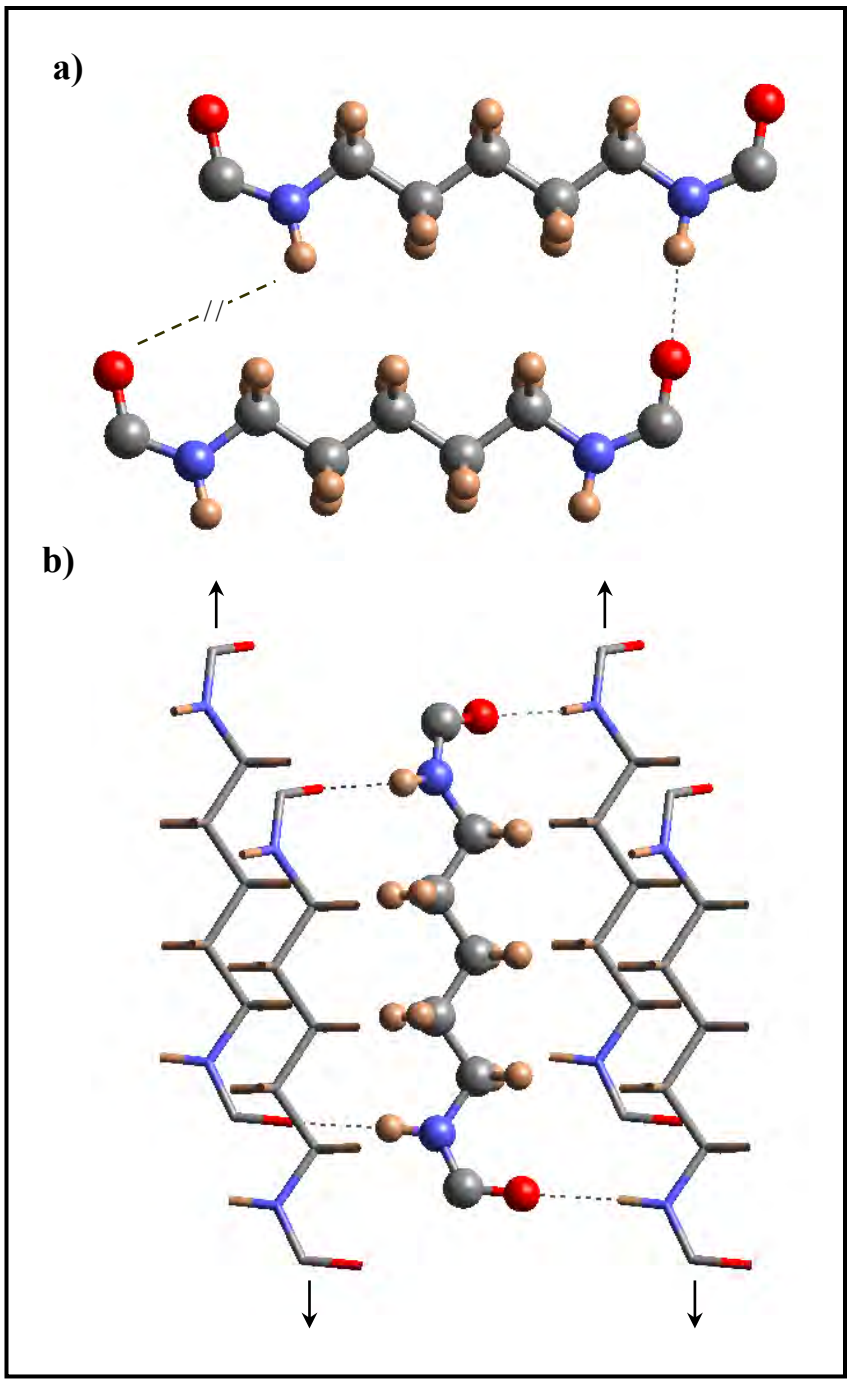

Figure 4.1.1 a) Scheme of the unfavorable hydrogen-bond geometry between odd diamide units of nylon 56 molecular chains with an all trans conformation. b) Scheme of the establishment of hydrogen bonds along two directions when consecutive amide planes of a molecular

Conventional polyamides usually have a temperature induced transition towards a pseudohexagonal unit cell (γ' form). This transition can be easily detected in the X-ray diffraction patterns since the two strong equatorial reflections characteristic of the sheet structure gradually merge by increasing temperature into a single reflection. The Brill transition temperature just defines the moment in which this pseudohexagonal packing is reached. Brill temperature depends on the sample history and is also observed with a hysteresis effect when samples are cooled from the melt state. Although, a large number of studies on the Brill transition have been reported for several nylons [9-20], the phenomenon is not yet fully understood and different explanations have been postulated. Most of them suggest that hydrogen bonds are not disrupted during the Brill transition and explain the pseudohexagonal packing as a consequence of the increasing mobility of the polymethylene segments [21,22]. At this stage, it seems highly interesting to bring new data about the Brill transition and the crystallization process of the above indicated polyamides. Nylon 56 has been chosen as a representative odd-even polyamide with a peculiar hydrogen bonding scheme. Nowadays, works concerning to odd-even polyamides are limited to nylons 11-10 and 11-12 which are derived from units with a large number of methylene units [23].

4.1.2 Experimental section

Materials

Nylon 56 was synthesized by interfacial polycondensation of 1,5-diaminopentane and adipoyl dichloride using toluene as organic solvent and sodium hydroxide as proton acceptor following the procedure previously described [4]. An intrinsic viscosity of 0.7 dL/g was determined in dichloroacetic acid at 25 ºC.

Measurements

Calorimetric data were obtained by differential scanning calorimetry using a TA Instruments Q100 series with T_{zero} technology and equipped with a refrigerated cooling system (RCS) operating at temperatures from -90 ºC to 550 ºC. Experiments were conducted under a flow of dry nitrogen with a sample weight of approximately 5 mg, while calibration was performed with indium. The T_{zero} calibration involved two experiments: the first was done without samples and the second was performed with sapphire disks.

The spherulite growth rate was determined by optical microscopy using a Zeiss Axioskop 40 Pol light polarizing microscope equipped with a Linkam temperature control system configured by a THMS 600 heating and freezing stage connected to a LNP 94 liquid nitrogen cooling system. Spherulites were grown from homogeneous melt-crystallized thin films produced by melting 1 mg of the polymer mixture on microscope slides. Next, small sections of these films were pressed or smeared between two cover slides and inserted in the hot stage. The thicknesses

of the squeezed samples were close to 10 μm in all cases. Samples were kept at 265 ºC (more than 10 ºC above the polymer melting point of 251-252 ºC) for 5 minutes to wipe out sample history effects, and then quickly cooled to the selected crystallization temperature. Alternatively samples were no isothermally crystallized at different cooling rates (8, 1 and 0.5 ºC/min) to increase the crystallization temperature range. The radius of the growing spherulites was monitored in both isothermal and non-isothermal crystallizations by taking micrographs with a Zeiss AxiosCam MRC5 digital camera at appropriate time intervals. A first-order red tint plate was employed to determine the sign of spherulite birefringence under crossed polarizers.

X-ray fiber diffraction data were obtained with Ni-filtered CuK_{α} radiation of wavelength 0.1542 nm from an Enraf Nonius rotating anode X-ray generator and using a modified Statton camera (W. H. Warhus, Wilmington, DE). Patterns were recorded at different temperatures using a temperature-controlled chamber provided by the manufacturer. Oriented fiber samples were obtained by drawing the polymer melt and performing a subsequent annealing under stress at 90 ºC.

Simultaneous time-resolved SAXS/WAXD experiments were carried out at the CRG beamline (BM16) of the European Synchrotron Radiation Facility of Grenoble. The beam was monochromatized to a wavelength of 0.098 nm. The capillary with the sample was held in a Linkam hot stage with temperature control within 0.1 ºC. WAXD/SAXS profiles were acquired during heating and non-isothermal crystallization experiments in time frames of 12 s. The heating and cooling rates varied between 20-8 ºC/min, respectively. Two linear position-sensitive detectors were used [24]: The SAXS detector was calibrated with different orders of diffraction from silver behenate whereas the WAXD detector was calibrated with diffractions of a standard of an alumina (Al2O3) sample. The diffraction profiles were normalized to the beam intensity and corrected considering the empty sample background. Deconvolution of WAXD peaks was performed with the PeakFit v4 program by Jandel Scientific Software using a mathematical function known as “Gaussian area”.

4.1.3 Results and discussion

Thermal properties of Nylon 56

Fusion of a nylon 56 sample directly obtained from synthesis was characterized by two melting peaks that appeared in the 228-251 ºC temperature range (**Figure 4.1.2**a). It should be pointed out that the high temperature melting peak was very broad and asymmetric, suggesting that it was really derived from the overlapping of two signals (peaks 2 and 3). Thus, fusion of nylon 56 seemed to be characterized by a complex behaviour. The DSC heating trace showed also a very broad endothermic peak (80-140 ºC) which could be assigned to adsorbed water since it was not detected in later heating runs, and furthermore a polymorphic transition could be discarded in this temperature range as then will be explained.

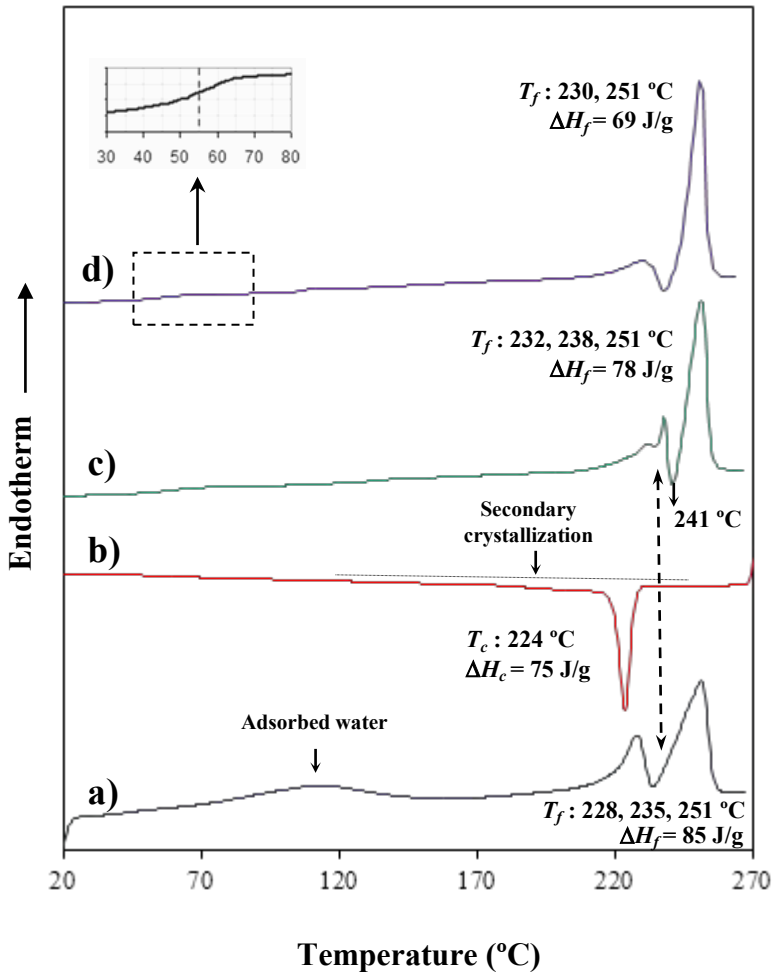

Figure 4.1.2 Sequence of DSC curves corresponding to a heating run of a solution crystallized sample (a), cooling run from the melt state (b), heating run of a melt-crystallized sample (c) and heating run of a quenched sample (d). Heating runs were performed at 20 ºC/min whereas the cooling run was performed at 10 ºC/min. Inset shows a magnification of the glass transition.

Nylon 56 crystallized easily during cooling runs from the melt state (e.g. an exothermic peak at 224 ºC was detected at a cooling rate of 10 ºC/min) giving rise to samples with a different melting behaviour. Thus, a posterior heating trace showed clearly as the broad high temperature peak was split in two peaks (peak 2 at 238 ºC and peak 3 at 251 ºC) and that an exothermic peak indicative of a recrystallization process appeared (241 ºC). The low temperature melting peak (peak 1 at ca. 232 ºC) could still be observed although with a very low intensity. Heating traces of melt quenched samples clearly indicate that a completely amorphous sample could not be obtained at the maximum cooling rate allowed by the equipment. However, the glass transition temperature was detected at a temperature close to 55 ºC. It is relevant that the melting behaviour was slightly different than observed for melt and solution crystallized samples since peak 2 was not detected. This feature suggests that peak 3 could be associated to thickest lamellae mainly produced during the heating process as a consequence of a melt/recrystallization of the thinner lamellae. This peak should be enhanced when more imperfect lamellae susceptible of reorganization were obtained as presumable in the melt quenched samples. The nature of peak 1 is more intriguing since at this stage two alternatives may be considered: a) the existence of very defective crystals and b) a polymorphic transition around 225-230 ºC.

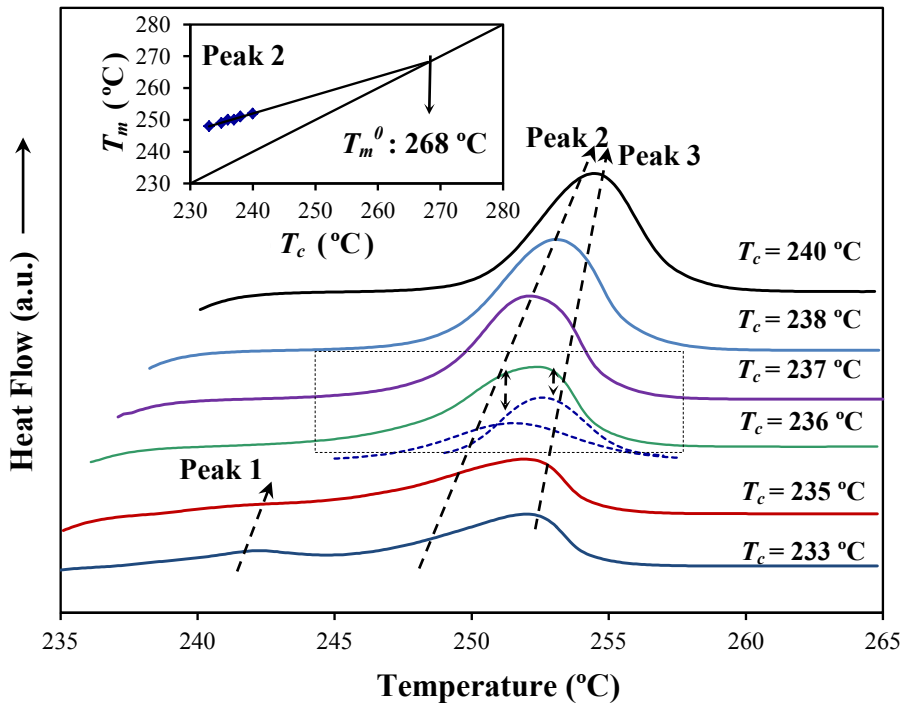

Figure 4.1.3 Melting peaks for isothermally melt crystallized samples. Deconvoluted profile is only shown for the sample crystallized at 236 ºC (dashed box). The inset shows the Hoffman-Weeks plot drawn for the crystallization temperature dependent melting peak (peak 2).

Figure 4.1.3 shows the heating traces of samples previously isothermally crystallized from the melt state at different temperatures. Peaks 2 and 3 appear generally overlapped and consequently is difficult to differentiate the two melting processes. However, it can be stated that peak 2 increased on intensity and shifted to higher temperatures when crystallization temperature did, whereas peak 3 remained at a practically constant temperature. This feature is consistent with the indicated melt/reorganization process where thinner lamellae convert into thicker ones. Furthermore, it is possible to infer the equilibrium melting temperature of nylon 56 by considering the temperature evolution of peak 2 with crystallization temperature. In this way, the Hoffman-Weeks plot [25] displayed in the inset of **Figure 4.1.3** indicates an extrapolated equilibrium temperature of 268 ºC, which is close to the value of 266 ºC previously postulated [26] from theoretical considerations based on the spherulite grown model forwarded by Hoffmann-Weeks [25]. Heating runs showed also the presence of the low temperature peak 1, but only when samples were isothermally crystallized at temperatures equal or lower than 235 ºC. Thus, this value is a limit for a possible crystalline transition or for the development of the indicated defective crystals.

Isothermal experiments allowed the determination of the overall crystallization kinetics, which depends on primary nucleation and crystal growth, for a very restrictive temperature range due to the experimental limitations caused by the high speed of the crystallization process.

The time evolution of the relative degree of crystallinity, $\chi(t)$, was determined from hot crystallization exotherms (**Figure 4.1.4** a) through the ratio area of the exotherm up to time t divided by the total exotherm area, i.e.:

$$\chi(t) = \int_{t0}^{t} (dH/dt)dt \; / \; \int_{t0}^{\infty} (dH/dt)dt \qquad (4.1.1)$$

where dH/dt is the heat flow rate and t_0 the induction time. The development of crystallinity always showed a characteristic sigmoidal dependence on time, as plotted in the inset of **Figure 4.1.4**a for six hot crystallization experiments.

Kinetic crystallization data were analyzed assuming the well known Avrami equation [27,28] for primary crystallization:

$$1 - \chi(t) = \exp[-Z\,(t-t_0)^n] \qquad (4.1.2)$$

where Z is the temperature-dependent rate constant and n the Avrami exponent whose value varies according to the crystallization mechanism. A normalized rate constant, $k = Z^{1/n}$, is usually evaluated for comparison purposes since its dimension (time^{-1}) is independent of the value of the Avrami exponent.

Table 4.1.1 Isothermal crystallization kinetic parameters deduced from DSC experiments for nylon 56.summarizes the main kinetic parameters of the primary crystallization process, which were deduced from the plots of $\log\{-\ln[1-\chi(t)]\}$ against $\log(t - t_0)$. The values of the Avrami

exponent for the hot isothermal crystallizations lie in a narrow range, from 2.15 to 2.80, 2.50 being the average value. This suggests a predetermined (heterogeneous) nucleation with spherical growth that occurred under slight geometric constraints since the theoretical value should be equal to 3. Both sporadic (heterogeneous) and homogeneous nucleation can be clearly discarded as a higher exponent, close to 4, should be derived and furthermore these nucleation mechanisms should mainly be favoured at high undercoolings.

The values of the reciprocal of the crystallization half-time, $1/\tau_{1/2}$, are also summarized in Table 1. This parameter is a direct measure of the crystallization process, and could therefore be used to check the accuracy of the Avrami analyses. In this way, a similar dependence with the crystallization temperature was found for this parameter and the kinetic rate constant, demonstrating the suitability of the deduced Avrami values.

Figure 4.1.4 b shows the crystallization exotherms obtained during cooling runs performed at the different rates used in the synchrotron radiation experiments. A well defined peak is always observed within a narrow temperature range, which obviously shifts to lower temperatures by increasing the cooling rate. However, it is interesting to note that peaks had a long tail which could be associated to a secondary crystallization process and which was more clearly observed at high cooling rates.

Table 4.1.1 Isothermal crystallization kinetic parameters deduced from DSC experiments for nylon 56.

T_c (°C)	n	$Z \cdot 10^8$ (s^{-n})	$k \cdot 10^3$ (s^{-1})	$1/\tau_{1/2} \cdot 10^3$ (s^{-1})
233	2.34	217.1	3.80	4.17
235	2.57	17.8	2.36	2.33
236	2.80	0.396	0.998	1.17
237	2.64	0.511	0.723	0.83
238	2.52	0.601	0.547	0.55
240	2.15	3.79	0.353	0.42

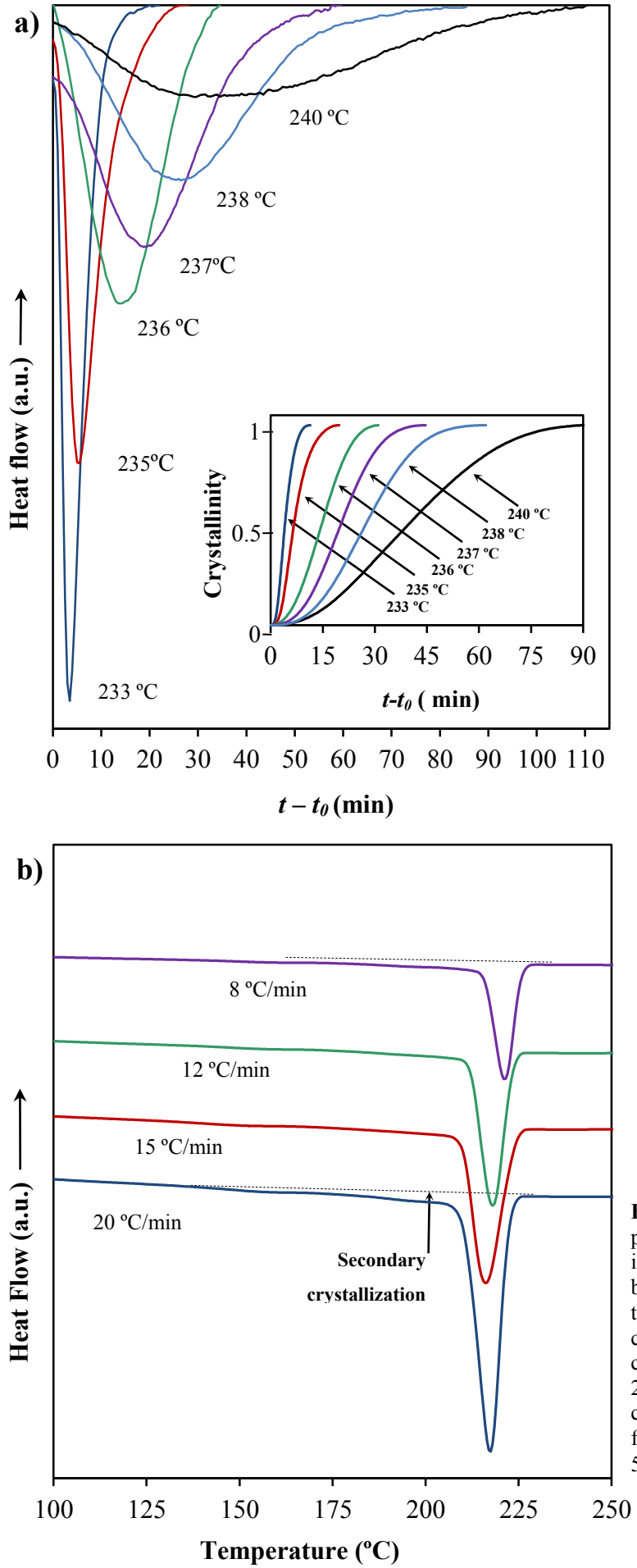

Figure 4.1.4 a) Exothermic DSC peaks corresponding to the hot isothermal crystallizations performed between 233 and 240 ºC. Inset shows the development of relative crystallinity over time for isothermal crystallizations performed between 233 and 240 ºC. b) Dynamic DSC curves obtained at the indicated rates for the hot crystallization of nylon 56.

- **Brill transition of nylon 56 on heating/cooling process**

Fiber diffraction patterns of nylon 56 were mainly characterized by strong equatorial reflections at 0.432 and 0.375 nm and an off meridional reflection at 1.272 nm (inset of **Figure 4.1.5**), which were indexed as the (020) and (110) reflexions on the basis of a monoclinic unit cell with a = 0.512 nm, b = 0.864 nm, c (chain axis) = 3.133 nm and β = 125.7º (form I) [4]. Structural modelling based on the diffraction data and energy calculations pointed towards the indicated model based on the establishment of two hydrogen bonding directions [4].

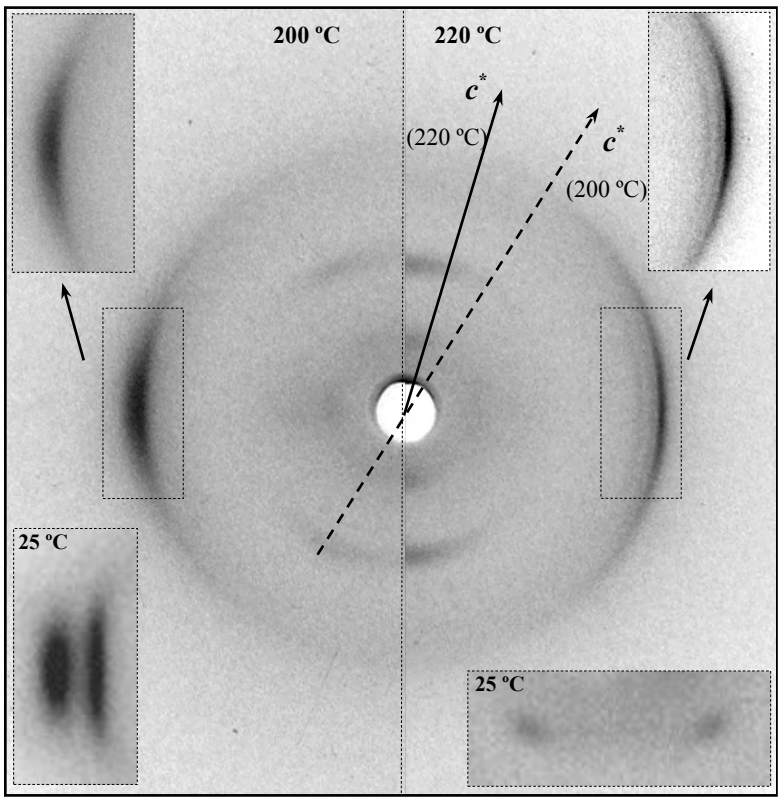

Figure 4.1.5 X-ray fiber diffraction patterns of nylon 56 at 200 ºC (left) and 220 ºC (right). Insets show the equatorial reflections observed at 25, 200 and 220 ºC and the 002 reflections (second layer line) observed at 25 ºC.

Figure 4.1.5 shows the X-ray fiber diffraction patterns of a nylon 56 sample taken under stress at 200 ºC and 220 ºC. At 200 ºC the pattern shows only one strong and diffuse equatorial reflection at 0.423 nm, which is an indication that the Brill transition took place. It is interesting to note that 00*l* reflections still appeared with an off meridional orientation which is an indication that the structure obtained at 200 ºC differed from a pseudohexagonal structure usually postulated for conventional polyamides. These 00*l* reflections seemed to have a close to meridional orientation in the patterns obtained at 220 ºC, although it is difficult to determine the *cc** angle due to their arched appearance and the overlapping between 00*l* and 00$\bar{l}$ reflections.

In this case, the new additional equatorial reflections observed at 0.454 nm and 0.436 nm are highly significant since allow to discard again a pseudohexagonal structure. Previous works suggested that at high temperature a monoclinic structure (form II) with a = 0.551 nm, b = 0.846 nm, c (chain axis) = 3.133 nm and β = 112.6º was achieved [4]. Note that the cc^* angle was 35.7º at room temperature whereas it decreased to 22.6º at 220 ºC justifying the close meridional orientation detected for the 00l reflections.

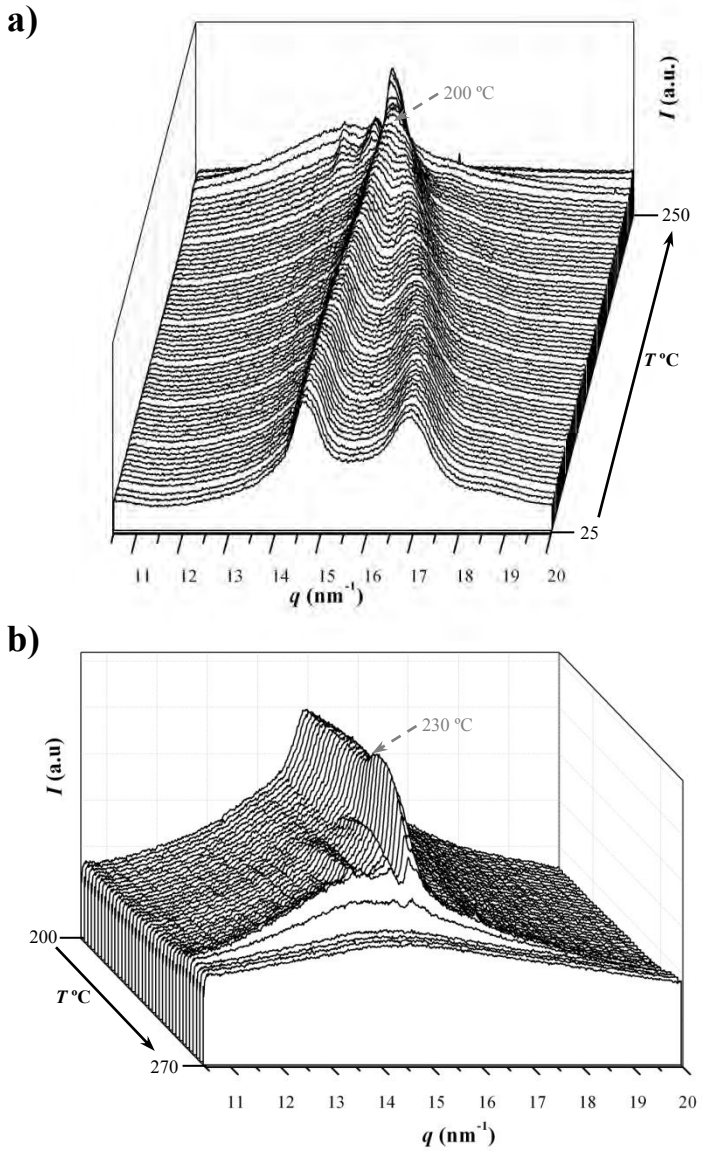

Figure 4.1.6 Three-dimensional representations of WAXD profiles of nylon 56 during cooling (12 ºC/min) from the melt to room temperature. All the temperature range is showed in a), whereas a different view covering only the last frames (up to 200 ºC) is shown in b).

Figure 4.1.6 shows three-dimensional representations of WAXD profiles obtained by synchrotron radiation during a heating process performed at 12 ºC/min from room temperature to fusion (q is the scattering vector given by $[4\pi/\lambda]$ sin (θ) or $2\pi/d_B$ where θ and d_B are the scattering angle and the Bragg spacing, respectively). Similar temperature dependent profiles were observed at heating rates of 8, 12, 15 and 20 ºC/min. Profiles showed that the spacings of the two equatorial reflections at 0.433 and 0.374 nm gradually merged into a single peak at 0.423 nm that was reached at a temperature close to 200 ºC. This process seems a typical Brill transition where a pseudohexagonal packing (γ*-form) is favoured at a temperature slightly lower than the melting point. It is worth mentioning that the Brill transition temperature of nylon 56 was practically independent of the heating rate as shown in **Figure 4.1.7**. After the Brill transition, new peaks (e.g. those above indicated at 0.454 nm and 0.436 nm) started to appear as shown in **Figure 4.1.6** b and a transition towards the indicated form II took place. All equatorial reflections became narrower (**Figure 4.1.5**) and increased on intensity (**Figure 4.1.6** b) during heating above the Brill transition temperature and before to start the melting process. Transition to form II occurred in a temperature range that was slightly lower (5 ºC) than the endothermic peak 1 observed in the calorimetric analyses. In this way, this small melting peak seems to be related to highly defective crystals formed between bundles of lamellae, a conclusion that has been reported for different polyamides [29-31].

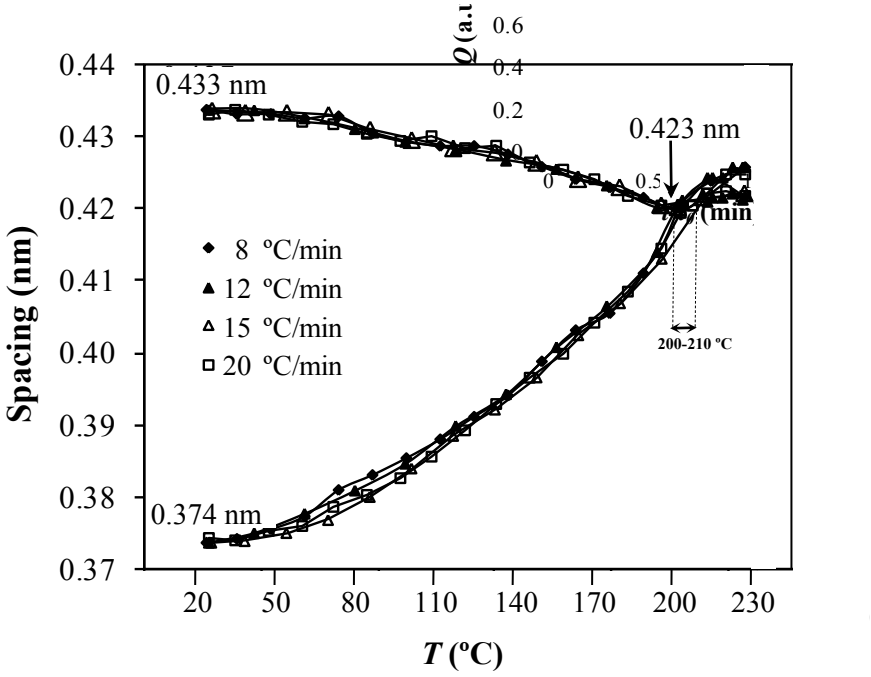

Figure 4.1.7 Plot showing the temperature evolution of the spacings corresponding to the two strongest equatorial reflections at different heating rates.

Figure 4.1.8 compares the deconvoluted WAXD profiles representative of the structures attained at room temperature, at the Brill transition temperature and at a temperature close to

fusion. In all cases, two amorphous halos (average values of 0.420 nm and 0.375 nm) were detected. However, the position of the maxima changed with temperature (i.e. the maximum of the first halo appeared at 0.409 and 0.430 nm in the patterns taken at 25 and 230 ºC, respectively). This feature suggests that the amorphous phase has a more compact molecular arrangement when temperature decreases, as it will be discussed in the next section. In fact, a similar increase in the average interchain distance in the amorphous phase above the Brill transition temperature was reported and analyzed in detail for nylon 66 [17].

It is worth to pointing out that Bragg reflections were very broad while temperature was lower or equal than the Brill transition temperature. Assuming that the low temperature structure (form I) is defined by a molecular arrangement where hydrogen bonds are established along two directions, it seems reasonable to expect clear differences on heating between conventional polyamides and nylon 56. Thus, the pseudohexagonal structure [32-34] (γ' form) attained with nylons characterized by a single hydrogen bond direction could not be observed in the diffraction patterns of nylon 56. Transitions induced by temperature on this polyamide may involve only slight changes in the torsional angles vicinal to amide groups or even an increase in the mobility of polymethylene segments without disrupting the initial hydrogen-bonding scheme. Note that the chain axis projection may correspond to a pseudohexagonal packing, as deduced from the single equatorial reflection at the Brill transition temperature, but a chain axis shift still remained between neighbouring chains. In this sense, fiber patterns with non-meridional 00*l* reflections are essential to support the finding that the Brill structure is different from the conventional γ' form.

Figure 4.1.9 a shows the WAXD profiles acquired during a cooling run (10 ºC/min) from the melt state. It is clear that nylon 56 crystallized into the form II characterized as above indicated by multiple narrow reflections with an equatorial or close equatorial orientation. Note that the profile showed in **Figure 4.1.9** is practically identical to that attained during the heating process (**Figure 4.1.8 c**) just at some degrees before fusion. **Figure 4.1.9** a shows also that the reflection at ca. 0.423 nm does not split when temperature is lowered up to room temperature and consequently it could be deduced that the Brill transition is not reversible on cooling. WAXD profiles showed also that characteristic reflections of form II moves to lower spacings by decreasing the temperature and overlapped the main equatorial reflection at ca. 120 ºC. Thus, the intensity of the reflection at 0.423 nm increased during cooling as well as the peak became broader.

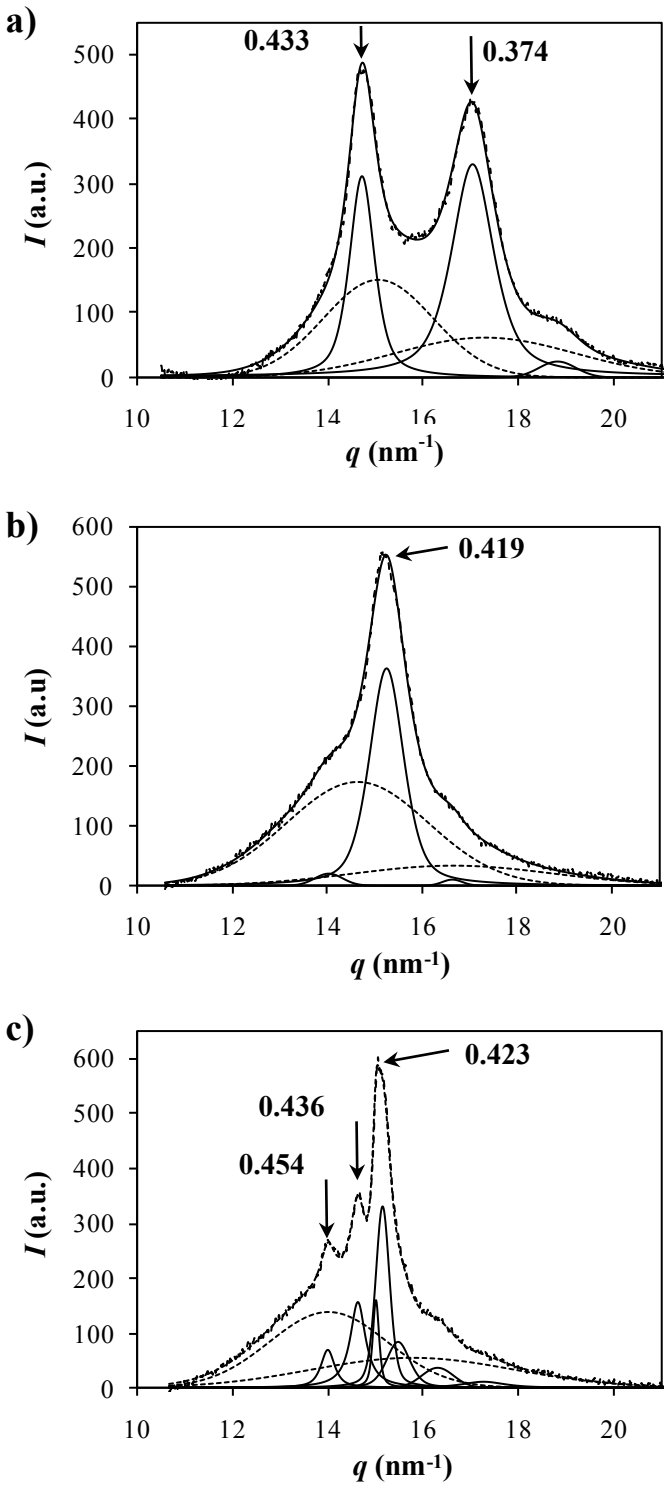

Figure 4.1.8 One-dimensional WAXD profiles for nylon 56 taken at room temperature (a), 200 ºC (b) and 230 ºC (c) during a heating scan (12 ºC/min). Spacings of main reflections are indicated together with the deconvoluted peaks.

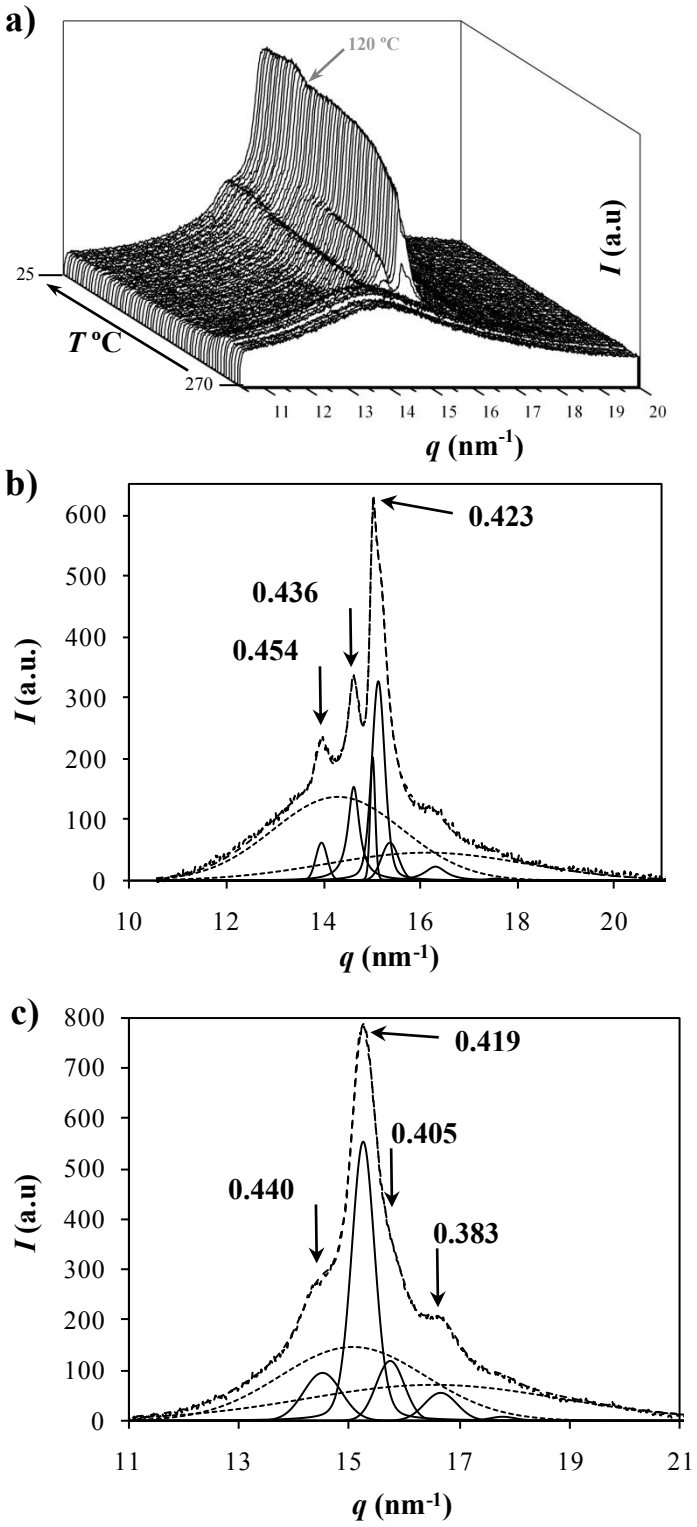

Figure 4.1.9 . a) Three-dimensional representation of WAXD profiles of nylon 56 during cooling (12 ºC/min) from the melt to room temperature. b) and c) One-dimensional WAXD profiles for nylon 56 taken at 220 ºC (b) and at room temperature (c) during a cooling run (12 ºC/min) from the melt state. Spacings of main reflections are indicated together with the deconvoluted peaks.

It should be pointed out that the characteristic reflections of form I appeared in the first stage of crystallization and increased on intensity during the cooling process. Logically these peaks slightly moved to lower spacings due the contraction of the unit cell when temperature decreased. At room temperature the deconvoluted profile (**Figure 4.1.9** c) was characterized by reflections associated to form I (0.440 and 0.383 nm) and reflections indicative of the pseudohexagonal packing (e.g. 0.419 nm) attained after the Brill transition temperature, which appeared predominant according to their relative intensity. It should also be indicated that form I could be completely recovered when fibers were annealed under stress at 90 ºC or the samples were recrystallized from diluted formic acid/ethanol (1:4 *v*/*v*) solutions [4].

- **Non-isothermal crystallization studies by simultaneous SAXS/WAXD synchrotron radiation experiments**

The crystallization process was simultaneously monitored by time-resolved WAXD and SAXS non-isothermal experiments. In this way, the evolution of the mass fraction of the crystalline phase in the sample, X_c^{WAXD}, was determined from the different WAXD deconvoluted profiles as the ratio between the total intensities of the crystalline reflections I_c and the overall intensity I_T. Values at the end of crystallization ranged between 0.26 and 0.40 and increased with decreasing the cooling rate (**Figure 4.1.10**).

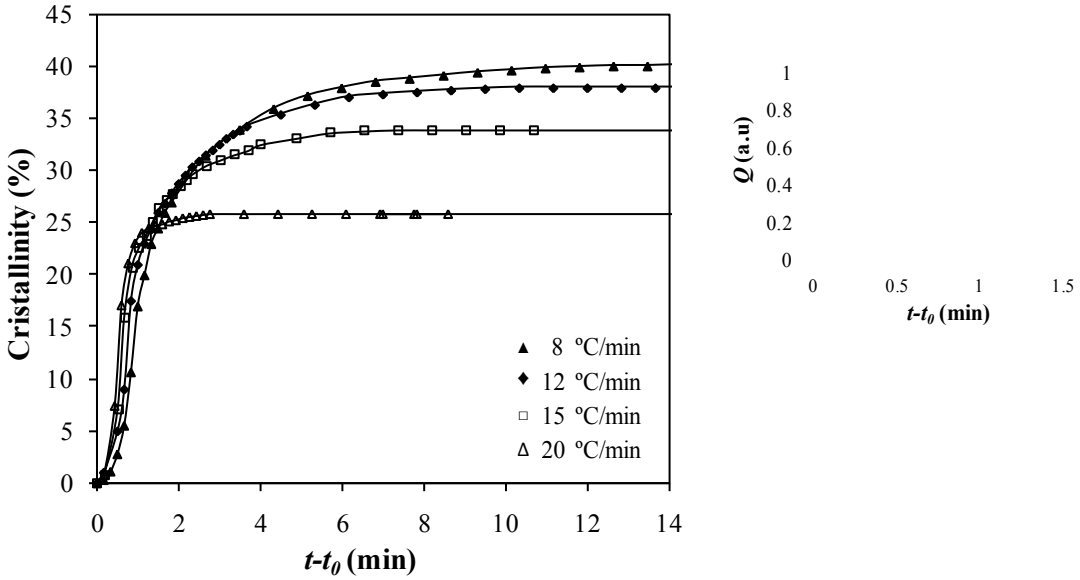

Figure 4.1.10 Time evolution of WAXD crystallinity during non-isothermal hot crystallizations performed at the indicated cooling rates.

Primary crystallization was very fast at all the assayed cooling runs and was completed within a range lower than 2 minutes after primary nuclei were formed (i.e. after achieving the induction time). Secondary crystallization was clearly dependent on the cooling rate and varied from 12 to 2 min for rates of 8 and 20 ºC/min, respectively.

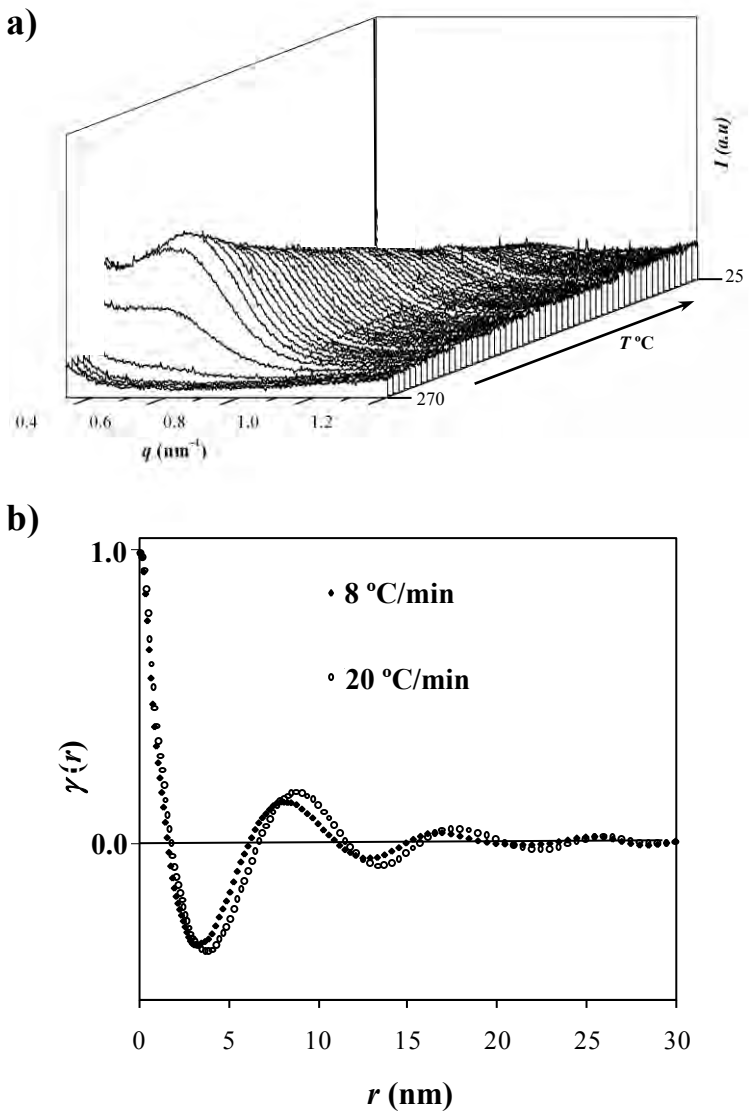

Figure 4.1.11 a) Three-dimensional representation of SAXS profiles of nylon 56 during cooling (12 ºC/min) from 270 ºC (melt state) to room temperature. b) Correlation functions corresponding to the end of secondary crystallization obtained during cooling runs performed at the indicated rates.

SAXS patterns showed a long period peak at a value of the scattering vector, q, close to 0.5-0.8 nm^{-1} after subtraction of the empty sample background observed near the beam stop (**Figure 4.1.11** a). This peak, which can be attributed to the lamellar structure of the spherulites, started to appear at the same temperature than crystalline reflections in the WAXD patterns, as presumable for a crystallization process controlled by nucleation and crystal growth. This temperature obviously decreased with increasing the cooling rate.

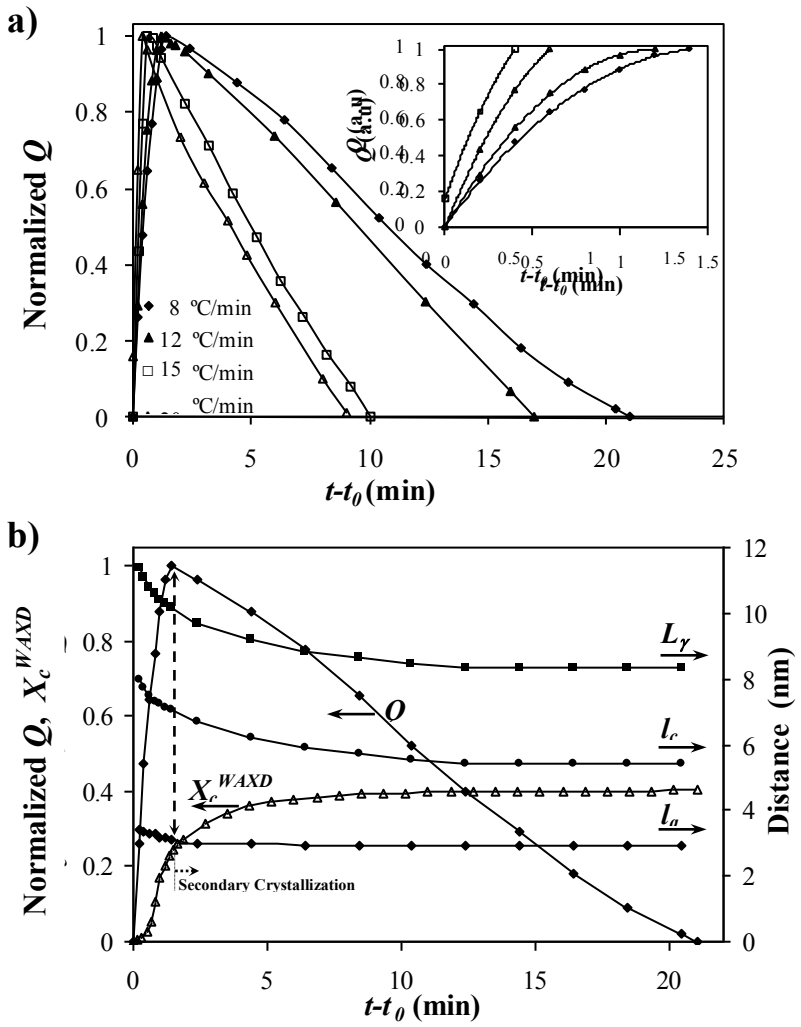

Figure 4.1.12 a) Temperature evolution of the scattering invariant, Q, at the indicated cooling rates. Inset shows its evolution during primary crystallization. b) Temperature evolution of the long period, Lγ, crystal thickness, lc, amorphous thickness, la, scattering invariant, Q, and degree of crystallinity, WAXD, during a non-isothermal melt crystallization performed at a cooling rate of 8 ºC/min.

SAXS data were analyzed by the normalized one-dimensional correlation function [35], $\gamma(r)$, which corresponds to the Fourier transform of the Lorentz-corrected SAXS profile:

$$\gamma(r) = \int_0^\infty q^2 I(q)\cos(qr)dq \;/\; \int_0^\infty q^2 I(q)dq \qquad (4.1.3)$$

The scattering intensity was extrapolated to both low and high q values using Vonk's model [36] and Porod's law, respectively.

Correlation functions (**Figure 4.1.11** b) were used to determine the scattering invariant, Q, which allows evaluating the peak intensity evolution during crystallization, and morphological

parameters like the long period, L_γ, crystalline lamellar thickness, l_c, and amorphous layer thickness, l_a.

The intensity of the SAXS peak increased during primary crystallization and then decreased. This observation is important because it suggests a change in the amorphous phase since the intensity of SAXS peaks depends on the degree of crystallinity but also on the difference between the electronic densities of amorphous and crystalline phases. It is clear that on cooling the amorphous interlamellar component should adopt a more compact molecular arrangement, probably as a result of the improved hydrogen-bonding interactions. Thus, the SAXS peak reached a maximum value before to start secondary crystallization, as it will then be explained, and practically disappeared when crystallization was complete.

Figure 4.1.12 a shows the time evolution of the invariant, Q, for the different crystallization rates. The time corresponding to the maximum value for the invariant clearly diminished by increasing the cooling rate as well as the range where the secondary crystallization process took place.

The evolution of morphological parameters during crystallization (**Figure 4.1.12** b) shows a slight change in the long period (e.g. from 11.7 to 8.2 nm in the cooling performed at 8 ºC/min), which is mainly due to the decrease in crystalline lamellar thickness (e.g. from 8.0 to 5.8 nm). The latter was also significant during the secondary crystallization step and indicates that new secondary lamellae inserted into the loosely stacked bundles of primary lamellae. New lamellae suffer spatial restrictions, leading to thinner defective crystals. Changes on the amorphous layer thickness mainly occurred during primary crystallization and were consistent with a reordering effect than conduced to a slight decrease (i.e. from 3.7 to 2.4 nm). It is worth to pointing out that this thickness remained practically constant during the entire long time interval where secondary crystallization took place. **Figure 4.1.12** b compares also the evolution of the invariant, Q, and the WAXD crystallinity allowing correlating the maximum value of the invariant with the end of the primary crystallization process.

Figure 4.1.11b shows the correlation functions calculated for the SAXS profiles obtained at the minimum (8 ºC/min) and the maximum (20 ºC/min) assayed cooling rates and at the temperature (time) corresponding to the end of crystallization (i.e. the last frame which peak still allowed the calculation of the correlation function). Differences in lamellar spacings are a consequence of the balance between two counter factors: enhanced insertion mechanism producing thinner secondary lamellae, and increased crystallization temperature resulting in thicker primary lamellae with decreasing the cooling rate.

Figure 4.1.13 a compares the evolution of morphological parameters during crystallization for the different studied cooling rates, whereas cooling rate dependence of initial and final values of

these parameters are shown in **Figure 4.1.13** b. The increase observed for the lamellar spacing with the cooling rate indicates the prevalence of the lamellar insertion effect.

Figure 4.1.11 also shows that the L_γ value associated with the most probable distance between the centers of gravity of two adjacent crystals (abscise of the first maximum of the correlation function) is greater than the long period determined from twice the abscise value of the first minimum of the correlation function, which is interpreted as the most probable distance between the centers of gravity of a crystal and its adjacent amorphous layer. This indicates a broader distribution of the layer widths of the major component [37], which corresponds to the crystal phase.

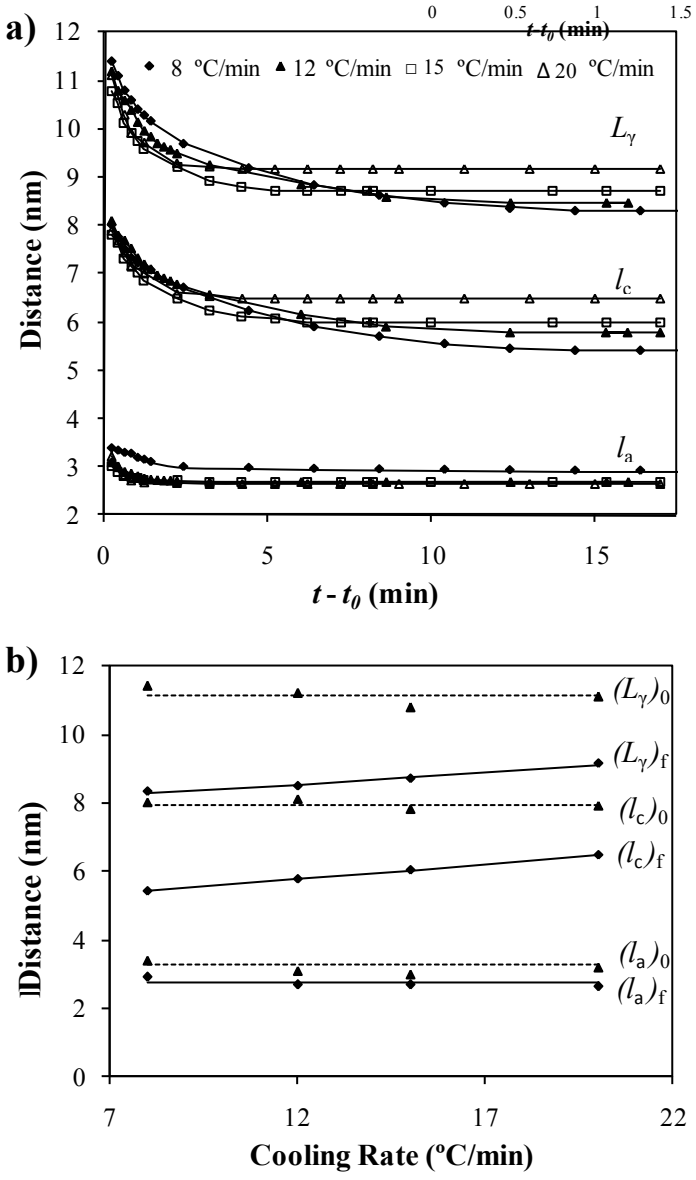

Figure 4.1.13 a) Evolution of L_γ, l_c and l_a values during non-isothermal crystallization at different cooling rates. b) L_γ, l_c and l_a values obtained at the end (subscript f) and the beginning (subscript 0) of non-isothermal hot crystallization performed at different cooling rates.

SAXS crystallinities, X^{SAXS}, in the 66%-70% range were calculated at the end of secondary crystallization from the values of the morphological parameters ($l_c/(l_c + l_a)$). It is well known that the correlation function method cannot distinguish between l_c and l_a thicknesses, which certainly constitutes an uncertainty of this analysis. However, it is also clear that the linear degree of crystallinity (X^{SAXS}) must be always greater than the crystallinity determined from WAXD experiments (26%-40%) since amorphous-rich interstack regions must exist [38,39]. Note, for example, that the crystallization performed at 8 ºC/min had a X^{SAXS}/X_c^{WAXD} ratio lower than unity with the other assignment, which is not physically meaningful. High discrepancies between SAXS and WAXD crystallinities are usual in the literature [37] and have been explained assuming the existence of amorphous phase domains. Note also that the given assignment lead to a crystalline lamellar thickness, l_c, close to 6 nm which is higher than the chain axis repeat 3.133 nm and close to predicted values for similar polyamides [40]. Moreover, a lamellar thickness of only 2 nm is difficult to combine with the *hkl* reflections detected in the X-ray diffraction patterns.

- **Isothermal and non-isothermal crystallization studies by optical microscopy**

Isothermal crystallization of nylon 56 from the melt rendered spherulites of appreciable size over the narrow temperature range of 238-220 ºC (**Figure 4.1.14**). This crystallization proceeded according to a heterogeneous nucleation as demonstrate by DSC analysis. The nucleation density increased exponentially with decreasing temperature in such a way that morphologies were difficult to examine at temperatures lower than 220 ºC. Specifically, densities of 15, 40, 90, 160 and 210 nuclei/mm^2 were measured at crystallization temperatures of 239, 237, 234, 230 and 227 ºC, respectively.

Spherulites exhibited variable optical properties and a fibrilar texture over the studied temperature range (**Figure 4.1.14** a). At temperatures higher than 237 ºC spherulites showed a high positive birefringence, although aggregates with a non defined optical sign were also observed when temperature was higher than 237 ºC. Negative spherulites with a low birefringence were developed in the narrow interval between 233 ºC and 237 ºC, whereas high positively birefringent spherulites were formed at temperatures lower than 233 ºC. Spherulites isothermally growth in three steps at the corresponding representative temperatures (**Figure 4.1.14** b) allowed to compare better the indicated optical properties and showed clearly that the birefringence sign changed in the sequence of positive-negative-positive when crystallization temperature was decreased. Furthermore, it can be observed (inset of **Figure 4.1.14** b) that the low birefringence zone can also be detected as a black ring justifying previous observations were only positive spherulites were reported together with a zero birefringent zone at temperatures close to 233 ºC [26]. Non-isothermal experiments (**Figure 4.1.14** c) showed also

the development of the three different birefringent zones with changes that took place at well defined temperatures (237 and 233 ºC).

It is interesting to note that the indicated birefringence changes are different to those observed in conventional polyamides like nylon 66 where birefringence changed from negative to positive by decreasing the crystallization temperature. In this case, the change in the optical properties was explained considering the structure based on the stacking of hydrogen-bonded sheets and different growth geometries [41,42]. Thus, positive and negative spherulites were interpreted as a consequence of the establishment of hydrogen bonds along a radial or a tangential spherulitic direction, respectively. The birefringence sign was directly associated with how lamellae with a single structure grow in the spherulite. However, the reason for such a drastic change in the growth mechanism at a well defined temperature remains unclear. The peculiar structure found for the high temperature form of the studied odd-even nylon where two hydrogen-bonding directions seem to exist may be one of the reasons for the unusual formation of positive spherulites at higher crystallization temperature. In any way, the synchrotron data acquired during cooling runs allowed discarding a direct relation between the change on the birefringence sign and possible polymorphic transitions. Furthermore, no changes on both texture and birefringence could be detected when the different spherulites were heated until fusion. Thus, the morphologies developed during crystallization of nylon 56 were not reversible.

Spherulitic growth rates were determined from isothermal experiments by following the change of the spherulite radius with time up to impingement (**Figure 4.1.15** a) within the studied temperature intervals. The measured radial growth rates, G, varied from a minimum value of 0.08 μm/s at 239 ºC to a maximum value close to 1.3 μm/s at 225 ºC. Non-isothermal procedures were also applied to study the temperature dependence of the spherulitic growth rate during hot crystallization. Thus, the spherulitic growth rate (G) can be estimated [43-45] by measuring the change of the spherulite radius (R) with temperature (T) when experiments are performed at a constant cooling rate ($\mathrm{d}T/\mathrm{d}t$):

$$G = \mathrm{d}R/\mathrm{d}t = (\mathrm{d}R/\mathrm{d}T)\,(\mathrm{d}T/\mathrm{d}t) \qquad (4.1.4)$$

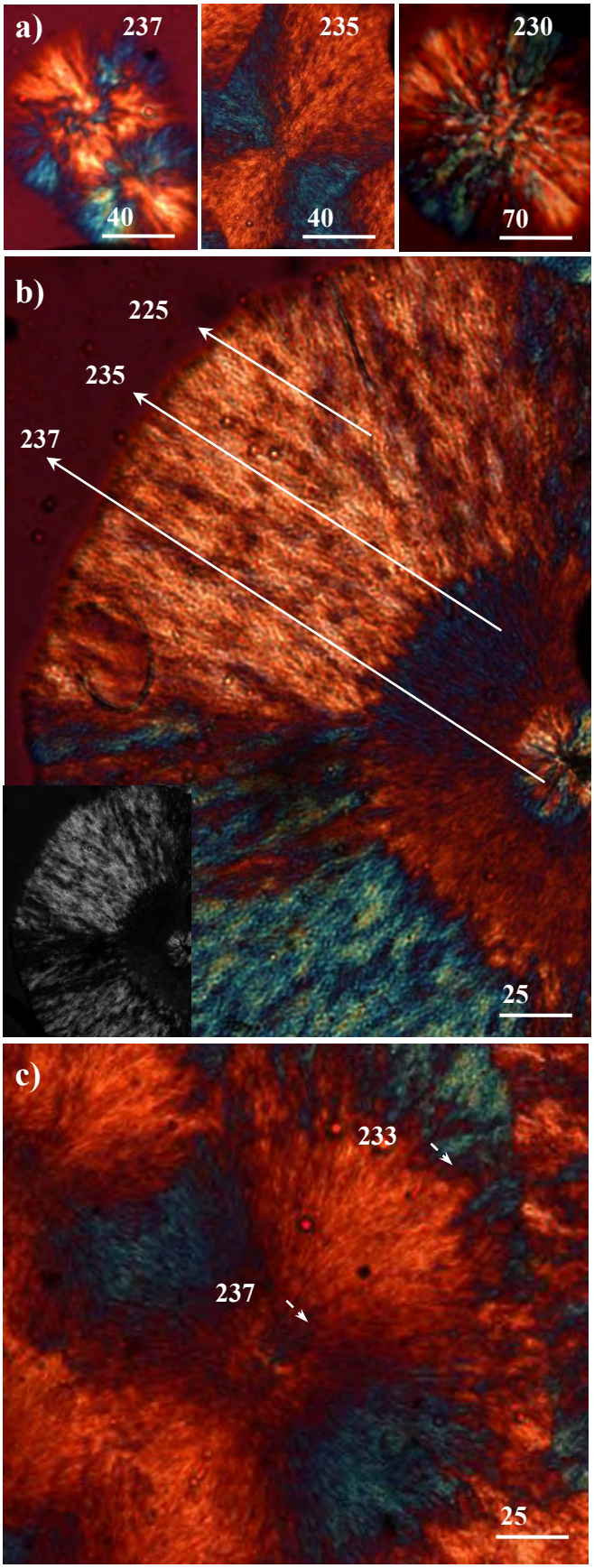

Figure 4.1.14 a) Optical micrographs of nylon 56 spherulites isothermally crystallized at 237 ºC (left), 235 ºC (middle) and 230 ºC (right). b) Optical micrograph of a nylon 56 spherulite that was isothermally crystallized at three different temperatures: Firstly at 237 ºC, secondly at 235 ºC and finally at 225 ºC. Inset shows a black and white micrograph where the low birefringence zone corresponding to the polymer crystallized at the intermediate temperature appeared as a black ring. c) Optical micrograph of a nylon 56 spherulite nonisother-mally crystallized at a cooling rate of 1 ºC/min.

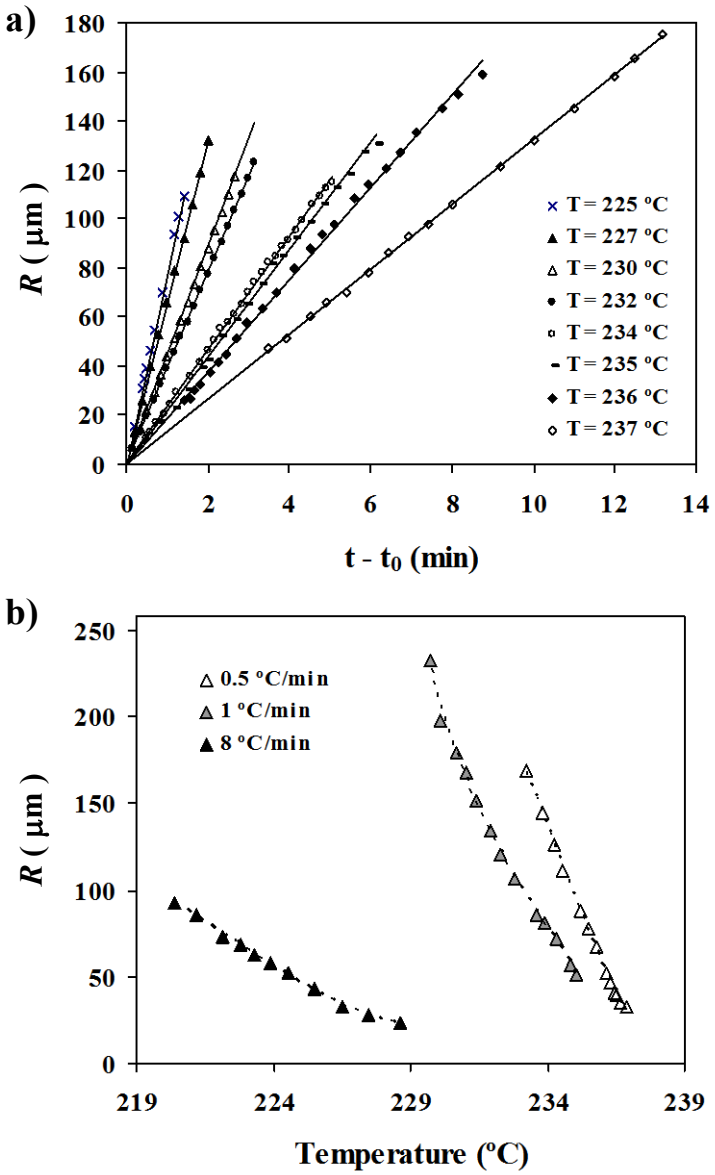

Figure 4.1.15 a) Plots of the radius of nylon 56 spherulites versus crystallization time for isothermal hot crystallizations performed at temperatures ranging between 225 and 237 ºC. b) Variation in spherulite radius with temperature during cooling at the indicated rates.

Experimental problems lie in the choice of the cooling rate required to maximize the crystallization temperature range where radii can be well measured. For this reason, the use of various rates is highly effective in expanding this range.

The plot of the radius versus temperature (**Figure 4.1.15** b) can be fitted to polynomial equations with a good regression coefficient (r) that allows the calculation of the value of its first derivative (dR/dT) for each cooling rate as a function of the crystallization temperature. Third-order equations were always chosen since the regression coefficients (≥ 0.998) were slightly better than those calculated for lower-order equations and remained practically constant when higher orders were assayed.

Figure 4.1.16 b plots the deduced *G* values from non-isothermal data and those measured from isothermal experiments. It should be pointed out that a good agreement was found and that non-isothermal experiments had several advantages: a continuous evolution could be determined and measures were less time consuming.

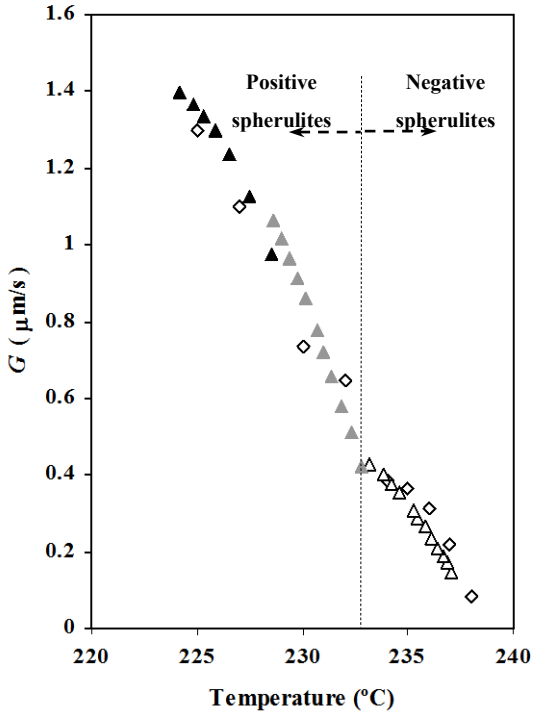

Figure 4.1.16 Spherulitic growth rates determined by the equations deduced for cooling runs of 8 (▲), 1 (▲) and 0.5 ºC/min (Δ). For the sake of completeness, experimental data deduced from isothermal experiments are also plotted (◇).

Experimental data defined the right side of the typical bell shaped curve that describes the temperature dependence of the growth rate, i.e. the zone controlled by secondary nucleation. Both isothermal and non-isothermal measures suggests the existence of a shoulder at high temperatures (> 233 ºC) which may be a consequence of a different secondary nucleation constant. Thus, at least experiments pointed out to the existence of two crystallization regimes which could be associated to different spherulites, e.g. positive at temperatures lower than 233 ºC and negative at higher temperatures.

4.1.4 Conclusions

Nylon 56 crystallized from solution according to a peculiar monoclinic structure (form I) where hydrogen bonds were established along two directions and where neighbouring chains were shifted along their chain axis direction. On heating, this structure showed a Brill transition resulting in a pseudohexagonal chain axis projected unit cell and a structure where the chain

axis shift was kept in order to optimize the hydrogen bonding interactions. At some degrees before fusion, the diffraction patterns showed new narrow reflections which could be indexed according to a new monoclinic unit cell (form II).

Brill transition was not reversible since nylon 56 mainly crystallized from the melt into form II, which on cooling gave rise to a pseudohexagonal packing. A minor crystallization into form I could also be detected and accounted into a significant ratio of this form when room temperature was achieved.

Nylon 56 crystallized on cooling into fibrillar spherulites with optical properties that were depended on the crystallization temperature and differed from those found in nylons having conventional sheet structures. During crystallization thinner lamellae inserted into the loosely stacked bundles of primary lamellae and the interlamellar amorphous regions became more compact.

4.1.5 References

[1] Bunn CW, Garner EV, Proc. R. Soc. London Ser. A 1947;189:39-68.

[2] Xenopoulos A, Clark ES. In Nylon Plastics Handbook; Kohan MI Ed.; Hanser Publishers: Munich, Vienna and New York, 1995; Chapter 5:108-137.

[3] Kinoshita Y, Makromol. Chem. 1959;33:1-20.

[4] Puiggalí J, Franco L, Alemán C, and Subirana JA. Macromolecules 1998;31: 8540-48.

[5] Franco L, Subirana JA, Puiggalí J. Macromolecules 1998;31:3912-24.

[6] Villaseñor P, Franco L, Subirana JA, Puiggali J. J Polym Sci Part B, Polym Phys Ed 1999;37:2383-95.

[7] Navarro E, Franco L, Subirana JA, Puiggalí J. Macromolecules 1995;28:8742- 50.

[8] Franco L, Cooper SJ, Atkins A DT, Hill M, Jones NA. Macromolecules 1998;36: 1153-65.

[9] Holmes DE, Bunn CW and Smith D. J Polym Sci Part A, General Papers 1955;17:159-177.

[10] Brill R. Makromol Chem 1956;18:294-309.

[11] Schmidt GF, and Stuart HA, Naturforsch Z. 1958;13A:222-26.

[12] Hirschinger J, Miura H, Gardner KH, EnglishAD, Macromolecules 1990;23:2153-59.

[13] Wendoloski JJ, Gardner KH, Hirschinger J, Miura H, English AD. Science 1990;247:431-436.

[14] Ramesh C, Keller A and Eltink S J E A. Polymer 1994;35:2483-87.

[15] Hill MJ, Atkins EDT, Macromolecules 1995;28(2):604-9.

[16] Vasanthan N, Murthy NS, Bray RG. Macromolecules 1998;31:8433-35.

[17] Murthy N S, Wang Z, Hsiao BS, Macromolecules 1999;32:5594-99.

[18] Ramesh C, and Gowd EB, Macromolecules 1999;32:3721-26.

[19] Jones NA, Atkins EDT, Hill MJJ, Polym. Sci. Part B, Polym. Phys. 2000;38:1209-21.

[20] Feldman A Y, Wachtel E, Vaughan G B M, Weinberg A and Marom G. Macromolecules 2006;39:4455-59.

[21] Tashiro K, Yoshioka Y, Polymer 2004;45:6349-55.

[22] Yoshioka Y, Tashiro K, Ramesh C, Polymer 2003;44:6407-17.

[23] Cui X, Yan D, Eur Polym J, 2005;41:863-870.

[24] Rueda DR, García-Gutiérrez MC, Nogales A, Capitán MJ, Ezquerra TA, Labrador A, et al. Rev Sci Instrum 2006;(77)Art. No. 033904 Part 1.

[25] Hoffman JD, Weeks JJ. J. Chem. Phys. 1962;37:1723-46.

[26] Magill JH. J. Polym. Sci. part A 1965;3:1195-1219.

[27] Avrami, M. J Chem Phys 1939;7:1103-12.

[28] Avrami, M. J Chem Phys 1940;8:212-24.

[29] Wunderlich B. Macromolecular Physics. Crystal Melting, vol. 3. New York : Academic Press ; 1980.

[30] Liu M, Zhao Q, Wang Y, Zhang C, Mo Z, Cao S. Polymer 2003;44:2537-45.

[31] Cui X, Qing S, Yan D. Eur Polym J 2005;41:3060-68.

[32] Biangardi JJ, Macromol Sci 1990;29:139-153.

[33] Jones NA, Atkins EDT, Hill M, Cooper SJ, Franco L. Polymer 1997; 38:2689-99.

[34] Feldman AY, Wachtel E, Vaughan GBM, Weinberg A, Marom G. Macromolecules 2006;39:4455-59.

[35] Vonk, C. G.; Kortleve, G. Kolloid Z Z Polym 1967;220:19-24.

[36] Vonk, C. G. J Appl Cryst 1975;8:340-341.

[37] Hsiao, B. S.; Wang, Z.; Yeh, F.; Yan, G.; Sheth, K. C. Polymer 1999;40:3515-23.

[38] Hsiao, B. S.; Gardner, K. H.; Wu, D. Q.; Chu, B. Polymer 1993;34:3986-95.

[39] Ikada, Y.; Jamshida, K.; Tsuji, H.; Hyoan, S. H. Macromolecules 1987; 20: 904-6.

[40] Dreyfuss, P. J. Polym Sci. Part B: Phys. Ed. 1973; 11:201-16.

[41] Lovinger AJ. J. Appl. Phys 1978;49:5003-13.

[42] Lovinger AJ. J. Appl. Phys 1978;49:5014-28.

[43] Chen M, Chung CT, J Polym Sci Part B: Polym Phys 1998;36:2393-99.

[44] di Lorenzo, M. L.; Cimmino, S.; Silvestre, C. Macromolecules 2000;33:3828-32.

[45] di Lorenzo, M. L. Polymer 2001;42:9441-46.

4.2

Study on the Brill transition and melt crystallization of Nylon 65: A polymer able to adopt a structure with two hydrogen-bonding directions.

Real time temperature dependence of X ray diffraction patterns and infrared spectra for nylon 65, a representative polymer of the even-odd nylon series, was studied. A particular structure based on the establishment of two hydrogen-bonding directions had previously been postulated for this polymer. Therefore, the determination of its temperature-induced transitions is a relevant topic. Results indicate that nylon 65 undergoes a reversible Brill transition at high temperature, leading to a pseudohexagonal chain axis projected unit cell. Furthermore, this polyamide shows a polymorphic transition around 100 ºC which is not completely reversible on cooling.

Crystallization of nylon 65 was also analyzed by simultaneous WAXD and SAXS synchrotron radiation experiments to determine the evolution of the degree of crystallinity and morphological parameters on cooling. Optical microscopy studies were also performed under isothermal and non-isothermal conditions to distinguish the different spherulitic morphologies. Results reveal that the optical properties of nylon 65 spherulites are different from those of conventional even-even nylon spherulites. Multiple melting peaks associated with lamellae of different thicknesses were observed in the calorimetric heating scan of melt-crystallized samples.

4.2.1 Introduction

It is well known that the structures of aliphatic polyamides are usually based on the stacking of sheets composed of hydrogen-bonded molecular chains with a planar zig-zag conformation (α and β forms).[1] Nylons derived from ω-aminoacids with an even number of carbon atoms (e.g. nylon 6[2]) or even diamines and even dicarboxylic acids (e.g. nylon 66[3]) are the most representative examples. X-ray fiber diffraction patterns of polymers with the above structures are characterized by two strong equatorial reflections that appear at spacings close to 0.44 and 0.37 nm. These reflections are associated with interchain distances within and between layers, respectively.

Energy considerations indicate that sheet structures are favored when NH and CO groups of neighboring chains face each other and form all possible hydrogen bonds with an appropriate geometry (e.g. angles close to 180º for N-H…O and H…OC interactions). However, depending on the number of methylene groups of the constitutive units, this cannot be achieved with an all trans molecular conformation. Thus, new structures should be favored as the γ form firstly postulated for nylon 77[4]. Furthermore, the γ form seems to be stabilized when the number of methylene groups is high, even if the hydrogen-bond geometry can be well established with an all trans conformation.[1,5]

The γ form is characterized by a pseudohexagonal molecular packing that gives rise to a characteristic diffraction pattern with a strong equatorial reflection at 0.415 nm. In this case, the torsional angles of the bonds adjacent to the amide groups tend to ± 120º, causing the amide plane to tilt by approximately 60º. The chain is shortened and the establishment of good hydrogen-bonding interactions along a single direction becomes possible.

Some polyamides, like nylon 6, show polymorphism between the α and γ forms. The first is commonly caused by slow cooling from the melt while the second occurs in melt-spun fibers or by rapid crystallization from the melt.[6,7] Stretching or annealing may favor the γ to α conversion[7,8] whereas the opposite is observed by treatment with iodine/potassium iodide aqueous solutions.[9]

Nylon 65 is also a polyamide that cannot form all favorable hydrogen-bonding interactions when molecular chains have an all trans conformation (**Figure 4.2.1** a). Recent diffraction data surprisingly revealed that solution-crystallized single crystals had characteristic reflections at 0.432 and 0.375 nm instead of those expected at ~0.415 nm (*γ*-form). In fact, a new structural model characterized by the establishment of hydrogen bonds along two different directions was inferred[10] (**Figure 4.2.1** b). The molecular conformation is close to the all trans one since only a slight deviation towards 150º (or -150º) for the two CH_2CH_2-CONH torsional angles of the dicarboxylic moiety was postulated. This conformation causes amide groups of the odd glutaric

unit to rotate in opposite senses from the plane defined by the methylene carbon atoms. Hydrogen bonds along two directions can be well established when neighboring chains are conveniently shifted, giving rise to a monoclinic unit cell.

Aliphatic polyamides usually show a not completely well understood phase transition that occurs on heating/cooling. It is named Brill transition and was discovered in nylon 66, with the detection of a reversible change from a triclinic to a pseudohexagonal structure.[11] Basically, on heating the two characteristic packing reflections of the triclinic sheet structure (0.44 and 0.37 nm) gradually merge into a single reflection (0.42 nm) indicative of a pseudohexagonal packing.

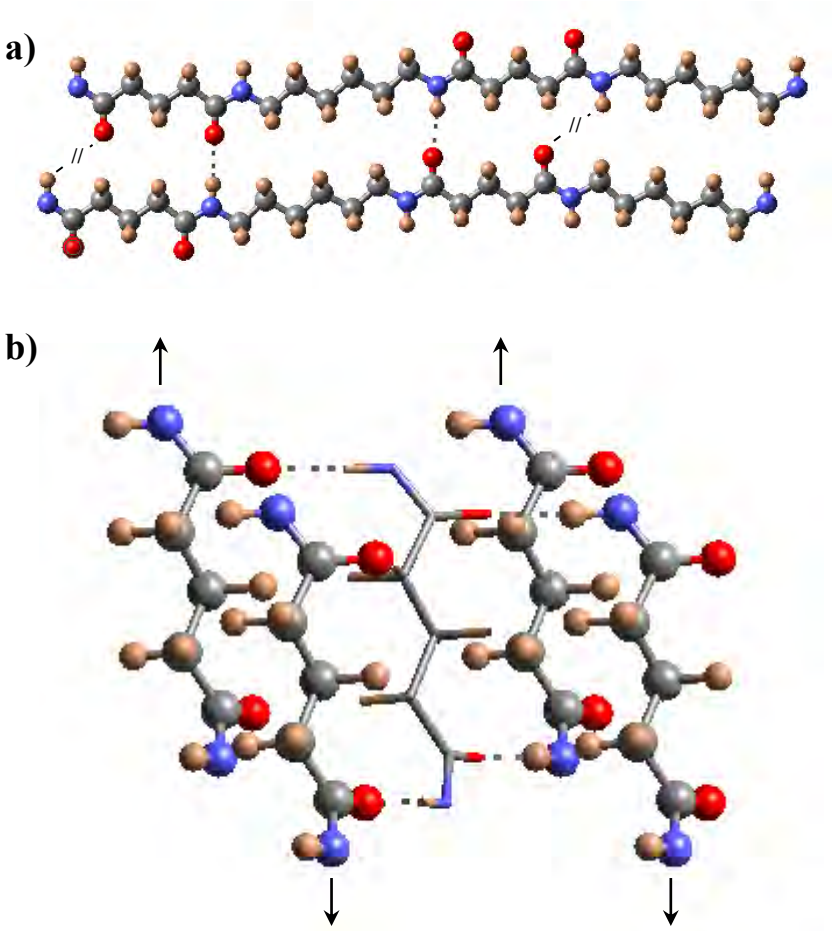

Figure 4.2.1 a) Scheme of the unfavorable hydrogen-bond geometry between nylon 65 molecular chains with an all trans conformation. b) Scheme of the establishment of hydrogen bonds along two directions when consecutive amide planes of a molecular chain slightly rotate in opposite directions from the plane defined by the methylene carbon atoms. External chains (ball and stick representation) should be shifted along the chain axis direction (see arrows) with respect to the central chain (stick representation), thus giving rise to a monoclinic unit cell. Color code: nitrogen, blue; oxygen, red; carbon, gray; hydrogen, brown.

Although a large number of studies have been reported for several nylons,[12-26] the phenomenon is not yet fully understood and some points still deserve special attention:

a) The temperature (T_B) at which the Brill transition is considered complete is variable since it depends on many factors (e.g. crystallization conditions, thermal history and heating rate).
b) The Brill transition is reversible (i.e. on cooling the single peak splits again into the two indicated packing spacings). A hysteresis effect is usually detected since T_B is higher on heating than on cooling.
c) Gradual crystallographic changes occur over a wide temperature range before and after the transition for heating and cooling processes, respectively. These changes reflect a variation in the dimensions of the unit cell associated with the layered structure.

The occurrence of a phase transition at T_B cannot be corroborated by DSC experiments or optical microscopy observations since no additional endothermic/exothermic peaks or changes in birefringence were respectively detected.

The aim of the present work is to gain insight into the structural transitions induced by temperature observed in even-odd polyamides having the new structure with two hydrogen-bonding directions. Nylon 65 was specifically chosen as a representative polymer. It should also be pointed out that the Brill transition has not yet been studied for any even-odd polyamide.

4.2.2 Experimental section

Materials

Nylon 65 was synthesized, as previously described,[10] by interfacial polycondensation of 1,5-diaminopentane and adipoyl dichloride using toluene as organic solvent and sodium hydroxide as proton acceptor. An intrinsic viscosity of 0.85 dL/g was determined in dichloroacetic acid at 25 ºC.

Measurements

Calorimetric data were obtained by differential scanning calorimetry using a TA Instruments Q100 series with T_{zero} technology and equipped with a refrigerated cooling system (RCS) operating at temperatures from -90 ºC to 550 ºC. Experiments were conducted under a flow of dry nitrogen with a sample weight of approximately 5 mg, while calibration was performed with indium. The T_{zero} calibration involved two experiments: the first was done without samples and the second was performed with sapphire disks.

The spherulite growth rate was determined by optical microscopy using a Zeiss Axioskop 40 Pol light polarizing microscope equipped with a Linkam temperature control system configured by a THMS 600 heating and freezing stage connected to a LNP 94 liquid nitrogen cooling

system. Spherulites were grown from homogeneous melt-crystallized thin films obtained by melting 1 mg of the polymer mixture on microscope slides. Next, small sections of these films were pressed or smeared between two cover slides and inserted into the hot stage. The thicknesses of the squeezed samples were close to 10 μm in all cases. Samples were kept at 265 ºC (more than 20 ºC above the polymer melting point of 243 ºC) for 5 minutes to wipe out sample history effects, and then quickly cooled to the selected crystallization temperature. Alternatively, samples were non-isothermally crystallized at a cooling rate of 2 ºC/min. Texture and birefringence was monitored in both isothermal and non-isothermal crystallizations by taking micrographs with a Zeiss AxiosCam MRC5 digital camera at appropriate time intervals. A first-order red tint plate was employed to determine the sign of spherulite birefringence under crossed polarizers.

Fiber X-ray diffraction data were obtained by Ni-filtered CuK_α radiation of wavelength 0.1542 nm and using a modified Statton camera (W. H. Warhus, Wilmington, DE). Patterns were recorded at different temperatures using a temperature-controlled chamber provided by the manufacturer.

Electron diffraction patterns from single crystals were obtained using a Phillips EM 301 electron microscope operating at 100 kV. Isothermal crystallizations were conducted in diluted glycerine solutions at 140 ºC. Patterns were recorded on Maco EM films by the selected-area method.

Simultaneous time-resolved SAXS/WAXD experiments were carried out at the CRG beamline (BM16) of the European Synchrotron Radiation Facility of Grenoble. The beam was monochromatized to a wavelength of 0.098 nm. The capillary with the sample was held in a Linkam hot stage with temperature control within 0.1 ºC. WAXD/SAXS profiles were simultaneously acquired during heating/cooling experiments in time frames of 12 s. The heating and cooling rates varied between 20-10 ºC/min and 20-4 ºC/min, respectively. Two linear position-sensitive detectors were used:[27] the WAXD detector was calibrated with diffractions of a standard of an alumina (Al_2O_3) sample, whereas SAXS detector was calibrated with different orders of diffraction from silver behenate. The diffraction profiles were normalized to the beam intensity and corrected considering the empty sample background. Deconvolution of WAXD peaks was performed with the PeakFit v4 program by Jandel Scientific Software using a mathematical function known as “Gaussian area”.

Infrared absorption spectra were recorded with a Fourier Transform FTIR 4100 Jasco spectrometer in a 4000-600 cm^{-1} range. A Specac Golden Gate Heated Diamond ATR Top Plate which can be used at up to 200 ºC and a Series 4000 High Stability Temperature Controler were also employed.

4.2.3 Results and discussion

- **Thermal properties of Nylon 65**

Figure 4.2.2 displays a sequence of heating/cooling runs performed to study the thermal behavior of nylon 65. A heating scan of a solution-crystallized sample showed a broad endothermic peak around 110 ºC (38 J/g) and a double melting peak (233 ºC and 243 ºC) associated with a typical recrystallization process occurring on heating. The cooling run after keeping this sample in the melt state for three minutes revealed a narrow exothermic crystallization peak around 203 ºC. A subsequent heating run showed a very small endotherm around 81 ºC and a fusion characterized by a main peak and a shoulder at 229 ºC and 233 ºC, respectively. Finally, a melt quenched sample allowed the determination of a glass transition temperature at 49 ºC and a single and broad melting peak at 233 ºC. It should be pointed out that the melting peaks of samples crystallized from the melt appeared at lower temperatures than from solution. The large gap suggests that they have a different origin.

Figure 4.2.3 a illustrates the melting behavior of samples isothermally crystallized at different temperatures. The thermograms are generally characterized by the presence of three melting peaks that gradually shifted to higher temperatures with increasing the crystallization temperature. The peak at the lowest temperature always has a very low intensity and seems to be associated with highly defective crystals, as previously described for different polymeric systems. The two peaks that appeared at higher temperatures seem to be associated with two populations of lamellar crystals of different thicknesses. It is remarkable that the peak at the highest temperature should not correspond to crystals formed during the heating run since it appeared at a variable temperature and its relative intensity increased with the crystallization temperature. Note that a melt-recrystallization process where thin lamellae convert into thicker lamellae should be more important when samples were less perfect, and consequently crystallized at lower temperatures. Thus, in this case the peak intensity associated with less perfect crystals should decrease while that associated with reorganized crystals should increase with decreasing the crystallization temperatures. Furthermore, the thickness of the lamellae formed during the heating scan should be independent of the temperature at which the initial lamellae crystallized. As a result, a constant peak temperature should be expected. The possible existence of different crystalline structures with different thermodynamic stability was discarded as the origin of the multiple melting points since, as discussed in the next section, nylon 65 has a transition to a single structure before melting (**Figure 4.2.4**). Some polyamides do not show a complete Brill transition before melting (e.g. nylon 6[28]). In this case the peaks observed at low and high melting temperatures are associated with the less thermodynamically stable γ-form and the more stable α-form, respectively.[4]

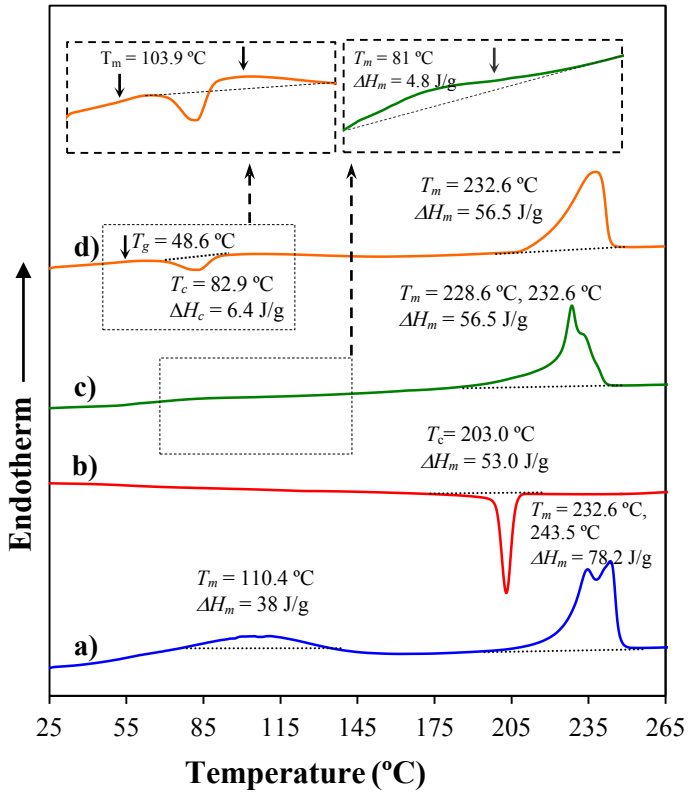

Figure 4.2.2 Sequence of DSC curves corresponding to a heating run of a solution crystallized sample (a), cooling run from the melt state (b), heating run of a melt-crystallized sample (c) and heating run of a quenched sample (d). Heating runs were performed at 20 ºC/min whereas the cooling run was performed at 10 ºC/min.

Samples coming directly from synthesis are constituted by defective crystals that easily undergo a melt-reorganization process on heating since crystallization took place at room temperature. Thus, the high melting peak temperature (243.5 ºC) observed in the first heating run (**Figure 4.2.2**) corresponds to the fusion of reorganized crystals. In fact, the origin of the high temperature melting peak was postulated in previous studies[10] as a consequence of lamellar thickening since it was enhanced when the heating rate was lowered. It is interesting to note that the melting temperature of 243.5 ºC was clearly higher than the peak temperatures observed in the melt-crystallized samples whose reorganization process was not significant.

A theoretical equilibrium melting temperature of 264 ºC was graphically determined (**Figure 4.2.3** b) according to the method of Hoffman and Weeks[29] (i.e. extrapolation of a plot of T_m versus T_c to $T_m = T_c$) and considering the data obtained from the endothermic peak observed at the highest temperature.

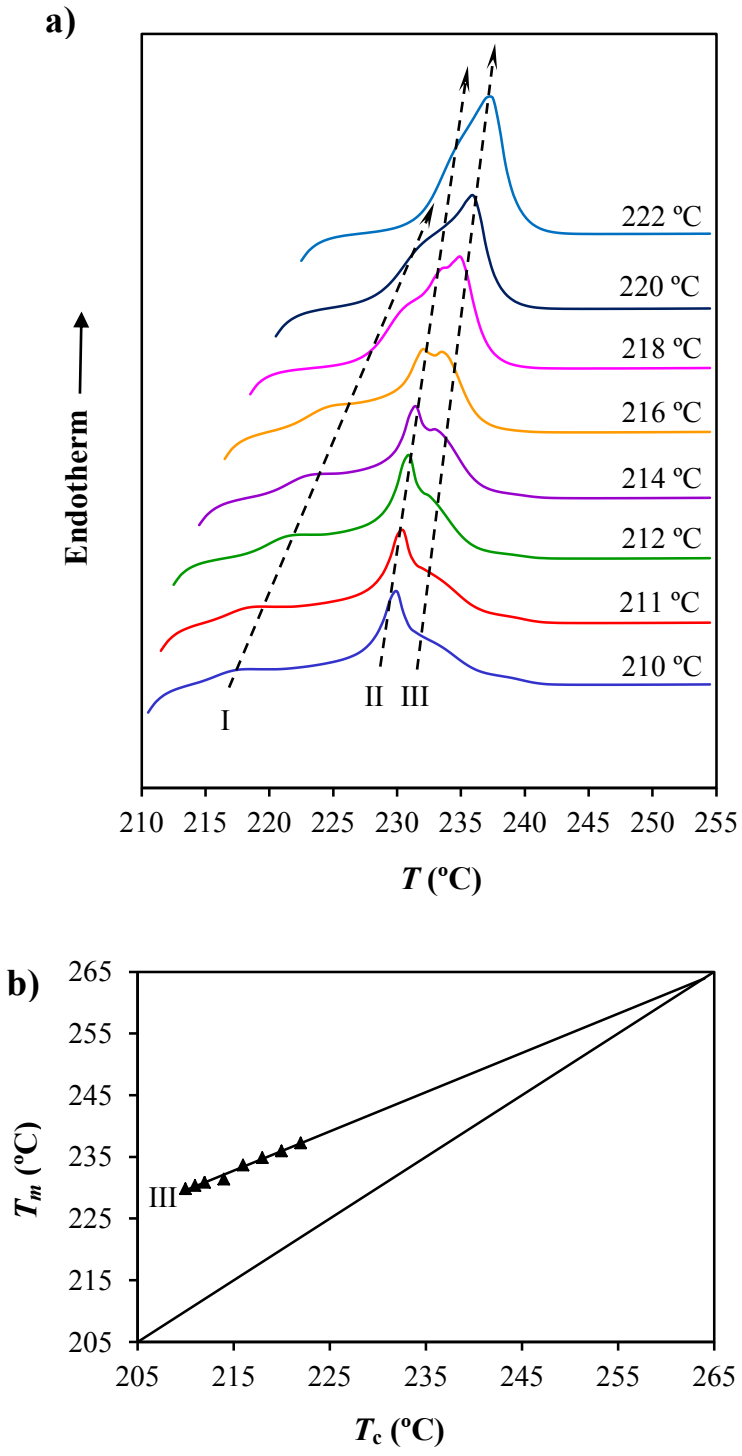

Figure 4.2.3 DSC curves corresponding to the heating run of samples isothermally crystallized from the melt at the indicated temperatures. b) Hoffman-Weeks plot drawn with the high temperature peak detected in the heating run of melt-crystallized samples.

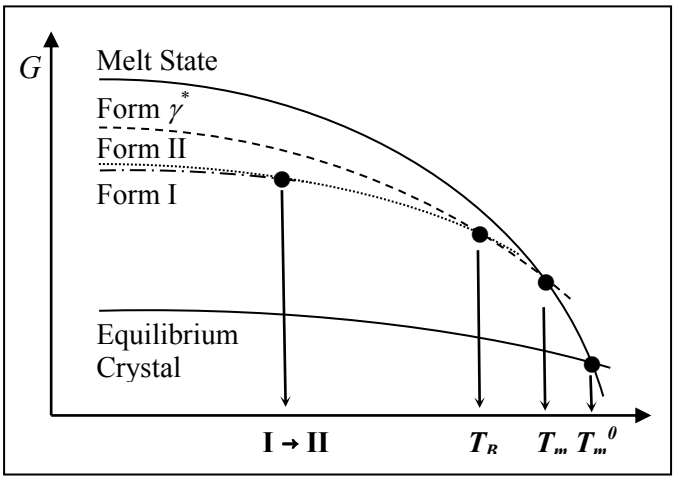

Figure 4.2.4 Gibbs free energy diagram for nylon 65 where form II transforms into a pseudohexagonal packing (γ^*) at the Brill transition temperature (T_B). In addition, a transition between forms I and II exists at low temperature. The equilibrium crystal melts at the equilibrium melting temperature (T_m^0) whereas the γ^* form melts at T_m.

Room temperature diffraction data of nylon 65

X-ray diffraction patterns of nylon 65 fibers annealed at 80 ºC were mainly characterized by two strong equatorial reflections at 0.432 and 0.375 nm and different 0*k*0 reflections that defined a bb^* angle of 24º (**Figure 4.2.5** a). Electron diffraction patterns of single crystals obtained from diluted solutions (glycerine and even other polyfunctional alcohols) had 2*mm* symmetry and a large number of *h*0*l* reflections (**Figure 4.2.5** b), allowing the inference of the same structure found in the annealed fibers. Thus, the stronger reflections of the electron diffraction patterns correspond to the 0.432 and 0.375 nm spacings. It is worth pointing out that the presence of some weak *hkl* reflections confirmed γ as the monoclinicity angle. All diffraction data were in agreement with the previously postulated monoclinic unit cell (a = 0.460 nm, b (chain axis) = 3.095 nm, c = 0.862 nm and γ = 114º), which was interpreted as a new structure with two hydrogen-bonding directions.[10]

A different pattern was observed only when samples were cooled from the melt state or even oriented without subsequent annealing. In these cases, a broad ring or a broad equatorial reflection was observed around 0.425 nm.

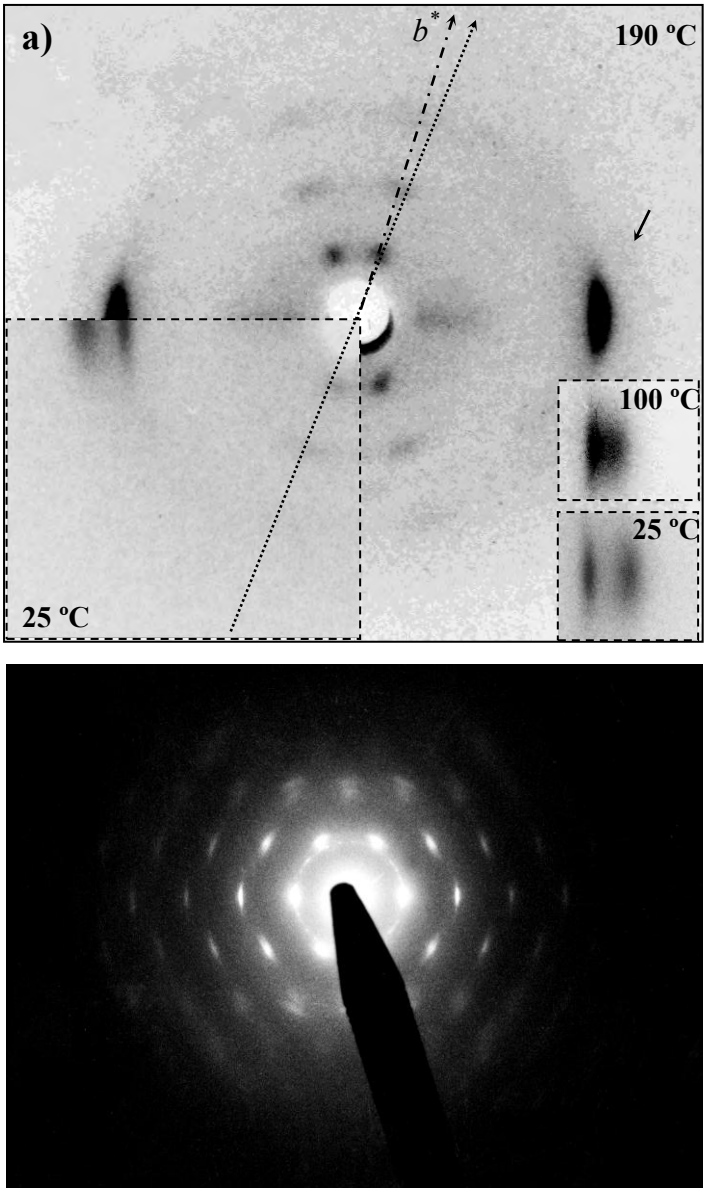

Figure 4.2.5 a) X-ray fiber diffraction pattern of nylon 65 at 190 ºC. Insets show the equatorial reflections observed at 100 and 25 ºC, and a quadrant of the fiber diffraction pattern obtained at 25 ºC. b* axes for fiber patterns at 190 (dotted and dashed line) and 25 ºC (dotted line) are also indicated. The arrow points to a non-equatorial reflection (0.379 nm) that is intensified in the high temperature pattern. b) Characteristic electron diffraction pattern of nylon 65 single crystals obtained in glycerine at 140 ºC.

- **Brill transition studies on nylon 65**

Figure 4.2.5 a shows the X-ray fiber diffraction pattern of a nylon 65 sample taken under stress at 190 ºC. It is clear that only one strong equatorial reflection (ca. 0.425 nm) was detected and that 0*k*0 reflections had an off-meridional orientation. Thus, the high temperature structure does not correspond to a typical hexagonal unit cell, although the existence of pseudohexagonal packing was suspected by considering only the *h*0*l* reflections. In fact, a monoclinic unit cell with a = 0.523 nm, b (chain axis) = 3.055 nm, c = 0.85 nm, $\alpha = \beta = 90^{\circ}$ and $\gamma = 110^{\circ}$ was previously reported.[10] The inset of **Figure 4.2.5** a contains the initial fiber pattern taken at room temperature, that is, before the start of the heating process. In this case, two equatorial reflections can be clearly distinguished as well as the 0*k*0 reflections defining a bb^* angle slightly higher than that measured in the pattern taken at 190 ºC (24º versus 20º). At intermediate temperatures (e.g. 100 ºC) equatorial spots appeared at intermediate positions, as shown in the insets of **Figure 4.2.5** a as well. It is also remarkable that the high temperature pattern suggests a highly crystalline sample since some new non-equatorial reflections appeared (see arrow in **Figure 4.2.1** a).

Figure 4.2.6 a shows a three-dimensional representation of WAXD profiles obtained by synchrotron radiation during a heating process performed at 10 ºC/min from room temperature to fusion. The same temperature dependent profiles were observed at heating rates of 13, 15 and 20 ºC/min. Representative profiles taken at selected temperatures are included in **Figure 4.2.6** b for comparison of the spacings of the main equatorial reflections. Diffraction profiles and fiber patterns obtained during the heating runs allow the inference of three highly significant features:

a) The spacings of the two equatorial reflections at 0.432 and 0.375 nm remained practically constant up to a temperature of approximately 70 ºC. Then, the intensity of these reflections diminished whereas new ones near 0.426 and 0.400 nm appeared with increasing intensity. A polymorphic transition seemed to occur which practically ended when a temperature of 120 ºC was reached. No significant changes were observed for the 0*k*0 reflections (as deduced from the fiber patterns), and consequently the transition seemed to involve only a modification of the dimensions of the chain axis projected unit cell. Thus, this rectangular cell is defined at room temperature by parameters of 0.412 and 0.862 nm which changed to 0.453 and 0.844 nm when the temperature reached 120º. This change implies a less compact structure since the packing surface increases from 0.355 nm^2 to 0.383 nm^2. The two structures found at low and high temperature will hereafter be called forms I and II, respectively.

b) After 120 ºC the two reflections at 0.426 and 0.400 nm gradually merged into a single peak at 0.425 nm that was obtained at a temperature of 190 ºC. This process seems a typical Brill transition where a pseudohexagonal packing (γ^*-form) is favored at a

temperature slightly lower than the melting point (**Figure 4.2.4**). It is worthing to point out that the Brill transition of nylon 65 was always observed at the same temperature (T_B) despite variations in the heating rate.

c) New peaks (e.g. 0.379 nm), which suggest an increase of the crystalline order, were detected when the temperature was higher than 190 ºC.

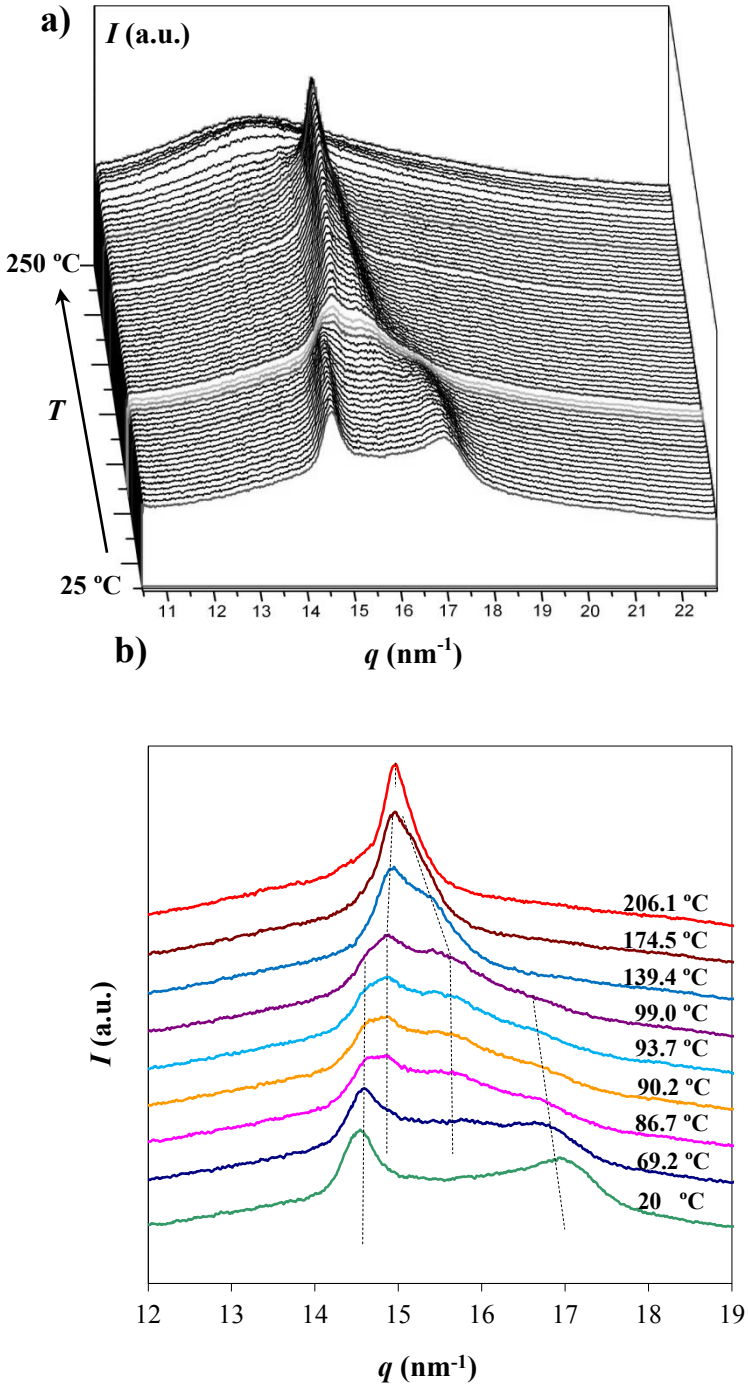

Figure 4.2.6 a) Three-dimensional representation of WAXD profiles of nylon 65 during heating (10 ºC/min) from room temperature to fusion. b) One-dimensional WAXD profiles of nylon 65 samples taken at selected temperatures during a heating scan (10 ºC/min). Spacings of main reflections are indicated.

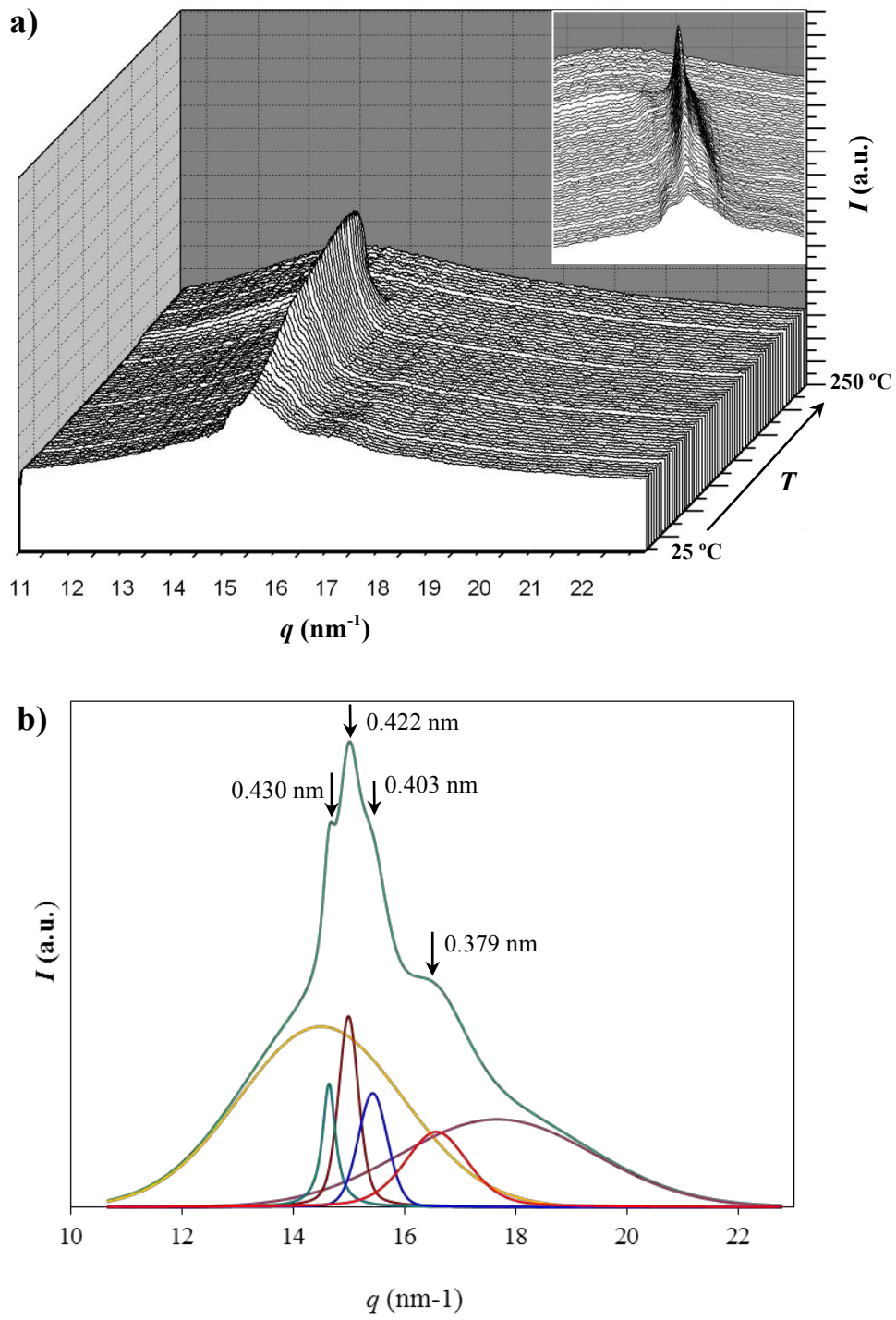

Figure 4.2.7 a) Three-dimensional representation of WAXD profiles of nylon 65 during cooling (10 ºC/min) from the melt to room temperature. Inset shows a different view of the temperature evolution of characteristic reflections. b) One-dimensional WAXD profile for nylon 65 taken at room temperature after a cooling run (10 ºC/min) from the melt state. Spacings of main reflections are indicated together with the deconvoluted peaks.

The form I to form II transition takes place in the temperature range where a broad endothermic peak (110 ºC) was observed in the DSC heating run of the sample coming directly from synthesis (**Figure 4.2.2**), whereas no calorimetric peak was detected around the Brill transition temperature, which is common in polyamides. Thus, for example DSC heating traces of nylon 66 do not show any endothermic peak at T_B with the exception of samples crystallized from solution.[14,20,30]

Assuming that form I corresponds to a structure with two hydrogen-bonding directions, it seems reasonable that thermal treatments result in structures different from the conventional γ form, which is characterized by a single hydrogen-bonding direction. Thus, transitions may involve only slight changes in the torsional angles vicinal to amide groups or even an increase in the mobility of polymethylene segments, which could lead to a pseudohexagonal packing without disrupting the initial hydrogen- bonding scheme. In this sense, fiber patterns with non-meridional 0*k*0 reflections are essential to support the finding that the Brill structure is different from the conventional γ form.

Figure 4.2.7 a shows the WAXD profiles acquired during a cooling run (10 ºC/min) from the melt state. It is clear that a narrow intense peak appeared around 0.420 nm during crystallization and that it progressively broadened and split into different peaks when the temperature decreased. **Figure 4.2.7** b shows the deconvolution of the diffraction profile obtained at room temperature where two amorphous halos and four crystalline peaks appearing at 0.430 and 0.379 nm (form I) and 0.422 and 0.403 nm (form II) could be observed. Thus, a Brill transition seemed to occur at a high temperature during the cooling process and was followed by a phase transition from form II to form I. Conversion between these two structures is only partial since the intensities of reflections associated with form I are similar to those related to form II (e.g. a form I to form II ratio of 0.45:0.55 was determined from the deconvoluted profile). The ratio between both forms was kept practically constant even if the cooling rate was decreased. Therefore, a value of 0.47:0.53 was determined for a rate of 4 ºC/min. It is also remarkable that the profile obtained at the end of crystallization (~ 165 ºC) is identical to that recorded at the end of the heating process, which was associated with a highly ordered structure.

The variation in intensity of the strongest peak (0.422-0.420 nm) could be useful in monitoring the different processes that occur on cooling, as is shown in **Figure 4.2.8**. Thus, this peak appeared and increased in intensity within the temperature range of 210-170 ºC, where crystallization took place. Two zones could be distinguished, i.e. 210-195 ºC and 195-170 ºC, with a quick and a slow increase in intensity, respectively. The maximum change was observed at approximately 203 ºC, in full agreement with DSC calorimetric data. Note also that the exothermic crystallization peak (**Figure 4.2.2**) is highly asymmetric and that the line base was only recovered when the temperature decreased to approximately 170 ºC. Thus, DSC and

WAXD data show a slow secondary crystallization process extending over the 195-170 ºC interval.

The peak intensity remained practically constant in the temperature range between 170 and 130 ºC. Then, it slightly decreased again with decreasing temperature due to the split of the peak caused by the Brill transition. Thus, this transition occurred at a lower temperature on cooling than on heating (190 ºC), indicating a clear hysteresis effect, as usually found in polyamides.[20] The transition was undetectable in the corresponding DSC cooling trace, in agreement with the lack of signal in the previous heating scan. At 100 ºC the decrease in the peak intensity was more pronounced as a consequence, in this case, of the new splitting caused by the form II to form I transition. This could not be detected by DSC because it was a partial conversion occurring in a broad temperature interval. However, it must be pointed out that, in a subsequent heating run (**Figure 4.2.2**) some endothermic signal was envisaged just after the glass transition. In any case, interpretation of endothermic peaks in this temperature region seems conflictive due to the overlapping with the broad endotherm corresponding to the evaporation of adsorbed water, which is clearly detected in the initial scanning run despite the sample was previously dried under vacuum.

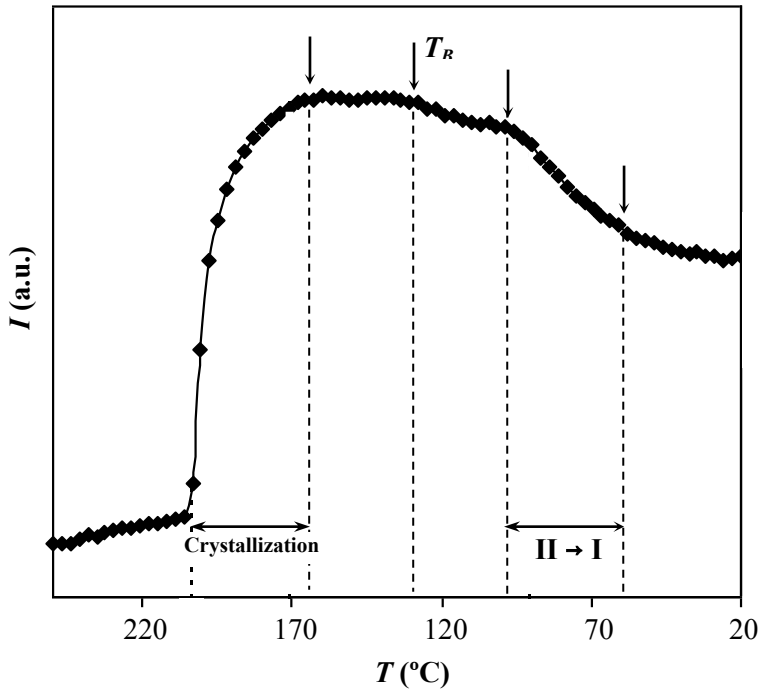

Figure 4.2.8 Temperature evolution of the peak intensity at 0.422-0.420 nm during a cooling run (10 ºC/min) from the melt state.

Crystallization of Nylon 65

The crystallization process was simultaneously monitored by time-resolved WAXD and SAXS non-isothermal experiments. In this way, the evolution of the mass fraction of the crystalline phase in the sample, X_c^{WAXD}, was determined from the different WAXD deconvoluted profiles as the ratio between the total intensities of the crystalline reflections I_c and the overall intensity I_T. Values at the end of crystallization ranged between 0.21 and 0.27 and increased with decreasing the cooling rate. SAXS patterns showed a long period peak at a value of the scattering vector, $q = [4\pi/\lambda] \sin(\theta)$, close to 0.4 nm^{-1} after subtraction of the empty sample background observed near the beam stop (**Figure 4.2.9**). This peak, which can be attributed to the lamellar structure of the spherulites, started to appear at the same temperature than crystalline reflections in the WAXD patterns (**Figure 4.2.10**), as presumable for a crystallization process controlled by nucleation and crystal growth. This temperature obviously decreased with increasing the cooling rate. The intensity of the SAXS peak increased during primary crystallization, then remained practically constant over a short temperature range and finally decreased. Thus, the SAXS peak practically disappeared before secondary crystallization was complete (**Figure 4.2.10**). This observation is important because it suggests a change in the amorphous phase since the intensity of SAXS peaks depends on the degree of crystallinity but also on the difference between the electronic densities of amorphous and crystalline phases. It is clear that on cooling the amorphous interlamellar component should adopt a more compact molecular arrangement, probably as a result of the improved hydrogen-bonding interactions.

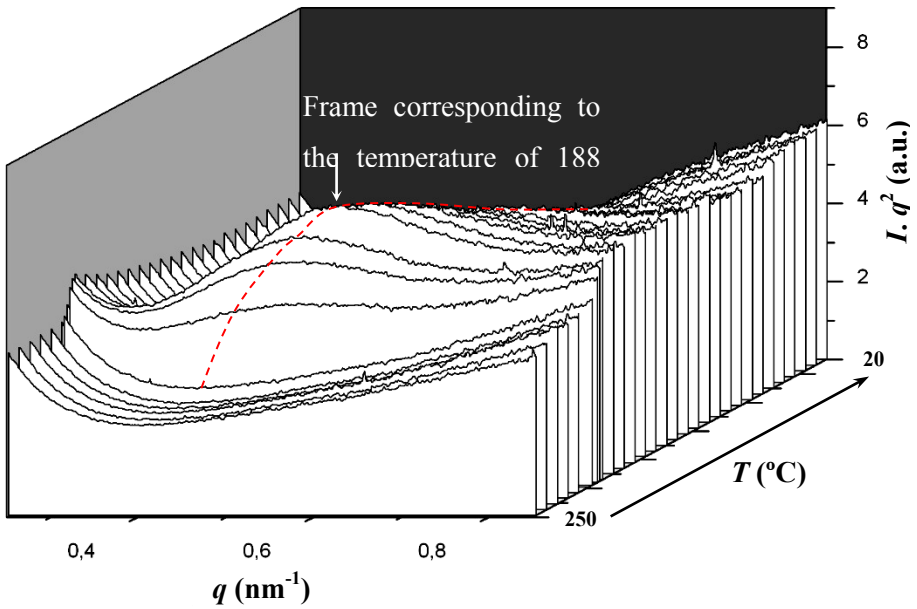

Figure 4.2.9 Three-dimensional representation of SAXS profiles of nylon 65 during cooling (10 ºC/min) from 250 ºC (melt state) to room temperature.

SAXS data were analyzed by the normalized one-dimensional correlation function,[31] $\gamma(r)$, which corresponds to the Fourier transform of the Lorentz-corrected SAXS profile:

$$\gamma(r) = \int_0^\infty q^2 I(q)\cos(qr)dq \; / \; \int_0^\infty q^2 I(q)dq \qquad (1)$$

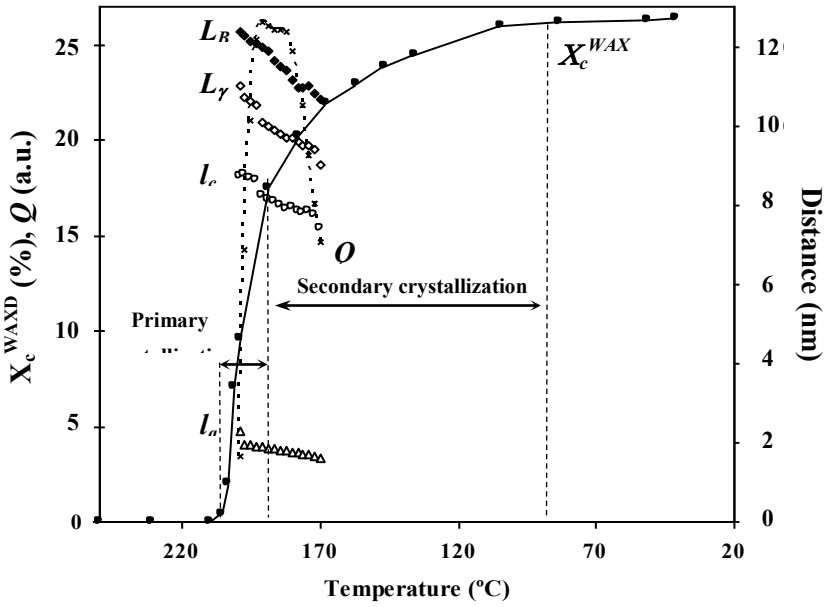

Figure 4.2.10 Temperature evolution of the long period, Lγ, crystal thickness, lc, amorphous thickness, la, scattering invariant, Q, and degree of crystallinity, XWAXD, during a non-isothermal melt crystallization performed at a cooling rate of 12 ºC/min.

The scattering intensity was extrapolated to both low and high q values using Vonk's model[32] and Porod's law, respectively. evaluate the peak intensity evolution during crystallization (**Figure 4.2.10**), and morphological parameters like the long period, L_γ, crystalline lamellar thickness, l_c, and amorphous layer thickness, l_a.

The evolution of these parameters during crystallization (**Figure 4.2.10**) shows a slight change in the long period (e.g. from 11.0 to 9.0 nm in the cooling performed at 12 ºC/min), which is mainly due to the decrease in crystalline lamellar thickness (e.g. from 8.7 to 7.4 nm). The latter was more significant during the secondary crystallization step (**Figure 4.2.10**) and indicates that new secondary lamellae inserted into the loosely stacked bundles of primary lamellae. New lamellae suffer spatial restrictions, leading to thinner defective crystals.

Correlation functions were used to determine the scattering invariant, Q, which allows to evaluate the peak intensity evolution during crystallization (**Figure 4.2.10**), and morphological parameters like the long period, L_γ, crystalline lamellar thickness, l_c, and amorphous layer thickness, l_a.

The evolution of these parameters during crystallization (**Figure 4.2.10**) shows a slight change in the long period (e.g. from 11.0 to 9.0 nm in the cooling performed at 12 ºC/min), which is mainly due to the decrease in crystalline lamellar thickness (e.g. from 8.7 to 7.4 nm). The latter was more significant during the secondary crystallization step (**Figure 4.2.10**) and indicates that new secondary lamellae inserted into the loosely stacked bundles of primary lamellae. New lamellae suffer spatial restrictions, leading to thinner defective crystals.

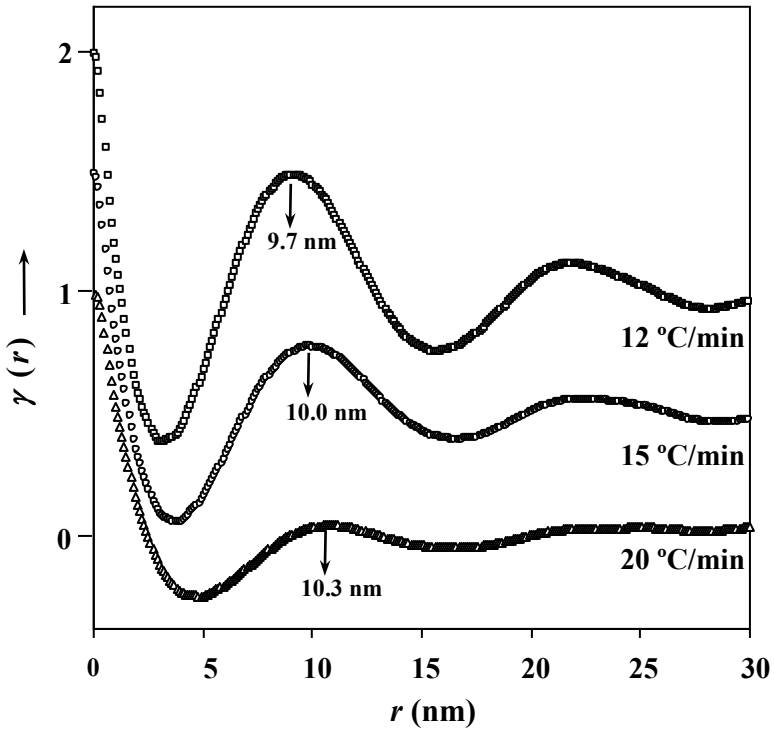

Figure 4.2.11 Correlation functions corresponding to the maximum intensity SAXS profile obtained during cooling runs of nylon 65 at the indicated rates.

Figure 4.2.11 compares the correlation functions calculated for the SAXS profiles obtained at different cooling rates and at the temperature (time) corresponding to the maximum peak intensity. Differences in lamellar spacings are minimal due to the balance between two counter factors: enhanced insertion mechanism producing thinner secondary lamellae, and increased crystallization temperature resulting in thicker primary lamellae with decreasing the cooling rate. However, the slight increase observed for the lamellar spacing with the cooling run

indicates the prevalence of the lamellar insertion effect. **Figure 4.2.11** also shows that the L_γ value associated with the most probable distance between the centers of gravity of two adjacent crystals (abscise of the first maximum of the correlation function) is greater than the long period determined from twice the abscise value of the first minimum of the correlation function, which is interpreted as the most probable distance between the centers of gravity of a crystal and its adjacent amorphous layer. This indicates a broader distribution of the layer widths of the major component,[33] which corresponds to the crystal phase.

SAXS crystallinities, X^{SAXS}, in the 0.80-0.83 range were calculated at the end of primary crystallization from the values of the morphological parameters ($l_c/(l_c + l_a)$). These crystallinities were considerably higher than those estimated from WAXD experiments, suggesting that amorphous phase domains exist between the lamellar stacks.

- **Spherulitic morphology of nylon 65**

Spherulites of even-even nylons (e.g. nylon 66) have been widely studied and their optical properties have been interpreted.[1,34,35] These polymers render negative spherulites at crystallization temperatures slightly lower than their melting point and positive spherulites at lower temperatures. The change in the optical properties is explained by a well established structure based on the stacking of hydrogen-bonded sheets. In fact, X-ray microbeam diffraction patterns suggested that positive and negative spherulites differ in the radial or tangential spherulitic direction where hydrogen bonds respectively form. Thus, the birefringence sign is directly associated with how lamellae with a single structure grow in the spherulite. However, the reason for such a drastic change in the growth mechanism at a well defined temperature remains unclear.

Surprisingly, the spherulitic morphology of even-odd nylons has been little studied. A detailed phenomenological description has only been reported for nylons 49, 67 and 69 by Magill.[36] In this case, rather puzzling observations suggesting a complex crystallization behavior were made. The main points of this work can be summarized as follows:

The three polymers exhibited a wide variety of spherulitic structures. Thus, a sample could render spherulites with a different birefringence sign and even a different texture (e.g. fibrilar or ringed) under certain crystallization conditions.

The birefringence sign often changed in the negative-positive-negative sequence with decreasing the crystallization temperature. The difference in behavior compared with the above even-even nylons, and in particular the different sign obtained at the lowest crystallization temperature, is worth noting.

Microbeam diffraction patterns indicated that spherulites always had a pseudohexagonal structure. Thus, no further investigation was undertaken to relate the variability observed in the spherulitic morphologies to different crystalline structures.

The birefringence sign of some spherulites (e.g. nylon 49 crystallized at low undercooling) could change in a reversible way by heating and cooling processes.

Isothermal crystallization of nylon 65 from the melt rendered spherulites of appreciable size over the narrow temperature range of 241-227 ºC. This crystallization proceeded according to a heterogeneous and thermal nucleation since spherulites of non-homogeneous size formed at a given crystallization temperature. The nucleation density increased exponentially with decreasing temperature in such a way that morphologies were difficult to examine at temperatures lower than 227 ºC. The induction time required for the first nuclei to be active at each temperature behaved oppositely to the nucleation density, as shown in **Figure 4.2.12**.

Spherulites exhibited a negative birefringence sign over the studied temperature range and a ringed texture (**Figure 4.2.13** a). The spacing between rings increased from ~ 0.15 nm at 238 ºC to ~ 0.30 nm at 232 ºC, where the ringed texture was better displayed. At 227 ºC the ringed texture was very difficult to be detected, although very close rings could be envisaged in the blue sectors, suggesting a trend towards a fibrillar texture.

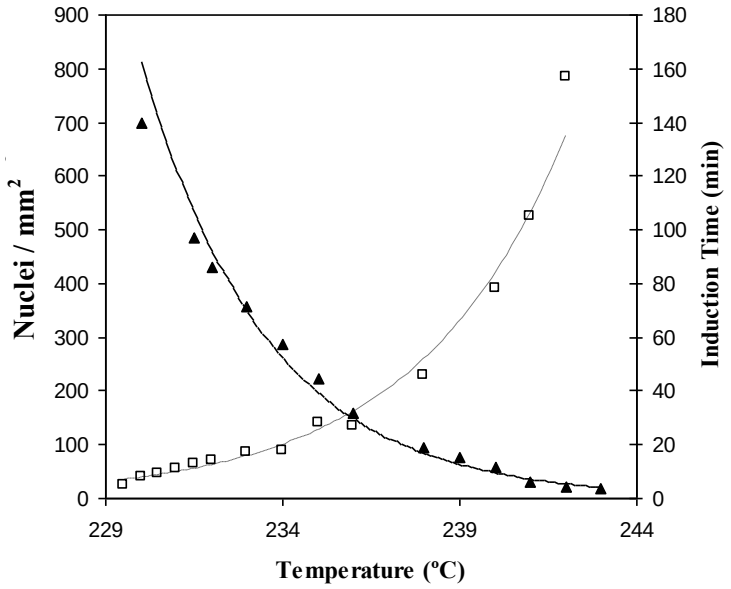

Figure 4.2.12 Variation in nucleation density and induction time with isothermal crystallization temperature.

Non-isothermal crystallization from the melt allowed the study of spherulitic growth at temperatures lower than isothermal crystallization due to the decrease in nucleation density. Furthermore, morphologic trends were more clearly stated in spherulites grown under the former conditions (**Figure 4.2.13** b). Thus, different textures were observed in a given spherulite according to the temperature at which the growth was conducted. The center of the spherulite always had a ringed texture that extended while the temperature was higher than 226 ºC. The outer parts of the spherulite, which were grown at temperatures lower than 224 ºC, had a fibrilar texture. It is remarkable that the birefringence sign became positive just at the temperature at which the change from a ringed to a fibrilar texture occurred. This zone with a positive birefringence developed at this intermediate position grown at temperatures between 226 and 224 ºC. **Figure 4.2.11**c shows a spherulite firstly isothermally crystallized at 235 ºC and then non-isothermally crystallized (0.5 ºC/min) until 180 ºC, which shows new insights. Thus, the center has the presumable ringed texture and negative birefringence which changed to positive in the zones grown at two precise temperatures: 226-224ºC (as above explained) and 200 ºC. Black and white micrographs (see inset) shows that the later change may be also associated to a variation on the spherulitic texture since at lower temperatures than 200 ºC (where the birefringence became again negative) a ringed texture can be envisaged again, whereas a fibrillar texture is clear at temperatures close to 224 ºC. No changes on both texture and birefringence could be detected when the different spherulites were heated until fusion. Thus, the complex morphologies developed during crystallization of nylon 65 were not reversible, in contrast with previous observations performed with nylon 49.[10]

X-ray diffraction data indicate that spherulitic growth of nylon 65 took place at temperatures at which only the structure characterized by pseudohexagonal packing develops. Thus, different textures and birefringence properties must only be related to changes in the growth mechanism. Properties of nylon 65 spherulites are in agreement with some observations on related nylons, specifically the negative-positive-negative change in the birefringence sign with decreasing temperatures, in contrast with the behavior of conventional polyamides. The peculiar structure found for the high temperature form of the studied even-odd nylon where two hydrogen-bonding directions seem to exist may be the reason for the unusual formation of negative spherulites at lower crystallization temperatures.

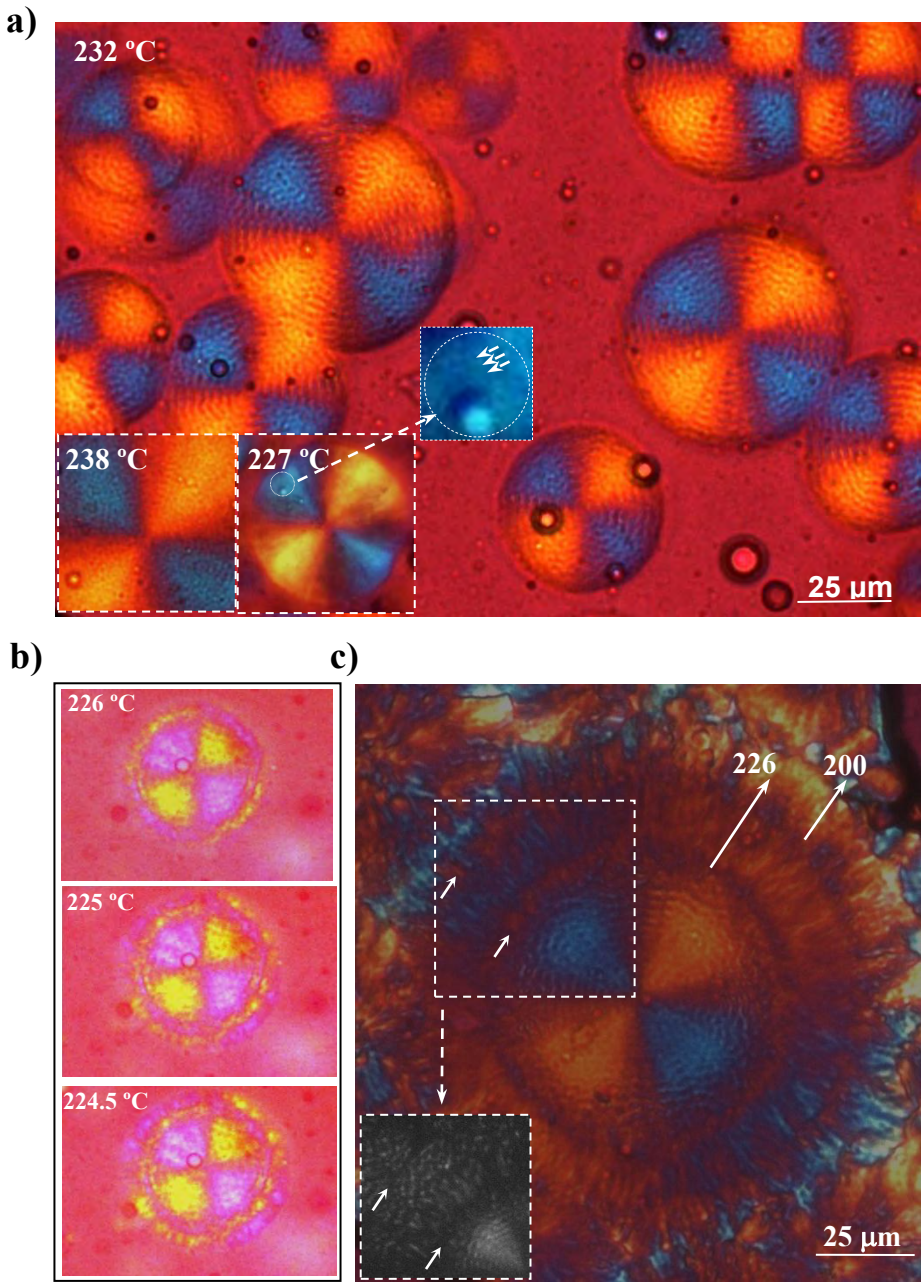

Figure 4.2.13 a) Optical micrograph of nylon 65 spherulites obtained at 232 ºC. Insets show spherulites obtained at 238 and 227 ºC. b) Optical micrograph of nylon 65 spherulites non-isothermally crystallized at a cooling rate of 2 ºC/min. c) Optical micrograph of a nylon 65 spherulite that was firstly isothermally crystallized at 235 ºC and then non-isothermally crystallized at a cooling rate of 0.5 ºC/min. Inset shows a black and white micrograph of a specific zone where different spherulitic textures can be better observed

Real Time Temperature Dependence of Infrared Spectra

Infrared spectroscopy has proved to be a useful tool in distinguishing the crystalline structures of aliphatic polyamides since some peak positions become dependent on vibrational coupling. In addition, this technique is especially appropriate for detecting thermally-induced structural transitions.

Independently of the nylon type, absorption bands appear at well defined wavenumbers, and have consequently been assigned to conventional polyamides.[37] Amide V and the CH_2 bending region (1500-1400 cm^{-1}) are usually considered to distinguish between the α/β sheet structure and the pseudohexagonal γ-phase. Thus, the first structure shows the amide V band at around 690 cm^{-1} and four scissoring mode peaks at around 1475, 1465, 1440 and 1420 cm^{-1}, whereas the γ-phase shows the amide V band at 715 cm^{-1}, which may be overlapped with the CH_2 rocking band, and only two scissoring peaks at 1460 and 1440 cm^{-1}. It should also be mentioned that bands associated with the amorphous phase (i.e. those observed in the molten state) appear at similar wavenumbers to those assigned to the γ-phase.

Table 4.2.1 summarizes the wavenumber data and the normal mode assignments of the main bands observed in the nylon 65 infrared spectrum taken at room temperature. Infrared spectra recorded in a heating run (2 ºC/min) are shown in **Figure 4.2.14** for three representative temperatures. It is worth noting that the main changes took place as the temperature was increased to 100 ºC, and then the spectra remained practically unaltered. This observation agrees with a structural transition around 100 ºC and suggests that minimum conformational changes occurred during the Brill transition.

Table 4.2.1 Assignment of Infrared Absorption Bands of Nylon 65 at Room temperature.

ν (cm^{-1})	Normal-mode
3294	Amide A (N-H stretching)
3079	Amide B
2928	CH_2 asym. stretching
2855	CH_2 sym. stretching
1632	Amide I
1540	Amide II
1472, 1459, 1434, 1420	CH_2 scissoring progression
1370	Amide III
1300-1220	CH_2 twisting progression
1204 (α), 1178 (γ)	CH_2 wagging progression
1120	C-NH stretching
1070-1024	C-C stretching progression
936	C-CO stretching
724	CH_2 rocking
683	Amide V (NH out of plane bend)

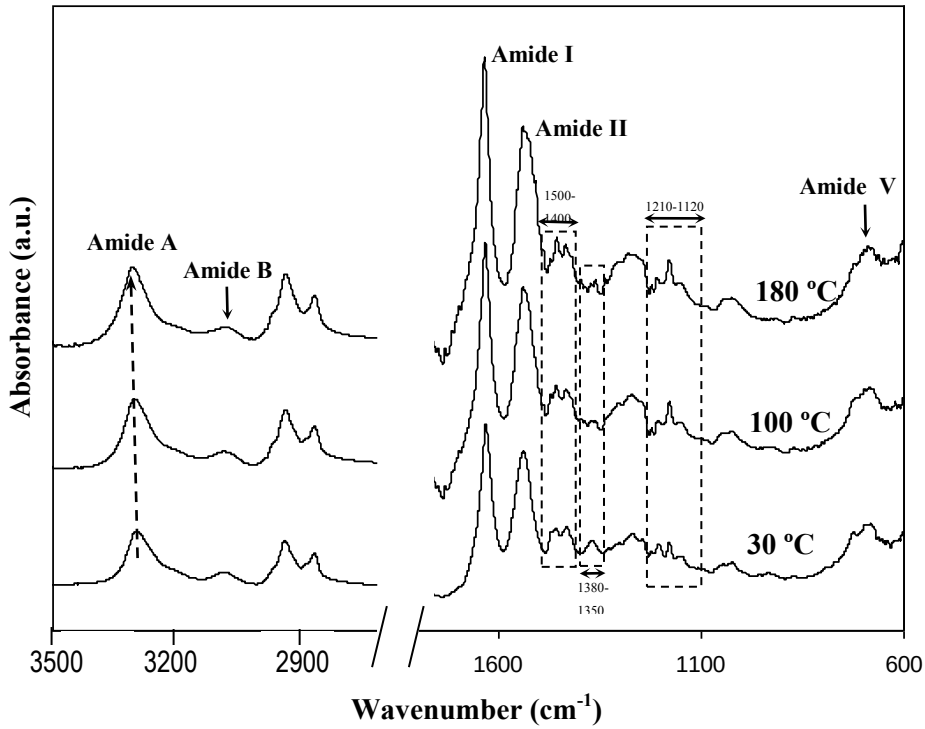

Figure 4.2.14 Infrared spectra recorded at the indicated temperatures during the heating run (2 ºC/min) of a nylon 65 sample coming directly from synthesis.

An Amide V band around 688-683 nm^{-1} was detected at all studied temperatures, revealing the existence of a crystalline structure different from the conventional γ-phase and close to the α/β forms. In this spectral zone the main change corresponds to the CH_2 rocking band, which appeared well defined at room temperature, whereas it progressively became a shoulder of the amide V band during heating. The four bending modes usually assigned to the α/β form could be distinguished at all temperatures although the intensity of the first band at 1472 cm^{-1} becomes weaker at high temperature, as usually observed for the hexagonal packing. In summary, these observations suggest that nylon 65 has a crystalline structure closer to the α/β form than to the γ-form at low temperature, although this similarity diminishes by increasing temperature.

Analysis of infrared spectra also reveals some additional points that deserve attention:

a) On heating, the amide A band (3302-3294 cm^{-1}) gradually shifts to higher frequencies, as shown in **Figure 4.2.15** a. The plot relating the wavenumber of the amide A band to the temperature (**Figure 4.2.15** b) indicates that around 100 ºC the slope of linear dependence clearly varies, suggesting the structural transition that was deduced from the change in WAXD spacings. It is well known that the wavenumber of the amide A absorption peak can be associated with the strength of the hydrogen bond in such a way

that an up-shift corresponds to a weakening of such interaction.[38] Spectroscopic data indicate that a greater change occurs during heating from room temperature to 100 ºC than from 100 to 190 ºC. This is in agreement with the deduced unit cell dimensions, which point to a larger increase in the average interchain distance during the first heating step. The amide A wavenumber shifts largely to higher values when the melting process starts (i.e. $T > 190$ ºC) and the hydrogen bonds become much weaker.

b) The wavenumber of the amide I band remains practically constant (1632-1635 cm^{-1}) during heating from 25 to190 ºC. The observed value is usually attributed to a semicrystalline sample with a predominant α/β form.[38] Furthermore, a small shoulder is detected at 1650 cm^{-1} for all indicated nylon 65 spectra. This absorption confirms the coexistence of an amorphous phase, whose ratio increases slightly on heating to 190 ºC. The amide II band is observed at 1540 cm^{-1} which is also a characteristic value for an α/β form since a shift towards 1560 cm^{-1} is usually reported for the pseudohexagonal γ-phase.[37]

c) On heating from 25 to 100 ºC the main changes correspond to the absorption band at 1370, which splits into two bands (1372 and 1361 cm^{-1}) with lower intensity (a), and the band at 1178 cm^{-1}, which becomes significantly more intense (b). The last band is usually attributed to the conventional γ form. That is why the low temperature transition seems to imply a conformational change where α/β form characteristics are reduced, in agreement with the change in the X-ray equatorial reflections.

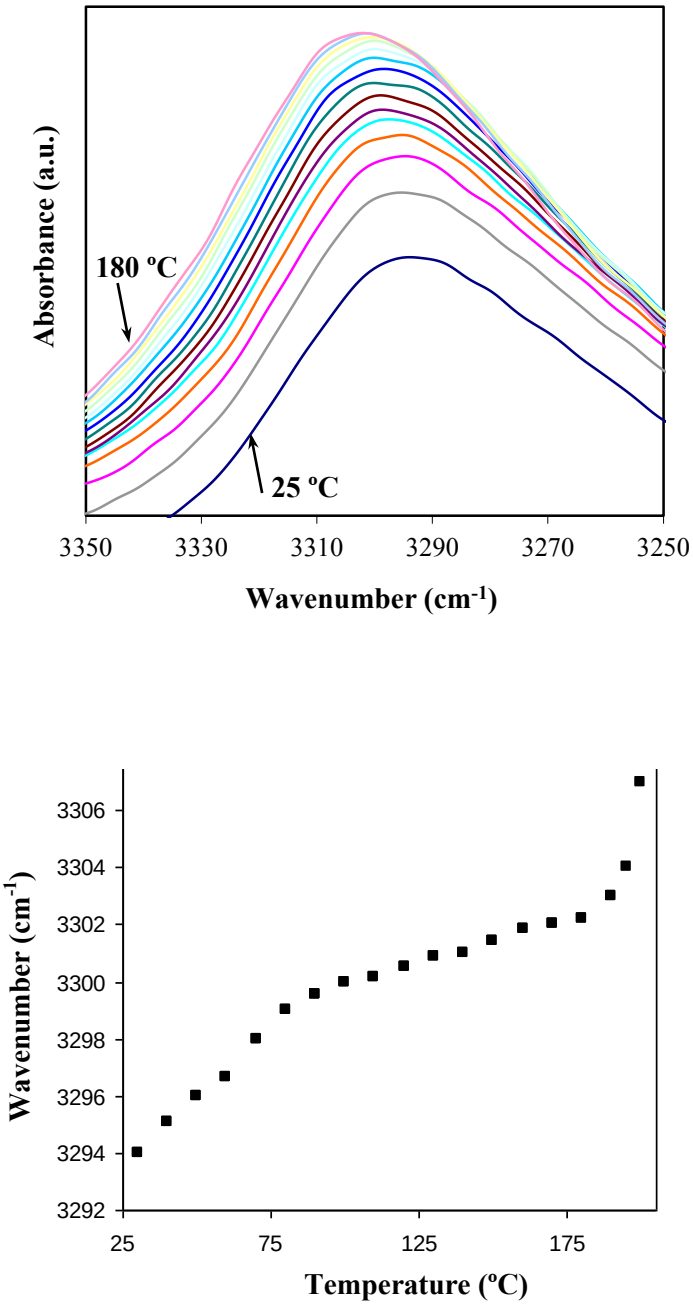

Figure 4.2.15 a) Change in the Amide A absorption band during a heating run of a nylon 65 sample coming directly from synthesis. b) Representation of the wavenumber corresponding to the amide A absorption band during a heating run of a nylon 65 sample coming directly from synthesis.

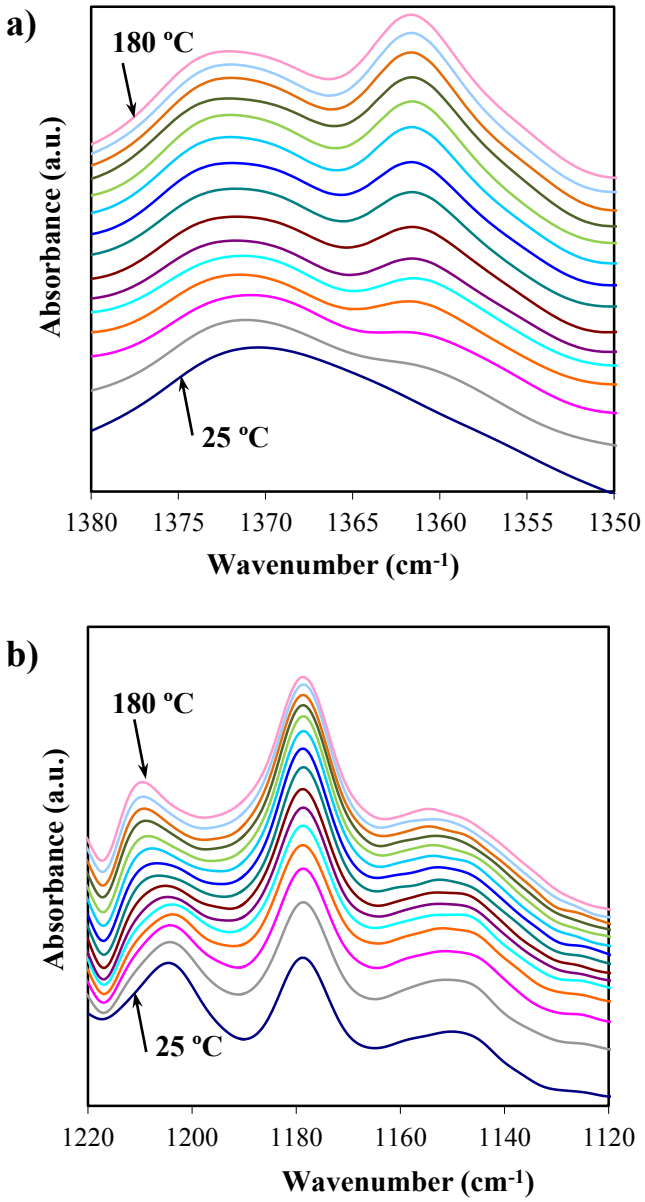

Figure 4.2.16 Change of the infrared absorption bands in the 1380-1350 cm^{-1} (a) and 1220-1120 cm^{-1} ranges during a heating run of a nylon 65 sample coming directly from synthesis.

4.2.4 Conclusions

Several conclusions can be drawn:

1. Nylon 65 samples coming directly from synthesis crystallize according to a peculiar structure (form I) that can be interpreted in terms of a packing where hydrogen bonds are established along two directions. On heating, this structure converts into a less compact structure (form II) whose X-ray diffraction pattern differs from the initial one in the closeness of the two strong equatorial reflections. A Brill transition occurs at some degrees before fusion, resulting in a pseudohexagonal chain axis projected unit cell. This high temperature structure is peculiar and is clearly different from the hexagonal arrangement found in conventional nylons since reflections related to the chain repeat have an unusual non-meridional orientation.
2. Nylon 65 crystallizes from the melt according to the high temperature structure obtained after the Brill transition. On cooling this structure transforms into form II, showing a hysteresis effect. The transition from form II to form I occurs at a lower temperature although it cannot be completed during the cooling run.
3. Crystallization from the melt gives rise to spherulites constituted by lamellae of different thicknesses, which accounts for the multiple melting peaks observed in the calorimetric heating runs. During crystallization thinner lamellae insert into the loosely stacked bundles of primary lamellae and the interlamellar amorphous regions become more compact.
4. Spherulites with different textures (ringed or fibrilar) and birefringences can be obtained by varying the crystallization conditions. Negative spherulites form in the low temperature region, indicating a molecular arrangement different from that found in conventional even-even nylons, whose low temperature spherulites show a positive birefringence.
5. Absorption bands observed in the room temperature infrared spectra suggest that nylon 65 has a structure related to conventional α/β forms despite its different hydrogen-bonding scheme. Spectra are sensitive to the structural changes; specifically the temperature evolution of the amide A band allows the form I to form II transition to be detected.

4.2.5 References

[1] Xenopoulos A, Clark ES. In Kohan MI, editor. Nylon plastics handbook. Hanser Publishers: Munich, Vienna and New York, 1995; Chapter 5.

[2] Holmes DE, Bunn CW, Smith DJ. J Polym Sci Part A, General Papers 1955;17:159-77.

[3] Bunn CW, Garner, EV. Proc R Soc London Ser A 1947;189:39-68.

[4] Kinoshita, Y. Makromol. Chem. 1959;33:1-20.

[5] Aharoni, SM. n-Nylons: their synthesis, structure and properties. John Wiley and Sons: New York, 1997.

[6] Murthy NS, Aharoni SM, Szollosi AB. J Polym Sci Part B, Polym Phys 1985;23:2549-65.

[7] Lincoln DM, Vaia RA. Macromolecules 2004;37:4554-61.

[8] Miyasaka K, Ishikawa K. J Polym Sci Part B, Polym Phys 1968;6:1317-29.

[9] Arimoto H, Ishibashi M, Hirai M. J Polym Sci Part A2 Polym Phys 1965;3:317-26.

[10] Navarro E, Franco L, Subirana JA, Puiggalí J. Macromolecules 1995;28:8742-50.

[11] Brill R. Makromol Chem. 1956;18:294-309.

[12] Itoh T. Jpn J Appl Phys. 1976;15:2295-2311.

[13] Newman BA, Sham TP, Pae KD. J Appl Phys 1976;48:4092-8.

[14] Starkweather HW, Jones GA. J Polym Sci Part B, Polym Phys 1981;19:467-77.

[15] Kim KG, Newman BA, Scheinbeim JI. J Polym Sci Part B, Polym Phys 1985;23:2477-82.

[16] Biangardi HJ. J Macromol Sci Phys B 1990;29:139-53.

[17] Hirschinger J, Miura H, Gardner KH, English AD. Macromolecules 1990;23:2153-2169.

[18] Wendoloski JJ, Gardner KH, Hirschinger J, Miura H, English AD. Science 1990;247:431-36.

[19] Radusch HJ, Stolp M, Androsch R. Polymer 1994;35:3568-71.

[20] Ramesh C, Keller A, Eltink SJEA. Polymer 1994;35:2483-87.

[21] Hill MJ, Atkins EDT. Macromolecules 1995;28:604-9.

[22] Vasanthan N, Murthy NS, Bray RG. Macromolecules 1998;31:8433-5.

[23] Murthy NS, Wang Z, Hsiao BS. Macromolecules 1999;32:5594-9.

[24] Ramesh C, Gowd EB. Macromolecules 1999;32:3721-6.

[25] Jones NA, Atkins EDT, Hill MJ. J Polym Sci Part B, Polym Phys 2000;38:1209-21.

[26] Feldman AY, Wachtel E, Vaughan GBM, Weinberg A, Marom G. Macromolecules 2006;39:4455-9.

[27] Rueda, DR, García-Gutiérrez MC, Nogales A, Capitán MJ, Ezquerra TA, Labrador A, Fraga E, Beltrán D, Juanhuix J, Herranz JF, Bordas, J. Rev Sci Instrum 2006, 77, Art. No. 033904 Part 1.

[28] Murthy NS, Curran SA, Aharoni SM, Minor H. Macromolecules 1991;24:3215-20.

[29] Hoffman JD, Weeks JJ. J Chem Phys 1962;37:1723-41.

[30] Xenopoulos A, Wunderlich B. Colloid Polym Sci 1991;269:375-91.

[31] Vonk CG, Kortleve G. Kolloid Z Z Polym 1967;220:19-24.

[32] Vonk CG. J Appl Cryst 1975;8:340-1.

[33] Hsiao BS, Wang Z, Yeh F, Yan G, Sheth KC. Polymer 1999;40:3515-23.

[34] Lovinger AJ. J. Appl. Phys 1978:49:5003-5013.

[35] Lovinger AJ. J. Appl. Phys 1978:49:5014-28.

[36] Magill JH. J. Polym. Sci. part A 1969;7:123-142.

[37] Sibila JP, Sanjeeva NS, Gabriel MK, McDonnell ME, Bray RG, Curran SA. In Nylon Plastics Handbook; Kohan MI Ed.; Hanser Publishers: Munich, Vienna and New York, 1995; Chapter 4.

[38] Skrovanek DJ, Painter PC, Coleman MM. Macromolecules 1986,19:699.

4.3

Crystallization studies on clay nanocomposites of nylon 47 having exfoliated or intercalated structures

Basic structural data on nylon 47 were obtained from X-ray diffraction of powder, and fiber samples and electron diffraction of thin spherulitic samples. The studied even-odd polyamide was characterized by a peculiar structure where hydrogen bonds were established along two directions. Nylon 47 showed reversible polymorphic transitions on heating/cooling processes that were analyzed by real time synchrotron WAXD experiments. Results indicate that nylon 47 had a first structural transition at low temperature and then underwent a gradual Brill transition towards a pseudohexagonal packing.

Optical and electron microscopy studies were also performed under isothermal conditions to distinguish the different spherulitic morphologies and changes on optical properties. Results revealed a different behaviour from that of spherulites of conventional even-even nylons. Interestingly, spherulites crystallized under a low supercooling had a reversible change of birefringence with temperature. This was due to the peculiar morphology attained at high temperature and the reversible structural changes that take place with temperature.

Intercalated and exfoliated nanocomposites based of nylon 47 were prepared by using Cloisites 25A and 30B, and different preparation methods (i.e. solution intercalation and melt mixing). The influence of the final silicate layer morphology on the hot crystallization behaviour was investigated by optical microscopy and differential scanning calorimetry. Crystallization rates of the neat polymer and its two nanocomposites were significantly different, mainly as a consequence of variations on primary nucleation.

4.3.1 Introduction

Aliphatic polyamides (nylons) constitute a family of polymers with exceptional properties because of their capability to establish strong intermolecular hydrogen bonding interactions.[1] Molecular conformation and packing preferences are basically conditioned to favour a close arrangement between amide groups. In this way, the crystalline structure of conventional even-even nylons (e.g. nylons 66 and 6-10) are based on a stacking of sheets composed of hydrogen-bonded molecular chains with a planar zig-zag conformation (α and β forms).[1,2] Similar arrangements with hydrogen bonds established along a single direction are also commonly found in some even nylons (i.e. nylon 6).[1,3] The corresponding X-ray fiber diffraction patterns of such structures are characterized by the presence of two strong equatorial reflections at spacings close to 0.440 and 0.380 nm which are associated to intrasheet and intersheet spacings, respectively.

Nylons can however crystallize according to other arrangements and molecular conformations depending on the parity of the constituent monomers (e.g. the pseudohexagonal γ phase postulated for some odd-odd nylons[1,4]) and indeed the presence of special units like glycine[5,6] (e.g. nylons 2/3, 2/6) and malonic acid[7] (e.g. nylons n,3). Furthermore, nylons can experiment phase transitions during heating and cooling processes, as for example the not completely well understood reversible structural change detected with nylons having conventional α/β forms at room temperature.[8-18] In this case, the evolution of the diffraction patterns on heating shows that the two characteristic equatorial reflections gradually merge on a single one (ca. 0.421 nm) indicative of a pseudohexagonal arrangement at the so called Brill transition temperature. On cooling from the melt state, the polymer firstly crystallized in the indicated pseudohexagonal packing and then the characteristic single reflection splits into the two above indicated reflections at a temperature lower than observed in the heating process.

A peculiar structure based on the establishment of hydrogen bonds along two different directions has lately been postulated for some even-odd and odd-even nylons (e.g. nylons 69,[19] 65,[20,21] 12-5,[22] 56,[23,24] 5-10[25] and 92[26]) which fibers rendered two strong equatorial reflections at similar spacings than reported for the α/β conventional structures. The new structure was postulated since good intermolecular hydrogen bonding interactions could not be established when nylons had a planar zig-zag molecular conformation and were derived from diamine and dicarboxylic acid units with different parity (i.e. even-odd and odd-even nylons). This feature is illustrated in Figure 1a for nylon 47 which is the polymer object of the present work.

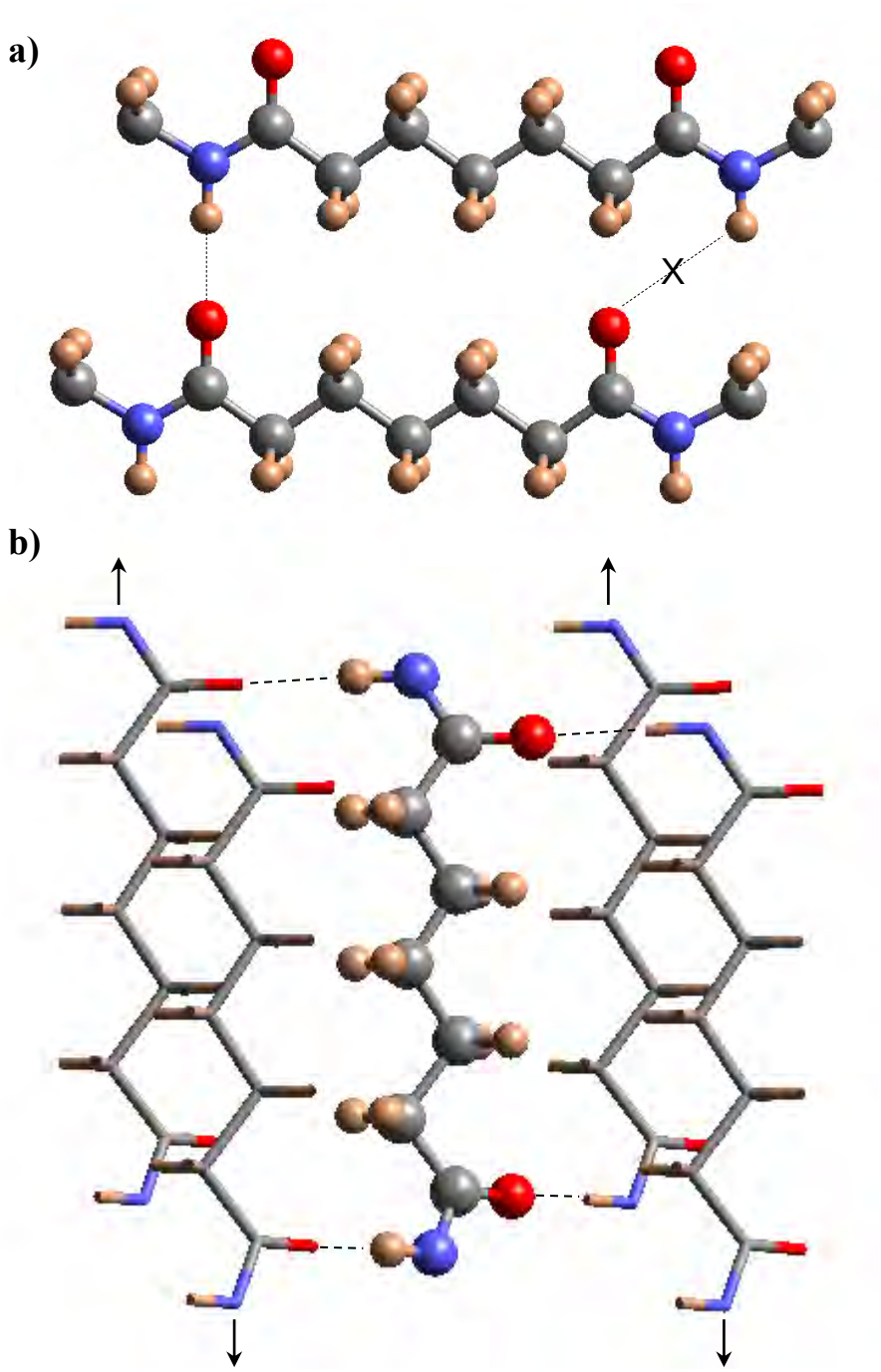

Figure 4.3.1 a) Scheme showing the unfavourable hydrogen-bonding geometry between pimelamide units having an all trans conformation. b) Scheme showing as hydrogen bonds could be well established along two directions when the two amide planes of the pimelamide unit rotate in opposite directions from the plane defined by its methylene carbons. External chains (stick representation) should be shifted along the chain axis direction (see arrows) with respect to the central chain (ball and stick representation), thus giving rise to a monoclinic unit cell. Color code: nitrogen, blue; oxygen, red; carbon, gray; hydrogen, brown.

Basically, the distinctive feature of the new molecular arrangement is the capability of establishing good hydrogen bonding interactions along two different directions with molecules having a practically all trans conformation. Thus, a slight deviation towards 150º (or -150º) for the two torsional angles vicinal to the odd diamide units seems necessary to face all NH and CO groups of neighbouring chains. The two amide groups of the odd unit rotated in opposite senses from the plane defined by the methylene carbon atoms allowing a good hydrogen bonding geometry when neighbouring chains became conveniently shifted along the chain axis direction (**Figure 4.3.1**). In this way, a monoclinic unit cell containing two molecular segments was derived and the chain axis projection corresponded to a rectangular unit cell.[19-26]

Polymers filled with a layered clay (or phyllosilicate) give rise to microstructural dispersions different from conventional ones obtained from inorganic fillers. Incorporation of nanoelements may provide commodity materials with a suite of characteristics that organic chemistry and traditional polymer-blending approaches cannot supply from an economical point of view.[27-29]

Pioneering works concerning clay nanocomposites were precisely carried out with polyamides having the conventional sheet structure (e.g. nylon 6).[30,31] Crystallization processes are also influenced by the incorporation of phyllosilicate particles since they may have an impact on the overall crystallization rate, crystal growth, nucleation type and morphological features. In fact, crystallization is determined by different factors which may be favoured or disfavoured when the clay particles are incorporated. In this way, published results suggested that the crystallization process highly depends of the type of clay dispersion (e.g. exfoliated or intercalated) and even on the interactions between clay and polymer matrix.[32-35]

It seems therefore interesting to bring new data on the crystallization behaviour of composites based on polyamides having different intermolecular interactions than conventional nylons. In this way, the present work is focused in the structural characterization of a new even-odd polyamide (i.e. nylon 47), the preparation of nanocomposites with different structures and finally the evaluation of the crystallization behaviour of the neat polymer and its nanocomposites.

4.3.2 Experimental section

- **Materials**

Nylon 47 was synthesized by interfacial polycondensation of 1,4-diaminobutane and pimeloyl chloride using toluene as organic solvent and sodium hydroxide as proton acceptor following the procedure previously described for similar nylons.[20] The polymer was purified by precipitation with water of a formic acid solution. Nylon 47 was obtained with a yield of 55% and an intrinsic viscosity of 0.85 dL/g (determined in dichloroacetic acid at 25 ºC).

Dimethyl hydrogenated-tallow 2-ethylhexyl ammonium montmorillonite (Cloisite 25A, Southern Clay Products, 2MHTEX) and methyl tallow bis(2-hydroxyethyl) ammonium montmorillonite (Cloisite 30B, Southern Clay Products, MT2EH) (tallow (~65% C18, ~30% C16, ~5% C14)) were used as received. The chemical structure of the specific surfactant of the organo-modified layered phyllosilicates are shown in **Table 4.3.1**.

Table 4.3.1 Characteristics of Organoclays[a].

Clay Type	Chemical Structure of Organic Modifier
Cloisite 30B	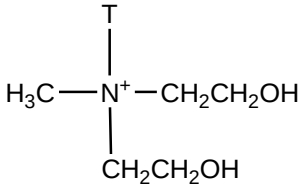
Cloisite 25A	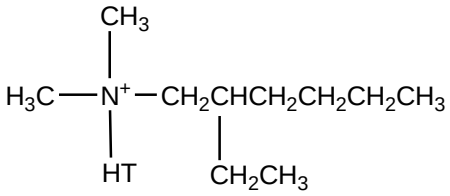

[a] HT is the hydrogenated-tallow. T ~65% C18, ~30% C16, ~5% C14.

- **Preparation of nanocomposites**

Nanocomposites containing 3% of C25A or C30B clay particles were prepared by melt mixing in two steps using a co-rotating tightly intermeshed twin-screw extruder (DSM Xplore 5ml microcompounder). All materials were dried under vacuum prior to mixing. The processing temperature, screw rotation and cycle time were 260 ºC, 100 rpm and 3 minutes, respectively.

Alternatively, nanocomposites were also prepared by the solution-intercalation film-casting technique. For each final nanocomposite composition 100 mg of nylon 47 was dissolved in 10 mL of 1,1,1,3,3,3-hexafluoroisopropanol. Clay dispersions (<0.1 wt %) were obtained by suspension of clay in a separate beaker of 1,1,1,3,3,3-hexafluroisopropanol. Both the Nylon 47 solution and clay suspension were agitated separately for 30 min. The final mixture was further sonicated for 120 min with a Sonorex Super 10P sonicator. The amount of OMMT loading was fixed at 3 wt%. The mixture was then cast on a glass surface and the solvent was removed in a vacuum oven at 40 ºC. Eventually, optically clear nanocomposite films with thicknesses ranging from 20 to 35 μm were obtained.

Measurements

X-ray fiber and power diffraction patterns of nylon 47 were obtained with Ni-filtered CuK_α radiation of wavelength 0.1542 nm from an Enraf Nonius rotating anode X-ray generator and using a modified Statton camera (W. H. Warhus, Wilmington, DE). Oriented fiber samples were obtained by melt drawing.

Time resolved WAXD experiments were carried out at the CRG beamline (BM16) of the European Synchrotron Radiation Facility of Grenoble. The beam was monochromatized to a wavelength of 0.098 nm. Polymer samples were confined between Kapton films and then held on a Linkam hot stage with temperature control within ± 0.1 ºC. WAXD profiles were acquired during heating and cooling runs in time frames of 12 s and rates of 3 ºC/min. The WAXD detector was calibrated with diffractions of a standard of an alumina (Al_2O_3) sample. The diffraction profiles were normalized to the beam intensity and corrected considering the empty sample background. Deconvolution of WAXD peaks was performed with the PeakFit v4 program by Jandel Scientific Software using a mathematical function known as "Gaussian area".

Spherulites of nylon 47 were grown from homogeneous melt-crystallized thin films placed between two cover glasses. These films were produced by evaporation of a dilute solution of the polymer in 1,1,1,6,6,6-hexafluoroisopropanol. Samples were crystallized isothermally at different temperatures below the melting point using a Linkam temperature control system configured by a THMS 600 heating and freezing stage connected to an LNP 94 liquid nitrogen cooling system. Additionally, non-isothermal experiments were carried out at cooling/heating rates of 1 ºC/min. The experimental procedure allowed films with thickness lower than 10 μm to be obtained. Optical photographs were taken using a Zeiss AxioCam MRC5 digital camera mounted on a Zeiss Axioskop 40 Pol light polarizing microscope. A first-order red tint plate was employed to determine the sign of spherulite birefringence under crossed polarizers.

Thin spherulites were also observed with a Philips TECNAI 10 electron microscope operating at 80 and 100 kV for bright field and electron diffraction modes, respectively.

After manual separation of the two glasses, the spherulites attached to the cover-slip were covered with a thin carbon film, floated off on water, picked up on copper grips and shadowed with Pt-Carbon at an angle of 15º. Bright field micrographs were taken with a SIS MegaView II digital camera. Selected area electron diffraction patterns were recorded on Maco EM films from not shadowed samples. The patterns were internally calibrated with gold (d_{111} = 0.235 nm).

Interlayer spacing of clay nanocomposites was studied by wide angle X-ray scattering (WAXD) using a PANalytical X´Pert diffractometer with Cu K_α radiation (λ = 0.1542 nm) using a silicium monocrystal sample holder. The structure and distribution of Cloisite in the

nanocomposites were also evaluated by morphologic observations using the Philips TECNAI 10 electron microscope at an accelerating voltage of 100 kV. Specimens were prepared by embedding the nanocomposite films in a low viscosity modified Spurr epoxy resin. The preparations were cured at 40°C for a few days and then at 60 °C for 6 h. Ultrathin sections (less than 100 nm) were cut at room temperature using a Sorvall Porter-Blum microtome equipped with a diamond knife. Finally, the sections were collected in a trough filled with water and lifted onto carbon coated copper grids.

Calorimetric data were obtained by differential scanning calorimetry with a TA Instruments Q100 series equipped with a refrigeration cooling system (RCS) which operates from -90 ºC to 550 ºC. Experiments were conducted under a flow of dry nitrogen with a sample weight of approximately 5 mg and the calibration was performed with indium.

Basic thermal characterization involved on cooling runs (10 ºC/min) of melted samples and heating runs (20 ºC/min) of as-synthesized, hot crystallized and quenched samples. Crystallization studies were performed with samples firstly heated at 20 ºC/min to 270 ºC and kept at this temperature for five minutes to erase the thermal history. Non-isothermal experiments were performed at a cooling rate of 10 ºC/min.

Spherulite growth rates of nanocomposites were determined by optical microscopy. Samples were prepared from homogeneous melt-crystallized thin films obtained by melting 1 mg of the polymer mixture on microscope slides. Next, small sections of these films were pressed or smeared between two cover slides and inserted in the hot stage. The thickness of the squeezed samples was in all cases close to 10 μm. Samples were kept at 270 ºC (approximately 10 ºC above the end of the polymer fusion at 260 ºC) for 5 minutes to eliminate sample thermal history effects and subsequently quickly cooled to the selected isothermal crystallization temperature. The radius of the growing spherulites was monitored by taking micrographs at appropriate time intervals. Nucleation densities were determined by counting the number of spherulites observed in representative areas of optical micrographs.

4.3.3 Results and discussion

- **Basic structural data of nylon 47**

Unit cell parameters of nylon 47 were determined from electron and X-ray diffraction patterns. The former were recorded from thin spherulites crystallized from the melt state as it will below be explained. These patterns (**Figure 4.3.2** a and b) are characterized by six strong reflections at 0.430 nm and 0.389 nm together with several weaker reflections, as summarized in **Table 4.3.2.** Patterns showed a 2*mm* symmetry and could be well indexed according to a rectangular unit cell with a = 0.437 nm and b = 0.860 nm. It should be pointed out that the spacings of the main reflections are clearly different from the value expected (0.415 nm) for the

pseudohexagonal arrangement postulated for the γ-form of nylons.[1,4] On the contrary, either the reported spacings and the observed symmetry suggest the establishment of a structure where amide groups form hydrogen bonds along two directions. The molecular packing becomes defined by a rectangular chain axis projected unit cell that contains two molecular segments. The calculated distance between the molecule placed at the middle and the molecule placed at the corner of the unit cell was 0.482 nm and consequently in close agreement with the expected distance between hydrogen bonded chains.

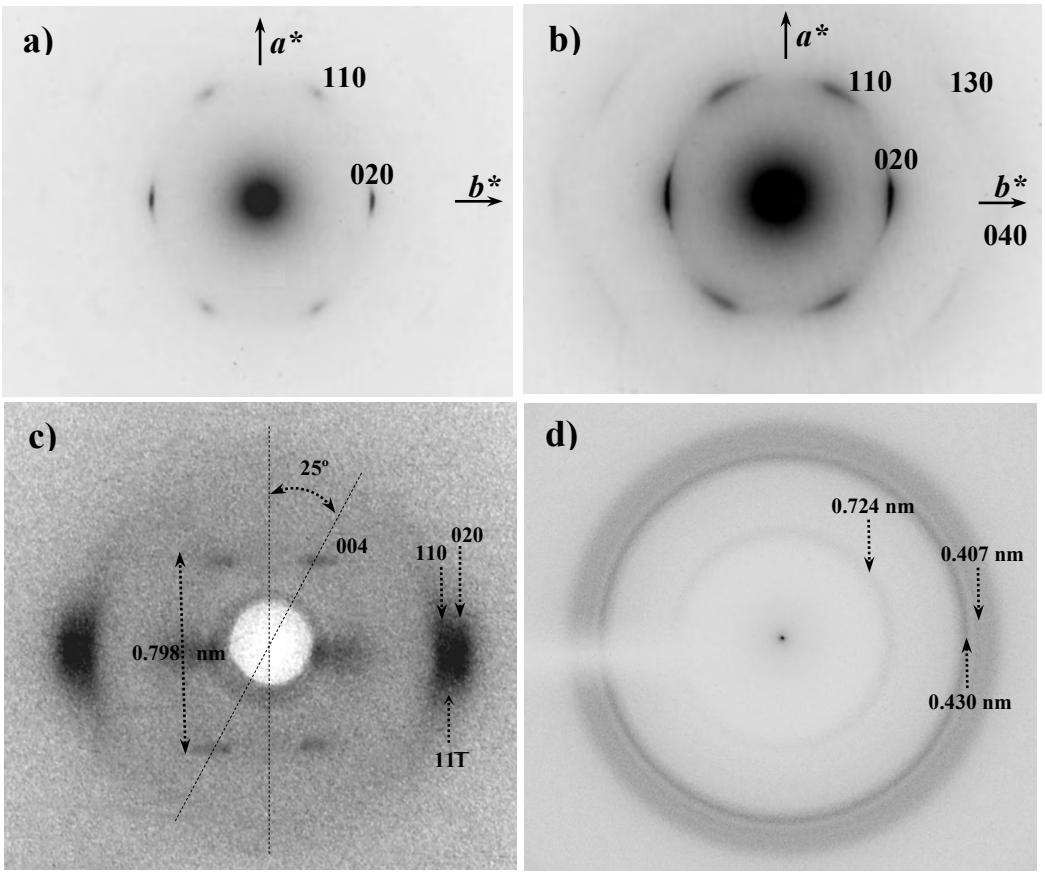

Figure 4.3.2 Electron diffraction patterns from spherulites crystallized at 218 ºC (a) and 232 ºC (b). X-ray diffraction patterns of a melt spun fiber (c) and a powder sample directly obtained from synthesis (d).

X-ray fiber patterns showed a scarce number of reflections (**Figure 4.3.2** c, **Table 4.3.2**) that were however sufficient to determine the parameters of the three dimensional unit cell. Thus, the non meridional 00*l* reflection allowed to estimate a *cc** angle close to 25º and consequently a β monoclinic angle of 115º. This reflection was indexed as 004 according to the previous reported data on the similar nylon 65.[20] A chain axis repeat close to 3.192 nm was directly determined from the 0.798 nm spacing defined by the fourth layer line (**Figure 4.3.2** c). This repeat suggested a practically all trans molecular conformation since the expected value assuming standard bond lengths and angles was 3.250 nm. Fiber patterns showed also a strong/medium equatorial reflection at 0.407 nm which can be indexed as the $11\bar{1}$ reflection, although it may be also indicative of a second polymorphic form as it will be then explained. In general, a mixture of two crystalline forms was observed when samples were obtained from the melt state. The achievement of a single structure strongly depended on the success of the annealing process at which the melt drawn fibers were subsequently submitted. The relatively low molecular weight of nylon 47 samples made difficult to favour a structural transition towards an extended conformation by the annealing process. In general, diffraction patterns showed also a near-meridional reflection in the second layer line which can be associated to the second polymorph.

X-ray powder patterns corresponding to samples crystallized from solution (**Figure 4.3.2** d) were also in agreement with the deduced unit cell (**Table 4.3.2**). The powder pattern was highly useful since the spacing of the 004 reflection could be more accurately measured than from fiber patterns where the 004 spot had a rather diffuse appearance.

Table 4.3.2 Diffraction data of nylon 47 from powder, fiber and spherulitic samples.

hkl [a]	d_{calcd} **(nm)**	d_{measd} [b] **(nm)**		
		X-ray		**Electron diffraction**
		Powder	**Fiber**	**Spherulite**
004	0.723	0.724 w	0.724 w off M	
006	0.482	0.482 vw		
040	0.430	0.430 vs	0.430 vs E	0.430 vs
11-1	0.407	0.407 m	0.407 s E	
110	0.389	0.389 m	0.389 vs E	0.389 s
130	0.240			0.240 w
040	0.215			0.215 w
102, 024	0.376, 0.370	0.377 m		

[a]On the basis of a monoclinic unit cell with a = 0.482 nm, b = 0.860 nm, c (fiber axis) = 3.192 nm and β = 115º.
[b]Abbreviations denote relative intensity and orientations: vs, very strong; s, strong; m, medium; w, weak; E, equatorial; off M, off meridional.

It should be pointed out the close agreement between the main packing parameters deduced for nylon 47 with those previously determined for nylon 65, an even-odd polyamide characterized by the structure with two hydrogen-bonding directions.[20,37] Thus, values of 0.420 nm and 0.862 nm defined the chain axis projected rectangular unit cell of nylon 65 and the corresponding X-ray fiber pattern allowed to determine a *cc** angle of 24º.

- **Thermal behaviour of nylon 47**

Figure 4.3.3 displays a sequence of heating/cooling runs performed to study the thermal behavior of nylon 47. A heating scan of a solution-crystallized sample showed a complex melting peak (shoulder at 214 ºC and defined peaks at 227 ºC and 244 ºC) associated with a typical recrystallization process occurring on heating. The cooling run after keeping this sample in the melt state for three minutes revealed a narrow exothermic crystallization peak around 214 ºC and a broad exotherm that should correspond to the secondary crystallization. A subsequent heating run showed again a complex fusion where the shoulder and peaks previously indicated can be observed. However, the intensity of the peak appearing at the highest temperature (244 ºC) clearly increased. Finally, a melt quenched sample allowed the determination of a glass transition temperature at 56 ºC and a single and broad melting peak at 243 ºC with a small shoulder at 228 ºC.

The possible existence of different crystalline structures with different thermodynamic stability was discarded as the origin of the multiple melting peaks since, as will be discussed in the next section, nylon 47 may experiment a first transition at a clearly lower temperature and a second one at high temperature but involving a great temperature range. Thus, the two endothermic peaks seem to be associated with two populations of lamellar crystals of different thicknesses whereas the shoulder may be related to highly defective crystals. Note that a melt-recrystallization process where thin lamellae convert into thicker lamellae should be more important when samples were less perfect, and consequently crystallized at lower temperatures as it is the case of the melt quenched sample (**Figure 4.3.3** d).

Nylon 47 was highly crystalline as deduced from the relative melting enthalpy of both solution and melt crystallized samples. Calorimetric scans indicated that the crystallization degree was logically higher when samples crystallized from solution, being crystallinity recovered by only 80% after melt crystallization. In any case, it is clear that samples easily crystallize since quenching was not successful at the maximum cooling rate allowed by the equipment (**Figure 4.3.3** d).

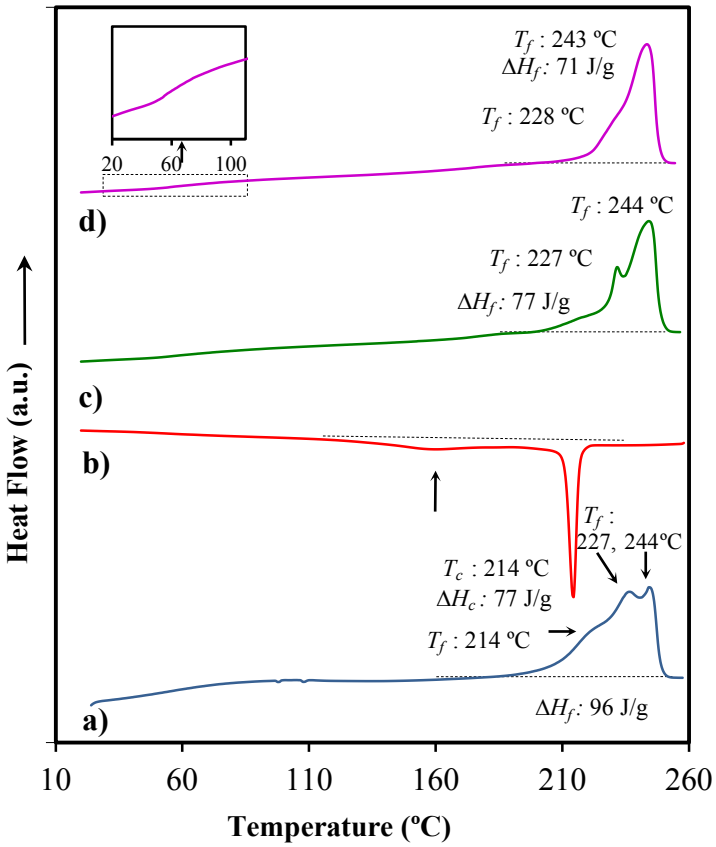

Figure 4.3.3 DSC scans corresponding to the heating run of the as-synthesized sample (a), the cooling run from the melt state (b), the heating run of a hot crystallized sample (c) and the heating run of a sample quenched from the melt state (d). The crystallization process (b) shows a main exothermic peak and an additional broad exotherm (see arrow). The inset of d) shows a magnification of the region corresponding to the glass transition.

Structural transitions f nylon 47 on heating/cooling processes

Figure 4.3.4 a shows a three-dimensional representation of nylon 47 WAXD profiles obtained by synchrotron radiation during a heating process performed at 3 ºC/min from room temperature to fusion, whereas one-dimensional profiles taken at some representative temperatures are given in **Figure 4.3.4** b. It is clear that structural changes occurred on heating and that two main features could be identified in a similar way as previously reported for the related nylon 65[37]: a) A polymorphic transition (from form I to form II) took place between 60 and 120 ºC since the intensity of the two equatorial reflections at 0.430 and 0.389 nm gradually diminished during heating and new reflections near 0.421 and 0.404 nm appeared with increasing intensity; and b) After 120 ºC the two indicated new reflections gradually merged into a single peak at 0.422 nm that was achieved at a temperature close to 190 ºC. This process suggests a typical Brill transition where a pseudohexagonal packing (γ*-form) is favoured at a temperature slightly lower than the melting point. It should be pointed out that the indicated peak had always a small

shoulder at a lower spacing (0.414 nm) as can be well observed after deconvolution of the corresponding diffraction profile (**Figure 4.3.5**a). Hence, nylon 47 could not adopt a perfect pseudohexagonal packing before fusion as characteristic of different polyamides (e.g. nylon 66 and even nylon 65). The two observed structural transitions could not be related with a defined peak in the corresponding DSC heating traces and furthermore took place in a wide temperature range according to the synchrotron diffraction data. It seems that gradual changes occurred probably as a consequence of slight variations of the two torsional angles vicinal to the odd diamide units that conduce to different angles between the hydrogen-bonding directions. Dimensions of the chain axis projected unit cell changed during heating and approached to a hexagonal cell at high temperature.

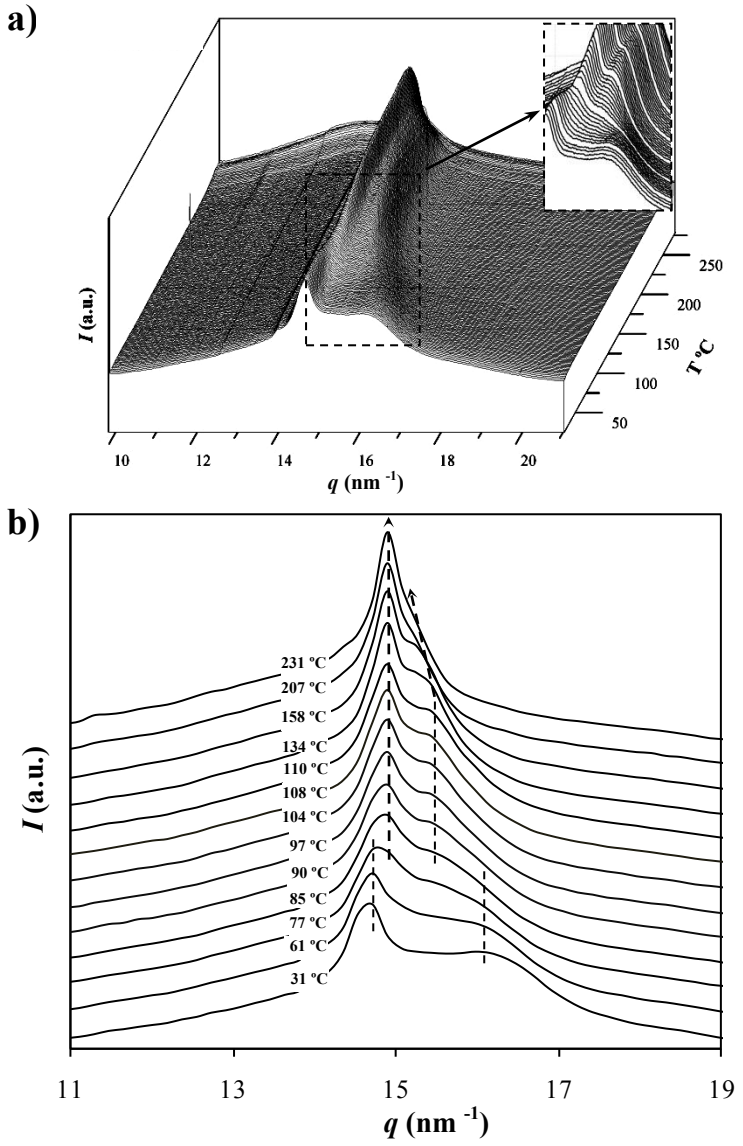

Figure 4.3.4 a) Three-dimensional representation of WAXD profiles of nylon 47 during heating (3 ºC/min) from room temperature to fusion. The inset corresponds to a magnification where the appearance and disappearance of characteristics peaks of forms I and II could respectively be observed. b) One-dimensional WAXD profiles of nylon 47 taken at selected temperatures during a heating scan (3 ºC/min). Dashed lines remarks the evolution of main reflections.

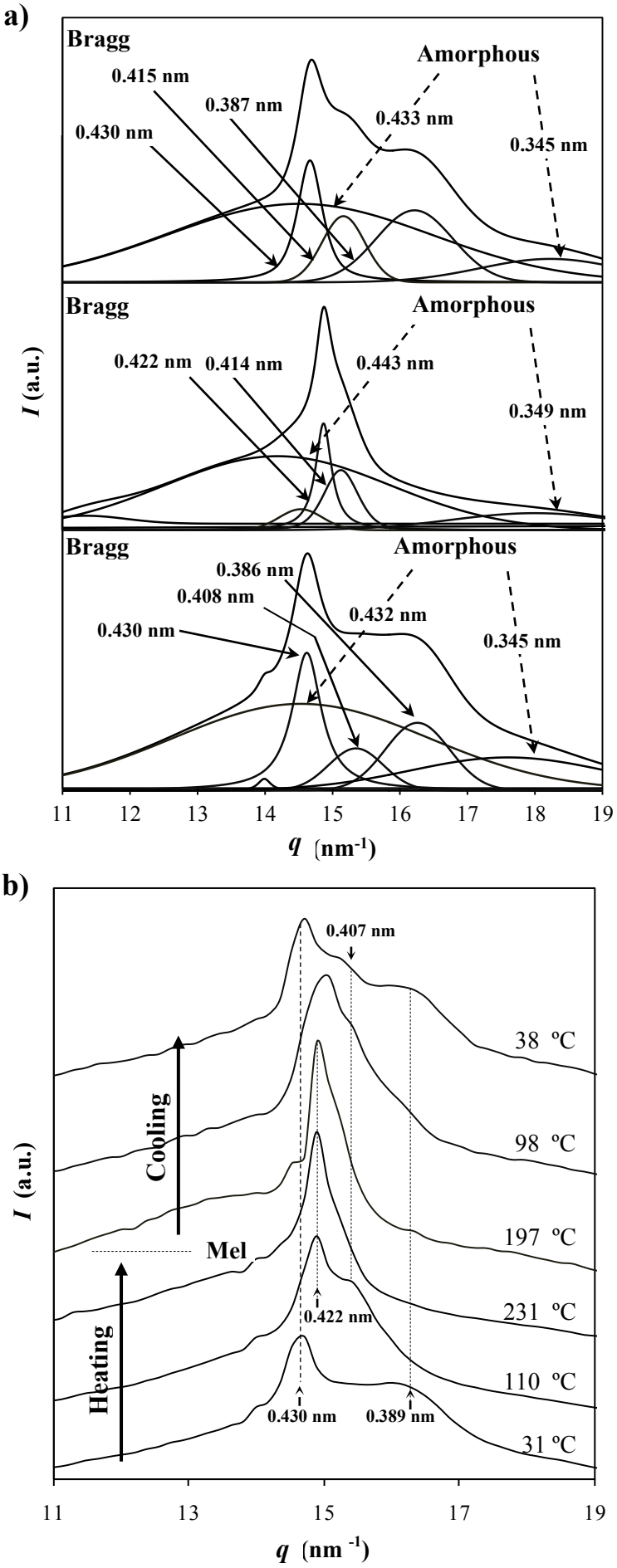

Figure 4.3.5 a) One-dimensional WAXD profiles of nylon 47 taken at room temperature (down) and just before starting the melting process (middle) and at the end of the cooling process (up). Deconvoluted Bragg and amorphous peaks are showed for both profiles. b) One-dimensional WAXD profiles of nylon 47 taken at selected temperatures during heating and cooling scans (3 ºC/min). Spacings of main reflections associated to forms II and I are indicated.

Figure 4.3.6 a shows the WAXD profiles acquired during a cooling run (3 ºC/min) from the melt state. It is clear that a narrow intense peak appeared around 0.420 nm during crystallization and that it progressively broadened and split into different peaks when the temperature decreased.

The variation in intensity of the strongest peak (0.422-0.420 nm) was useful in monitoring the different processes that occur on cooling, as is shown in **Figure 4.3.6** b. Thus, this peak appeared and increased in intensity within the temperature range of 240-197 ºC, where crystallization took place. The peak intensity remained practically constant in the temperature range between 197 and 168 ºC and then, it slightly decreased again with decreasing temperature due to the split of the peak caused by the Brill transition. Thus, this transition occurred at a lower temperature on cooling than on heating (190 ºC), indicating a clear hysteresis effect, as usually found in polyamides.[16] At 130 ºC the decrease in the peak intensity was more pronounced as a consequence, in this case, of the new splitting caused by the form II to form I transition. This could not be detected by DSC because it was a partial conversion occurring in a broad temperature interval. Structural changes could not take place when temperature became close to the glass transition temperature and consequently the peak intensity was constant at temperatures lower than 65 ºC. It is important to note that form I could not be completely recovered during the cooling process and that the X-ray profile attained at room temperature corresponded to a mixture of structures. Thus, the final diffraction profile became clearly different to that obtained from the as-synthesized sample.

Figure 4.3.5 a compares also the deconvoluted profiles taken at room temperature with the initial and the hot crystallized samples. Specifically, the major difference correspond to the peak close to 0.415-0.408 nm that appeared with a different intensity. It may correspond to the weak $11\bar{1}$ reflection of form I and also to the characteristic strong reflection of form II. Logically the intensity of the peak at 0.415-0.407 nm will depend on the ratio between form I and form II that is achieved after the cooling process. **Figure 4.3.5** a shows also as the amorphous halos slightly changed with temperature as a consequence of thermal dilatation and specifically peaks shifted to higher a spacing with increasing temperature.

Figure 4.3.5 b shows for the sake of completeness some representative X-ray profiles taken during heating and cooling runs. Specifically, those corresponding to the achievement of form II (110 ºC on heating and 98 ºC on cooling), those corresponding to the similar structures attained on heating just before melting (231 º) and on cooling at the end of crystallization (206 ºC), and finally the dissimilar profiles taken at room temperature with the as-synthesized sample before starting and at the end of the process, respectively.

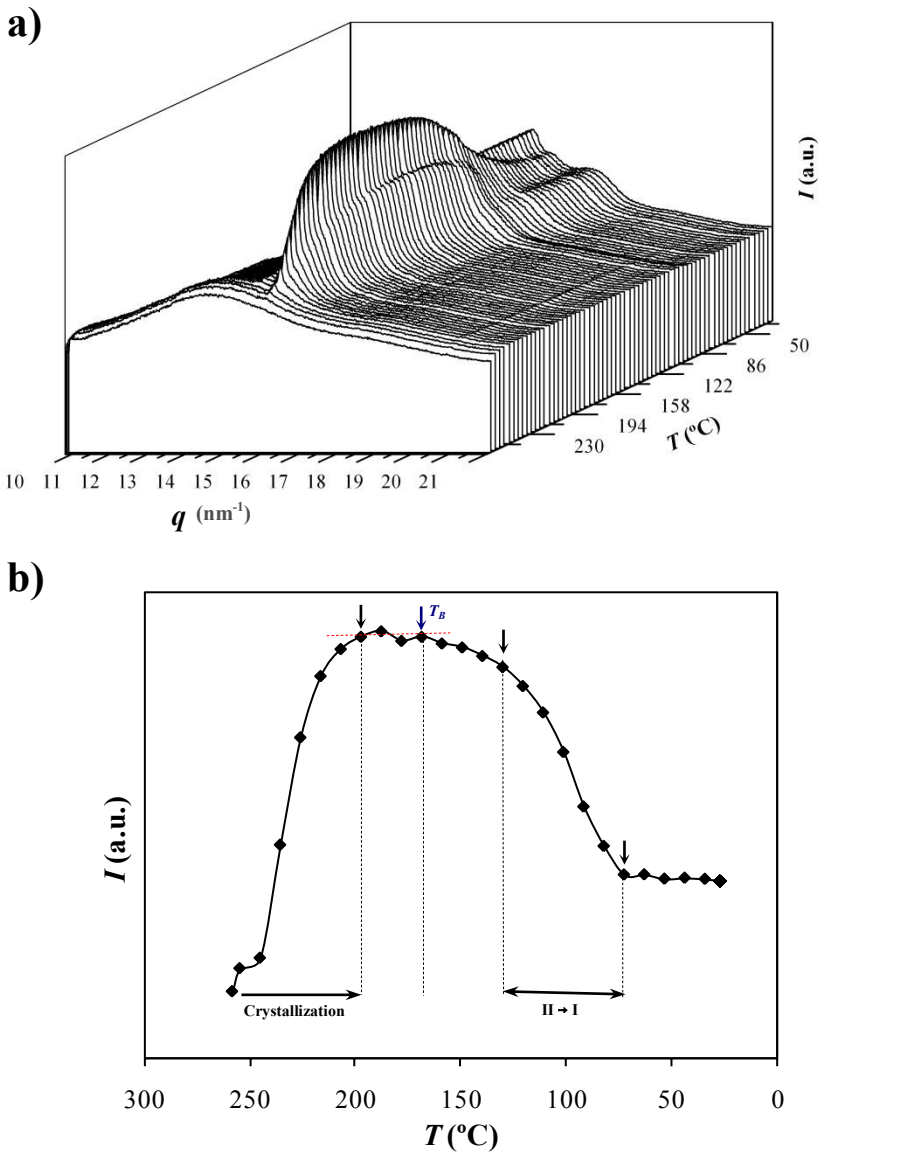

Figure 4.3.6 a) Three-dimensional representation of WAXD profiles of nylon 47 during cooling (3 ºC/min) from the melt to room temperature. b) Temperature evolution of the peak intensity at ca. 0.422 nm during a cooling run (3 ºC/min) from the melt state.

Spherulitic morphologies of nylon 47

Scarce works concern the study of optical properties and morphologic characteristics of spherulites obtained from even-odd nylons. A detailed phenomenological description has been reported for nylons 49, 67 and 69 by Magill[38] and some additional data has also recently been given for nylon 65.[37] Rather puzzling observations were reported but in general a wide variety of spherulitic structures with different optical birefringence were found. The birefringence sign often changed in the negative-positive-negative sequence with decreasing the crystallization temperature. This behavior was clearly different to that reported for even-even nylons which are characterized by a stacking of hydrogen-bonded sheets. In this case, polymers rendered negative

spherulites at crystallization temperatures slightly lower than their melting point and positive spherulites at lower temperatures. The change in the optical properties was explained assuming that positive and negative spherulites differ in the radial or tangential spherulitic direction where hydrogen bonds respectively form. Thus, the birefringence sign is directly associated with how lamellae with a single structure grow in the spherulite.[38,39] However, the reason for such a drastic change in the growth mechanism at a well defined temperature remains unclear.

Isothermal crystallizations of nylon 47 from the melt state rendered different kinds of spherulites depending specifically on the selected crystallization temperature. Thus, peculiar spherulites with well defined crystalline domains and a negative birefringence were observed (**Figure 4.3.7** a) when crystallization temperature was higher than 228 ºC. Electron micrographs (**Figure 4.3.8**) revealed a complex morphology where an arborescent growth with curved arms develop from the primary nucleus (**Figure 4.3.8** a and b). Micrographs taken at higher magnifications showed the flat appearance of constitutive crystals (**Figure 4.3.8** c) and indeed the presence of single crystals which in some cases had a lozenge shape (e.g. see the dashed area of **Figure 4.3.8** d). This crystals gave rise to *hk*0 electron diffraction patterns with intense reflections (**Figure 4.3.2** b) that corresponded to form I as expected since patterns were recorded at at room temperature .

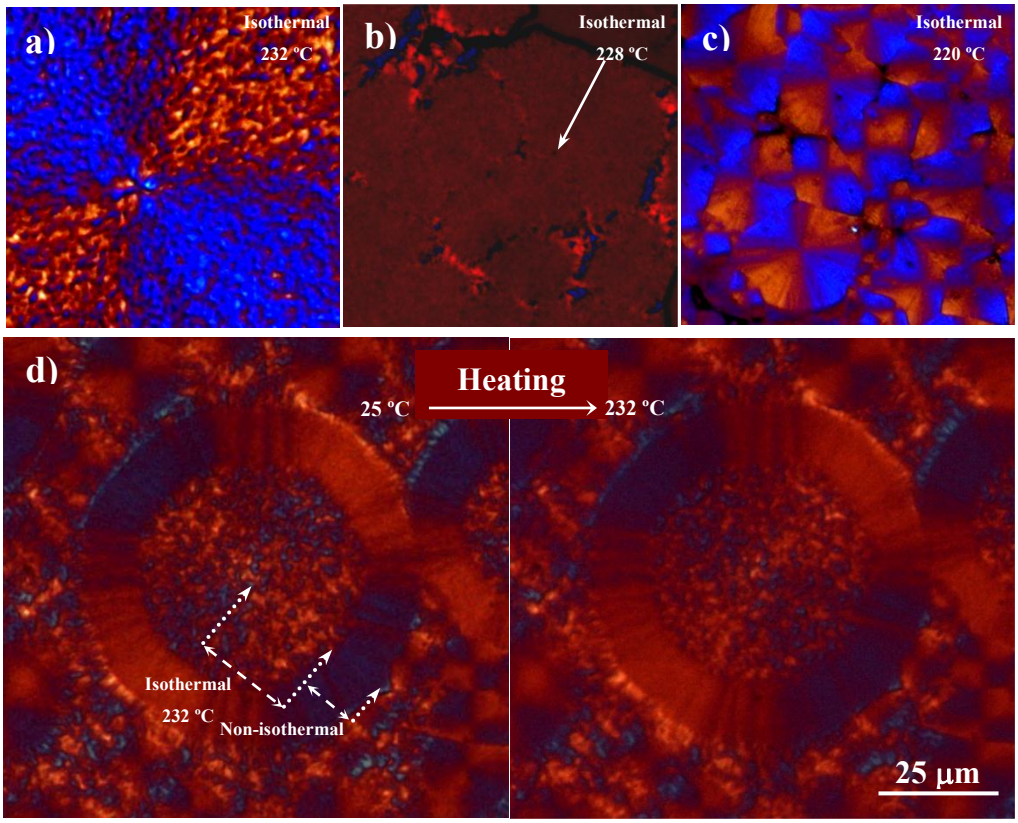

Figure 4.3.7 Optical micrographs taken at the respective crystallization temperature of nylon 47 spherulites obtained at 232 ºC (a), 228 (b) and 220 ºC (c). d) Optical micrographs taken at room temperature and after heating up to 232 ºC of a nylon 47 spherulite that was firstly isothermally crystallized at 232 ºC and then non-isothermally crystallized until room temperature at a cooling rate of 1 ºC/min.

At lower temperatures than 228 ºC spherulites tended to have a fibrilar texture and kept a negative birefringence. In fact, ringed spherulites with a small inter-ring spacing could be envisaged in the optical micrographs when temperature was close to 228 ºC (**Figure 4.3.7** c). Electron micrographs clearly revealed (**Figure 4.3.9** a) that samples crystallized at 218 ºC had a regular banding produced by a lamellar twisting with a spacing close in this case to 0.5 μm. Bright zones consisted of lamellae lying practically flat whereas dark zones were associated to lamellae standing on edge. Spherulites were sufficiently thin to get *hk*0 electron diffraction patterns (e.g. **Figure 4.3.2** a) from zones corresponding to the flat lamellae (**Figure 4.3.9** b). Again these patterns corresponded to form I (i.e. the most stable structure at room temperature). It is also highly interesting that spherulites grown at the specific temperature of 228 ºC were clearly not birefringent (**Figure 4.3.7** b).

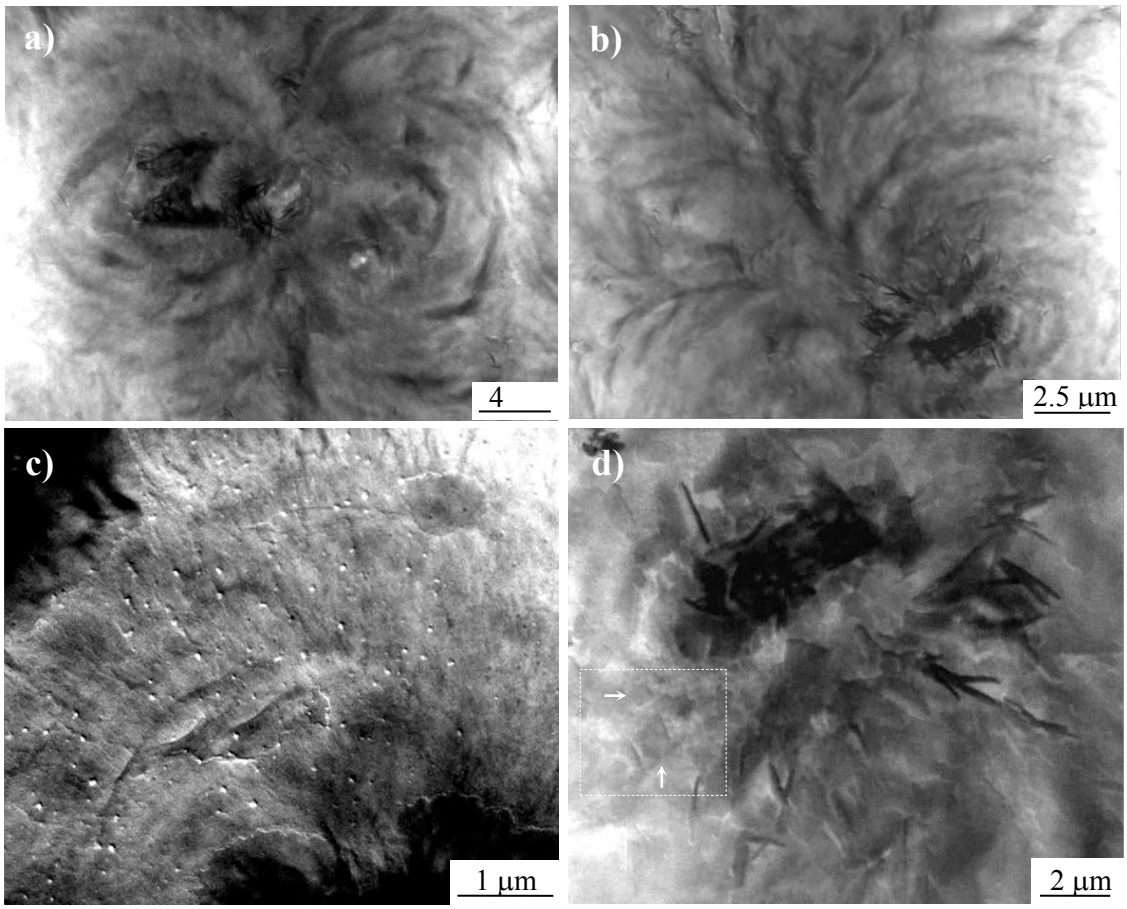

Figure 4.3.8 Transmission electron micrographs of nylon 47 spherulites obtained by isothermal crystallization at 232 ºC. Different magnifications are given to show specific morphologic details. Dashed area in d) shows the presence of lozenge crystals (see arrows).

Figure 4.3.7 d shows polarized optical micrographs taken at room temperature and at 232 ºC (i.e. after a subsequent heating) of a spherulite that was firstly isothermally crystallized at 232 ºC and then non-isothermall crystallized by cooling up to room temperature at a rate of 0.5 ºC/min. It is clear that the central zone isothermally crystallized and constituted by flat crystal domains have a reversible change of the birefringence sign with temperature. Note that it was negative at the crystallization temperature (**Figure 4.3.7** a), became positive at room temperature and finally negative after the heating process. By contrast the outer non-isothermally crystallized zone was characterized by a fibrilar texture and had always a negative birefringence sign. This feature was clearly distinctive to typical even-even nylons which show a positive birefringence when they were crystallized at low temperatures. The reversible birefringence change observed for nylon 47 seems a consequence of a structural transition (from the Brill or form II structure to the form I expected at high and low temperatures, respectively). Probably, the structural transition involved small changes on the molecular conformation and a variation on the angle defined by the two hydrogen bonding directions. This change on the packing mode should greatly influence on optical properties when crystals had a flat disposition that emphasized the molecular and hydrogen bonding arrangements. In this way, reversible changes could only be envisaged in the spherulitic textures developed at higher temperatures (i.e. > 228 ºC).

- **Dispersion structure of C25A and C30B organomodified clays in their nanocomposites with nylon 47**

The nanocomposite structures were first analyzed by reflection X-ray diffraction of film samples. The diffraction patterns show evidence of intercalation of polymer chains into the silicate galleries in the range of 2θ = 1-10º (θ is the scattering angle) when the characteristic 001 silicate diffraction peak appears at a lower diffraction angle (larger spacing) than in the pattern of the neat clay. Similarly, the absence of this peak may suggest an exfoliated structure.

Cloisite C30B has hydroxyl polar groups (Table 1) that can interact with the amide groups of nylon 47 and consequently can favour the achievement of an exfoliated structure. This structure was found to be enhanced when nanocomposites were prepared by the melt mixing technique instead of solution-intercalation, probably as a consequence of the high melting temperature of nylon 47 that could favour the exfoliation of silicate layers. Hence, nylon 47/C25A and nylon 47/C30B nanocomposites obtained by solution-intercalation and melt mixing methods, respectively, were selected as the best preparations corresponding to intercalated and exfoliated structures.

Figure 4.3.10 a shows the shift of the characteristic 001 reflection of the C25A clay from 1.94 nm (2θ = 4.55º) to 2.25 nm (2θ = 3.93º) when the nanocomposite sample was prepared. This

observation indicates the achievement of a regular intercalated structure with an increase of the interlayer spacing caused by the insertion of polymer molecular chains. Direct observation of the morphology and phase distribution of ultrathin sections of nylon 47/C25A specimens by transmission electron microscopy (**Figure 4.3.10** a) revealed the presence of well-ordered layered structures as presumable when an intercalated structure was predominant.

Figure 4.3.10 b clearly demonstrates that an exfoliated structure was characteristic of the nylon 47/C30B nanocomposite. Thus, the 001 reflection of the C30B clay (1.80 nm, 2θ = 4.91º) disappeared in the X-ray profile of the nanocomposite, whereas TEM micrographs revealed the presence of practically dispersed silicate layers.

The structure of nylon 47 changed also according to the nanocomposite preparation method as shown in the X-ray diffractograms of **Figure 4.3.11**. Hence, samples obtained from solution showed the characteristic reflections of form I (e.g. those appearing at 0.430 and 0.388 nm), whereas samples coming from the melt had reflections of both structures: form I (e.g. 0.388 nm) and form II (e.g. 0.419 nm). Note also that in this case, the 002 reflection shifted to a lower spacing (i.e. 0.696 nm) which may indicate a shortening of the chain axis repeat or alternatively an increase of the shift between neighbouring chains along the *c* crystallographic axis.

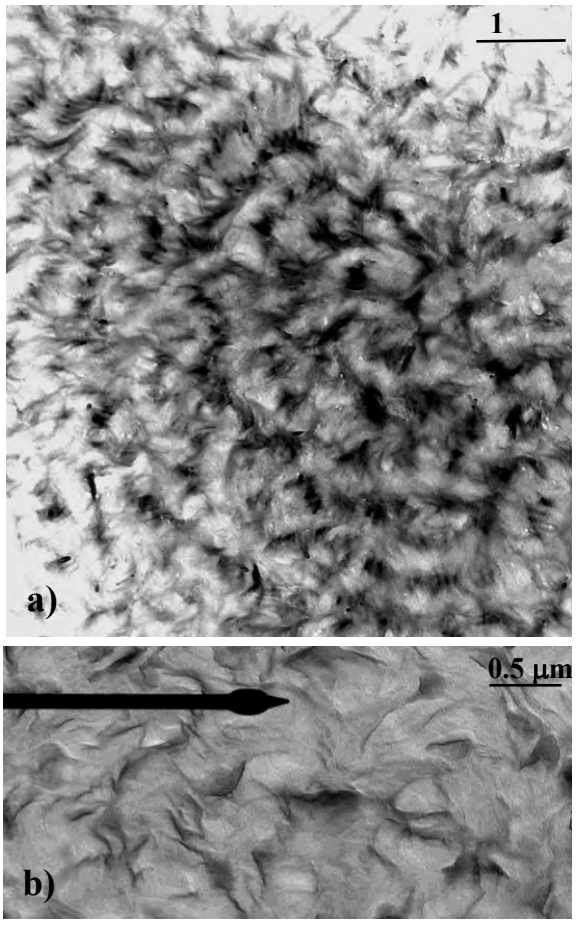

Figure 4.3.9 a) Transmission electron micrograph of nylon 47 spherulites obtained by isothermal crystallization at 218 ºC. b) Specific zone of a non shadowed sample where a hk0 electron diffraction pattern of form I was obtained.

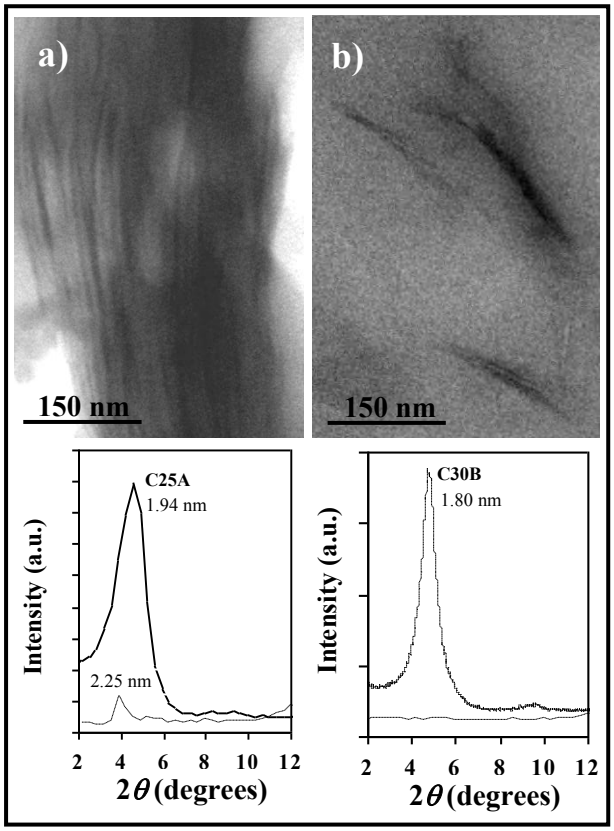

Figure 4.3.10 Transmission electron micrographs and X-ray diffraction patterns showing the morphology and the zone corresponding to the 001 clay reflection of the Nylon 47/C25A (a) and Nylon 47/C30B (b) nanocomposites with a Cloisite concentration of 3%. X-ray diffraction patterns of the neat clays are also shown.

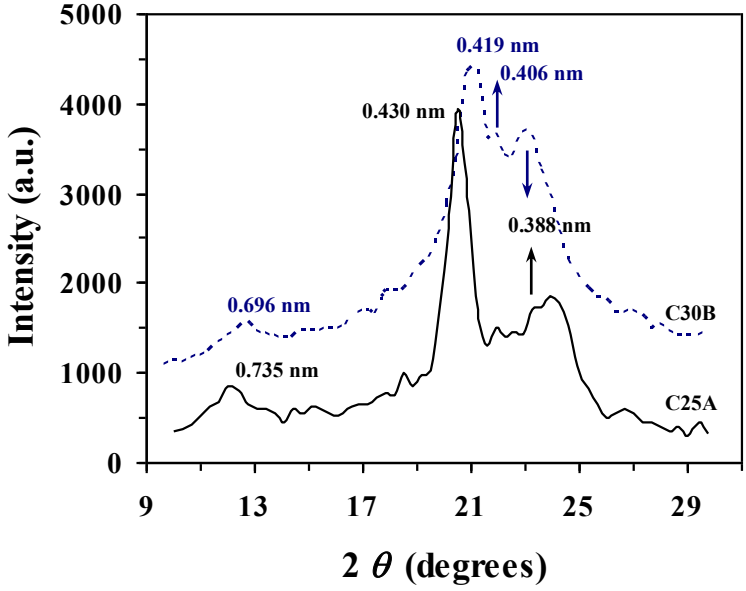

Figure 4.3.11 X-ray diffraction profiles showing the main reflections of nylon 47 in nanocomposites with Cloisite 25A and 30B prepared by solvent casting and melt mixing methods, respectively.

- **Influence of C25A and C30B clay particles in the thermal behaviour of nylon 47**

Calorimetric analyses showed differences between the non-isothermal crystallization of the neat polymer and its nanocomposites with the C25A and C30B clays. Thus, the peak crystallization temperature increased and the exothermic peak became broader respect to the neat polymer when the nanocomposite had an intercalated structure as shown in **Figure 4.3.10** for a representative cooling rate (i.e. 10 ºC/min). Crystallization was consequently favoured by the presence on the layered structure (nucleation effect) although the corresponding crystallization rate decreased. The exfoliated structure led to a disfavoured crystallization process due to both the decrease of the peak crystallization temperature and the slight peak broadening.

Differences on the crystallization process were clearer when isothermal experiments (**Figure 4.3.13**) were carried out. Note that in this case, the crystallization peak of nanocomposites with an exfoliated structure appeared at later times than required for the neat polymer, and also that this peak became clearly broader. Differences were enhanced when experiments were conducted at the higher temperatures (i.e. when the overall crystallization rate was slower).

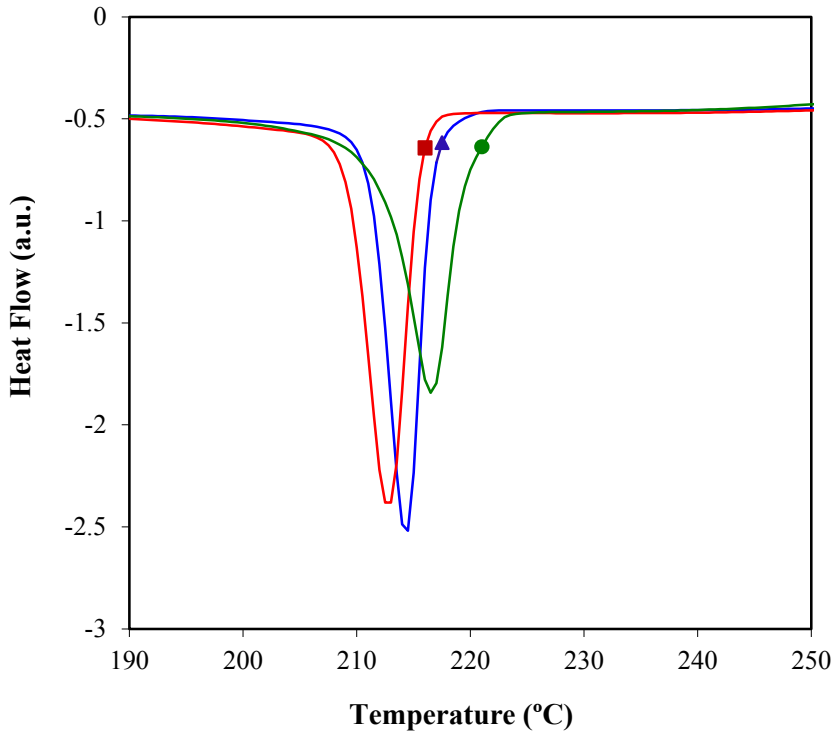

Figure 4.3.12 DSC cooling runs (10 ºC/min) from the melt state of a nylon 47/C25A (●), nylon 47 (▲) and nylon 47/C30B (■) samples.

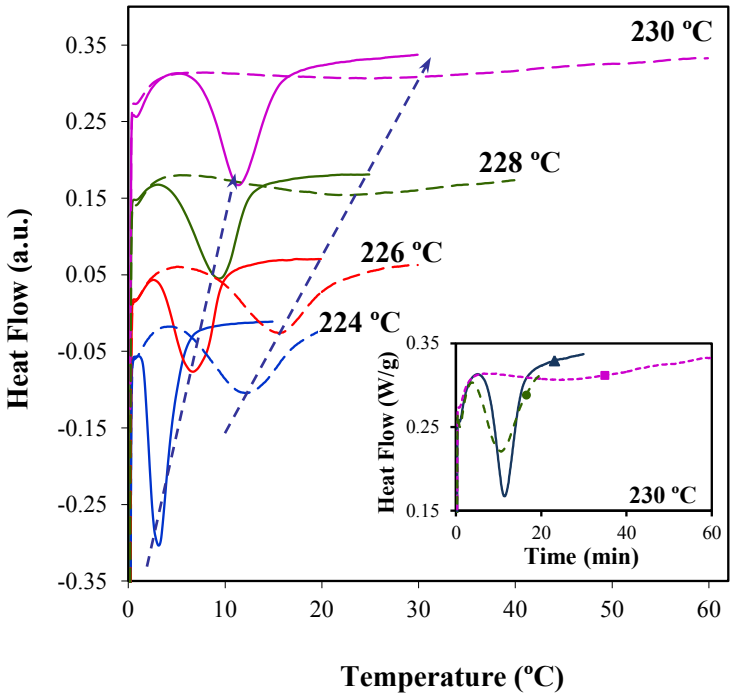

Figure 4.3.13 DSC curves of isothermal crystallization at selected temperatures of the nylon 47/C30B (dashed lines) and nylon 47/C25A (solid lines) nanocomposites. The inset compares the isothermal curves at 230 ºC of the neat polymer (▲) and its nanocomposites with C30B (■) and C25A (●).

Crystallization exotherms started earlier when nanocomposites had the intercalated structure as expected for a favoured nucleation. However, the overall crystallization rate decreased again respect to the neat polyamide since the corresponding exothermic peak became slightly broader. In summary, both isothermal and non-isothermal crystallizations suggest that primary nucleation was enhanced or disfavoured when intercalated or exfoliated silicate layers were respectively present. The crystallization rate decreased in both cases suggesting that the crystal growth was hindered as will be described in the next section. Note that the neat polymer and its nanocomposite with the C25A clay had similar DSC crystallization curves (**Figure 4.3.10** and **Figure 4.3.11**) due to the two opposing effects observed for the intercalated nanocomposites.

- **Optical microscopy studies on nylon 47/C25A and nylon47/C30B nanocomposites**

Accurate measurements of the evolution of the spherulitic radius with crystallization time were only feasible in the restricted temperature range between 218 and 243 ºC. Thus, the kinetic analysis was limited to a region close to the polymer melting point and consequently crystallization was mainly governed by the secondary nucleation process.

In all cases, spherulites had similar textures and birefringence to those above described for the neat polymer. Note that the crystallization range was large enough to cover the two regions where different kinds of spherulites were favoured.

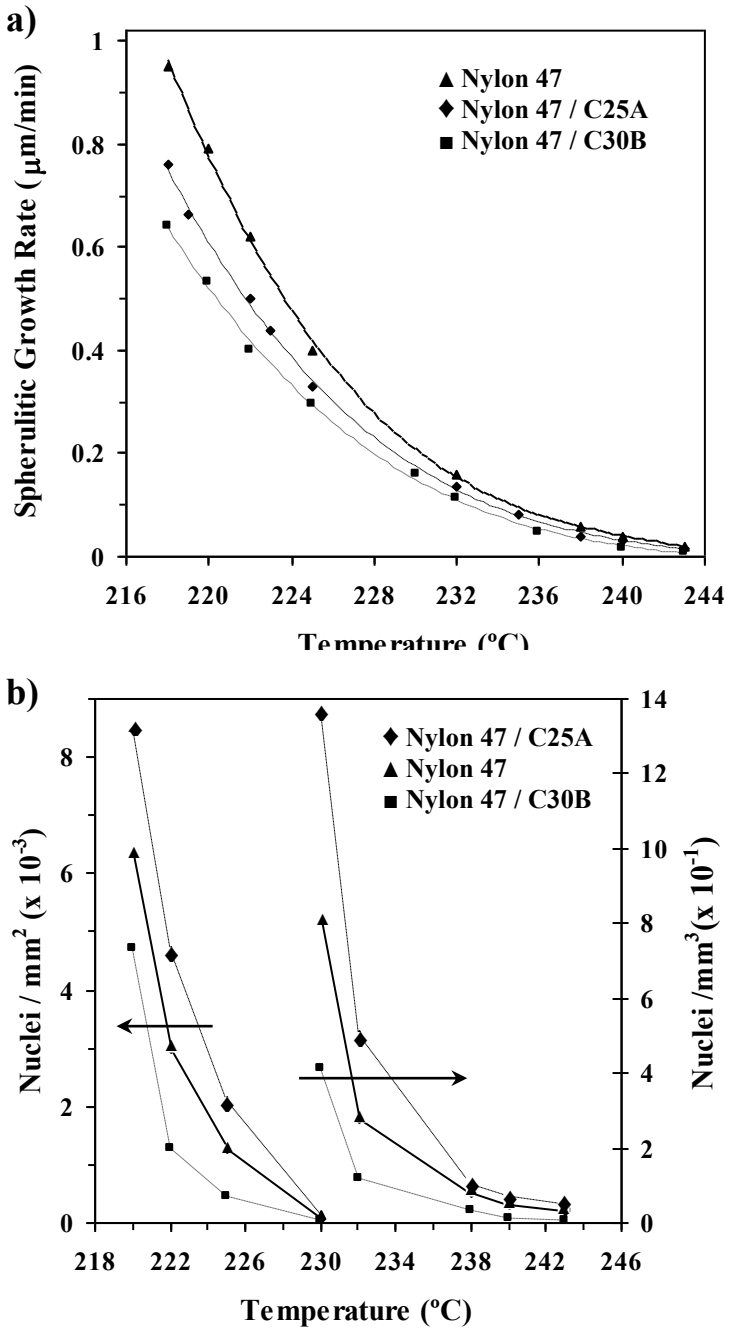

Figure 4.3.14 a) Plot of the spherulitic growth rate of the neat nylon 47 (▲) and its nanocomposites with 3% of C30B (■) and C25A (♦) versus crystallization temperature. b) Plot of the nucleation density of the neat nylon 47 (▲) and its nanocomposites with 3% of C30B (■) and C25A (♦) versus crystallization temperature. Data are plotted using different ordinate scales depending on the crystallization temperature (i.e. higher or lower than 230 ºC.

Radial growth rates at different isothermal crystallization temperatures (**Figure 4.3.14** a) were determined from the slopes of the linear dependence between spherulitic radius and crystallization time. Significant differences were found between the crystal growth rate curves of the neat polymer and its nanocomposites with C25A and C30B clays. Nanocomposites had always a lower growth rate, being the decrease more pronounced when the crystallization temperature decreased and when exfoliated structures were attained. The presence of organoclay particles hampered the lamellar growth but experimental data points also out that no deviation from a linear spherulitic growth (not shown) was produced. Thus, clay particles did not seem to be excluded towards the growth front during crystallization in a manner that hindered the transport of crystallizable molecules from the melt to the growing edge.

Optical micrographs taken at the end of the crystallization process revealed noticeable differences on the primary nucleation between the neat polymer and its nanocomposites and consequently in the number and size of spherulites observed in a given surface. **Figure 4.3.14** b shows as the nucleation density of the neat polymer and the nanocomposite samples logically increased with lowering the crystallization temperature and also that exfoliated and intercalated structures led to a decrease and an increase of the nucleation density, respectively. Like reported data on other systems, these observations reveal that when good compatibility between silicate layers and the polymer matrix is achieved (i.e. an exfoliated structure), spherulite nucleation is low as a result of the fine dispersion of silicate layers in the matrix. On the other hand, poor compatibility renders an intercalated structure where silicate particles may act as effective nucleating agents.[36]

In summary, the decrease of the radial growth rate detected for the nanocomposite with the C25A clay and prepared by solution intercalation is well compensated by the increase on the primary nucleation. Hence, the overall crystallization rate becomes comparable to that determined for the neat polymer. In the case of the exfoliated nanocomposite with the C30B clay and prepared by melt mixing, crystallization rate decreases as a consequence of both nucleation and crystal growth factors.

4.3.4 Conclusions

Nylon 47 crystallizes at room temperature according to a peculiar structure (form I) that can be interpreted in terms of a packing where hydrogen bonds are established along two directions. On heating, a structural transition took firstly place at low temperature and then a gradual Brill transition towards a pseudohexagonal packing was produced. Structural changes were almost reversible on cooling since a Brill transition with a hysteresis effect was firstly detected and

then the form II to form I transition partially developed, although it could not be completed during the cooling run.

Spherulites with different textures and birefringences were obtained by varying the crystallization temperature. Negative spherulites formed in the low temperature region, indicating a molecular arrangement different from that found in conventional even-even nylons that gave rise to spherulites with a positive birefringence. Spherulites obtained at low supercoolings were mainly constituted by flat micro-crystals that showed reversible optical properties with temperature. This peculiar behaviour may be a consequence of the postulated structure where small changes on the torsional angles of the odd diamide units could induce a variation on the angle between the two hydrogen boding directions and on the birefringence sign of the crystalline micro-domains.

Nanocomposites with intercalated and exfoliated structures could be obtained from nylon 47 and the C25A and C30B organomodified clays. The final structure mainly depended on the preparation method. Specifically, melt mixing favoured the exfoliated distribution whereas intercalated structures were obtained by solution intercalation. Incorporation of clay particles influenced the overall crystallization rate under both isothermal and non-isothermal conditions. In all cases, clay particles decelerated the crystal growth process and had a strong influence on the primary nucleation which could be enhanced or disfavoured when intercalated or exfoliated structures were respectively achieved.

4.3.5 References

[1] Xenopoulos A, Clark ES. In Nylon Plastics Handbook; Kohan MI Ed.; Hanser Publishers: Munich, Vienna and New York, 1995; Chapter 5:108-137.

[2] Bunn CW, Garner EV. Proc R Soc London Ser A 1947;189:39-68.

[3] Holmes DE, Bunn CW, Smith D. J Polym Sci Part A, General Papers 1955;17:159-177.

[4] Kinoshita Y. Makromol Chem 1959;33:1-20.

[5] Puiggalí J, Muñoz-Guerra S, Lotz B. Macromolecules º986;19:1119-1124.

[6] Puiggalí J, Muñoz-Guerra S, Subirana JA. Polymer 1987;28:209-212.

[7] Puiggalí J, Aceituno JE, Navarro E, Campos JL, Subirana JA. Macromolecules 1996;29:8170-8179.

[8] Brill R. Makromol Chem 1956;18:294-309.

[9] Schmidt GF, Stuart HA. Naturforsch Z 1958;13A:222-226.

[10] Hirschinger J, Miura H, Gardner KH, English AD. Macromolecules 1990;23:2153-59.

[11] Wendoloski JJ, Gardner KH, Hirschinger J, Miura H, English AD. Science 1990;247:431-436.

[12] Ramesh C, Keller A and Eltink S J E A. Polymer 1994;35:2483-2487.

[13] Hill MJ, Atkins EDT, Macromolecules 1995;28(2):604-609.

[14] Vasanthan N, Murthy NS, Bray RG. Macromolecules 1998;31:8433-35.

[15] Murthy N S, Wang Z, Hsiao BS. Macromolecules 1999;32:5594-5599.

[16] Ramesh C, and Gowd EB. Macromolecules 1999;32:3721-3726.

[17] Jones NA, Atkins EDT, Hill MJ. J Polym Sci Part B, Polym Phys 2000;38:1209-1221.

[18] Feldman A Y, Wachtel E, Vaughan G B M, Weinberg A, Marom G. Macromolecules 2006;39:4455-4459.

[19] Franco L, Cooper SJ, Atkins A DT, Hill M, Jones NA. Macromolecules 1998;36: 1153-1165.

[20] Navarro E, Franco L, Subirana JA, Puiggalí J. Macromolecules 1995;28:8742- 8750.

[21] Morales-Gámez L, Soto D, Franco L, Puiggalí J. Polymer 2010;51:5788-5798.

[22] Navarro E, Subirana JA, Puiggalí J. Polymer 1997;38:3429-3432.

[23] Puiggalí J, Franco L, Alemán C, Subirana JA. Macromolecules 1998;31: 8540-8548.

[24] Laura Morales-Gámez L, Albert Ricart A, Lourdes Franco L, Jordi Puiggalí J. Eur Polym J 2010;46:2063-2077.

[25] Villaseñor P, Franco L, Subirana JA, Puiggali J. J Polym Sci Part B, Polym Phys Ed 1999;37:2383-2395.

[26] Franco L, Subirana JA, Puiggalí J. Macromolecules 1998;31:3912-3924.

[27] Yano K, Usuki A, Okada A, Kurauchi T, Kamigaito O, J Polym Sci, Part A: Polym Chem 1993;31:2493-2498.

[28] Kojima Y, Usuki A, Kawasumi M, Okada A, Fukushima Y, Kurauchi T, Kamigaito O, J Mater Res 1993; 8:1185-1189.

[29] Gianelis EP, Krishnamoorti R, Manias E. Adv Polym Sci 1999;138:107-147.

[30] Usuki A, Kojima Y, Kawasumi M, Okada A, Fukushima Y, Kurauchi T, Kamigato O. J Mater Res 1993;8:1179-1184.

[31] Kawasumi M, J Polym Sci Part A: Polym Chem 2004;42:819-824.

[32] Maiti P, Nam PH, Okamoto M, Kotaka T, Hasegawa N, Usuki A. Macromolecules 2002;35:2042–2049.

[33] Sinha Ray S, Okamoto M. Prog Polym Sci 2003;28:1539-1641.

[34] Q. Yuan Q, S. Awate S, Misra RDK. Eur Polym J 2006;42:1994-2003.

[35] Wu D, Wu L, Wu L, Xu B, Zhang Y, Zhang M. J Polym Sci Part B: Polym Phys 2007;45:1100-1113.

[36] S. Sinha Ray, J. Bandyopadhayay, M. Bousmina. Eur Polym J, 44, 3133 (2008).

[37] L. Morales-Gámez, A. Ricart, L. Franco, J. Puiggalí. Eur. Polym J, 2010;46:2063-2077.

[38] Magill JH. J. Polym. Sci. part A 1969;7:123-142.

[39] Lovinger AJ. J. Appl. Phys 1978:49:5003-5013.

[40] Lovinger AJ. J. Appl. Phys 1978:49:5014-28.

5

STUDY OF NANOCOMPOSITES PREPARED FROM BIODEGRADABLE POLYESTERS AND POLY(ESTER AMIDE)S

The work described in this chapter previously appeared in:

[1] Morales, L. Franco, L. Casas, M. T.; Puiggalí, J. *Journal of Polymer Science Part A: Polymer Chemistry* **2009**, *47*, 3616-3629.

[2] Morales, L. Franco, L. Casas, M. T.; Puiggalí, J. *Journal of Polymer Science Part B: Polymer Physics* **2010**, *48*, 33-46.

[3] Morales-Gamez, L. Jones, I. Franco, L.; Puiggalí, J. *Express Polymer Letters* **2011**, *5*, 717-731.

[4] Morales-Gámez, L. Franco, L. Casas, M. T.; Puiggalí, J. *Polymer Engineering & Science* **2011**, *51*, 1650-1661.

[5] Morales-Gámez, L. Franco, L.; Puiggalí, J. Thermochimica Acta 2011, 512, 142-149.

[6] Puiggalí, J. Morales-Gamez, L. Franco, L. Casas, M. del Valle, luis J.; Rodriguez-Galan, A. Society of Plastics Engineers. Plastics research online 2011, 10-12.

5.1

Poly(Ester Amide) / Clay nanocomposites prepared by in situ polymerization of the sodium salt of N-chloroacetyl-6-amino-hexanoic acid.

Preparation of nanocomposites of organo-modified montmorillonites and the biodegradable poly(ester amide) derived from glycolic acid and 6-aminohexanoic acid has been evaluated by the in situ polymerization technique. The reaction was based on the thermal polycondensation of sodium chloroacetylaminohexanoate, which has the formation of the sodium chloride salt as the driving force of the process. Polymerized samples were studied by means of X-ray diffraction and transmission electron microscopy. The most dispersed structure was obtained by addition of C25A organoclay. Evaluation of thermal stability and crystallization behavior of these samples showed significant differences between the neat polymer and its nanocomposite with C25A.

Isothermal and nonisothermal calorimetric analyses of the polymerization reaction revealed that the kinetics was highly influenced by the presence of the silicate particles. Crystallization of the polymer was observed to occur when the process was isothermally conducted at temperatures lower than 145 ºC. In this case, dynamic FTIR spectra and WAXD profiles obtained with synchrotron radiation were essential to study the polymerization kinetics. Clay particles seemed to reduce chain mobility and the Arrhenius pre-exponential factor.

5.1.1 Introduction

Preparation of polymer nanocomposites is nowadays an important research subject since polymer properties can be enhanced and their range of applications extended by using molecular or nanoscale reinforcements rather than conventional fillers.[1] Nanocomposites consist in a combination of two or more phases where at least one of them is in the nanoscale regime, giving rise to a high surface-to-volume ratio.[2] The origin of polymer-clay nanocomposites started in 1986 under Toyota Central Research and Development laboratories as has been widely explained by Kawasumi.[3] This pioneering work was centered on the preparation of nylon 6 nanocomposites,[4] and used different methodologies as melt mixing[5] and thermal polymerization.[6] First results clearly indicated that characteristics of the neat polymer like water-absorption rate, thermal-expansion coefficients and gas barrier properties were modified by the incorporation of small amount of clay.[7]

Layered silicate particles have some characteristics that make them especially interesting for nanocomposite preparation, e.g. their possibility to be dispersed into individual layers with a thickness close to 1 nm, and to tune surface interactions through exchange reactions with organic and inorganic cations.[2,8] The final structure of the composite depends on the extend to which the organic matrix and the inorganic clay components are made compatible[9] and varies from an intercalated to a fully exfoliated nanostructure.

The in situ intercalation method proceeds via the monomer-induced swelling of the organoclay, followed by the in situ polymerization step, initiated either thermally or by the addition of a suitable compound. Chain growth within the clay galleries is known to accelerate clay exfoliation and nanocomposite formation. In situ interlayer polymerization is a highly attractive technique due to its versatility and compatibility with various reactive monomers, making it a valuable process for commercial applications.[10,11] Several examples concern the preparation of polystyrene,[12] polycaprolactone[13] and nylon 6[14] nanocomposites.

Poly(ester amide)s constitute a promising family of materials with some advantages associated with the hydrophilic character of their amide groups and the ability to establish strong hydrogen bond interactions that may influence both thermal and mechanical properties.[15-17] Furthermore, the presence of ester groups should ensure degradability, although at a lower rate than in parent polyesters.

We have recently developed a synthesis procedure (**Scheme 5.1.1**) that allows poly(ester amide)s constituted by glycolic acid units and ω-amino acid units with a regular sequence distribution to be obtained.[18] The new synthesis is based on a thermal polycondensation reaction where the formation of a metal halide salt becomes the driving force of the process.[19,20] The great simplicity of this method raises interest in this family of polymers characterized by a

semicrystalline character that contrasts with the more amorphous nature of copolymers prepared by ring opening polymerization.[21] Different works have been performed to gain insight into the polymerization kinetics, crystalline structure, crystallization kinetics, thermal stability and hydrolytic and enzymatic degradability of these new polymers.[22-25]

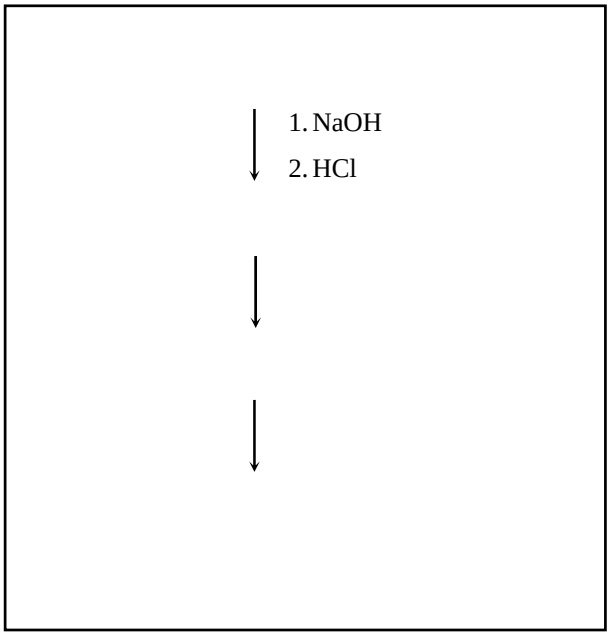

Scheme 5.1.1 Synthesis of poly(glc-*alt*-amh) by a thermal polyconensation reaction.

The main purpose of this work is the preparation of nanocomposites of the alternating poly(ester amide) constituted by glycolic and 6-aminohexanoic acid units (which will be hereafter named poly(glc-*alt*-amh)) via in situ intercalation polymerization. The polymer has been chosen as a representative of the new family which in addition is characterized by its good performance properties. Furthermore, its composition is based on the most usual units existing in polyesters employed for biomedical applications (e.g. polyglycolide) and the commercial polyamides (e.g. nylon 6). The second goal is the study of how the presence of a compatible organomodified clay may influence the thermal polymerization kinetics of the monomer salt. In this sense, calorimetric, spectroscopic and diffraction techniques are combined to gain further insight.

5.1.2 Experimental Section

Materials

Five different layered phyllosilicates were investigated: pristine sodium montmorillonite (NANOFIL 757), organoclay octadecyl ammonium montmorillonite (NANOFIL 848, Süd Chemie, ODA), methyl tallow bis(2-hydroxyethyl) ammonium montmorillonite (CLOISITE 30B, Southern Clay Products, MT2EH), dimethyl dihydrogenated-tallow ammonium

montmorillonite (CLOISITE 20A, Southern Clay Products, 2MH2HT) and dimethyl hydrogenated-tallow 2-ethylhexyl ammonium montmorillonite (CLOISITE 25A, Southern Clay Products, 2MHTEX). All the clays were used as received. The chemical structure of the specific surfactant of each OMMT (organo-modified montmorillonite) is presented in Table 1.

The monomer, sodium chloroacetylaminohexanoate, was synthesized following the previously reported method[18,22] (**Scheme 5.1.1**).

Preparation of nanocomposites

For each nanocomposite preparation, 10 mg of monomer was dissolved in 10 mL of water, and, separately, the appropriate clay was dispersed in water (< 0.1 wt %). Both the monomer solution and clay dispersion were stirred for two hours, and then mixed and liophilizated. The ratio of the solution and dispersion was conveniently adjusted to obtain a clay content of 3% in the final solid. Polymerization was carried out by heating the monomer/clay mixture to 160ºC. A white solid was recovered and extensively washed with water, methanol and acetone.

No significant differences were found between the molecular weights of the neat poly(ester amide) and the different nanocomposites. Thus, average M_w and M_n molecular weights were always in the 15,000-17,000 and 37,000-43,000 ranges, respectively, according to GPC measurements using 1,1,1,3,3,3-hexafluoroisopropanol as solvent and poly(methyl methacrylate) standards.

Measurements

Interlayer spacing of the clay was studied by means of wide angle X-ray scattering (WAXD) using a Siemens D-500 diffractometer (Karlsruher, Germany) with Cu K_α radiation (λ = 0.1542 nm).

Thermogravimetric analyses (TGA) were performed at a heating rate of 20 ºC/min with approximately 10 mg samples using a Perkin-Elmer TGA-6 thermobalance and under a flow of dry nitrogen.

The structure and distribution of Cloisite were observed with a Philips TECNAI 10 transmission electron microscope (TEM) at an accelerating voltage of 100 kV. TEM specimens were prepared by embedding in a low viscosity modified Spurr epoxy resin and curing them at 40°C for a few days and then at 60 °C for 6 h. Ultrathin sections (less than 100 nm) were cut at room temperature using a Sorvall Porter-Blum microtome equipped with a diamond knife. Finally, the sections were collected in a trough filled with water and lifted onto carbon coated copper grids. In order to prevent diffusion of the epoxy resin into the polymer film, a thin layer of carbon was evaporated over the film surface.

Calorimetric data were obtained by differential scanning calorimetry using a TA Instruments Q100 series with T_{zero} technology and equipped with a refrigerated cooling system (RCS) operating at temperatures from -90 ºC to 550 ºC. Experiments were conducted under a flow of dry nitrogen with a sample weight of approximately 5 mg, while calibration was performed with indium. The T_{zero} calibration involved two experiments: the first was done without samples and the second was performed with sapphire disks.

The spherulite growth rate was determined by optical microscopy using a Zeiss Axioskop 40 Pol light polarizing microscope equipped with a Linkam temperature control system configured by a THMS 600 heating and freezing stage connected to a LNP 94 liquid nitrogen cooling system. Spherulites were grown from homogeneous melt-crystallized thin films produced by melting 1 mg of the polymer mixture on microscope slides. Next, small sections of these films were pressed or smeared between two cover slides and inserted in the hot stage. The thicknesses of the squeezed samples were close to 10 μm in all cases. Samples were kept at 170 ºC (more than 10 ºC above the polymer melting point of 157 ºC) for 5 minutes to wipe out sample history effects, and then quickly cooled to the selected crystallization temperature. The radius of the growing spherulites was monitored during crystallization by taking micrographs with a Zeiss AxiosCam MRC5 digital camera at appropriate time intervals. A first-order red tint plate was employed to determine the sign of spherulite birefringence under crossed polarizers.

Simultaneous time-resolved SAXS/WAXD experiments were carried out at the CRG beamline (BM16) of the European Synchrotron Radiation Facility of Grenoble. The beam was monochromatized to a wavelength of 0.098 nm. The capillary with the sample was held in a Linkam hot stage with temperature control within 0.1 ºC. WAXD profiles were acquired during polymerization and crystallization experiments in time frames of 12 s. The WAXD detector was calibrated with diffractions of a standard of an alumina (Al_2O_3) sample. The diffraction profiles were normalized to the beam intensity and corrected considering the empty sample background. Deconvolution of WAXD peaks was performed with the PeakFit v4 program by Jandel Scientific Software using a mathematical function known as “Gaussian area”.

Infrared absorption spectra were recorded with a Fourier Transform FTIR 4100 Jasco spectrometer in the 4000-600 cm^{-1} range. A Specac model MKII Golden Gate attenuated total reflection (ATR) with a heated Diamond ATR Top-Plate which can be used up to 200 ºC, and a Series 4000 High Stability Temperature Controller were also utilized.

Table 5.1.1 Characteristics of organoclays.[a]

Clay Type	Chemical Structure of Organic Modifier
Nanofil 757	Natural Montmorillonite (Na^+)
Nanofil 848	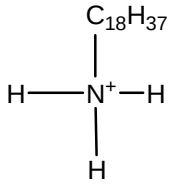
Cloisite 30B	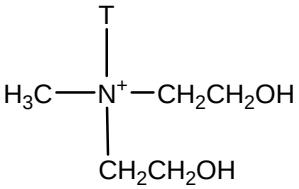
Cloisite 20A	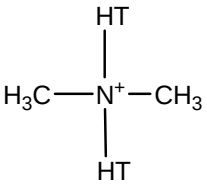
Cloisite 25A	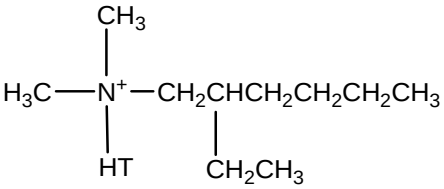

[a] T: tallow (~65% C18, ~30% C16, ~5% C14); HT: hydrogenated-tallow.

5.1.3 Results and Discussion

- **Dispersion structure of clay in the composites**

The nanocomposite structure is usually analyzed by X-ray diffraction and transmission electron microscopy. Evidence of intercalation of polymer chains into the silicate galleries can be obtained from diffraction patterns in the range of 2θ = 1-10º when the characteristic silicate diffraction peaks appear at larger spacings than neat clay ones. Similarly, the absence of these peaks may suggest an exfoliated structure.

The position of the silicate (001) diffraction peak, shown by X-ray diffraction profiles, was almost the same for the neat clay and the mixture with natural montmorillonite. This result implies that the monomer could not establish good interactions with neat Nanofil 757 clay. It is worth noting that we might be led to think otherwise by the ionic character of the monomer. However, the best experimental results were attained when an organo-modified clay was employed. Indeed, the more hydrophobic character of the polymer formed during reaction may have also played a significant role.

In the case of composites with Nanofil 848 and C20A composites, a shift of the silicate diffraction peak to larger spacing was observed, suggesting that polymer chains were intercalated in the silicate galleries. These shifts changed from 0.89 to 1.46 nm and from 1.26 to 1.50 nm, respectively.

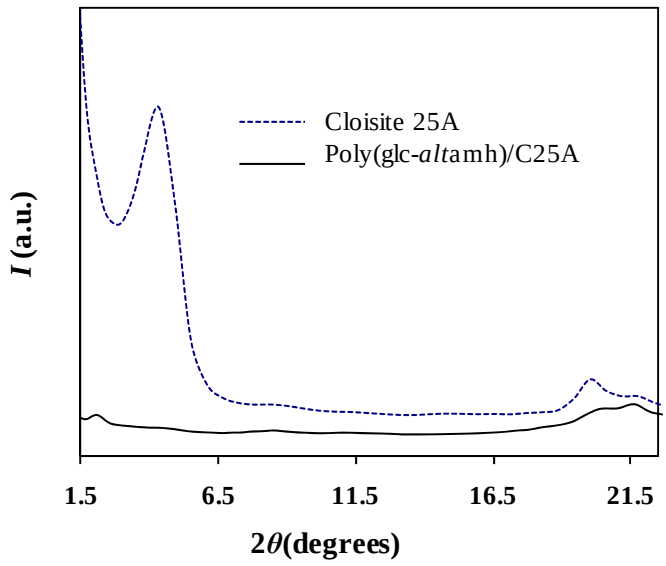

Figure 5.1.1 X-ray diffraction patterns of neat Cloisite 25A (dotted line) and the nanocomposite obtained by in situ polymerization of N-chloroacetyl-6-aminohexanoic acid with 3% clay content (solid line).

The poly(glc-*alt*-amh)/C30B nanocomposite showed that the 001 peak was significantly reduced and also shifted to a larger spacing (from 0.91 nm to 1.52 nm). It appears that, in this mixture, strong interactions between the carbonyl groups of the monomer and the two hydroxyl groups of the modified montmorillonite can be established, giving rise to a certain ratio of an exfoliated structure after polymerization. Disordered and exfoliated silicate layers have no periodic stacking, and therefore the X-ray diffraction pattern remains silent. This kind of mixed intercalated and/or exfoliated structures may be caused by chemical and size inhomogeneities in silica layers. Thus, intercalated structures can be due to larger (in lateral size) silicate layers, whereas delamination is more favoured by smaller layers.[26]

The most interesting result was obtained with the poly(glc-*alt*-amh)/C25A nanocomposite since the characteristic peak of C25A (0.98 nm) disappeared (**Figure 5.1.1**), suggesting either an exfoliated structure or an intercalated one with a wide interlayer spacing distribution. Direct observation of the morphology and phase distribution of the ultrathin sections of C25A specimens by transmission electron microscopy (**Figure 5.1.2**) clearly showed that an intercalated structure was predominant, varying the interlayer spacings from 1.4 to 3.2 nm. This appears as a first step towards a fully exfoliated structure.

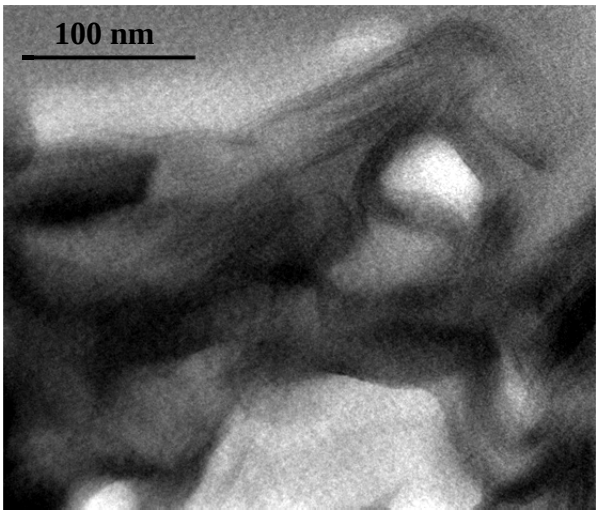

Figure 5.1.2 Transmission electron micrograph showing the morphology of the nanocomposite obtained by in situ polymerization of N-chloroacetyl-6-aminohexanoic acid in the presence of 3% clay content. Sample was previously washed with water to eliminate all NaCl crystals.

The C25A organo-modified clay can be easily added in the last step of the monomer synthesis (after neutalzation with NaOH, **Scheme 5.1.1**) and consequently the preparation of the nanocomposite seems economically suitable taking also into account the great simplicity of the polymerization process. The new nanocomposites may be of great interest since their biodegradability confers potential applications as commodity materials.

Thermal Stability

Thermogravimetric scans (**Figure 5.1.3)** performed with poly(glc-*alt*-amh) point to a degradation process that involved two well differentiated steps. Previous studies suggested that the first step was mainly associated with the decomposition of glycolide units.[23] The degradation process started at over 300 ºC, had a weight loss close to 45% after the first degradation stage (420 ºC) and left a significant remaining residue at 550 ºC.

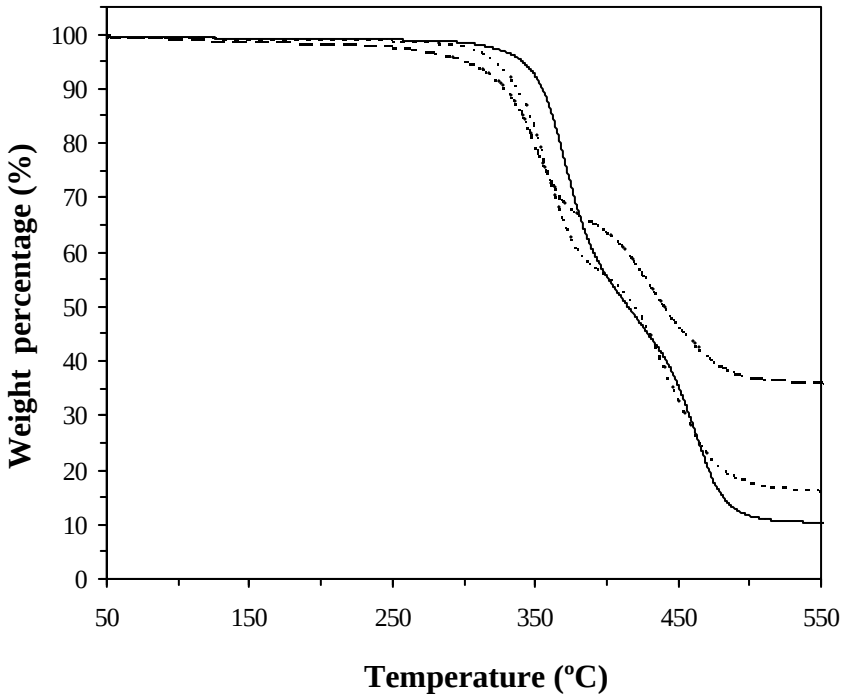

Figure 5.1.3 Thermogravimetric analysis of neat poly(glc-*alt*-amh) (solid line) and its nanocomposite with C25A after (dotted line) and before (dashed line) washing NaCl particles.

Incorporation of C25A slightly decreased the thermal stability of poly(glc-*alt*-amh)), as shown in **Figure 5.1.3**. Thermogravimetric traces indicated a lower onset degradation temperature and that the first decomposition step was attained at a lower temperature (400 ºC). The second decomposition step was slower for the nanocomposite since both samples reached a constant weight percentage at practically the same temperature. This remaining residue was logically greater for the nanocomposite (13% versus to 9%) due to the clay content. The lower onset degradation temperature was probably a consequence of the lower stability of the organo-modifier that was added to match the polarity of the clay surface with that of the monomer and to expand the clay galleries in order to facilitate monomer/polymer penetration. Differences in thermal stability may be also a consequence of the nanoconfinement, which may alter the chemical behaviour of

confined polymer chains, as has recently been proposed.[27] The thermogravimetric trace of the nanocomposite before water washing mainly differed in the increase of the residue percentage, which reached a value close to 40 % due to the inorganic salt content. The temperature at which the first decomposition step finished was found again to be close to 400 ºC, although in this case, it is remarkable the significant decrease in the onset degradation temperature which became close to 150 ºC. Thus, the presence of chlorine anions seems to increase the thermal instability of the system, and consequently special care must be taken with the control of the polymerization reaction temperature in the presence of the organo-modified clay.

- **Melt crystallization of the neat poly(ester amide) and its nanocomposite with C25A**

The spherulite radial growth rates (*G*) of the neat poly(glc-*alt*-amh) sample and its nanocomposite with C25A were determined by means of the evolution of the spherulite radius versus time. Data for a representative crystallization temperature of 130 ºC are plotted in **Figure 5.1.4** a. It is worth pointing out that the linear increase in the spherulite radius indicated that the growth rate was independent of spherulites size and suggested that clay particles may not be excluded during spherulite growth. Exclusion would imply that non crystallizable particles built up on the crystallization growth front and hindered the transport of crystallizable species from the melt to the growing edge. Thus, in this case a deviation from the linear spherulite growth should be observed.[28] Nucleation density was higher for the neat poly(ester amide), as deduced from the number of spherulites measured in the field of view of the optical microscope (400 versus 240 nucleii/mm^2). **Figure 5.1.4** b and c show optical micrographs obtained at the end of the crystallization process. It can be observed that spherulites of the nanocomposite sample became bigger when the impingement was attained due to the decrease in its nucleation density. For the same reason, the induction time of the crystallization process increased in the case of nanocomposite (data not shown).

Dispersed clays clearly influenced the overall crystallization kinetics since both primary nucleation and crystal growth rate led to a deceleration of the crystallization process. Similar observations were reported for nanocomposites of poly(butylene succinate-*co*-adipate) with organically modified synthetic fluorine mica where a practically exfoliated structure was observed.[29] This result contrasts with the increase usually observed in the primary nucleation, especially when the clay shows an intercalated structure.[30]

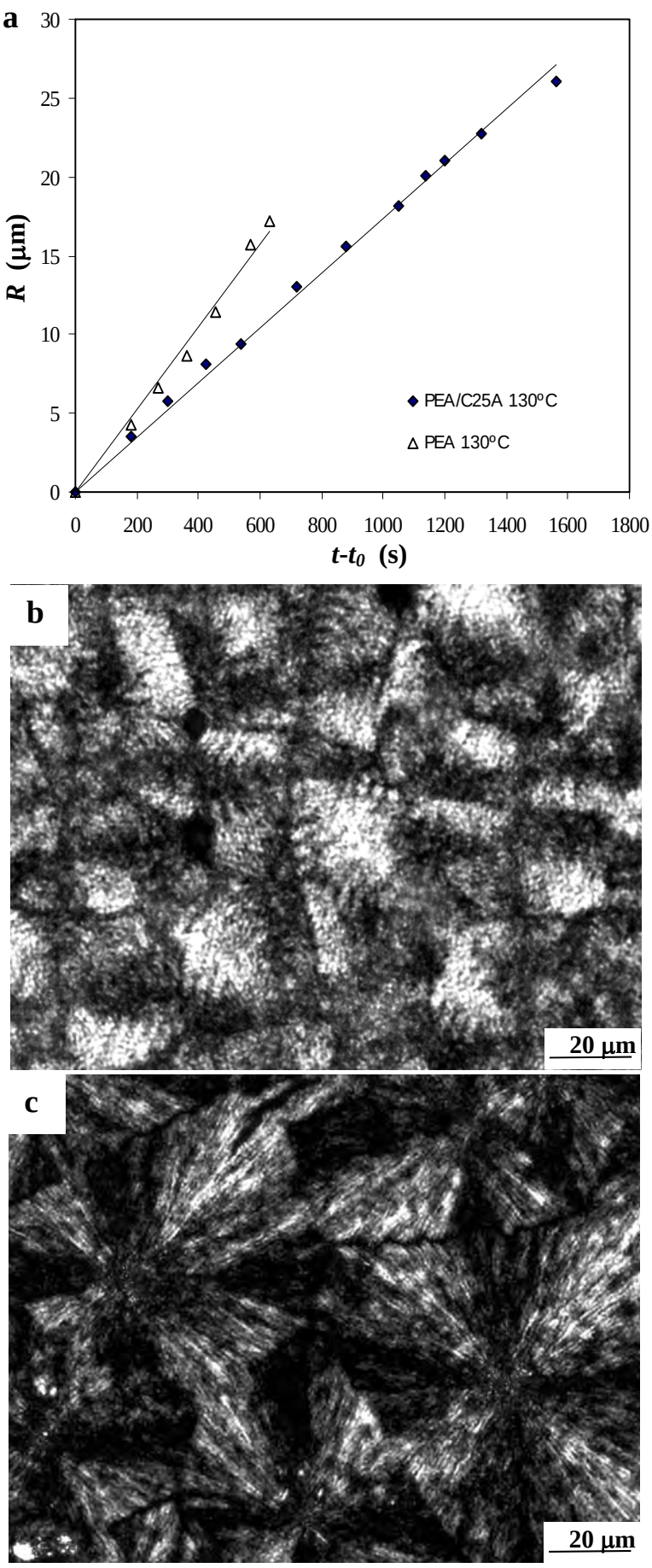

Figure 5.1.4 a) Plot of the radius of spherulites of the neat polymer and its nanocomposite with C25A versus crystallization time for an isothermal crystallization temperature of 130 ºC. b) and c) Polarized optical micrographs showing spherulites of the neat poly(glc-*alt*-amh) sample and its nanocomposite with C25A, respectively. Samples were isothermally crystallized at 130 ºC and then quenched. The nanocomposite sample was previously washed to remove all NaCl crystals formed during polymeri-zation.

Spherulitic textures were also clearly differentiated depending on the presence of clay particles. Thus, ringed spherulites with negative birefringence (**Figure 5.1.4** b) formed in the neat poly(ester amide) at the studied temperature, in agreement with previous works which also reported the development of fibrilar textures at crystallization temperatures close to 140 ºC.[24] Nanocomposite spherulites obtained at 130 ºC also showed negative birefringence and a fibrilar texture (**Figure 5.1.4** c) that was close to that observed in the neat polymer at higher temperatures. Furthermore, the lamellar structure appeared slightly irregular or fragmented due to the random incorporation of clay particles (deep black regions in the micrograph) into the spherulite.

- **Nonisothermal polymerization of the sodium salt of N-chloroacetyl-6-aminohexanoic acid and its nanocomposites**

Thermal analysis of polymerization of the neat monomer and its mixture with the different clays was performed by differential scanning calorimetry (DSC). Heating scans (**Figure 5.1.5**) showed exothermic peaks indicative of the condensation reaction and the formation of the corresponding sodium chloride.

At the 20 ºC min^{-1} heating rate, the condensation reaction of the neat monomer took place at a temperature (159 ºC) that was slightly higher than the melting temperature of the polymer (157 ºC). Hence, the polymer formed during the reaction could not crystallize and a simple exothermic peak was found, as previously reported.[22]

The scans in **Figure 5.1.5** indicate a different thermal behavior when polymerization was performed in the presence of clay particles. In this case, a double exothermic peak could be clearly detected for all mixtures except for that prepared with Closite 20A, where a single broad peak appeared at an intermediate position. It must be pointed out that the relative peak areas changed with the type of clay employed. The new exothermic peak appeared at a higher temperature than that observed for the neat monomer, which seems an indication of a disfavoured polymerization reaction. Clay may influence the polycondensation process since chain mobility should be reduced, and consequently the probability that reactive groups reached a close position would decrease. For all assayed clays, polymerization always seemed to finish at a similar temperature (185 ºC). It is also interesting to note that the intensity of the new exothermic peak was more significant when C25A was used. Note that in this case the nanocomposite is characterized by an intercalated structure with a large stacking distance. Thus, the decrease on the chain mobility may be a consequence of confinement but also by a high degree of interaction with the organoclay. DSC heating scans also showed a small endothermic peak around 100-130 ºC, which may be associated with a polymorphic transition and/or the elimination of adsorbed water molecules.

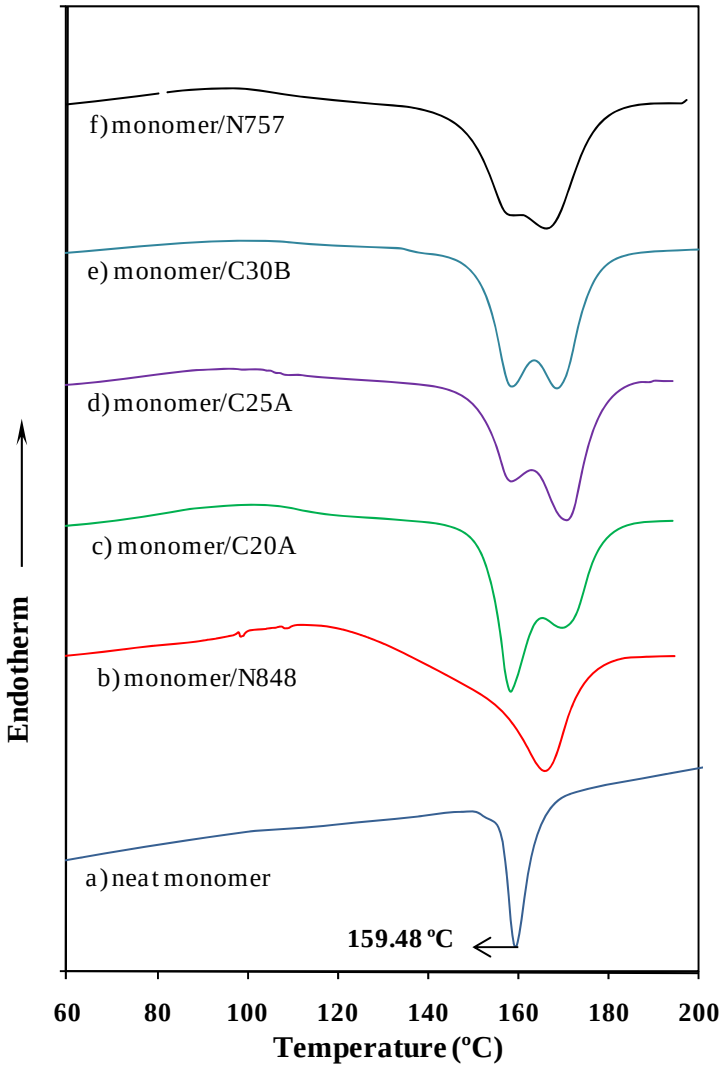

Figure 5.1.5 DSC heating runs performed with the sodium salt of N-chloroacetyl-6-aminohexanoic acid (a) and its mixture with Cloisite 20A (b), Nanofil 848 (c), Cloisite 25A (d), Cloisite 30B (e) and Nanofil 757 (f). The clay content is 3% in all mixtures.

Synchrotron experiments were also performed to gain insight the nonisothermal polymerization process (**Figure 5.1.6** a). These experiments were conducted from room temperature to 200 ºC by heating the monomer/C25A mixture at 20 ºC/min. X-ray profiles clearly showed that all diffraction peaks were shifted to lower angles when temperature was increased, as expected from the thermal expansion of the unit cell. The profiles showed two peaks at 2θ ~ 19 and 22º corresponding to the (100) and (110) reflections of the NaCl structure (~ 0.326 and 0.282 nm, respectively) and different peaks in the 14-17º 2θ range between 14 and 17º corresponding to the monomer structure. The intensity of the NaCl peaks clearly increased with temperature, reaching a saturation level at the end of the heating scan. In fact, polymerization kinetics could be evaluated by the intensity

evolution of the representative NaCl peaks. It is worth pointing out that a very small NaCl peak could be detected even in the initial sample, suggesting the occurrence of some degree of polymerization during storage.

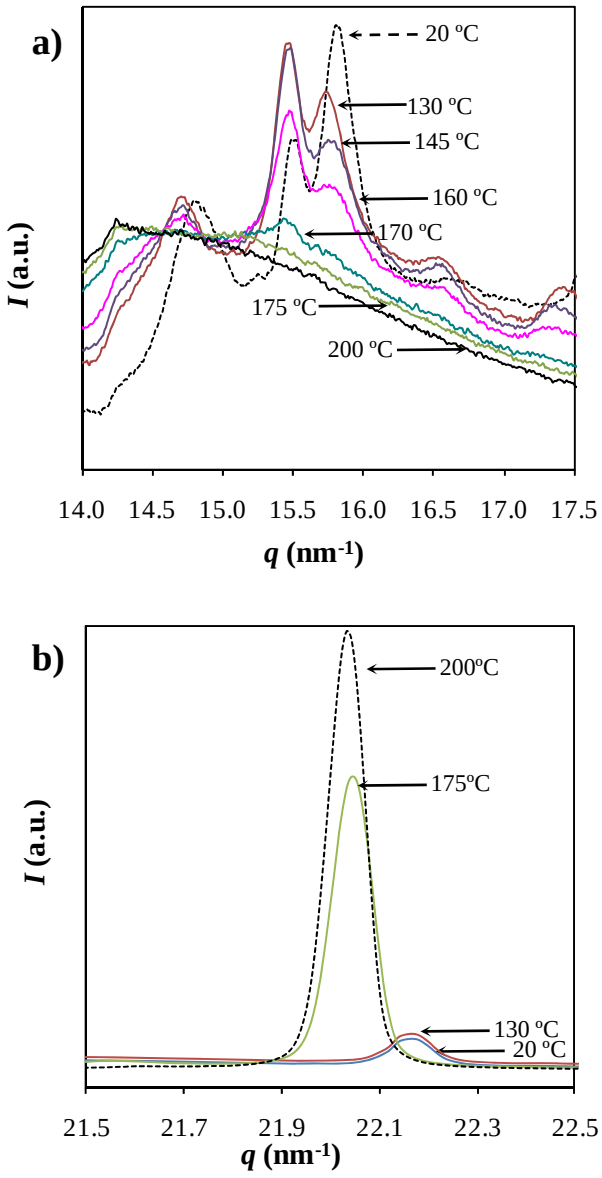

Figure 5.1.6 WAXD profiles taken during the nonisothermal polymerization performed at a heating rate of 20 ºC/min with the monomer / C25A mixture. The area where the characteristic monomer and polymer reflections can be observed is shown in (a), whereas the evolution of the main NaCl reflection is plotted in (b).

Figure 5.1.6 a shows also that a remarkable variation in the intensity profile of the peaks attributed to the monomer took place during the heating step at a temperature between 100-130 ºC, suggesting a change on the crystalline structure that could explain the weak endothermic peak

observed in the DSC heating scans. It should be pointed out that polymerization was not highly significant during this first step since the intensity of NaCl peaks remained practically constant. After this polymorphic transition, the intensity of NaCl peaks started to increase and at the same time the monomer peaks gradually became weaker. Finally, an amorphous halo and small peaks attributed to (*hk*0) reflections of the clay were observed when temperature reached a value close to 190 ºC. It is interesting to note that polymerization finished in an amorphous or liquefied state since at this temperature the intensity of NaCl peaks did not reach the saturation level. No polymer crystallization was observed in the heating scan, in agreement with DSC observations.

X-ray diffraction patterns taken during a subsequent cooling run (**Figure 5.1.7**) revealed that polymerization was successful since the characteristic diffraction peaks of poly(glc-*alt*-amh)[25] appeared progressively. A peak shift towards higher 2θ values was logically detected in this scan due to the thermal contraction of both polymer and NaCl unit cells. Note also that the intensity of NaCl peaks remained constant.

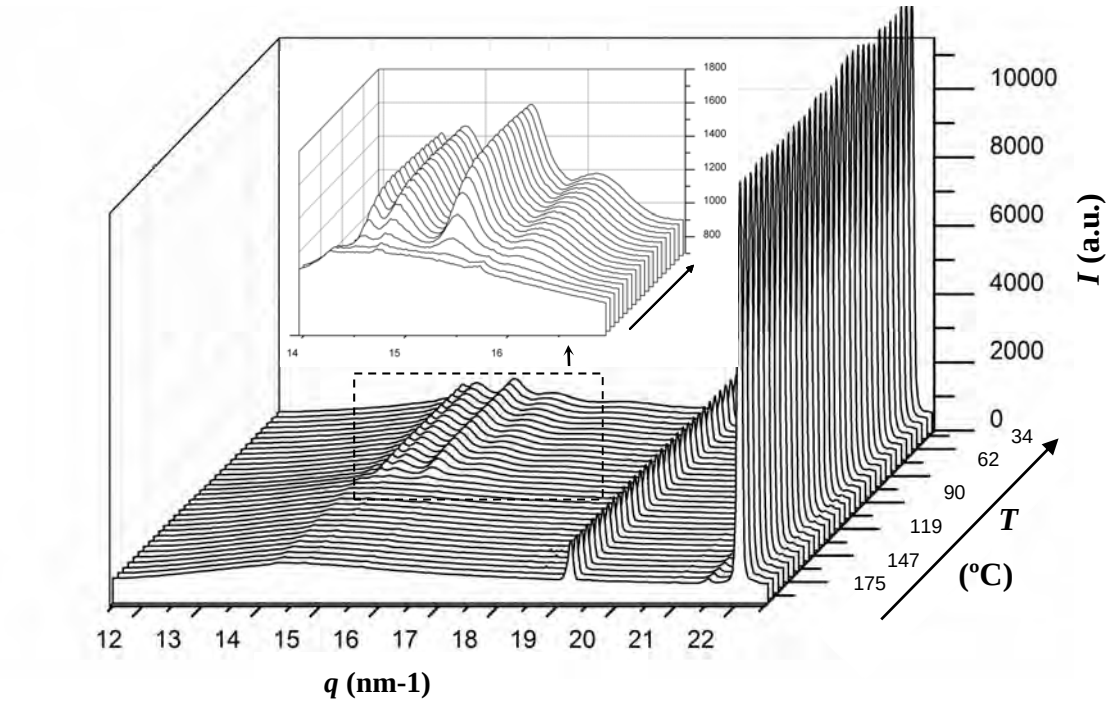

Figure 5.1.7 WAXD profiles taken during the nonisothermal crystallization that occurred during a cooling run performed at 20 ºC/min of a nonisothermally polymerized monomer / C25A mixture at a heating run of 20 ºC/min.

Isothermal polymerization study of the neat monomer and its nanocomposite with C25A.

DSC traces for the isothermal polymerization of the monomer / C25A mixture at different temperatures are shown in **Figure 5.1.8** together with the trace corresponding to neat monomer at a representative temperature, which is included for comparative purposes. In fact, studies on the polymerization of the neat monomer have already been performed and published.[25] The DSC traces indicated a complex polymerization behavior where an exothermic peak was observed at very short reaction times together with a broader one that appeared at higher times. This second peak was clearly temperature dependent since it became broader and shifted to higher times when the polymerization temperature was decreased, whereas the first peak appeared practically at the same reaction time for all the assayed temperatures. This first peak suggests a solid state polycondensation process where the terminal groups in the crystal are close enough to react in a process that is not strongly temperature dependent. On the contrary, the second peak suggests a reaction in an amorphous state where molecular chains must move in order to approach and face up the corresponding reactive groups. Thus, temperature became consequently an essential factor that allows increasing chain mobility. For all assayed temperatures the polymerization process of the neat monomer was faster than for its nanocomposite with C25A, these differences corresponding to the time interval at which the second exotherm appeared.

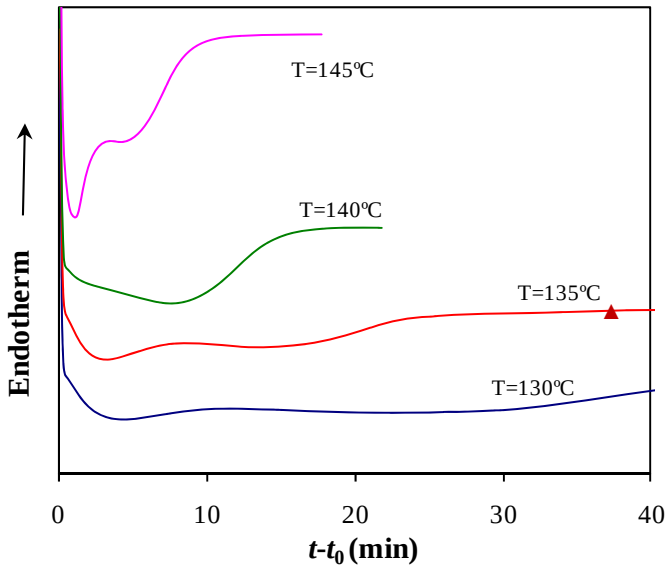

Figure 5.1.8 Isothermal DSC polymerization curves obtained with the monomer / C25A mixture (clay content of 3%) at the indicated temperatures. For comparative purposes, the polymerization DSC curve of the neat monomer at a temperature of 135 ºC is also plotted (▲ red line)

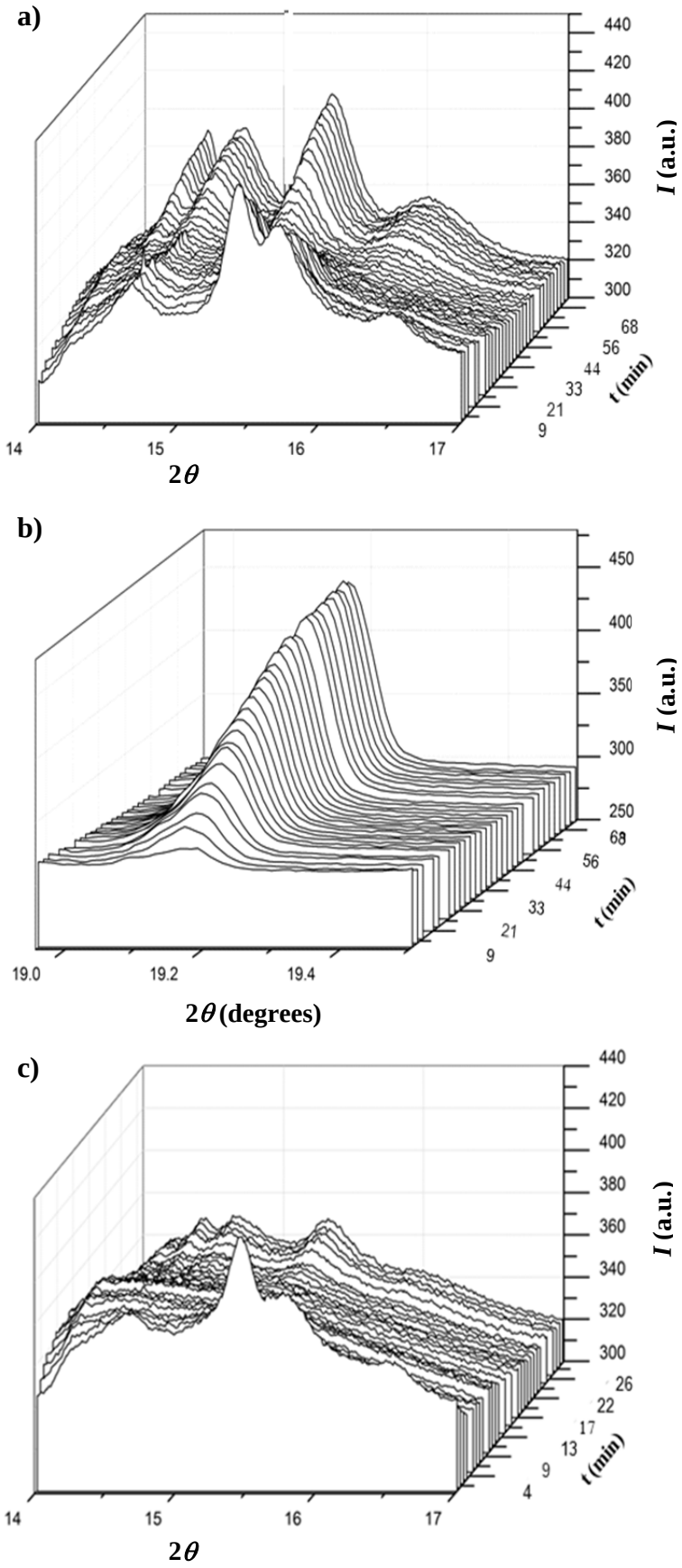

Figure 5.1.9 WAXD profiles taken during the isothermal polymerization of the monomer / C25A mixture performed at 125 (a, b) and 145 ºC (c). The area where the characteristic monomer and polymer reflections can be envisaged is shown in (a) and (c), whereas the evolution of the weak NaCl reflection at 2θ ≈ 19º is shown in (b).

WAXD profiles were also taken during isothermal polymerizations performed at 125 and 145 ºC with the monomer/C25A mixture. **Figure 5.1.9** clearly shows that monomer peaks progressively disappeared whereas, after a certain induction time, the crystallization of the polymer took place. Several features can be indicated:

a) The change in the monomer structure was not noted since it occurred before the high isothermal polymerization temperature (125 or 145 ºC) was reached.
b) Polymerization was not finished when crystallization began, as deduced by comparing the evolution of NaCl peaks and those attributed to the polymer.
c) The time necessary for "melting" as well as the crystallization rate decreased with increasing temperature. On the contrary, the polymerization rate increased. Thus, at 125 ºC the last polymerization stages should occur in a polymer matrix with a significant degree of crystallinity, whereas at 145 ºC the polymer matrix remained mostly in the amorphous state (note the low intensity of polymer reflections due to the slower crystallization rate).
d) The peaks of the monomer, polymer and NaCl were not shifted since the temperature remained constant.

Synchrotron experiments clearly showed that the polymerization and crystallization exothermic processes occurred more o less simultaneously when the reaction was isothermally conducted at the indicated temperatures. This overlapping made it practically unfeasible to undertake a kinetic polymerization analysis considering calorimetric measures. Thus, an approach using infrared spectroscopic data was alternatively chosen.

Figure 5.1.10 a illustrates the change of the infrared spectra at both the beginning and the end of polymerization for a selected reaction temperature. Note that amide bands are present in both monomer and polymer samples but the corresponding wavenumber is logically shifted because of the different crystalline structure and the different molecular interactions. The continuous evolution of the amide I band is shown in **Figure 5.1.10** c as an example. The polymerization process could be followed more easily considering bands coming from specific groups originated by the condensation reaction, such as the C=O absorption band at 1742 cm^{-1}, as can be observed in **Figure 5.1.10** b. Finally, the intensity of specific bands of the monomer decreased significantly during reaction, as in the case of the carboxylate group at 1553 cm^{-1}. However, its overlapping with the amide II band made its use unfeasible for kinetic evaluation purposes.

Absorbance measurements of representative peaks were used to evaluate the relative conversion degree, $\alpha(t)$, for a given reaction time, t. Thus, for a peak that appears during reaction the following equation can be applied:

$$\alpha(t) = [A_t - A_0] / [A_\infty - A_0] \qquad (5.1.1)$$

where A_t is the absorbance measurement at time t, and A_∞ and A_0 are, respectively, the final and initial peak intensities during the isothermal polymerization.

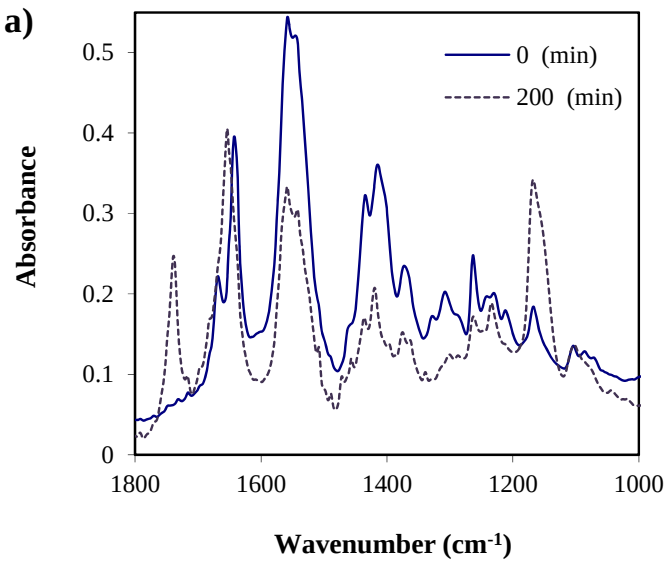

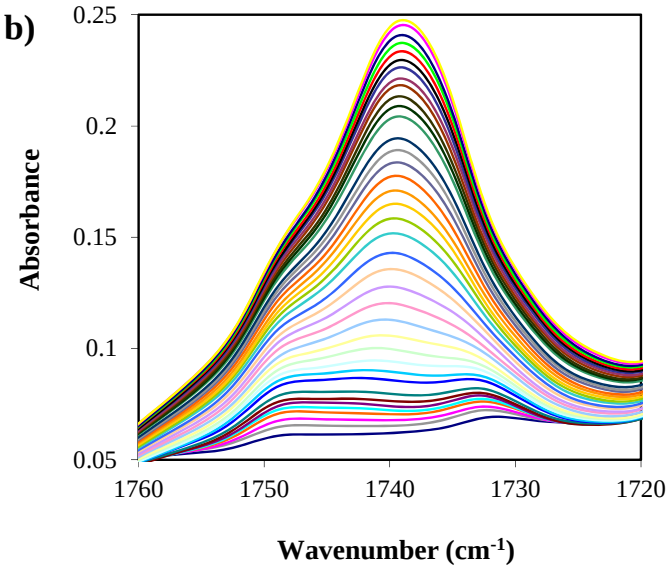

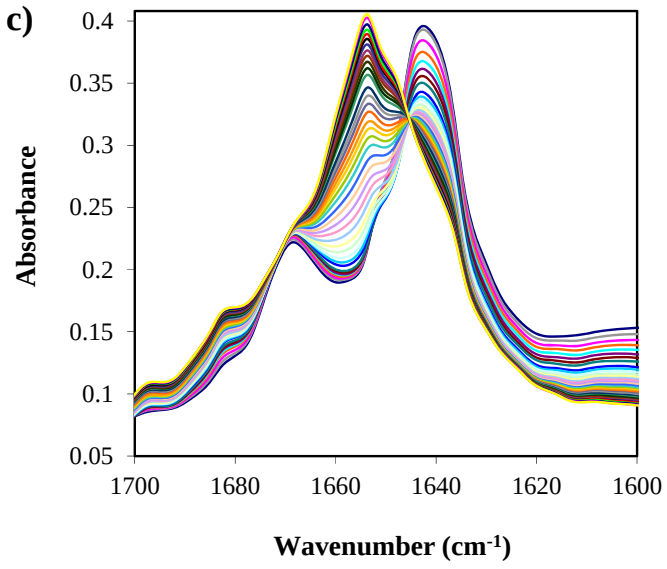

Figure 5.1.10 a) Absorbance FTIR spectra (1800-1000 cm^{-1}) at the beginning and at the end of the polymerization reaction performed at 100 ºC with the monomer / C25A mixture. b) Evolution of the bands associated with the carboxylic ester group (1742 cm^{-1}). c) Evolution of the bands associated with the amide I (1680-1620 cm^{-1})

Figure 5.1.11 illustrates a similar evolution for the bands at 1741 and 1153 cm^{-1}, which are associated with the C=O and C-O bonds of the ester groups formed during polycondensation. In fact, the relative conversion degree reached the maximum value at 140 ºC after 18 minutes of reaction in both cases. It is also clear that the amide I band of the polymer sample (1654 cm^{-1}) evolved with an initial delay, which may indicate that an induction period was required for the initial monomer structure to become the final polymer structure. However, it should also be considered that this absorbance band is difficult to be measured with accuracy due to the two strong close bands and consequently the observed discrepancy bay not be of a fundamental nature.

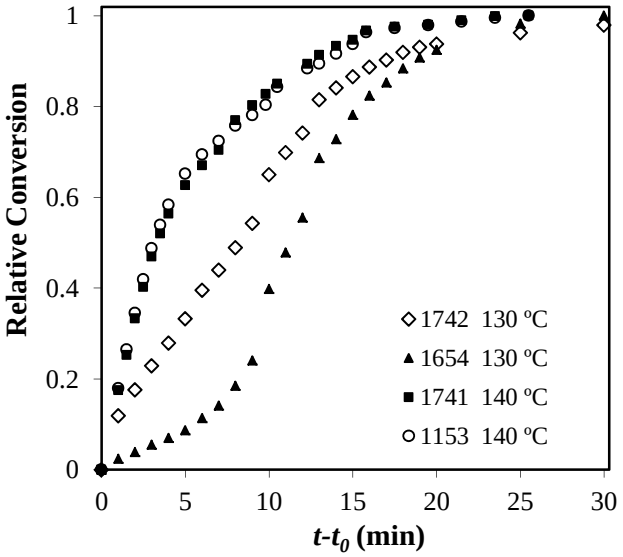

Figure 5.1.11 Plots of conversion versus reaction time for the isothermal polymerization performed with the monomer / C25A mixture at temperatures of 140 and 130 ºC. Conversions were determined by absorbance measures of different IR peaks during the reaction process.

Data plotted at a temperature at which the polymer crystallized completely at the end of reaction (e.g. 130 ºC) show that the maximum degree of conversion was reached after approximately 28 minutes, regardless of using this band or that associated with the appearing C=O ester group.

The 1742 cm^{-1} band was selected to perform a kinetic polymerization analysis since it seemed capable of rendering the most accurate data. For all studied polymerization temperatures, the reaction took place more rapidly for the neat monomer than for the monomer/clay mixture, as shown in **Figure 5.1.12** a, for a representative temperature of 130 ºC, a feature that was in agreement with the DSC calorimetric data. **Figure 5.1.13** plots the relative conversion curves at the studied temperatures of 100, 120, 130 and 140 ºC for the polymerization of the monomer/C25A mixture. The values of the half conversion time ($\tau_{1/2}$) are summarized in **Table 5.1.2** for all experiments. Note that they could be easily estimated from the conversion curves (e.g. those given

in **Figure 5.1.13**), and consequently the assumption of a determined kinetic model was unnecessary.

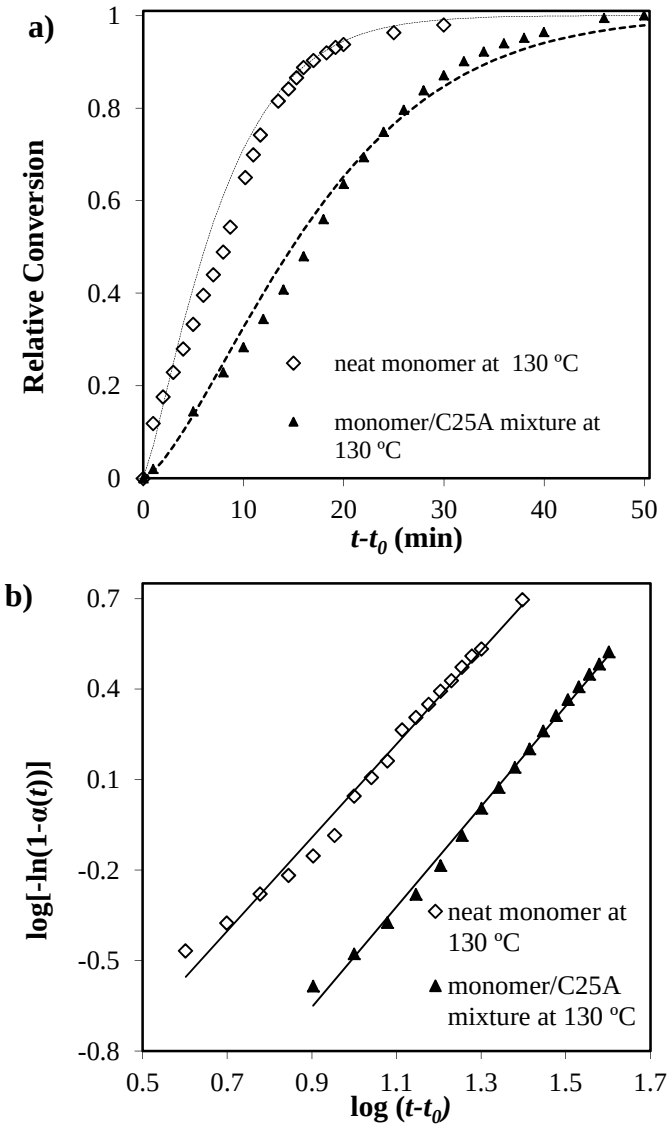

Figure 5.1.12 a) Comparison of the conversion evolution between the neat monomer and the monomer / C25A mixture at the isothermal polymerization temperature of 130 ºC. Only the absorbance of the 1742 cm^{-1} band was considered. b) Avrami plots for the polymerizations carried out with the neat monomer and the monomer / C25A mixture at a representative temperature of 130 ºC

Evolution of the relative conversion degree with reaction time could also be estimated by the measurement of the area of a NaCl reflection observed in the WAXD profiles acquired with synchrotron radiation (i.e. that appearing near 22.5º). Equation 5.1.1 was applied by changing the absorbance values by the corresponding areas. **Figure 5.1.13** also plots the conversion curves deduced from diffraction data for the polymerization of the monomer/clay mixture at 125 and 145 ºC. It is clear that good agreement exists between analyses performed by FTIR and WAXD

methodologies. However, in this case, FTIR has an economic advantage if only a kinetic study must be performed.

Table 5.1.2 Polymerization kinetic parameters deduced from the 1740 cm^{-1} band.

	T (ºC)	$\tau_{1/2}$ (min)	log Z	Z (min^{-n})	n	k (min^{-1})
Neat monomer	100	89.0	-3.30	$5.0 \cdot 10^{-4}$	1.59	0.0084
Neat monomer	120	23.5	-2.13	$7.4 \cdot 10^{-3}$	1.50	0.0380
Neat monomer	130	7.8	-1.12	$7.5 \cdot 10^{-2}$	1.22	0.1196
Neat monomer	140	5.0	-0.64	$2.3 \cdot 10^{-1}$	0.87	0.1847
Monomer/C25A mixture	100	102.9	-3.95	$1.1 \cdot 10^{-4}$	1.80	0.0063
Monomer/C25A mixture	120	27.9	-1.99	$1.0 \cdot 10^{-2}$	1.31	0.0297
Monomer/C25A mixture	130	16.5	-1.82	$1.5 \cdot 10^{-2}$	1.42	0.0519
Monomer/C25A mixture	140	7.0	-0.74	$1.8 \cdot 10^{-2}$	0.93	0.1583

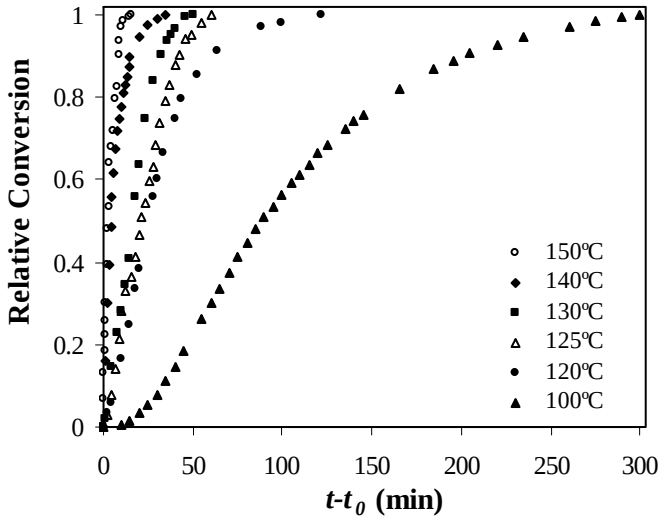

Figure 5.1.13 Relative conversion curves for the monomer / C25A mixture at different temperatures. Data were obtained from FTIR spectra considering the absorbance of the 1742 cm^{-1} band (full symbols) and WAXD profiles considering the intensity associated with the most intense NaCl peak (empty symbols).

Evolution of the relative conversion degree with reaction time could also be estimated by the measurement of the area of a NaCl reflection observed in the WAXD profiles acquired with synchrotron radiation (i.e. that appearing near 22.5º). Equation 5.1.1 was applied by changing the absorbance values by the corresponding areas. **Figure 5.1.13** also plots the conversion curves deduced from diffraction data for the polymerization of the monomer/clay mixture at 125 and 145

ºC. It is clear that good agreement exists between analyses performed by FTIR and WAXD methodologies. However, in this case, FTIR has an economic advantage if only a kinetic study must be performed.

In a first approximation, the Avrami model was considered adequate to analyze the polymerization kinetics since it was previously applied for similar systems.[22,31] Obviously, an accurate analysis requires the determination of the best kinetic model. In this way, conversion was considered to be defined by Equation 5.1.2, where *Z* and *n* are the corresponding Avrami parameters:

$$\alpha(t) = 1 - \exp(-Z\,t^{n}) \qquad (5.1.2)$$

Plots of log [-ln(1- $\alpha(t)$)] versus log (t) at different reaction temperatures always gave straight lines (i.e. those in **Figure 5.1.12** b, where the polymerizations of the neat monomer and its mixture with C25A are compared) which confirm the suitability of the Avrami reaction model. The slopes of these lines correspond to the Avrami exponent, *n*, and their intercepts at the origin to log *Z*. Moreover a kinetic constant (k) with units independent of the Avrami exponent was calculated from $Z^{1/n}$. These parameters are summarized in **Table 5.1.2** for the two studied systems and the four assayed temperatures. As expected, the kinetic constant increased with the polymerization temperature. The given data clearly indicate that the kinetic constant for the polymerization of the neat monomer was higher than the corresponding one for the reaction in the presence of the clay.

The activation energy for the polymerization of the neat monomer and its mixture with C25A was derived by assuming an Arrhenius-type dependence on temperature for the kinetic constant (Equation 5.1.3), where *E*, *A* and *R* are the activation energy, the pre-exponential frequency factor and the universal gas constant, respectively:

$$k = A\exp\left(-\frac{E}{RT}\right) \qquad (5.1.3)$$

Plots of ln *k* versus 1/*T* (**Figure 5.1.14**) allowed activation energies of 101.0 and 99.3 kJ/mol to be deduced for the polymerization of the sodium salt of N-chloroacetyl-6-aminohexanoic acid and its mixture with C25A, respectively. The values of the activation energies were practically identical, and therefore the differences in the kinetic constant value were only a consequence of the frequency factor, which was clearly lower for the nanocomposite, suggesting again more restricted chain mobility when the clay was present.

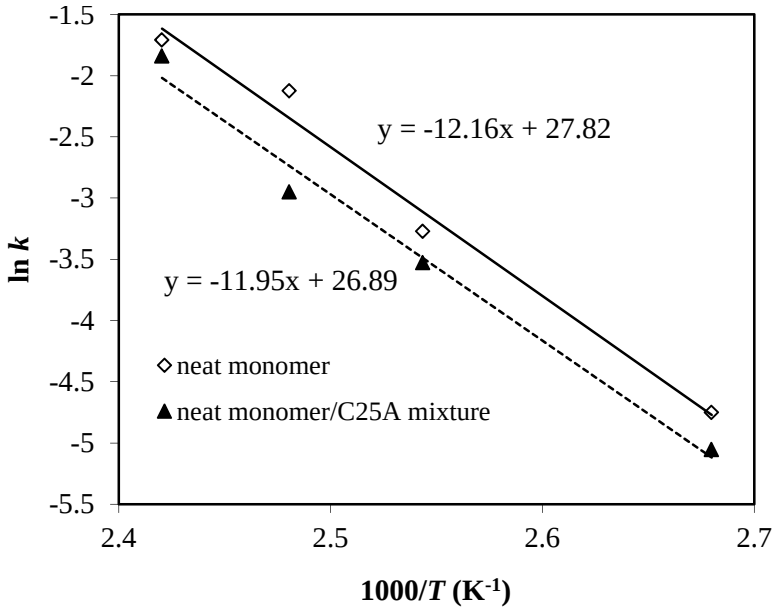

Figure 5.1.14 Plot of ln *k* versus the reciprocal of the polymerization temperature for the neat monomer and the monomer/C25A mixture

5.1.4 Conclusions

C25A organo-modified montmorillonite has proved to be effective for the preparation of nanocomposites of the degradable alternating poly(ester amide) constituted by glycolic acid and 6-aminohexanoic acid units by the in situ polymerization technique. X-ray diffraction patterns indicate that the characteristic interlayer peak of the silicate structure was absent in the nanocomposite, whereas transmission electron micrographs reveal that an intercalated structure with a wide interlayer spacing distribution was obtained. The presence of clay slightly diminished the thermal stability of the polymer, probably due to the presence of the organo-modifier compound. Nevertheless, the melting temperature was clearly lower than the temperature at which decomposition started. Optical microscopy studies revealed that the crystallization rate diminished in the nanocomposite since both nucleation density and crystal growth rate were lower for the nanocomposite sample. This feature has been reported for nanocomposites of materials characterized by an exfoliated structure.

Polymerization kinetics was strongly influenced by the presence of organo-modified montmorillonites under both nonisothermal and isothermal conditions. Furthermore, the reaction process was rather complicated when polymerization temperatures lower than 145 ºC were selected. In this case polymer crystallization occurred before the polymerization reaction was finished. WAXD profiles revealed changes in the monomer structure and the range where the reaction proceeded in a liquefied state. Polymerization kinetics was evaluated by both FTIR and WAXD experiments following the time evolution of the 1742 cm^{-1} absorption band of the ester

groups or the diffraction intensity of the (110) NaCl reflection, respectively. The temperature dependence of the polymerization kinetic constant allowed inferring that kinetic differences between the polymerization of the neat monomer and its mixture with C25A could be attributed to the pre-exponential frequency factor. In this way, clay particles seemed to reduce chain mobility and the frequency at which reactive groups were close enough to facilitate the condensation reaction.

5.1.5 References

[1] Burnside, S. D.; Giannelis, E. P. Chem Mater 1995, 7, 1597.
[2] Gonsalves, K.; Chen, X. In Materials Research Soc. Symposium Proceedings; Materials Research Society: Warrendale, PA, 1996; Vol. 435, p 55.
[3] Kawasumi, M. J Polym Sci Part A: Polym Chem 2004, 42, 819.
[4] Kojima, Y.; Usuki, A.; Kawasumi, M.; Okada, A.; Fukushima, Y.; Kurauchi, T.; Kamigaito, O. J Mater Res 1993, 8, 1185.
[5] Usuki, A.; Kawasumi, M.; Kojima, Y.; Okada, A.; Kurauchi, T.; Kamigaito, O. J Mater Res 1993, 8, 1174.
[6] Usuki, A.; Kojima, Y.; Kawasumi, M.; Okada, A.; Fukuhima, Y.; Kurauchi, T.; Kamigaito, O. J Mater Res 1993, 8, 1179.
[7] Kojima, Y.; Usuki, A.; Kawasumi, M.; Okada, A.; Kurauchi, T.; Kamigaito, O. Mater Life 1993, 5, 13.
[8] Ishida, H.; Campbell, S.; Blackwell, J. Chem Mater 2000, 12, 1260.
[9] Akelah, A.; Salahuddin, N.; Hiltner, A.; Baer, E.; Moet, A. Nanostructured Mater 1994, 4, 965.
[10] Wang, D.; Zhu, J.; Yao, Q.; Wilkie, C. A. Chem Mater 2002, 14, 3837.
[11] LeBaron, P. C.; Wang, Z.; Pinnavaia, T. J Appl Clay Sci 1999, 12, 11.
[12] Akelah, A.; Moet, A. J Mater Sci 1996, 31, 3589.
[13] Messersmith, P. B.; Giannelis, E. P. Chem Mater 1993, 5, 1064.
[14] Fukushima, Y.; Okada, A.; Kawasumi, M.; Kurauchi, T.; Kamigaito, O. Clay Miner 1988, 23, 27.
[15] Bouma, K.; Gorrot, G. M. M.; Feijen, J.; Gaymans, R. J. Polymer 2000, 41, 2727.
[16] Katsarava, R.; Beridze, V.; Arabuli, N.; Kharadze, D.; Chu, C. C.; Won, C. Y. J Polym Sci Part A: Polym Chem 1999, 37, 391.
[17] Tuominen, J.; Sépala, J. V. Macromolecules 2000, 33, 3530.
[18] Vera, M.; Rodríguez-Galán, A.; Puiggalí, J. Macromol Rapid Común 2004, 25, 812.
[19] Epple, M.; Kirschnick, H. Chem Ber 1996, 129, 1123.
[20] Herzberg, O.; Epple, M. Eur J Inor Chem 2001, 1395.
[21] Bezwada, R. S.; Jamiolkowski, D. D.; Lee, I. Y.; Agarwal, V.; Persivale, J.; Trenka-Bethin, S.; Erneta, M.; Suryadevara, J.; Yang, A.; Liu, S., Biomaterials 1995, 16, 1141.
[22] Vera, M.; Franco, L.; Puiggalí, J. Macromol Chem Phys 2004, 205, 1782.
[23] Botines, E.; Franco, L.; Puiggalí, J. J Appl Polym Sci 2006, 102, 5545.
[24] Botines, E.; Puiggalí, J. Eur Polym J 2006, 42, 1595.
[25] Botines, E.; Casas, M. T.; Puiggalí, J. J Polym Sci Part B: Polym Phys 2007, 45, 815.
[26] Sinha Ray, S.; Yamada, Y.; Okamoto, A.; Ogami, A.; Ueda, K. Chem Mater 2003, 15, 1456.
[27] Chen, K.; Wilkie, C. A.; Vyazovkin, S. J Phys Chem 2007, 111, 12685.
[28] Krikorian, V.; Pochan, D. J. Macromolecules 2004, 37, 6480.
[29] Sinha Ray, S.; Bousmina, M. Macromol Chem Phys 2006, 207, 1207.
[30] Jog, J. P. Mater Sci Technol 2006, 22, 797.
[31] Rodríguez-Galan, A.; Vera, M.; Jiménez, K.; Franco, L.; Puiggalí, J. Macromol. Chem. Phys. 2003, 204, 2078.

5.2

Poly (ester amide) nanocomposites by in situ polymerization: kinetic studies on polycondensation and crystallization

Preparation of nanocomposites by in situ polymerization of sodium chloroacetylaminohexanoate in the presence of cloisite 20A (C20A) or cloisite 30B (C30B) organo-modified montmorillonites was studied. Both clays rendered an intercalated structure that contrasts with the exfoliated structure previously found with the use of the C25A montmorillonite. Polymerization under non-isothermal and isothermal conditions was evaluated by Wide Angle X-ray Diffraction (WAXD) synchrotron radiation and Fourier Transform Infrared Spectroscopy (FTIR) experiments. Results indicate that C20A and C30B had a similar influence on the polymerization kinetics. Thus, the activation energy and the Arrhenius preexponential factor decreased compared to those calculated for the neat monomer. Clear differences were also found when using the C25A clay since, in this case, polymerization had similar activation energy to that determined for the neat monomer. The crystallization kinetics of the intercalated C20A and C30B nanocomposites was studied by FTIR and optical microscopy. The incorporation of clay particles increased the overall rate kinetic constant due to the enhancement of the primary nucleation. On the contrary, the spherulitic growth rate was slightly disfavored by the clay.

5.2.1 Introduction

The preparation of new polymer nanocomposites is a promising topic since material properties can be enhanced and their range of applications extended by using molecular or nanoscale reinforcements rather than conventional fillers [1-5]. Since the first works performed with nylon 6 [6,7], several polymer based systems and preparation methodologies such as melt-mixing, solution intercalation and in situ polymerization have been developed. Results clearly demonstrate that properties of the neat polymer like water-absorption rate, thermal-expansion coefficients, Young modulus, thermal stability and gas barrier effect can be improved by the incorporation of a small amount of clay, and also that the crystallization kinetics can be affected.

Layered silicate particles are especially interesting for nanocomposite preparation as they may be dispersed into individual layers with a thickness close to 1 nm to tune surface interactions with the polymer/monomer through exchange reactions with organic and inorganic cations [8]. The final structure of the composite depends on the extent to which the organic matrix and inorganic clay components are made compatible [9], and varies from an intercalated to a fully exfoliated nanostructure, which has an obvious impact on the final properties. Despite extensive research, the influence of nanocomposite structure on nucleation and crystal growth rate is not entirely clear in view of the conflicting results reported in some cases [10-14].

Aliphatic poly(ester amide)s constitute a promising family of materials since the presence of hydrolyzable ester groups may enhance degradability, and the establishment of intermolecular hydrogen bonding interactions between amide groups may provide suitable thermal and mechanical properties for most applications [15-19]. Furthermore, several monomers and synthetic routes have been developed to obtain materials with variable composition and chemical microstructure, which can consequently meet numerous requirements. The alternating poly(ester amide) derived from glycolic acid and 6-aminohexanoic acid (poly(glc-*alt*-amh)) has recently received attention for two main reasons: a) The simple synthesis procedure based on only two reaction steps (**Figure 5.2.1** a) and b) A composition based on the main units of biodegradable polyesters (glycolic acid) and aliphatic polyamides (6-aminohexanoic acid).

Poly(glc-alt-amh)) is obtained by a thermal polycondensation reaction based on the formation of a metal halide salt as the driving force of the condensation reaction [20,21], which seems an appropriate procedure to prepare nanocomposites by in situ polymerization. This is a highly attractive technique due to its versatility and compatibility with various reactive monomers, making it a valuable process for commercial applications [22,23]. Several examples in the literature concern the preparation of polystyrene [24], polycaprolactone [25] and nylon 6 [26] nanocomposites.

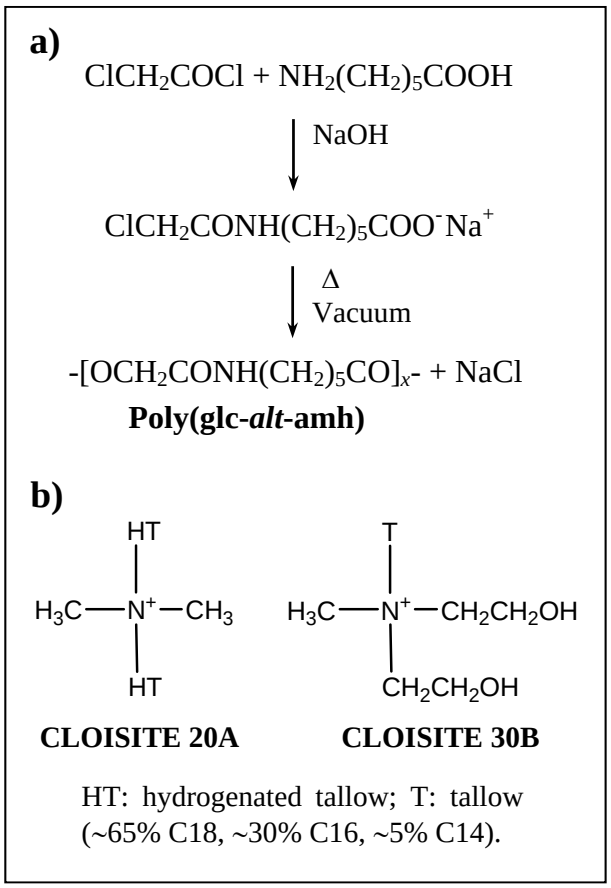

Figure 5.2.1 a) Synthesis scheme for the poly(ester amide) studied in this work. b) Chemical structure of Cloisites 20A and 30B.

The in situ polymerization technique was effective and rendered practically exfoliated nanocomposites of poly(glc-*alt*-amh) and the Cloisite 25A (C25A) organo-modified montmorillonite [27]. Typical calorimetric techniques were not suitable for proper evaluation of the polymerization kinetics at temperatures lower than 145 ºC due to the overlapping of the exothermic polymerization peak with an endothermic peak associated with polymer crystallization. Thus, Fourier Transform Infrared Spectroscopy (FTIR) was a basic tool to compare and study the influence of clay particles on the polymerization kinetics. Nanocomposites prepared by the above in situ polymerization and the melt mixing technique gave rise to two different structures (i.e. exfoliated and intercalated) that clearly influenced the crystallization kinetics [27,28]. The main purpose of the present work is to determine the effect of montmorillonites based on two different surfactants (Cloisite C30B and Cloisite C20A) on in situ polymerization and to study the crystallization kinetics of the derived nanocomposites. The polymerization kinetics is evaluated through real-time synchrotron and FTIR experiments whereas the crystallization kinetics is studied through FTIR to obtain the overall crystallization rate and optical microscopy measurements to determine the nucleation and crystal growth rates.

5.2.2 Experimental section

Materials

The monomer, sodium chloroacetylaminohexanoate, was synthesized following a previously reported method [20,21]. All reagents and solvents were purchased from Aldrich Chemical Company, (Milwaukee, WI, USA) and used as received. Polymerization was based on a thermal polycondensation which rendered sodium chloride as a byproduct **(Figure 5.2.1**a) [20,21].

The nanocomposites were based on two organomodified layered phyllosilicates: methyl tallow bis(2-hydroxyethyl) ammonium montmorillonite (Cloisite 30B, Southern Clay Products, MT2EH Gonzales, Texas, USA) and dimethyl dihydrogenated-tallow ammonium montmorillonite (Cloisite 20A, Southern Clay Products, 2MH2HT. Gonzales, Texas, USA). The chemical structure of the employed montmorillonite surfactants is shown in **Figure 5.2.1** b.

Preparation of nanocomposites

For both nanocomposite preparations, 10 mg of monomer was dissolved in 10 mL of water, and separately, the appropriate clay was dispersed in water (< 0.1 wt %). The monomer solution and clay dispersion were stirred for two hours, and then mixed and liophilizated. The ratio of the solution and dispersion was conveniently adjusted to obtain a clay content of 3 wt% in the final solid. Polymerization was carried out by heating the monomer/clay mixture to 160 ºC. A white solid was recovered and extensively washed with water, methanol and acetone. For comparison purposes, polymerization without organoclay was also performed and the final sample purified as above.

No significant differences were found between the molecular weights of the neat poly(ester amide) and the two prepared nanocomposites. Thus, average Molecular weight (M_w) and Number Average Molecular Weight (M_n) molecular weights were always in the 14,000-17,000 and 37,000-43,000 ranges, respectively, according to Gel Permeation Chromatography (GPC) measurements using 1,1,1,3,3,3-hexafluoroisopropanol as the solvent and poly(methyl methacrylate) standards.

Measurements

Interlayer spacing of the clay was studied by wide angle X-ray diffraction (WAXD) using a Siemens D-500 diffractometer (Karlsruher, Germany) with Cu K_α radiation (λ = 0.1542 nm).

The structure and distribution of Cloisite were observed with a Philips TECNAI 10 (FEI/Philips Electron Optics, Eindhoven, Netherlands) transmission electron microscope (TEM) at an accelerating voltage of 100 kV. TEM specimens were prepared by embedding in a low viscosity modified Spurr epoxy resin and curing at 40°C for a few days and then at 60 °C for 6 h. Ultrathin sections (less than 100 nm) were cut at room temperature using a Sorvall Porter-Blum microtome equipped with a diamond knife. Finally, the sections were collected in a trough filled with water

and lifted onto carbon coated copper grids. In order to prevent diffusion of the epoxy resin into the polymer film, a thin layer of carbon was evaporated over the film surface.

The spherulitic growth rate was determined by optical microscopy using a Zeiss Axioskop 40 Pol light polarizing microscope equipped with a Linkam temperature control system configured by a THMS 600 heating and freezing stage connected to a Liquid Nitrogen Pump (LNP) 94 cooling system. Spherulites were grown from homogeneous melt-crystallized thin films produced by melting 1 mg of the polymer mixture on microscope slides. Next, small sections of these films were pressed or smeared between two cover slides and inserted in the hot stage. The thicknesses of the squeezed samples were close to 10 μm in all cases. Samples were kept at 170 ºC (more than 10 ºC above the polymer melting point of 157 ºC) for 5 minutes to wipe out sample history effects, and then quickly cooled to the selected crystallization temperature. The radius of the growing spherulites was monitored during crystallization by taking micrographs with a Zeiss AxiosCam MRC5 digital camera at appropriate time intervals. A first-order red tint plate was employed to determine the sign of spherulite birefringence under crossed polarizers.

Time-resolved WAXD experiments were carried out at the Collaborating Research Group (CRG) beamline (BM16) of the European Synchrotron Radiation Facility of Grenoble. The beam was monochromatized to a wavelength of 0.098 nm. Monomer/clay samples were confined between Kapton films and then held in a Linkam hot stage with temperature control within 0.1 ºC. WAXD profiles were acquired during polymerization and crystallization experiments in time frames of 12 s. The WAXD detector was calibrated with diffractions of a standard of an alumina (Al_2O_3) sample. The diffraction profiles were normalized to the beam intensity and corrected considering the empty sample background. Deconvolution of WAXD peaks was performed with the PeakFit v4 program by Jandel Scientific Software using a mathematical function known as “Gaussian area”.

Infrared absorption spectra were recorded with a Fourier Transform FTIR 4100 Jasco spectrometer Jasco International Co. Ltd. (Tokyo, Japan) in the 4000-600 cm^{-1} range. A Specac model MKII Golden Gate attenuated total reflection (ATR) with a heated Diamond ATR Top-Plate which can be used up to 200 ºC, and a Series 4000 High Stability Temperature Controller were also utilized.

5.2.3 Results and discussion

- **Dispersion structure of C20A and C30B clays in the poly(glc-*alt*-amh) composites**

C20A and C30B organomodified clays were easily mixed with the sodium salt of *N*-chloroacetyl-6-aminohexanoic acid before performing thermal polycondensation at a temperature close to 160 ºC. The final nanostructures were analyzed by X-ray diffraction and transmission electron microscopy. Evidence of intercalation of polymer chains into the silicate galleries can be obtained from diffraction patterns in the range of 2θ = 1-10º, when the characteristic silicate diffraction peaks appear at larger spacings than neat clay ones. Similarly, the absence of these peaks may

suggest an exfoliated structure. Direct TEM morphological observation is always advisable to corroborate diffraction data although TEM images show a local distribution that also depends on how the sample was previously cut.

Direct observation of the morphology and phase distribution of ultrathin sections of poly(glc-*alt*-amh)/C20A specimens by transmission electron microscopy clearly showed that an intercalated structure was predominant (**Figure 5.2.2** a). X-ray diffraction profiles of the nanocomposite sample also revealed the existence of a low angle reflection associated with the stacking of silicate layers. The measured spacing was close to 3.58 nm, a higher value than that observed in the profile of C20A clay (2.52 nm). Thus, polymer chains in the nanocomposite sample were intercalated in the galleries of the dispersed clay and increased the interlayer spacing.

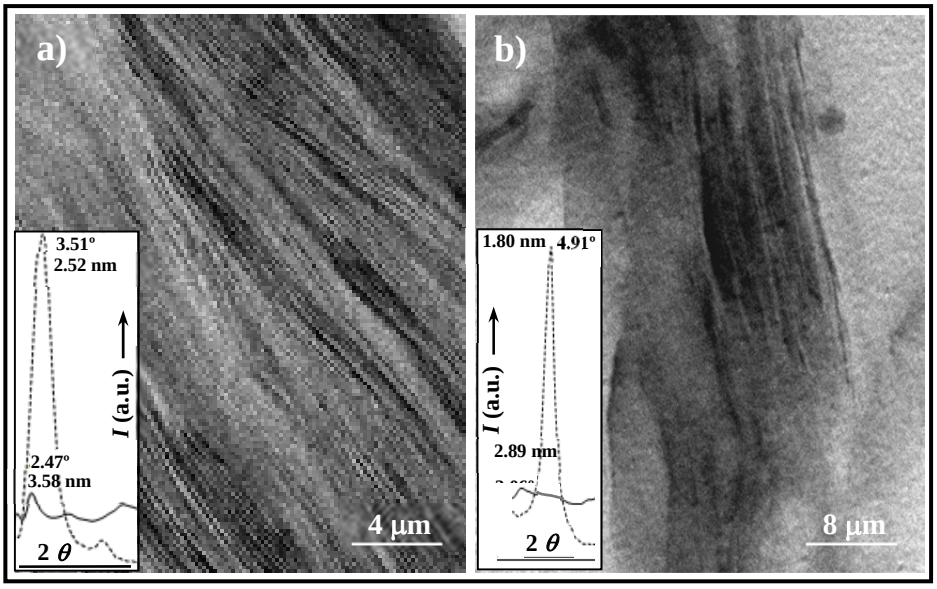

Figure 5.2.2 Transmission electron micrographs showing the morphology of the poly(glc-*alt*-amh)/C20A (a) and poly(glc-*alt*-amh)/C30B nanocomposites with a Cloisite concentration of 3%. Inset shows the diffraction peak associated with the interlayer spacing observed in the pure organomodified clay (solid line) and the corresponding nanocomposite sample (dashed line).

The poly(glc-*alt*-amh)/C30B nanocomposite showed that the 001 peak was significantly reduced and also shifted to a larger spacing (from 1.80 nm to 2.89 nm). Interactions between the carbonyl groups of the monomer and the two hydroxyl groups of the modified montmorillonite may be established, thus favouring a certain ratio of an exfoliated structure after polymerization. This feature is however only supported by the great decrease of the silicate reflection and a certain loose of the layer stacking order as shown in the electron micrograph of **Figure 5.2.2** b. Despite the final structure could be considered intercalated, a less regular layer disposition than poly(glc-*alt*-amh)/C20A samples was found.

- **Non-isothermal polymerization of the sodium salt of N-chloroacetyl-6-aminohexanoic acid with C20A and C30B organomodified clays**

Synchrotron experiments were performed to compare the non-isothermal polymerizations of the monomer mixtures with each of the considered clays. The diffraction profiles initially showed the characteristic Bragg reflections of the monomer, which were most intense at values of the scattering vector, $q = [4\pi/\lambda] \sin(\theta)$, in the 14-17 nm^{-1} range (**Figure 5.2.3**). At a temperature close to 130 ºC the monomer underwent a structural change, as evidenced by the variation in intensities and spacings of the main reflections (**Figure 5.2.4**). Note that the intensities of reflections close to 15.4 nm^{-1} and 15.7 nm^{-1} increased and slightly decreased, respectively. The intensity increase is relevant since the occurrence of polycondensation reactions should lead to the destruction of the monomer crystal structure, and consequently to a gradual disappearance of all corresponding reflections.

At temperatures higher than 150 ºC, the X-ray diffraction profiles showed the appearance of two peaks at $q \sim 19$ and 22 nm^{-1} of gradually increasing intensity (**Figure 5.2.3**). These, which could be indexed as the (100) and (110) reflections of the NaCl structure (~ 0.326 and 0.282 nm, respectively), demonstrated the occurrence of the polycondensation reaction. Note that a delay between polymerization and formation of the inorganic salt crystal may occur since ions must move towards the growing crystal.

The evolution of NaCl peak intensities is useful to follow the polymerization process and even to demonstrate that polycondensation started in the solid state. It is worth pointing out that reflections related to the monomer structure were still visible when NaCl peaks developed. Logically these reflections became weaker when NaCl peaks started to increase and disappeared completely before these peaks reached maximum intensity. Diffraction profiles clearly revealed that the polymer was not able to crystallize under the assayed non-isothermal conditions since some of its characteristic reflections [29] were not detected. The polymer structure is defined by an orthorhombic unit cell having $a = 0.477$ nm, $b = 0.873$ nm and $c = 1.057$ nm and the corresponding diffraction pattern is characterized by strong Bragg reflections in the 14.4-16.2 nm^{-1} range. Specifically, the (020), (101), (110) and (111) reflections that appeared at 0.437, 0.435, 0.418 and 0.389 nm. At high temperature (190-200 ºC) only an amorphous halo, the NaCl reflections and even small peaks attributed to (*hk*0) reflections of the clay were observed.

Figure 5.2.5 plots the area of the (100) NaCl peak versus temperature for the two studied polymerizations. A similar evolution was observed but, remarkably, some differences were detected, indicating that clay type has some influence on the polymerization kinetics. Specifically, the polymerization induction time was shorter when C20A clay was employed (i.e. the peak started to develop at temperatures of 110 and 140 ºC for C20A and C30B, respectively) whereas the

reaction proceeded more rapidly when C30B was used (i.e. the peak developed in the 140-193 ºC and 110-196 ºC ranges for C20A and C30B, respectively).

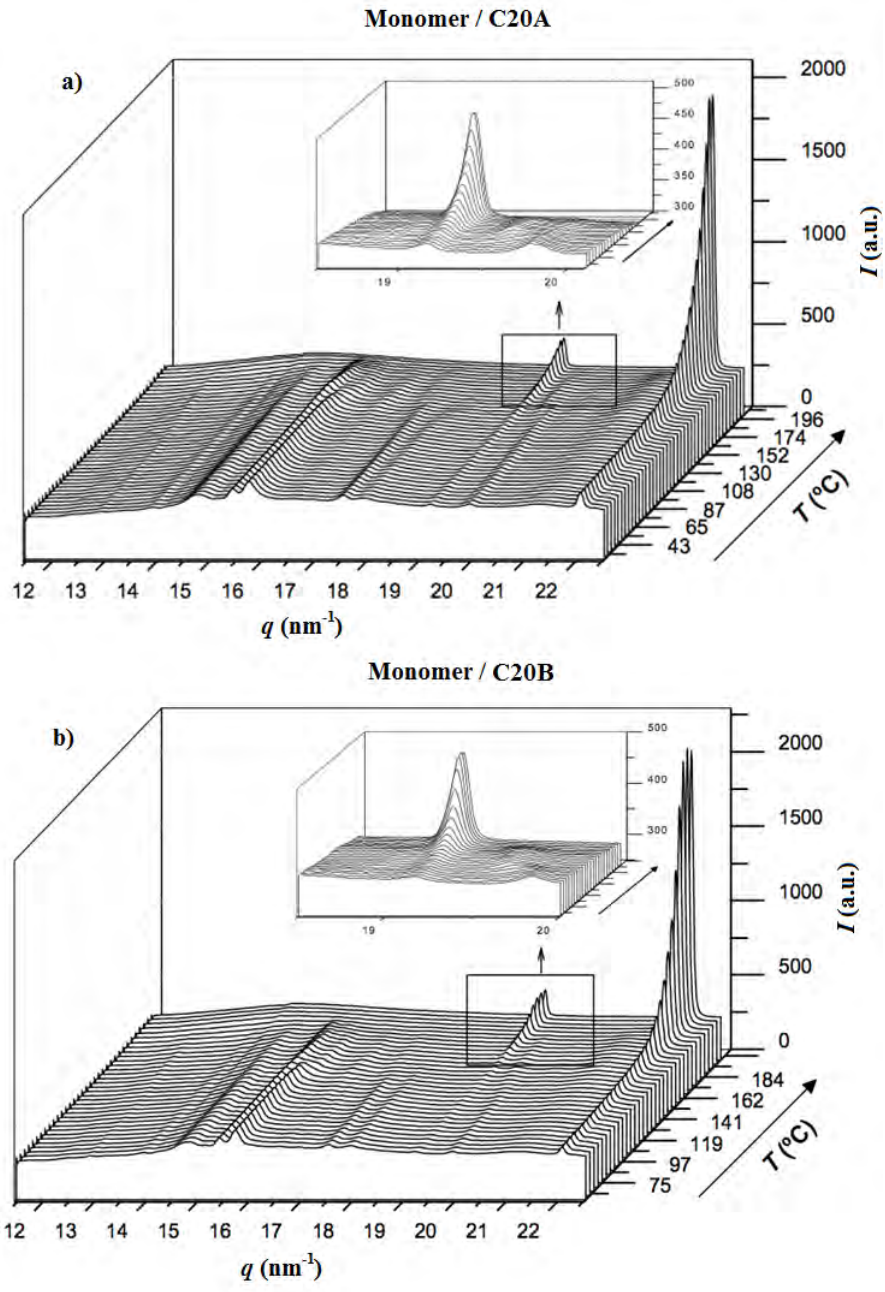

Figure 5.2.3 WAXD profiles taken during the non-isothermal polymerization performed at a heating rate of 20 ºC/min with the monomer / C20A mixture (b) and the monomer / C30B mixture (b). Insets show the evolution of the weak (100) NaCl reflection.

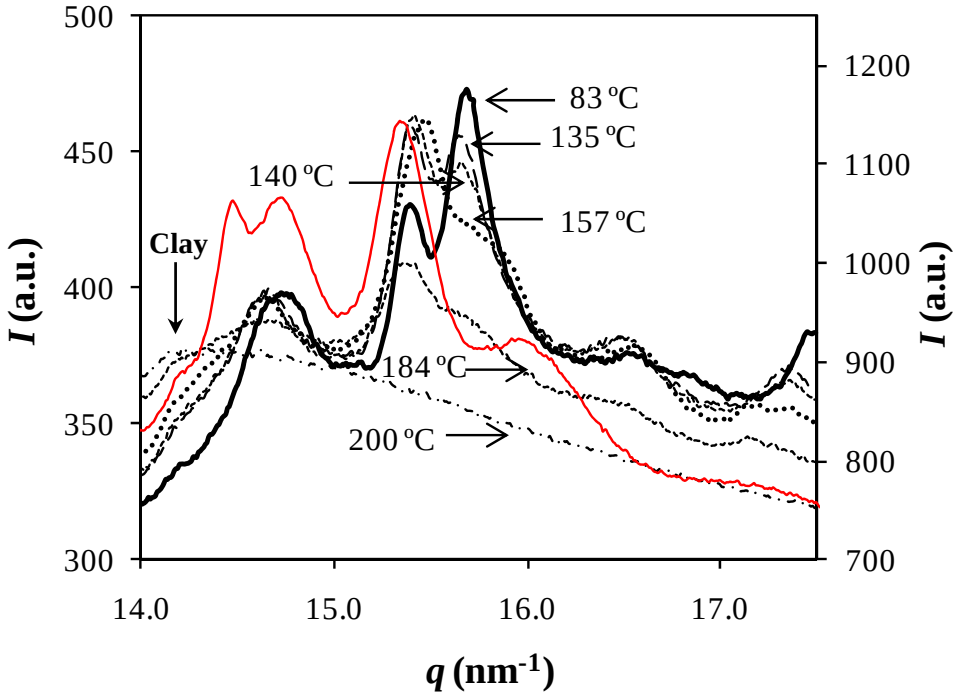

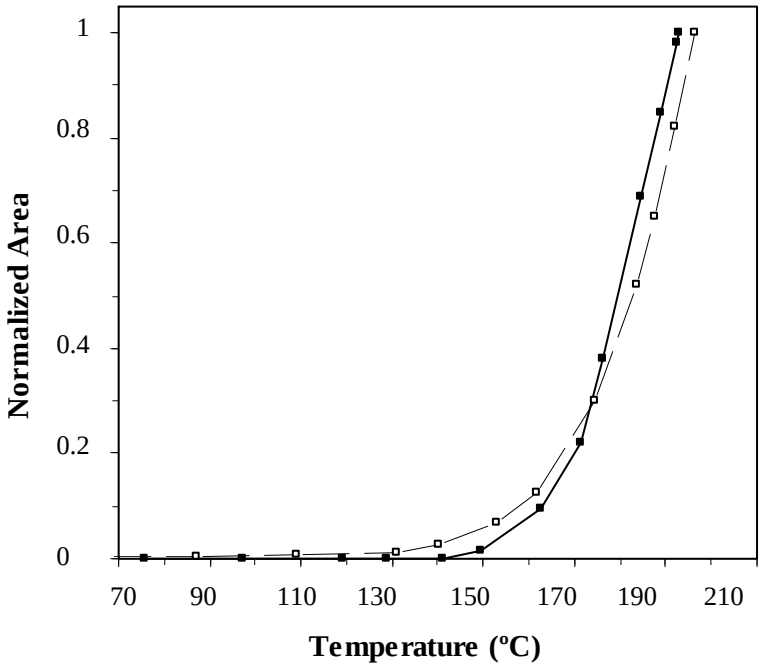

Figure 5.2.5 Intensity evolution of the (100) Bragg reflections of the NaCl structure (~ 0.326 nm) during non-isothermal polymerization (20 ºC/min) of the monomer / C20A (□) and monomer / C30B (■) mixtures.

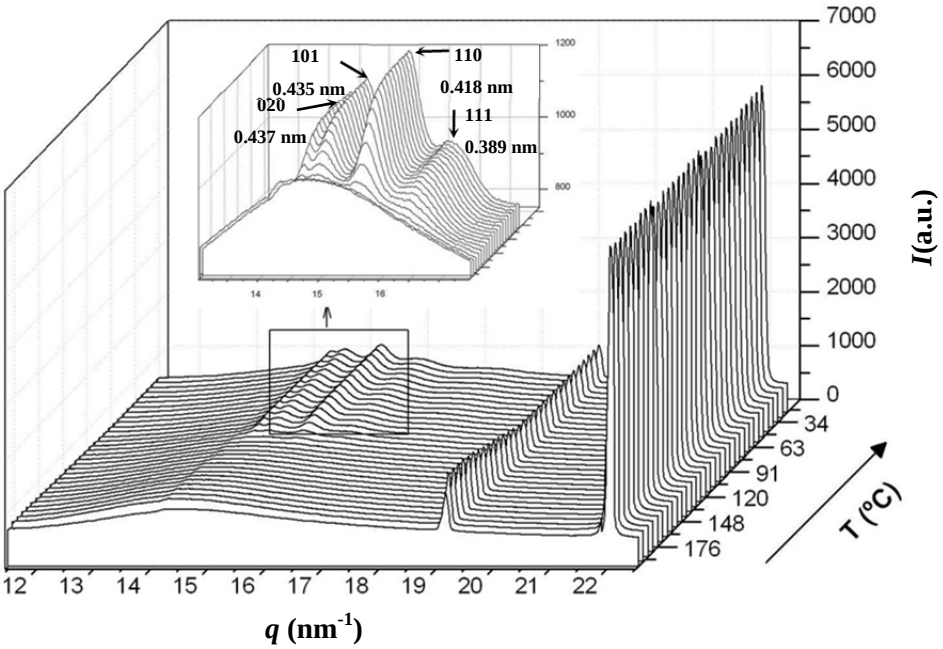

Figure 5.2.6 WAXD profiles taken during the non-isothermal crystallization performed at a cooling rate of 20 ºC/min and after non-isothermal polymerization of the momomer/C20A mixture at a heating rate of 20 ºC/min. Insets show a magnification of the Bragg reflections corresponding to the poly(glc-*alt*-amh) structure.

X-ray diffraction patterns taken during a subsequent cooling run (e.g. **Figure 5.2.6**) revealed that polymerizations were successful since the mentioned characteristic diffraction peaks of poly(glc-*alt*-amh) [29] appeared and progressively increased in intensity. Logically, the intensity of NaCl peaks remained constant during the cooling run.

- **Isothermal kinetic analysis of in situ polymerization of C20A and C30B clay mixtures with *N*-chloroacetyl-6-aminohexanoic acid**

The occurrence of the above monomer polymorphic transition and polymer crystallization should have endothermic/exothermic effects that make it impossible to evaluate the isothermal polymerization kinetics by DSC experiments. Note that these should only measure the exothermic enthalpy associated with the polycondensation reaction, which, in the studied case, is not possible due to the overlapping with the above processes. Thus, FTIR spectroscopy seems an ideal alternative technique given that the polymerization rate can be determined from the absorbance evolution of the new bonds that are formed.

The main changes in the FTIR spectra occurring during polymerization correspond to the appearance of a C=O absorption band at 1742 cm^{-1}, which is associated with the ester bond formed during polycondensation and a change in the wavenumber of the amide I absorption band (**Figure 5.2.7**). The latter should be found in both monomer and polymer samples but the different intermolecular hydrogen bond interactions should lead to a variation in the peak position and corresponding intensity.

Absorbance measurements of the above peaks during isothermal polymerizations were used (Equation 5.2.1) to evaluate the relative conversion degree, $\alpha(t)$, for a given reaction time, t:

$$\alpha(t) = [A_t - A_0] / [A_\infty - A_0] \qquad (5.2.1)$$

where A_t is the absorbance at time t, and A_∞ and A_0 are, respectively, the final and initial absorbances.

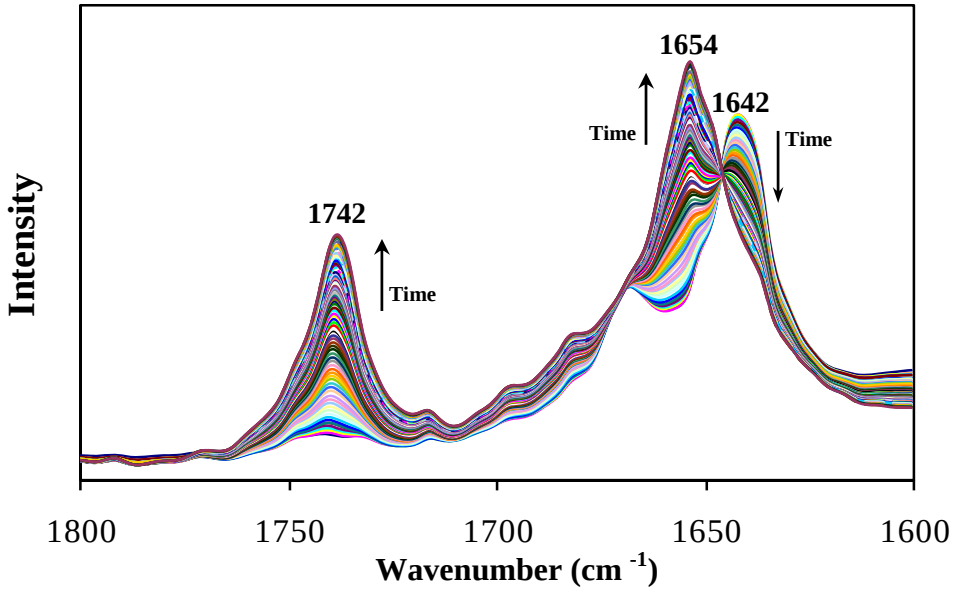

Figure 5.2.7 Absorbance FTIR spectra showing the evolution of the bands associated with the carboxylic ester group (1742 cm^{-1}) and amide I (1680-1620 cm^{-1}) during isothermal polymerizations of the momomer/C30B mixture at 110 ºC.

Figure 5.2.8 a compares the time evolution of the bands at 1742 and 1654 cm^{-1} for polymerizations carried out at different temperatures and in the presence of the C20A clay. For a given clay the evolution of the two bands is quite similar although slight differences were found when polymerization was performed at higher temperatures (i.e. at higher polymerization rates). As will be explained, the addition of clay particles and even their nature had an influence on the polymerization kinetics.

The 1742 cm^{-1} band was selected to perform a polymerization kinetic analysis since it seemed capable of rendering the most accurate data since it is not overlapped with other bands. The Avrami model was considered to examine the polymerization kinetics as it was previously applied for in situ polymerization using C25A clay and other similar systems [21,27,30]. This is a rough approximation that makes unnecessary a detailed study of the kinetic model but can provide useful values for comparison purposes. Conversion was then calculated by equation 5.2.2:

$$\alpha(t) = 1 - \exp(-Z\,(t-t_0)^n) \qquad (5.2.2)$$

where Z and n are the corresponding Avrami parameters and t_0 the time at which polymerization starts.

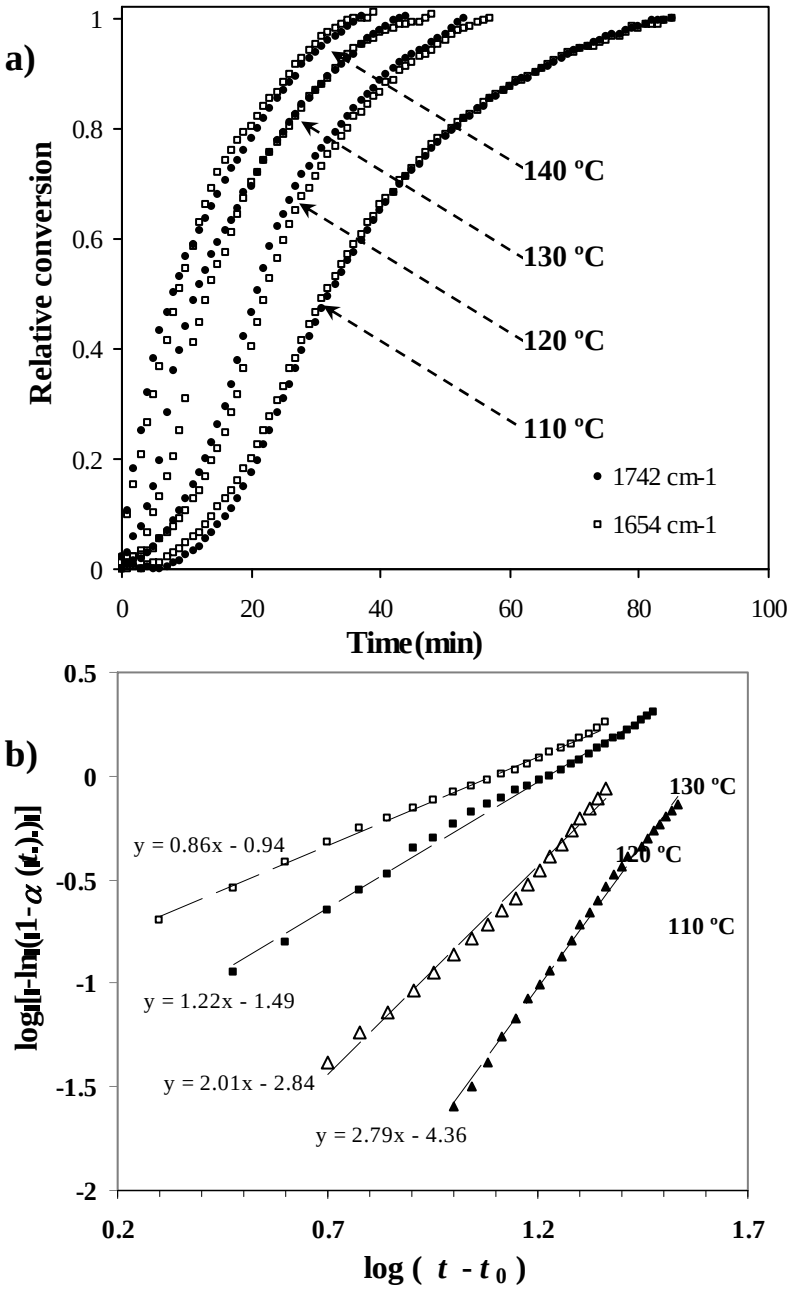

Figure 5.2.8 a) Plots of conversion versus reaction time for the isothermal polymerization of the momomer/C20A mixture at 140, 130, 120 and 110 ºC. Conversions were determined by absorbance measurements of 1742 and 1654 cm^{-1} FTIR peaks during the reaction process. b) Avrami plots for the polymerizations of the momomer/C20A mixture at the indicated temperatures.

Table 5.2.1 Polymerization kinetic parameters deduced from FTIR absorbance measurements of the 1742 cm^{-1} band.

	T (ºC)	$1/\tau_{1/2}$ (min^{-1})	Z (min^{-n})	n	k(min^{-1})
Monomer/C20A mixture	110	0.033	$4.00\ 10^{-5}$	2.79	0.027
Monomer/C20A mixture	120	0.049	$1.43\ 10^{-3}$	2.01	0.038
Monomer/C20A mixture	130	0.087	$3.20\ 10^{-2}$	1.22	0.060
Monomer/C20A mixture	140	0.120	$1.11\ 10^{-1}$	0.86	0.081
Monomer/C30B mixture	110	0.033	$3.89\ 10^{-3}$	1.51	0.025
Monomer/C30B mixture	120	0.050	$3.18\ 10^{-3}$	1.76	0.038
Monomer/C30B mixture	130	0.083	$3.89\ 10^{-3}$	1.98	0.060
Monomer/C30B mixture	140	0.134	$7.19\ 10^{-2}$	1.14	0.098
Monomer/C25A mixture[a]	100	0.010	$1.12\ 10^{-4}$	1.80	0.006
Monomer/C25A mixture[a]	120	0.036	$1.02\ 10^{-2}$	1.31	0.030
Monomer/C25A mixture[a]	130	0.060	$1.51\ 10^{-2}$	1.42	0.052
Monomer/C25A mixture[a]	140	0.142	$1.82\ 10^{-1}$	0.93	0.158
Neat monomer[a]	100	0.011	$5.01\ 10^{-4}$	1.59	0.008
Neat monomer[a]	120	0.042	$7.41\ 10^{-3}$	1.50	0.038
Neat monomer[a]	130	0.128	$7.58\ 10^{-2}$	1.22	0.120
Neat monomer[a]	140	0.200	2.2910^{-1}	0.87	0.185

[a] Data from reference [27]

Plots of log [-ln(1- $\alpha(t)$)] versus log (t) at different reaction temperatures gave straight lines with slopes corresponding to the Avrami exponent, n, and their intercepts at the origin to log Z (e.g. **Figure 5.2.8** b for polymerizations carried out with C20A). Moreover, a kinetic constant (k) with units independent of the Avrami exponent was calculated from $Z^{1/n}$. These parameters are summarized in **Table 5.2.1** for the two studied systems and the four assayed temperatures, together with the reciprocal of half conversion times ($\tau_{1/2}$). Note that these times could be easily estimated from the conversion curves, and consequently without assuming a specific kinetic model. As expected, the kinetic constant increased with the polymerization temperature and evolved similarly to the reciprocal of the half polymerization time, $1/\tau_{1/2}$, as shown in **Figure 5.2.9** a for the polymerization with C20A. This good agreement is relevant since the Avrami analysis results are corroborated by direct experimental measurements such as half polymerization times.

For comparative purposes, **Table 5.2.1** also includes previous data on the polymerization of the neat monomer and its mixture with C25A (3 wt%) [27]. It is clear that the overall rate kinetic

constant of these two samples increased drastically with increasing temperature whereas a moderate change was observed for polymerizations carried out with C20A and C30B. In this way, the neat monomer had a lower and higher polymerization rate than the C20A and C30B mixtures at 110 and 140 ºC, respectively. The influence of temperature on the conversion degree is shown in **Figure 5.2.9** b, where simulated curves from Avrami parameters are plotted for all samples at the intermediate temperatures of 130 and 120 ºC. It is worth pointing out that the neat monomer has the fastest conversion at 130 ºC but its polymerization rate becomes comparable with that found for the C20A and C30B mixtures when the temperature decreased to 120 ºC. Comparison data clearly demonstrated that clay particles influenced the polymerization rate and that the effect of clays that rendered a predominant intercalated structure (C20A and C30B) and C25A clay, which gave rise to an exfoliated structure, was different.

The polymerization activation energies of the mixtures between the neat monomer and C20A and C30B clays were derived by assuming an Arrhenius-type temperature dependence of the kinetic constant (Equation 5.2.3), where *E*, *A* and *R* are the activation energy, the preexponential frequency factor and the universal gas constant, respectively:

$$k = A\exp\left(-\frac{E}{RT}\right) \qquad (5.2.3)$$

Plots of ln *k* versus 1/*T* (**Figure 5.2.10**) allowed activation energies of 49.4 and 59.8 kJ/mol to be deduced for in situ polymerization of C20A and C30B mixtures, respectively. These energies were practically identical, but differed significantly from the value previously deduced for the neat monomer (101.0 kJ/mol) and even for its C25A mixture (99.3 kJ/mol), which gave rise to an exfoliated structure [27]. In this way, the activation energy clearly decreased when in situ polymerization rendered an intercalated structure. The preexponential frequency factor was also lower for the nanocomposites than for the neat monomer (3.28 1012 min-1), indicating that chain mobility was restricted by the incorporation of clay particles. Both C20A and C30B clays led to frequency factors of a similar magnitude order (1.4 105 min-1 and 3.4 106 min-1, respectively), but significantly lower than that found for the C25A mixture (4.77 10^{11} min^{-1}).

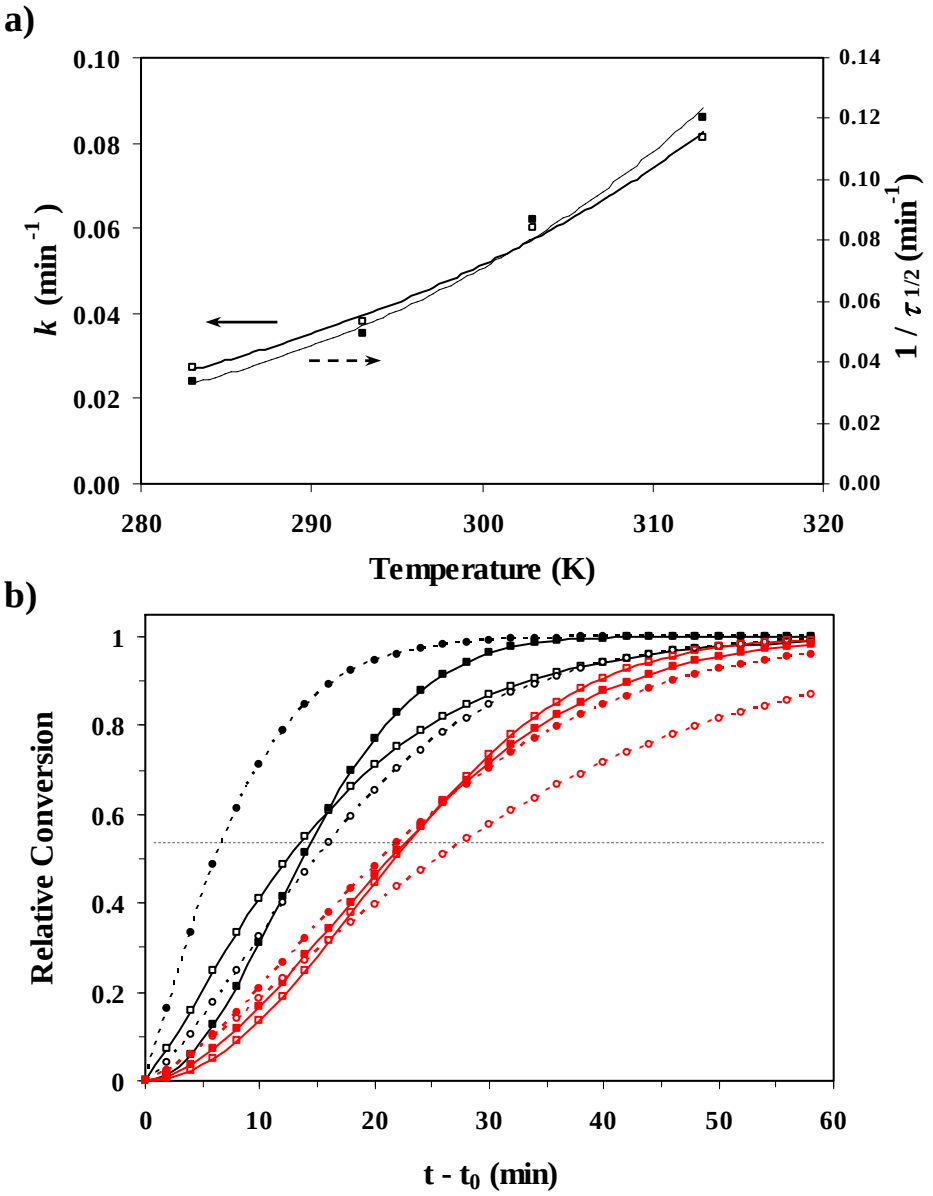

The polymerization kinetics of monomer/C20A and monomer/C30B mixtures was enhanced at low temperatures due to their low activation energy, which compensated for the decrease caused by their low frequency factor. On the contrary, this factor was determinant at high temperatures, where the corresponding overall rate kinetic constants became minima. The changes observed in the

activation energy and frequency factor may suggest that nanoconfinement in the intercalated structure favored the polycondensation reaction and reduced molecular mobility.

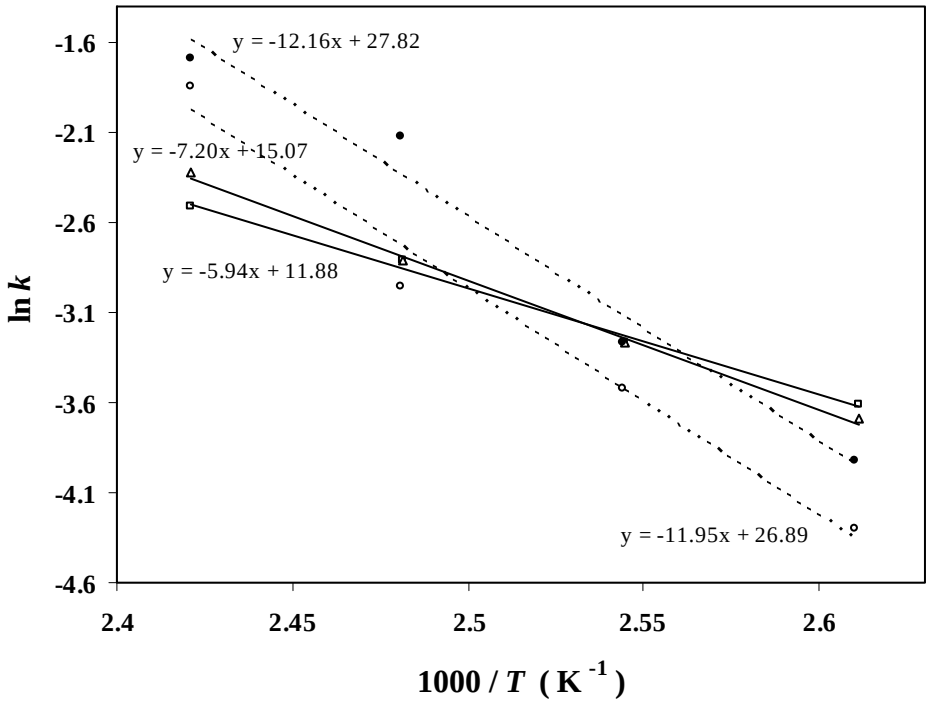

Figure 5.2.10 . Plots of ln*k* versus the reciprocal of the polymerization temperature for the neat monomer (•, dashed line)[27] and monomer/C25A (○, dashed line),[27] momomer/C20A (□, solid line) and monomer/C30B (Δ, solid line) mixtures.

Isothermal crystallization kinetics of poly(glc-*alt*-amh) and its C20A and C30B nanocomposites from FTIR analyses

FTIR is highly sensitive to molecular conformation and packing density, hence its usefulness in polymer crystallization studies. Characteristic bands can be correlated to the crystalline and amorphous phases of the bulk and typically remain distinguishable over the course of crystallization. Isothermal studies are preferred to avoid shape and intensity susceptibility of FTIR bands with temperature.

FTIR spectra of poly(glc-*alt*-amh) showed that 3298, 1653, 1419 and 1166 cm^{-1} bands were characteristic of the crystalline phase. Thus, these bands appeared and their absorbance gradually increased during the isothermal crystallization of samples rapidly cooled to the selected temperature from the melt (amorphous) state.

The continuous evolution of these absorption bands is shown in **Figure 5.2.11** a for the C20A nanocomposite at a representative crystallization temperature of 135 ºC. The time evolution of the relative degree of crystallization, $\chi(t)$, was evaluated similarly to that of the degree of conversion (i.e. changing $\alpha(t)$ by $\chi(t)$ in equations 5.2.1 and 5.2.2). **Figure 5.2.11** b shows that the four

selected bands exhibit a similar behavior for a given crystallization temperature. Thus, in all cases the maximum crystallinity change was detected at a similar time. However, absorbance measurements seemed more accurate when the signal corresponding to the Amide A (3298 cm^{-1}) was considered. The establishment of stronger hydrogen bond interactions in the crystalline structure gave rise to a well defined band which, in addition, was not overlapped by other peaks.

Figure 5.2.12 compares the evolution of the degree of crystallinity at different temperatures for the C30B nanocomposite, as well as the evolution of the neat polymer and its C30B and C20A nanocomposites at a representative temperature (135 ºC). Note that the crystallization rate is clearly slower for the neat polymer

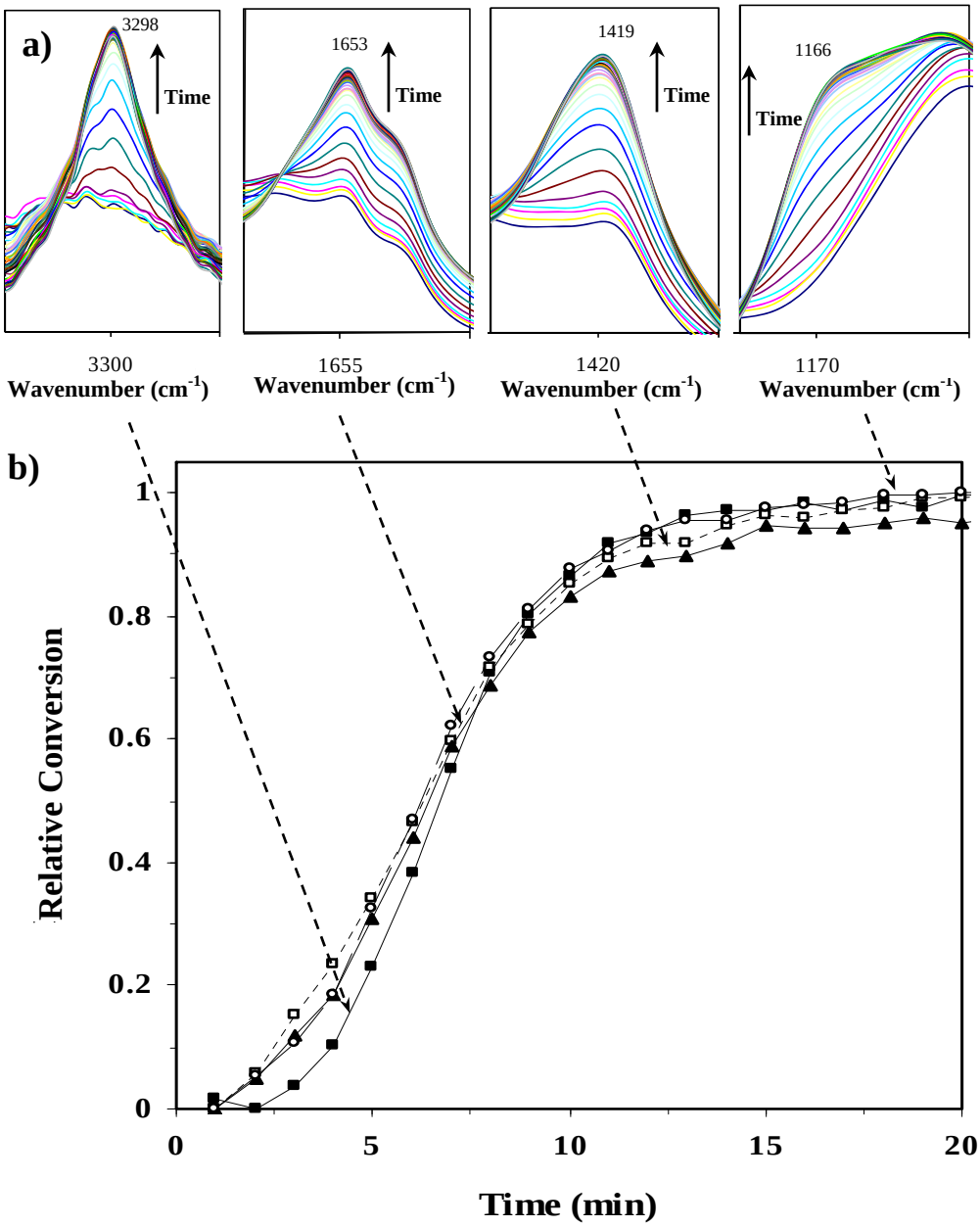

Figure 5.2.11 . a) Changes in the infrared absorption bands at 3298, 1653, 1419 and 1166 cm^{-1} of the poly(glc-*alt*-amh)/C20A nanocomposite during isothermal crystallization at 135ºC. b) Time evolution of the relative crystallinity determined from absorbance measurements of the 3298 (■), 1653 (▲), 1419 (□) and 1166 (○) cm^{-1} FTIR bands of the poly(glc-*alt*-amh)/C30B nanocomposite during isothermal crystallization at 135 ºC.

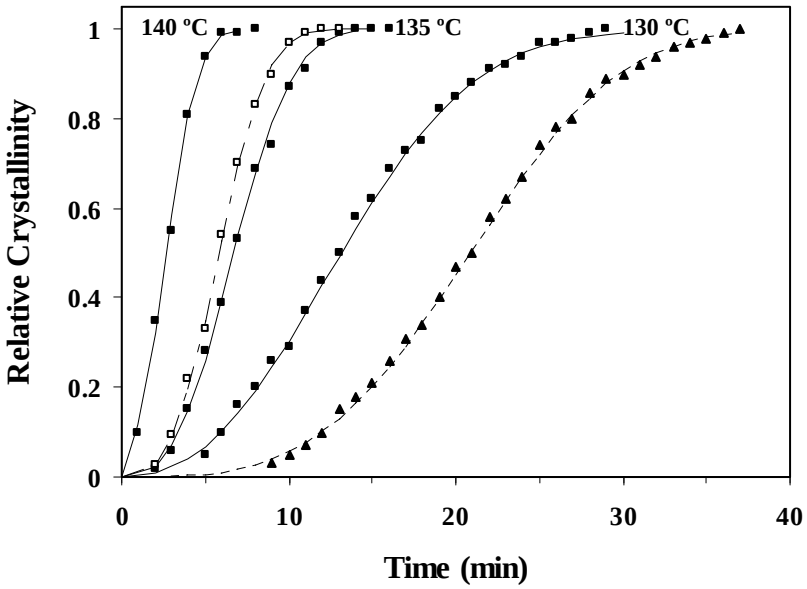

Figure 5.2.12 Time evolution of the relative crystallinity determined from absorbance measurements of the 3298 cm^{-1} FTIR band of the poly(glc-*alt*-amh)/C30B nanocomposite (■) during isothermal crystallization at 140, 135 and 130 ºC. For comparative purposes, the evolution for the poly(glc-*alt*-amh)/C20A nanocomposite (□, dashed line) and the neat polymer at 135 ºC is also shown (▲, dashed line).

Avrami plots (as shown in **Figure 5.2.13** for the C30B nanocomposite) allowed determining an exponent close to 3, which is the theoretical value for heterogeneous nucleation and three-dimensional spherulitic growth. In the same way, the kinetic constant, *k*, was calculated from the deduced *Z* and *n* values. **Table 5.2.2** compares the kinetic parameters of the three studied samples at a common temperature (135 ºC). The Avrami exponents of the three samples were close enough to deduce that nucleation type and crystal dimensionality remained unaffected by the addition of clay particles. On the contrary, the incorporation of silicate layers with an intercalated structure clearly increased the overall rate kinetic constant. This effect was more pronounced with C20A clay, as shown in **Table 5.2.2**. Note that the same trend was observed when the reciprocal of the half crystallization time, $1/\tau_{1/2}$, was considered. This good correlation with a direct experimental measurement may validate the Avrami analysis of the crystallization process.

- **Optical microscopy studies on the isothermal crystallization of poly(glc-*alt*-amh) and its C20A and C30B nanocomposites**

The spherulites of the neat poly(ester amide) and its C20A and C30B nanocomposites had negative birefringence, as demonstrated by the position of the blue and yellow arms in the optical micrographs in the inset of **Figure 5.2.14**. Different spherulitic morphologies were observed depending on the crystallization temperature and the addition of clay particles. Thus, the neat

polymer gave rise to speckled, ringed and fibrilar spherulites at temperatures close to 140, 130 and 125 ºC, respectively. The addition of a clay that rendered an exfoliated structure (i.e. C25A) favored the development of fibrilar textures [27] and hindered lamellar twisting, whereas the incorporation of clays associated with a final intercalated structure (i.e. C20A and C30B) led to the formation of speckled textures, as shown in **Figure 5.2.13**.

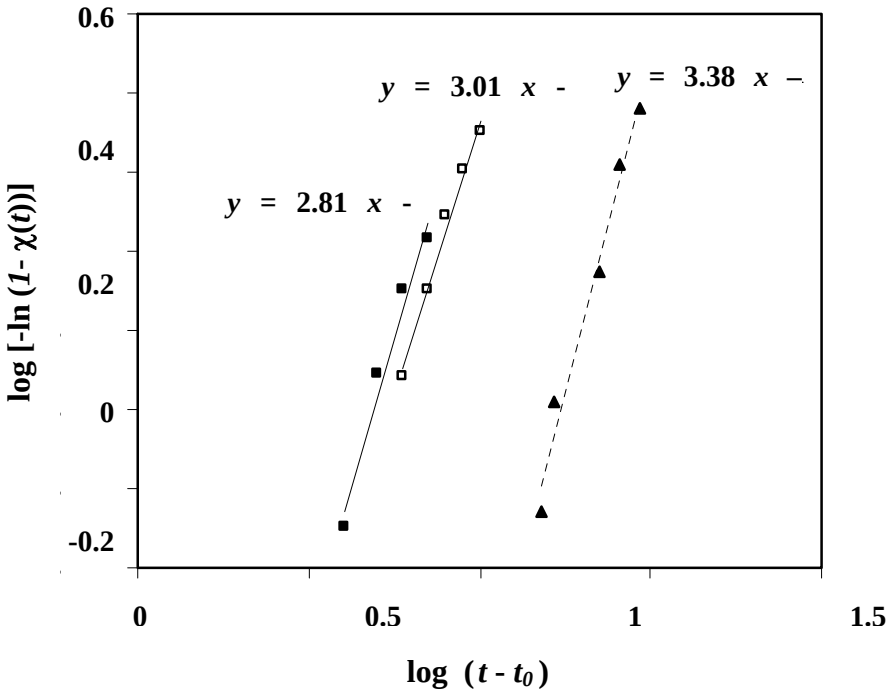

Figure 5.2.13 Avrami plot considering FTIR data (3298 cm^{-1} band) for isothermal crystallization of the neat poly(ester amide) (▲) and its C20A (□) and C30B (■) nanocomposites at 135 ºC.

Nucleation density was higher for the nanocomposites derived from C20A and C30B (i.e. those with an intercalated structure), as deduced from the number of spherulites measured in the field of view of the optical microscope. At all temperatures, the nucleation density decreased in the order C20A > C30B > neat polymer, as shown in **Figure 5.2.15** a.

The change in the primary nucleation was responsible for the difference in overall crystallization rates between the neat polymer and C20A and C30B nanocomposites found by FTIR. The incorporation of a clay that favors an intercalated structure increased the nucleation density. In fact, the experimental data indicate that the effect was more pronounced with the addition of C20A clay. It should be pointed out that the crystallization of the C25A nanocomposite was previously studied and that a lower nucleation density was derived for this sample with an exfoliated silicate structure [27]. Furthermore, the overall crystallization rate decreased when this clay was incorporated.

The change in the primary nucleation was responsible for the difference in overall crystallization rates between the neat polymer and C20A and C30B nanocomposites found by FTIR. The incorporation of a clay that favors an intercalated structure increased the nucleation density. In fact,

the experimental data indicate that the effect was more pronounced with the addition of C20A clay. It should be pointed out that the crystallization of the C25A nanocomposite was previously studied and that a lower nucleation density was derived for this sample with an exfoliated silicate structure [27]. Furthermore, the overall crystallization rate decreased when this clay was incorporated.

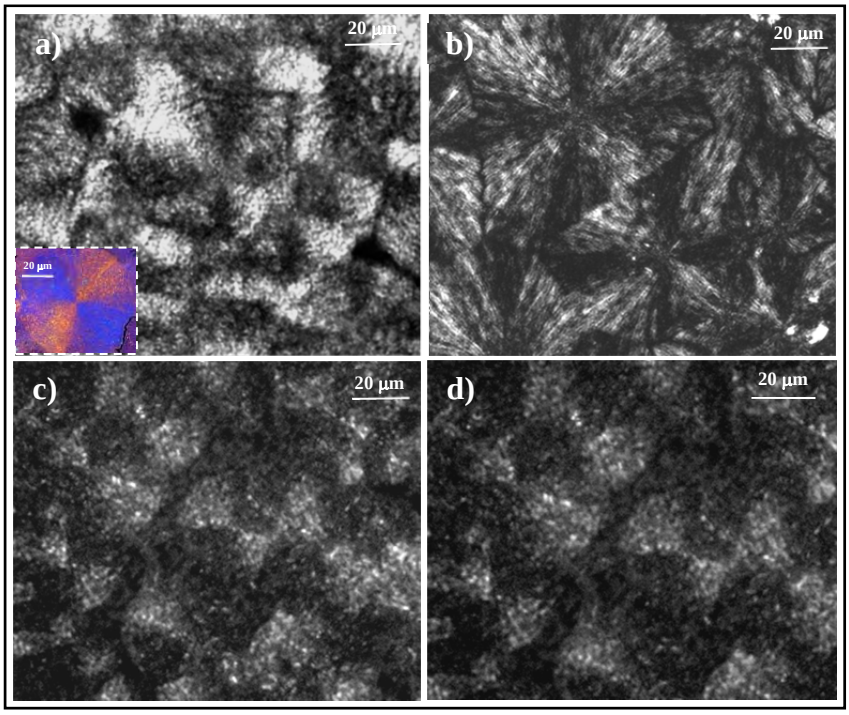

Figure 5.2.14. Polarized optical micrographs showing the isothermal hot crystallizations of the neat poly(ester amide) (a) and its C25A (b), C20A (c) and C30B nanocomposites (d) at 130 ºC. Inset shows a color micrograph of a speckled spherulite attained at 140 ºC with the neat polymer sample.

The spherulic radial growth rates (*G*) of the neat sample and its C20A and C30B nanocomposites were determined with the evolution of the spherulite radius versus time. It is worth pointing out that a linear increase in the spherulite radius was always found, suggesting that clay particles were not segregated during spherulite growth. Data for crystallization temperatures of 125, 130 and 140 ºC (**Figure 5.2.15** b) showed that the growth rate of the two nanocomposites was similar although a slightly lower value was found for C30B. Differences were more significant at a high crystallization temperature (e.g. 140 ºC), with measurements clearly indicating that the incorporation of clay particles reduced the spherulitic growth rate (i.e. 0.015 µm/s versus 0.014-0.013 µm/s). Note that the overall crystallization process did not decelerate with the addition of clay particles since the accelerative effect caused by the increase in the primary nucleation density was more significant than the decrease in the crystal growth rate.

Table 5.2.2 Crystallization kinetic parameters at 135 ºC deduced from FTIR absorbance measures of the 3298 cm^{-1} band.

Sample	$1/\tau_{1/2}$ (min^{-1})	Z (min^{-n})	n	k (min^{-1})
Neat polymer	0.048	$2.40\ 10^{-5}$	3.38	0.043
Nanocomposite with C20A	0.174	$3.40\ 10^{-3}$	3.01	0.153
Nanocomposite with C30B	0.149	$3.28\ 10^{-3}$	2.81	0.131

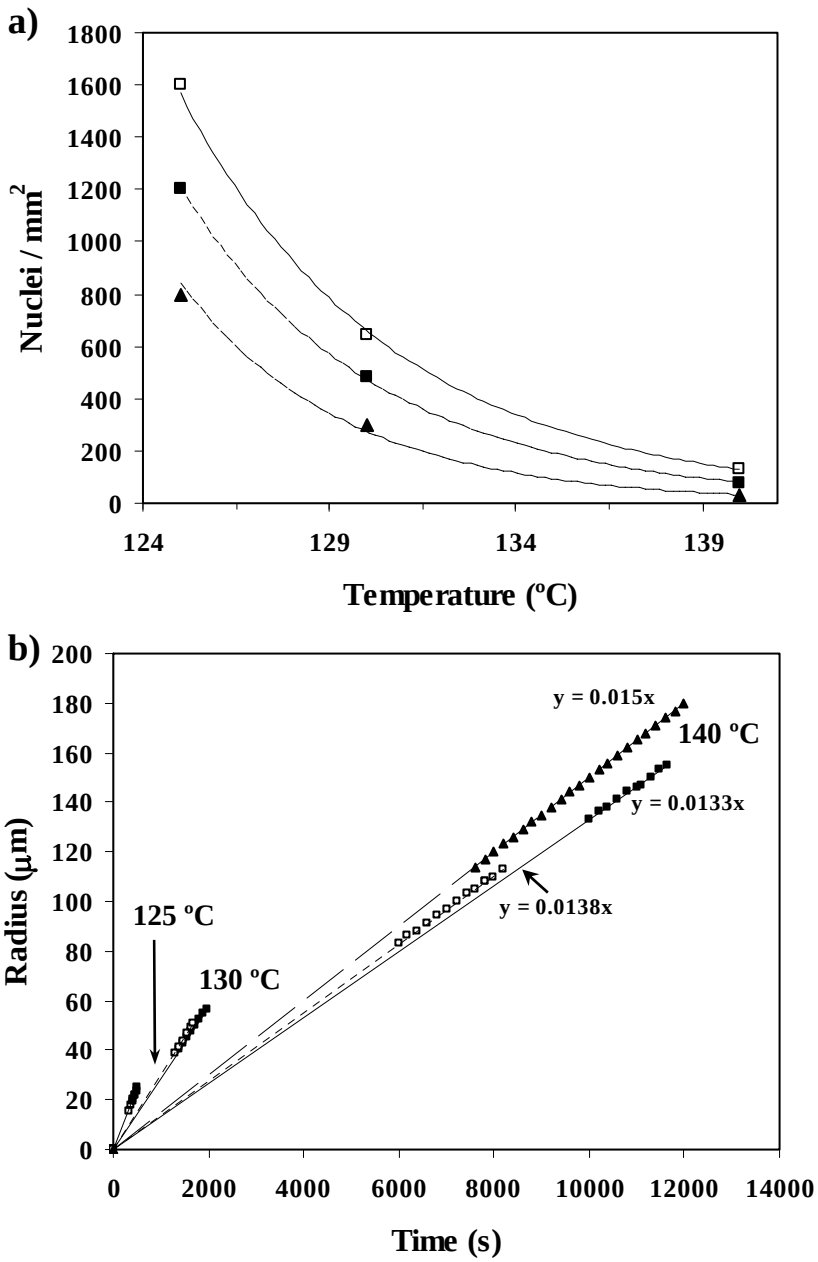

Figure 5.2.15 . a) Variation in nucleation density with isothermal crystallization temperature for the neat polymer (▲) and its C20A (□) and C30B (■) nanocomposites. b) Plot of the radius of spherulites of the neat polymer (▲) and its C20A (□) and C30B nanocomposites (■) versus crystallization time for isothermal crystallizations at 125 ºC, 130 and 140 ºC.

5.2.4 Conclusions

Nanocomposites constituted by a poly(ester amide) matrix and C20A or C30B organomodified clays were obtained by in situ polymerization of sodium chloroacetylaminohexanoate. They showed an intercalated silicate structure, as determined by X-ray diffraction and transmission electron microscopy.

The polymerization kinetics under both non-isothermal and isothermal conditions was quite similar after the incorporation of the two clays. However, great differences were found with the polymerization of the neat monomer. The temperature dependence of the polymerization kinetic constant allowed inferring the activation energies and preexponential frequency factors, which were lower when polymerization was performed in the presence of clay particles. Nanoconfinement in the intercalated silicate galleries may favor the occurrence of polycondensation reactions and reduce the corresponding activation energy. This confinement should logically result in decreased chain mobility and consequently lower frequency factor.

Optical microscopy and FTIR studies revealed that the crystallization rate of the nanocomposites increased due to the nucleation effect of clay particles. On the contrary, spherulitic crystal growth was slightly hindered when particles were added. Spherulites always showed negative birefringence but their texture was influenced by the incorporation of clay and obviously by the crystallization temperature.

5.2.5 References

[1] Pavlidou S., Papaspyrides C. D.: A review on polymer-layered silicate nanocomposites. Progress in Polymer Science, **12**, 1119-1198 (2008). DOI :10.1016/j.progpolymsci.2008.07.008.

[2] Ray S. S.: Biodegradable polymers and their layered silicate nanocomposites: In greening the 21st century materials world. Progress in Materials science, **50**, 962-1079 (2005). DOI :10.1016/j.pmatsci.2005.05.002.

[3] Ray S. S., Okamoto M.: Polymer/layered silicate nanocomposites: a review from preparation to processing. Progress in Polymer Science, **28**, 1539-1641 (2003). DOI :10.1016/j.progpolymsci.2003.08.002.

[4] Carrado K. A.: Synthetic Organo- and Polymer-. Clays: Preparation, Characterization and Materials. Applications. Applied Clay Science, **17**, 1-23 (2000). DOI :10.1016/S0169-1317(00)00005-3

[5] Alexandre M., Dubois P.: Polymer-layered silicate nanocomposites: preparation, properties and uses of a new class of materials. Materials Science & Engineering R-Reports, **28**, 1-63 (2000). DOI :10.1016/S0927-796X(00)00012-7

[6] Usuki A., Kojima Y., Kawasumi M., Okada A., Fukushima Y., Kurauchi T., Kamigato O.: Synthesis of nylon 6-clay hybrid. Journal of Materials Research, **8**, 1179-1184 (1993). DOI : 10.1557/JMR.1993.1179

[7] Kawasumi M.: The discovery of polymer-clay hybrids. Journal Polymer Science Part A: Polymer Chemistry, **42**, DOI : 819-824 (2004). 10.1002/pola.10961

[8] Ishida H., Campbell S., Blackwell J.: General approach to nanocomposite preparation. Chemistry of Materials **12**, 1260-1267 (2000). 10.1021/cm990479y

[9] Akelah A., Salahuddin N., Hiltner A., Baer E., Moet A.: Morphological hierarchy of butadieneacrylonitrile/montmorillonite nanocomposite. Nanostructured Materials **4**, 965-978 (1994). DOI: 10.1016/0965-9773(94)90103-1

[10] Kennedy M., Brown G., Stpierre L: Crystallization of isotactic (D,L) poly(propylene oxide) in the presence of fine-particle silica. I: Radial growth rates of spherulites Polymer Engineering Science **30**, 769-775 (1990). DOI: 10.1002/pen.760301304

[11] Nitta K., Asuka K., Boping L., Terano M.: The effect of the addition of silica particles on linear spherulite growth rate of isotactic polypropylene and its explanation by lamellar cluster model Polymer **47**, 6457-6463 (2006). DOI: 10.1016/j.polymer.2006.06.054

[12] Somwangthanaroj A., Lee E. C., Solomon M. J.: Early Stage Quiescent and Flow-Induced Crystallization of Intercalated Polypropylene Nanocomposites by Time-Resolved Light Scattering. Macromolecules 36, 2333-2342 (2003). DOI: 10.1021/ma021454e

[13] [13] Nowacki R., Monasse B., Piorkowska E., Galeski A., Haudinb J. M.: Spherulite nucleation in isotactic polypropylene based nanocomposites with montmorillonite under shear. Polymer **45**, 4877-4892 (2004). 10.1016/j.polymer.2004.04.058

[14] Burke M., Young R., Stanford J.: The relationship between structure and properties in titanium dioxide filled polypropylene. Polymer Bulletin 30, 361-368 (1993). 10.1007/BF00343073

[15] Stapert H. R., Bouwens A. W., Dijkstra P. J., Feijen J.: Environmentally degradable aliphatic poly(ester-amide)s based on short, symmetrical and uniform bisamide-diol blocks, 1 : Synthesis and interchange reactions. Macromolecular Chemistry & Physics **200**, 1921-1929 (1999). DOI: 10.1002/(SICI)1521-3935(19990801)200:8

[16] Guo K., Chu C. C.: Synthesis, characterization, and biodegradation of copolymers of unsaturated and saturated poly(ester amide)s. Jounal of Polymer Science Part A: Polymer Chemistry **45**, 1595-1606 (2007). DOI: 10.1002/pola.2192

[17] Paredes N., Rodríguez-Galán A., Puiggali J.: Synthesis and characterization of a family of biodegradable poly(ester amide)s derived from glycine. Journal of Polymer Science Part A: Polymer

Chemistry 36, 1271-1282 (1998). DOI: 10.1002/(SICI)1099-0518(199806)36:8<1271::AID-POLA10>3.3.CO;2-U

[18] Guo K., Chu C. C.: Synthesis, characterization and biodegradation of novel poly(ether ester amide)s based on L-phenylalanine and oligoethylene glycol. Biomacromolecules **8**, 2851-2861 (2007). DOI: 10.1002/pola.20463

[19] Rodríguez-Galán A., Pelfort M., Aceituno J. E., Puiggalí J.: Comparative studies on the degradability of poly(ester amide)s derived from L- and L, D-alanine. Journal of Applied Polymer Science **74**, 2312-2320 (1999). 10.1002/(SICI)1097-4628(19991128)74:9<2312::AID-APP21>3.0.CO;2-0

[20] Vera M., Rodríguez-Galán A., Puiggali J.: New method of synthesis of poly(ester amide)s derived from the incorporation of glycolic acid residues to aliphatic polyamides. Macromolecular Rapid Communications **25**, 812- 817 (2004). DOI: 10.1002/marc.200300273

[21] Vera M., Franco L., Puiggalí J.: Synthesis and characterization of poly(glycolic acid-*alt*-aminohexanoic acid) and poly(glycolic acid-*alt*-aminoundecanoic acid). Macromolecular Chemistry & Physics, **205**, 1782-1792 (2004). DOI: 10.1002/macp.200400191

[22] Wang D., Zhu J., Yao Q., Wilkie C. A.: A Comparison of Various Methods for the Preparation of Polystyrene and Poly(Methyl Methacrylate) Clay Nanocomposites. Chemistry of Materials **14**, 3837- 3843 (2002). DOI: 10.1021/cm011656+

[23] LeBaron P. C., Wang Z., Pinnavaia T. J: Polymer-Layered Silicate Nanocomposites: an Overview. Applied Clay Science **12**, 11-29 (1999). DOI: 10.1016/S0169-1317(99)00017-4

[24] Akelah, A., Moet A.: Polymer-clay nanocomposites: Free-radical grafting of polystyrene on to organophilic montmorillonite interlayers. Journal of Materials Science **31**, 3589-3596 (1996). DOI: 10.1007/BF00360767

[25] Messersmith P. B., Giannelis E. P.: Polymer-layered silicate nanocomposites: In situ intercalative polymerization of ε-caprolactone in layered silicates. Chemistry of Materials **5**, 1064-1066 (1993). DOI: 10.1021/cm00032a005

[26] Fukushima Y., Okada A., Kawasumi M., Kurauchi T., Kamigaito O.: Swelling behavior of montmorillonite by poly-6-amide. Clay Minerals **23**, 27-34 (1988).

[27] Morales L. T., Franco L., Casas M. T., Puiggalí J.: Poly(ester amide)/clay nanocomposites prepared by in situ polymerization of the sodium salt of N-chloroacetyl-6-aminohexanoic acid. Journal Polymer Science Part A: Polymer Chemistry, **47**, 3616-3629 (2009). DOI: 10.1002/pola.23430

[28] [28] Morales L., Franco L., Casas M. T., Puiggalí J.: Crystallization studies on a clay nanocomposite prepared from a degradable poly(ester amide) constituted by glycolic acid and 6-aminohexanoic acid. Polymer Engineering & Science, in press (2010).

[29] Botines E., Casas M. T., Puiggalí J.: Alternating poly(ester amide)s of glycolic acid and ω-amino acids: Crystalline morphology and main crystallographic data. Journal of Polymer Science Part B: Polymer Physics **45**, 815-825 (2007). DOI: 10.1016/j.eurpolymj.2006.01.013

[30] Rodríguez-Galan A., Vera M., Jiménez K., Franco L., Puiggalí J.: ynthesis of poly(ester amide)s derived from glycolic acid and the amino acids: β-alanine or 4-aminobutyric acid. Macromolecular Chemistry & Physics **204**, 2078-2089 (2003). DOI: 10.1002/macp.200350064

5.3

Crystallization studies on a clay nanocomposite prepared form a degradable poly(ester amide) constituted by glycolic acid and 6-aminohexanoic acid

An intercalated nanocomposite was prepared from dimethyl hydrogenated-tallow 2-ethylhexyl ammonium modified Cloisite 25A (C25A) and a new biodegradable poly(ester amide) characterized by an alternating arrangement of glycolic acid and 6-aminohexanonoic acid units by the melt mixing technique. This nanocomposite was previously obtained with a practically exfoliated structure by in situ polymerization. The influence of the final silicate layer morphology on hot and cold crystallization behaviour was investigated by optical microscopy, differential scanning calorimetry and simultaneous Small Angle X-ray Scattering (SAXS) and Wide Angle X-Ray Diffraction (WAXD) measurements by synchrotron radiation. Primary nucleation increased significantly with the incorporation of nanoparticles, in contrast with the decrease previously observed when exfoliated structures were obtained. The secondary nucleation constant was higher for the nanocomposite sample, indicating that the growth mechanism was hampered by the presence of clay particles. However, the increase in primary nucleation had a greater effect, resulting in a faster overall crystallization rate for the nanocomposite. The addition of clay particles slightly reduced the degree of crystallinity attained after the hot and cold crystallization processes and favored a lamellar insertion mechanism.

5.3.1 Introduction

The development of biodegradable polymers is one of the most interesting topics since these materials have potential applications as commodities and specialities, mainly in the biomedical field. In this sense, biodegradable polymers are regarded as a potential alternative to existing petroleum-based polymers because trends focus on promoting the use of environmentally friendly materials despite their higher production costs [1, 2]. Aliphatic polyesters are the most commonly employed family of polymers due to the presence of hydrolyzable ester groups. However, mechanical and thermal properties are often not sufficient to meet the requirements of commodity applications. Several alternatives have therefore been considered to improve performance properties, like the incorporation of amide groups in the main chain, which allows establishing strong hydrogen bonding intermolecular interactions. Thus, interest is increasing in poly(ester amide)s [3-11] to the point that this new family of biodegradable polymers is even being considered for commercialization (e.g. BAK^{TM}, a poly(ester amide) derived from 1,4-butanediol, adipic acid and 6-aminohexanoic acid [12]).

The properties of polymers can also be significantly modified by adding layered silicates, as demonstrated by pioneering works performed with nylon 6-clay nanocomposites [13, 14]. Since then, the preparation of nanocomposites based on biodegradable polymer matrices has been extensively studied [15-17] despite potential problems associated with low production level and high costs.

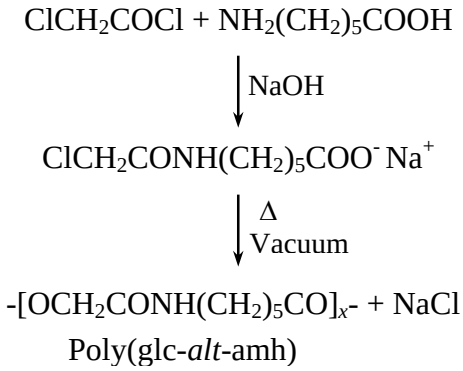

Scheme 5.3.1

We developed a promising synthesis procedure based on a thermal polycondensation that allows obtaining new poly(ester amide)s constituted by an alternating arrangement of glycolic acid and ω-amino acid units (**Scheme 5.3.1**) [18, 19]. The derivative of 6-aminohexanoic acid (hereafter named poly(glc-*alt*-amh)) was mainly studied since its related homopolymers (i.e. polyglycolide and nylon 6) are samples with well known applications as biodegradable and commodity materials, respectively. This polymer was found to be biocompatible [20] and to crystallize according to a

peculiar structure which exhibits characteristics of both polyesters and polyamides [21]. Its crystallization behavior was also investigated [22] and its thermal degradation mechanism was determined [23].

It was also demonstrated that nanocomposites with a practically exfoliated structure and based on a poly(glc-*alt*-amh) matrix can be prepared by *in situ* polymerization of the sodium salt of N-chloroacetyl-6-aminohexanoic acid in the presence of the dimethyl hydrogenated-tallow 2-ethylhexyl ammonium modified Cloisite 25A (C25A) [25]. Furthermore, significant differences in thermal stability and crystallization behavior were found between this kind of nanocomposites and the neat polymer [24].

In the present work we study the poly(glc-*alt*-amh)/C25A nanocomposite prepared by the melt intercalation technique, which has the advantage of using a polymer sample with a defined molecular weight (i.e. the variation intrinsically caused by the *in situ* polymerization method is avoided). Moreover, the arrangement of the clay in the polymer matrix is expected to be different from that found in the nanocomposite prepared by *in situ* polymerization since an intercalated system with preservation of the stacking of silicate layers may be favored. In this case, the study of crystallization becomes interesting as it provides insight into the influence of clay arrangement on nucleation and crystal growth rate. In addition to hot crystallization, crystallization from the glass state is also performed since studies concerning cold crystallization of nanocomposites are scarce.

5.3.2 Experimental section

Materials

Poly(glc-*alt*-amh) was synthesized by thermal polyesterification of the sodium salt of N-chloroacetyl-6-aminohexanoic acid with an 80% yield [19, 20] (**Figure 5.3.1**).

The Cloisite 25A (Southern Clay Products) was used as received. The chemical structure of the specific surfactant of the organomodified layered phyllosilicate is shown in **Scheme 5.3.2**.

Preparation of nanocomposites

Nanocomposites with 3% C25A clay content were prepared by melt mixing in two steps using a corotating tightly intermeshed twin-screw extruder (DSM Xplore 5 ml microcompounder). All materials were dried under vacuum prior to mixing. The processing temperature, screw rotation and cycle time were 170 ºC, 100 rpm and 3 minutes, respectively.

CLOISITE 25A

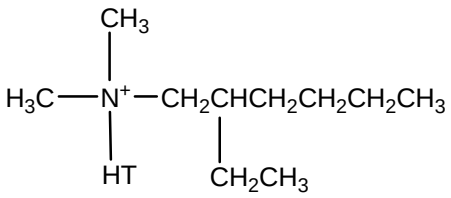

HT: hydrogenated tallow; T: tallow
(~65% C18, ~30% C16, ~5% C14).

Scheme 5.3.2

- **Measurements**

Intrinsic viscosity was determined using a Cannon-Ubbelhode microviscometer and a dichloroacetic acid solution at 25 ± 0.1 ºC. The molecular weight was estimated by size exclusion chromatography (SEC) using a liquid chromatograph (Shimadzu, model LC-8A) equipped with an Empower computer program (Waters). A PL HFIP gel column (Polymer Lab) and a refractive index detector (Shimadzu RID-10A) were employed. The polymer was dissolved and eluted in hexafluoroisopropanol at a flow rate of 0.5 mL/min (injected volume 100 μL, sample concentration 1.5 mg/mL). The number and weight average molecular weights were calculated using polymethyl methacrylate standards.

Interlayer spacing of the clay was studied by Wide Angle X-ray Scattering (WAXD) using a PANalytical X´Pert diffractometer with CuK_α radiation (λ = 0.1542 nm).

Calorimetric data were obtained by differential scanning calorimetry with a TA Instruments Q100 series equipped with a refrigeration cooling system (RCS) operating from -90 ºC to 550 ºC. Experiments were conducted under a flow of dry nitrogen with a sample weight of approximately 5 mg and calibration was performed with indium. For the hot crystallization studies, samples were first heated at 20 ºC/min to 170 ºC and kept at this temperature for five minutes to erase the thermal history. Next, cooling runs were performed at 3 and 10 ºC/min. For the cold crystallization studies, samples were previously quenched from the melt state at the maximum rate allowed by the refrigeration system and then heated at 3 and 20 ºC/min.

The structure and distribution of Cloisite were observed with a Philips TECNAI 10 transmission electron microscope (TEM) at an accelerating voltage of 100 kV. TEM specimens were prepared by embedding the film in a low viscosity modified Spurr epoxy resin and curing it at 40°C for a few days and then at 60 °C for 6 h. Ultrathin sections (less than 100 nm) were cut at room temperature using a Sorvall Porter-Blum microtome equipped with a diamond knife. Finally, the sections were collected in a trough filled with water and lifted onto carbon coated copper grids.

The spherulitic growth rate was determined by optical microscopy using a Zeiss Axioskop 40 Pol light polarizing microscope equipped with a Linkam temperature control system configured by a THMS 600 heating and freezing stage connected to an LNP 94 liquid nitrogen cooling system.

Spherulites were studied using homogeneous melt-crystallized thin films obtained by melting 1 mg of the polymer mixture on microscope slides. Next, small sections of these films were pressed or smeared between two cover slides and inserted into the hot stage. All squeezed samples, which had a thickness close to 10 μm, were kept at 170 ºC (approximately 10 ºC above the temperature at the end of the fusion of the polymer) for 5 minutes to eliminate thermal history effects. Hot crystallization samples were rapidly cooled to the selected crystallization temperature whereas cold crystallization samples were rapidly cooled to -5 ºC and then rapidly heated to the selected crystallization temperature. During hot crystallization, the radius of growing spherulites was monitored with micrographs taken with a Zeiss AxiosCam MRC5 digital camera at appropriate time intervals. A first-order red tint plate was employed to determine the sign of spherulite birefringence under crossed polarizers.

Simultaneous time-resolved Small Angle X-ray Scattering (SAXS) and Wide Angle X-Ray Diffraction (WAXD) experiments were carried out at the CRG beamline (BM16) of the European Synchrotron Radiation Facility of Grenoble. The beam was monochromatized to a wavelength (λ) of 0.098 nm. Polymer and nanocomposite samples were confined between Kapton films and then held in a Linkam hot stage with temperature control within ±0.1 ºC. Samples were heated/cooled to the desired crystallization temperature similarly to optical microscopy samples. SAXS and WAXD profiles were acquired simultaneously during crystallization experiments in time frames of 12 s. Two linear position-sensitive detectors were used [25]: the SAXS detector was calibrated with different orders of diffraction from silver behenate whereas the WAXD detector was calibrated with diffractions of a standard of an alumina (Al_2O_3) sample. The diffraction profiles were normalized to the beam intensity and corrected considering the empty sample background. WAXD peaks were deconvoluted with the PeakFit v4 program by Jandel Scientific Software assuming Gaussian peak profiles. The correlation function and the corresponding parameters were calculated with the CORFUNC program provided by the Collaborative Computational Project 13 for Fiber Diffraction / Non-Crystalline Diffraction, CCP13.

5.3.3 Results and discussion

- **Molecular weight of poly(glc-*alt*-amh)**

The intrinsic viscosity measured in dichloroacetic acid at 25ºC was 0.92 dL/g. The weight average molecular weight and polydispersity index, estimated by SEC, were 50,100 g/mol and 2.10, respectively.

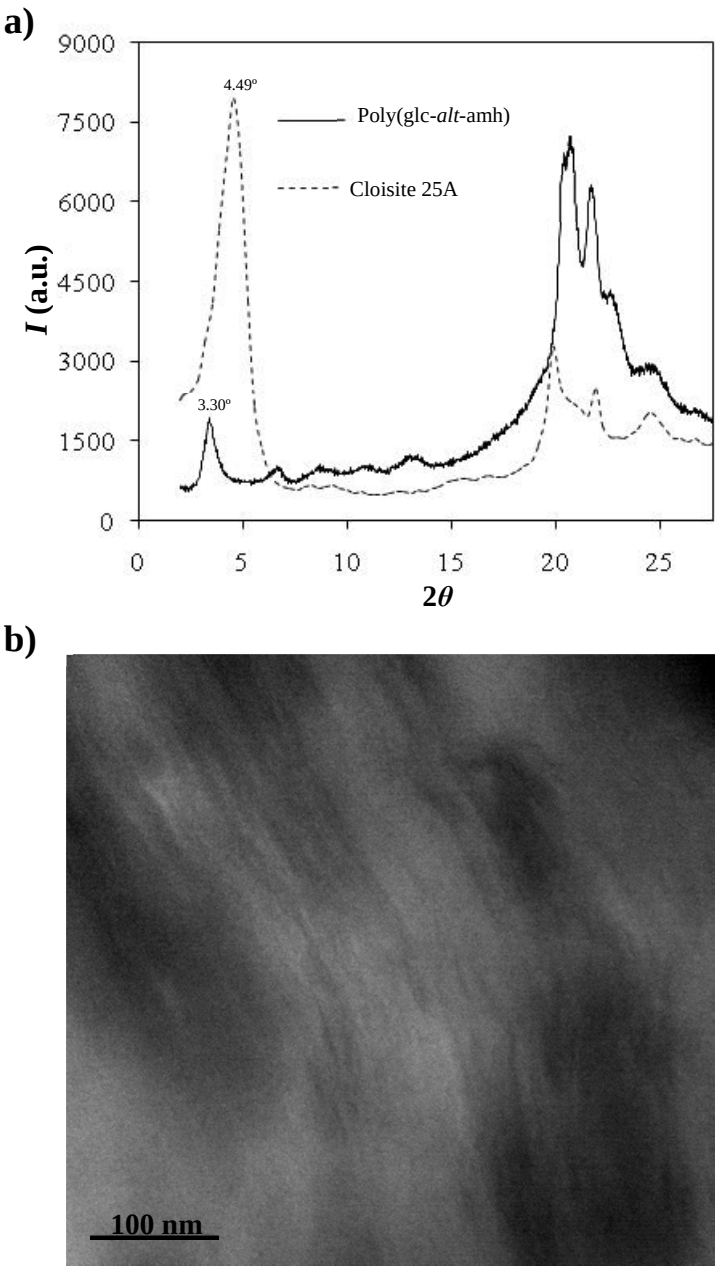

Figure 5.3.1 a) X-ray diffraction patterns of the poly(glc-*alt*-amh)/C25A nanocomposite and the neat clay. b) Transmission electron micrograph showing the morphology of the poly(glc-*alt*-amh)/C25A nanocomposite with a Cloisite concentration of 3%.

- **Dispersion structure of the C25A clay in the composite with poly(glc-*alt*-amh)**

The nanocomposite structure was first analyzed by reflection X-ray diffraction of a film sample using a silicium monocrystal sample holder. The diffraction patterns show evidence of intercalation of polymer chains into the silicate galleries in the range of 2θ = 1º-10º (θ is the scattering angle) when the characteristic silicate diffraction peak appears at a lower diffraction angle (larger spacing) than in the pattern of the neat clay. Similarly, the absence of this peak may suggest an exfoliated structure.

The shift of the characteristic 001 reflection of the C25A clay (1.97 nm, $2\theta = 4.49^{o}$) to 2.68 nm ($2\theta = 3.30^{o}$) in the nanocomposite sample, suggesting that a regular intercalated structure was attained by the melt mixing method, can be seen in a. This result contrasts with the absence of the 001 silicate peak when the sample was prepared by *in situ* polymerization [25].

Direct observation of the morphology and phase distribution of ultrathin sections of poly(glc-*alt*-amh) / C25A specimens by transmission electron microscopy (**Figure 5.3.1** b) clearly showed that an intercalated structure was predominant.

- **Optical microscopy studies on the poly(glc-*alt*-amh)/C25A nanocomposite**

Figure 5.3.2 contains polarized optical micrographs of nanocomposite and neat polymer samples isothermally hot crystallized at temperatures of 140 and 130 ºC. The nanocomposite spherulites always had the smallest size at the end of crystallization as a consequence of their higher nucleation density (e.g. 2900 nuclei/mm^2 versus 1300 nuclei/mm^2 at 130 ºC). This result contrasts with the lower density of the nanocomposite prepared by in situ polymerization, which rendered a practically exfoliated structure. Like reported data on other systems, these observations reveal an increase and a decrease in the primary nucleation density with obtaining an intercalated or exfoliated structure after incorporation of the clay, respectively [26]. In this way, when good compatibility between silicate layers and the polymer matrix is achieved (i.e. an exfoliated structure), spherulite nucleation is low as a result of the fine dispersion of silicate layers in the matrix. On the other hand, poor compatibility renders an intercalated structure where silicate particles may act as effective nucleating agents [26].

The nucleation density of neat polymer and nanocomposite samples logically increased with lowering the crystallization temperature (**Figure 5.3.3** a). Thus, at 130 ºC (**Figure 5.3.2**) spherulites had diameters of only 45 μm (neat polymer) and 35 μm (nanocomposite), making it difficult to measure the spherulitic growth rate at lower temperatures.

All spherulites had negative birefringence and a ring texture at all studied temperatures. The rings, which are associated with a characteristic lamellar twisting, could not however be clearly distinguished because of the speckle pattern obtained at temperatures higher than 140 ºC. Ring spacing remained close to 2-3 μm in the pristine and nanocomposite samples crystallized at 130 ºC. It is worth pointing out that the ring texture observed in the nanocomposite sample crystallized at 130 ºC differs from the fibrilar texture observed at the same temperature when the sample was prepared by in situ polymerization. It seems that exfoliated silicate layers somehow hinder lamellar twisting in polymer spherulites. In any case, the incorporation of organomodified clays may change the spherulitic texture, hampering lamellar growth, favoring a more disordered arrangement and weakening the birefringence [27].

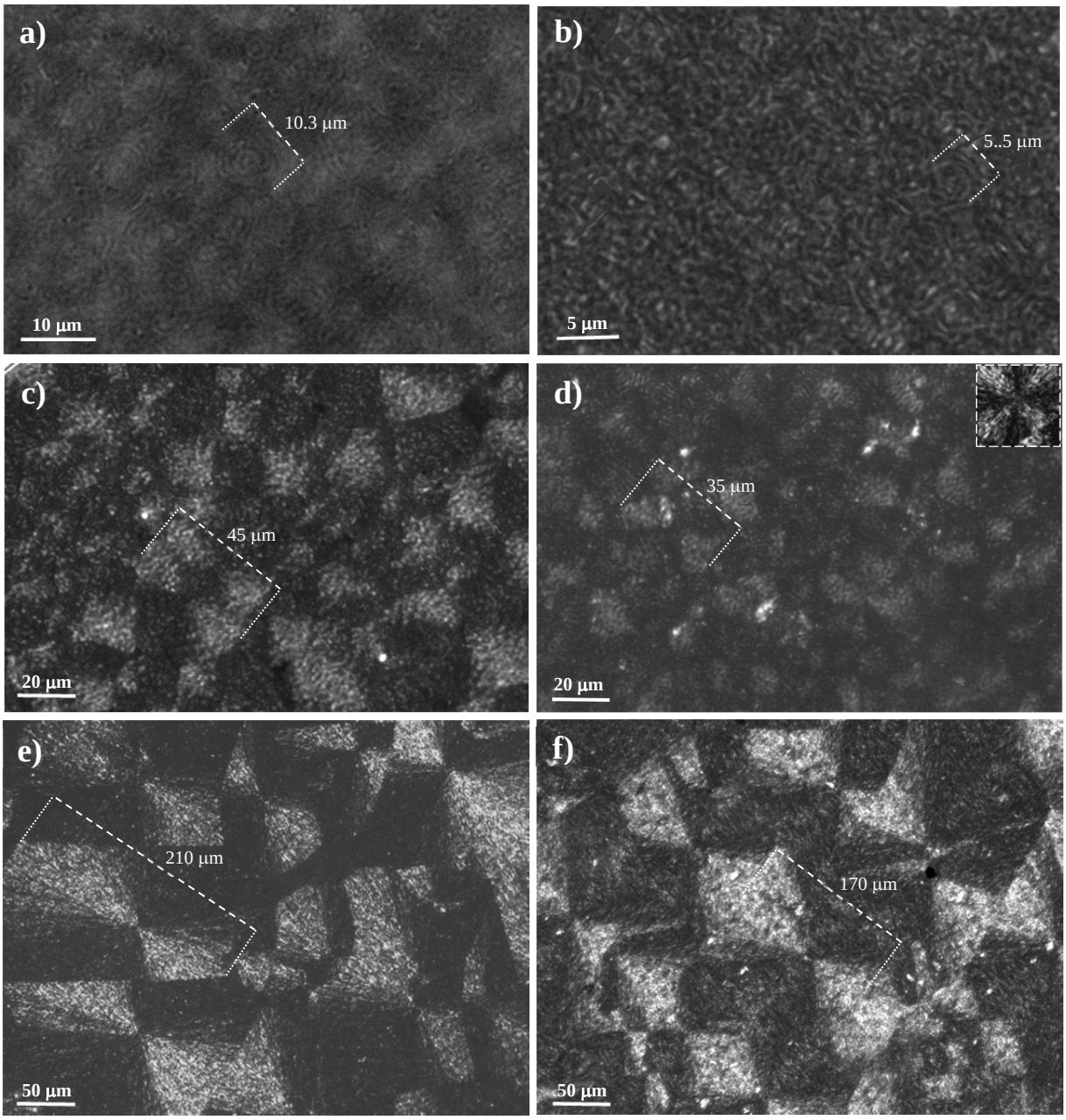

Figure 5.3.2 Polarized optical micrographs corresponding to the isothermal cold (a,b) and hot (c-f) crystallizations performed at 62 ºC (a, b), 130 ºC (c, d) and 140 ºC (e, f) with the neat poly(ester amide) (a, c, e) and its nanocomposite with C25A (b, d, f). Inset of d) shows a spherulite grown at 130 ºC of the nanocomposite prepared by in situ polymerization.

The influence of clay particles on the secondary nucleation rate was analyzed by the classical Lauritzen-Hoffman theory [28]:

$$G = G_0 \exp[-U^*/(R(T_c - T_\infty))] \exp[-K_g/(T_c \Delta T f)] , \qquad (1)$$

where G is the experimental radial growth rate, G_0 is a constant preexponential factor, U^* represents the activation energy characteristic of the transport of crystallizing segments across the liquid-crystal interface, T_∞ is a hypothetical temperature below which such motion ceases, T_c is the

crystallization temperature, R is the gas constant, K_g is the secondary nucleation constant, ΔT is the degree of supercooling measured as T_m^0-T_c, and f is a correction factor accounting for the variation in the bulk melting enthalpy per unit volume with temperature *($f = 2\ T_c / (T_m^0 + T_c)$).*

Accurate measurements of the evolution of the spherulitic radius with crystallization time were only feasible in the restricted temperature range between 130 and 140 ºC, and consequently the kinetic analysis was limited to a region mainly governed by the nucleation process. The plots in **Figure 5.3.3** b clearly show that the radial growth rate was lower for the nanocomposite (e.g. 0.84 μm/min versus 1.30 μm/min at 130 ºC), which seems insufficient to balance the opposite effect on the overall crystallization rate caused by the increase in nucleation density. Lamellar growth seems clearly hampered by the presence of organoclay particles. It is also interesting to point out that no deviation from a linear spherulitic growth was observed in the nanocomposite sample. Thus, clay particles did not seem to be excluded towards the growth front during crystallization in a manner that hindered the transport of crystallizable molecules from the melt to the growing edge. The radial growth rate of the nanocomposite sample varied significantly with the crystallization temperature, suggesting a higher secondary nucleation constant.

Following the Lauritzen-Hoffman analysis (LH), the experimental spherulitic growth rates were plotted as $\ln G + U^*/R(T_c\text{-}T_\infty)$ versus $1/(T_c\ \Delta T\ f)$ (**Figure 5.3.3** c). The data fit well with linear plots representative of one crystallization regime if the U^* and T_∞ parameters take the conventional values reported by Suzuki and Kovacs [29] (U^* = 1500 cal/mol and $T_\infty = T_g$ - 30 K). Nucleation parameters of 0.32 10^5 K^2 and 0.40 10^5 K^2 were respectively derived for the neat polymer and the nanocomposite from the slopes of these linear plots, indicating a slight increase in the secondary nucleation constant when clay particles were added. The analysis was performed using the same values for the glass transition (15 ºC) and equilibrium melting (168 ºC) temperatures for both samples since these temperatures were not significantly affected by the incorporation of clay particles into the polymer matrix. It is interesting to note that systems with good compatibility between the clay and the polymer matrix may show a decrease in the secondary nucleation constant, which was interpreted as a demonstration that exfoliated silicate layers acted as effective secondary nucleation sites [30].

Figure 5.3.2 shows that negative and ringed spherulites also formed when both the pristine and the nanocomposite samples crystallized from the glass state. Again smaller sizes and higher nucleation densities were determined for the nanocomposite. These nucleation data suggest single exponential dependences on the crystallization temperature (**Figure 5.3.3** a), which resulted in more active nuclei (i.e. more favorable thermodynamic conditions for nuclei generation) with progressively decreasing temperature.

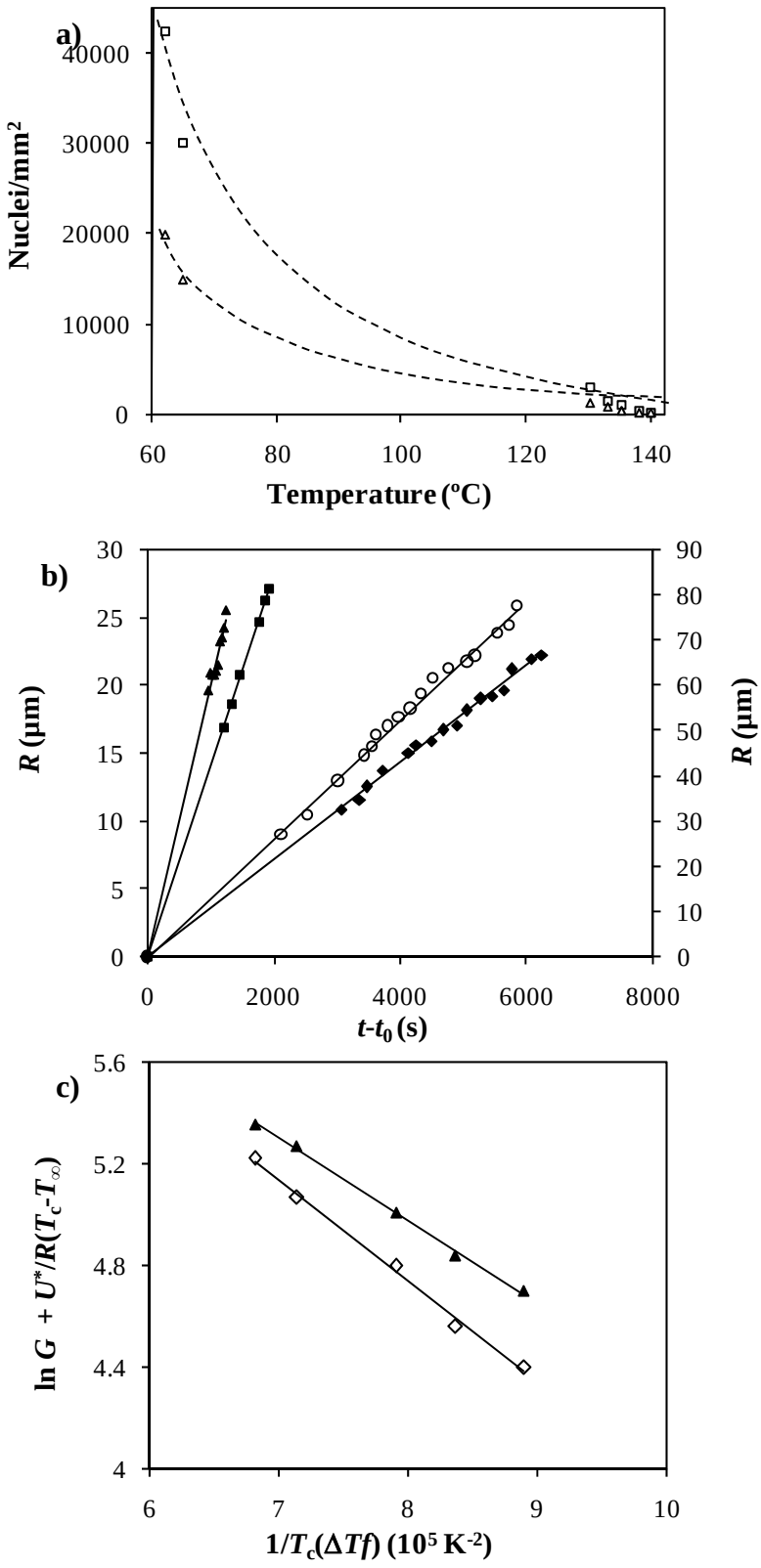

Figure 5.3.3 a) Variation in nucleation density with isothermal crystallization temperature for the nanocomposite sample (□) and the neat polymer (Δ). b) Plot of the radius of spherulites of the neat polymer (▲,○) and its nanocomposite with C25A (■,♦) versus crystallization time for isothermal crystallizations performed at 130 ºC (▲,■) and 140 ºC (○,♦). c) Lauritzen-Hoffman plot of the neat poly(ester amide) (▲) and its nanocomposite with C25A (◊).

- **Influence of C25A clay particles on the thermal behaviour of poly(glc-*alt*-amh)**

Calorimetric analyses showed differences between the nonisothermal crystallization of the neat polymer and its intercalated nanocomposite with the C25A clay. The clay mainly influenced the hot crystallization of melted samples, as shown in **Figure 5.3.4** for two representative cooling rates.

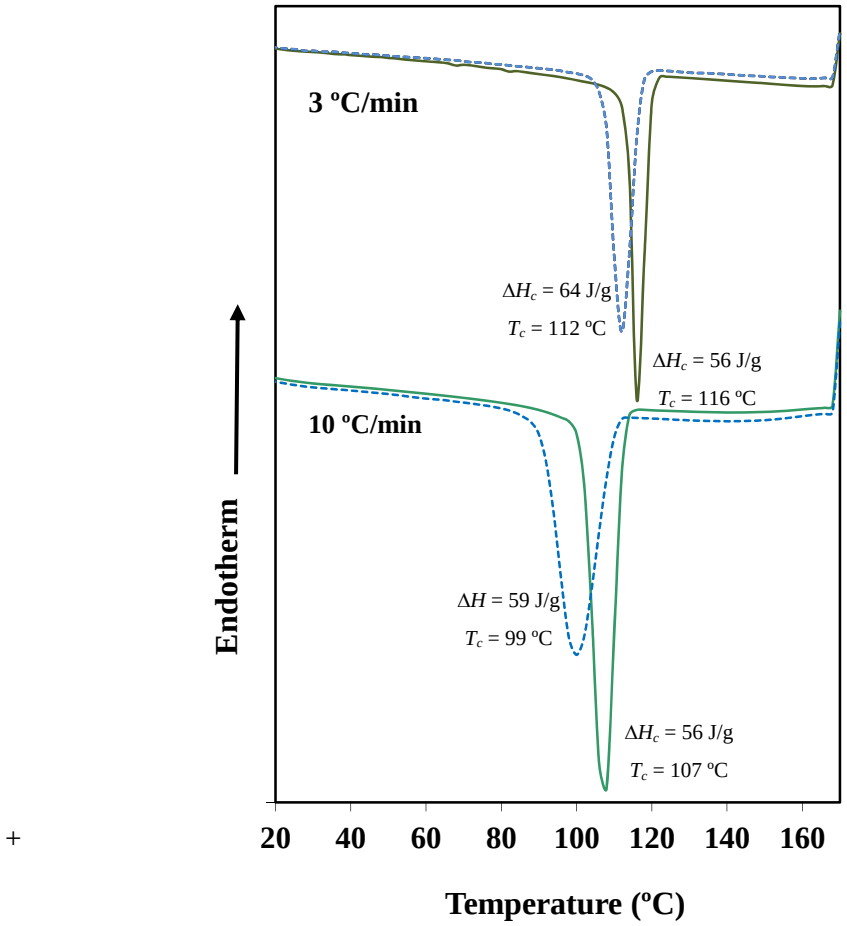

Figure 5.3.4 DSC curves of the non-isothermal hot crystallization performed at 3 and 10 ºC/min with the poly(glc-*alt*-amh)/C25A nanocomposite (solid lines) and the neat poly(ester amide) (dashed lines). The ordinate scale was magnified for DSC traces performed at 3 ºC/min for comparison.

As expected, the peak crystallization temperature decreased and the exothermic peak became sharper when the cooling rate increased. Comparison between hot crystallization curves of the neat polymer and its nanocomposite allowed inference of the following points:

a) The crystallization peak temperature was always higher for the nanocomposite, the difference increasing with the cooling rate (i.e. 4 and 8 ºC for cooling rates of 3 and 10 ºC/min, respectively).

b) The exothermic peaks of both samples showed a tail associated with the secondary crystallization in the low temperature region.

c) The exothermic peak of the nanocomposite sample was always narrower than that of the neat polymer, indicating a greater overall crystallization rate. In addition, as discussed above, the increase in primary nucleation density is more influential than the decrease in radial growth rate.

d) The peak of the nanocomposite sample was more asymmetric if the small tail at the end of crystallization was not considered. Note that the peak temperature of the nanocomposite was only a few degrees lower than the onset crystallization temperature (3 ºC at the rate of 3 ºC/min), a behavior significantly different from that of the pristine sample (temperature difference of 5 ºC at the same rate). Thus, primary crystallization of the nanocomposite occurred almost immediately after the end of the induction period.

e) The crystallization enthalpies were quite similar, although slightly lower values were determined for the nanocomposite once the weight of the sample was referred to the polymer content (e.g. 64 versus 56 J/g for the neat polymer and the nanocomposite, respectively, at a cooling rate of 3 ºC/min). Thus, clay particles slightly hindered the hot crystallization process, slowing down crystal growth, as above indicated. However, differences were smaller when the cooling rate increased since the crystallization enthalpy of the neat polymer was significantly reduced (e.g. 64 versus 59 J/g for cooling rates of 3 and 10 ºC/min, respectively).

f) Differences in the onset crystallization temperature were practically insignificant, although the nanocomposite always started to crystallize 1-2 ºC before the pristine sample.

Figure 5.3.5 shows the heating traces of quenched samples that allow comparing the cold crystallization behavior of the nanocomposite and the pristine sample. The exothermic peak shifted to higher temperatures with increasing the heating rate. The difference in the magnitude of the shifts was such that at 3ºC/min the pristine sample had the lower peak temperature whereas at 20ºC/min the lower peak temperature was observed for the nanocomposite sample. The influence on the crystallization rate was minimal since the exothermic peaks of both samples always had similar widths. In this case, the increase in primary nucleation density seems insufficient to compensate for the decrease in the spherulitic growth rate caused by a disturbance of the silica layers.

Unfortunately, both nanocomposite and neat polymer samples partially crystallized during the quenching process performed at the maximum cooling rate allowed by the refrigeration system. This made it difficult to determine the influence of clay particles on the degree of crystallinity attained after the cold crystallization process from DSC experiments. However, the data in **Figure**

5.3.5 indicate a lower enthalpy for the cold crystallization peak of the nanocomposite sample, which supports the assumption of a disturbance of crystal growth.

The heating runs also revealed that the clay particles had practically no effect on the glass transition and the melting temperature. Furthermore, both samples showed a similar hot crystallization exothermic peak just some degrees before fusion. It is interesting to note that the melting behavior of both samples depended on the heating rate. Thus, a typical melt/recrystallization process of the initial lamellae occurred at a low rate (e.g. 3 ºC/min) and a double melting peak (152-153 and 161-162 ºC) was detected. On the contrary, recrystallization to thicker lamellae was not possible at a high heating rate (e.g. 20 ºC/min), and consequently only the low temperature melting peak (i.e. 153 ºC) was detected. The melting enthalpies were similar although lower values were always found for the nanocomposite sample. This difference was enhanced when the heating rate was lowered.

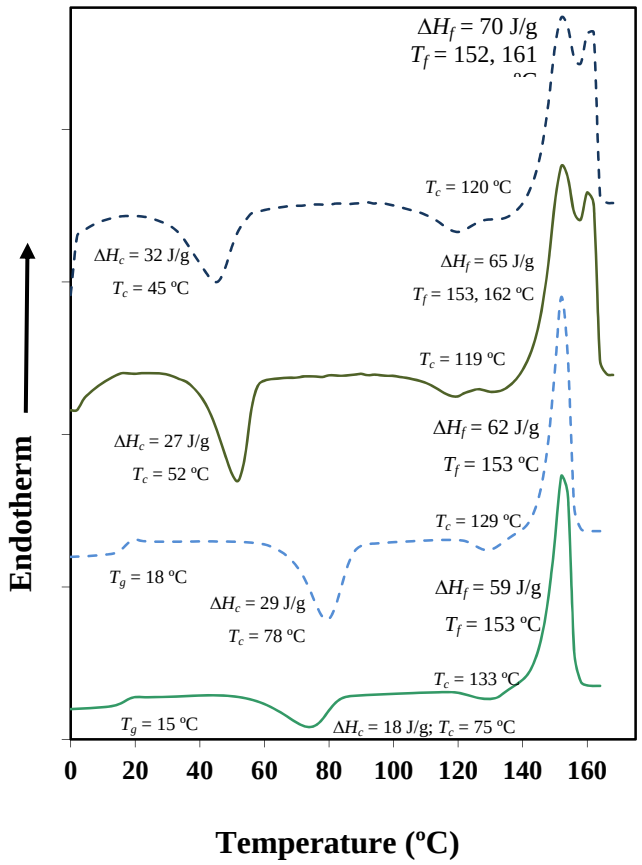

Figure 5.3.5 DSC curves of the non-isothermal cold crystallization performed at 3 and 20 ºC/min with the poly(glc-*alt*-amh)/C25A nanocomposite (solid lines) and the neat poly(ester amide) (dashed lines). The ordinate scale was magnified for DSC traces performed at 3 ºC/min for comparison.

Non-isothermal crystallization data of poly(glc-*alt*-amh)/C25A nanocomposite and the neat polymer from WAXD data

Figure 5.3.6 a plots the time evolution of the nanocomposite WAXD profiles during a non-isothermal hot crystallization performed at a cooling rate of 3 ºC/min. The initial profiles show only small reflections corresponding to the clay particles and one amorphous halo whose intensity decreases when crystallization occurs, and on which Bragg reflections form. 020, 101, 110, 111 and 102 correspond to the most intense and significant reflections of a structure defined by an orthorhombic unit cell having a = 0.477 nm, b = 0.873 nm and c = 1.057 nm. The time evolution of the profiles corresponding to the two studied samples was significantly different. This difference in the crystallization behavior could be easily demonstrated by considering only the variation in intensity of the strongest 110 reflection at 0.418 nm, as shown in **Figure 5.3.6** b. Both samples started to crystallize practically at the same temperature. However, the peak intensity suddenly increased for the nanocomposite whereas a progressive and slower evolution was detected for the neat polymer. The degree of crystallization was also evaluated from the deconvoluted profiles at selected temperatures. Values of 21% and 13% were determined at 115 ºC for the nanocomposite and the neat polymer, respectively. These observations clearly indicate a faster primary crystallization for the nanocomposite, which results from the increased primary nucleation density. Note that higher undercooling was required for the neat polymer to reach the above value of 21% (i.e. 97 ºC versus 115 ºC).

The WAXD profiles also showed that the 110 reflection of both samples became increasingly more intense over a wide temperature range (e.g. up to approximately 40 ºC). This occurred at a lower rate when temperatures were less than 115 ºC (nanocomposite) and 97 ºC (neat polymer), as expected for a secondary crystallization process. The nanocomposite was slightly less crystalline at the end of the process (28% versus 32%).

Figure 5.3.9 a and b show the time evolution of the nanocomposite WAXD profiles during a non-isothermal cold crystallization performed at a cooling rate of 3 ºC/min and the evolution of the 110 reflection intensity during crystallization for both samples, respectively. These profiles and those obtained in the hot crystallization experiments mainly differ in the lower resolution between the 020 and 101 peaks. Diffraction data clearly indicate that the cold crystallization behaviors of the neat polymer and the nanocomposite are practically identical. Thus, cold crystallizations practically ended at the same temperature (60 ºC) and a subsequent hot crystallization process occurred which ended at approximately 130 ºC. The nanocomposite became slightly less crystalline (21 versus 23%) after the end of the first cold crystallization step. This difference was similar (20 versus 22 %) when experiments were performed at 20 ºC/min (data not shown).

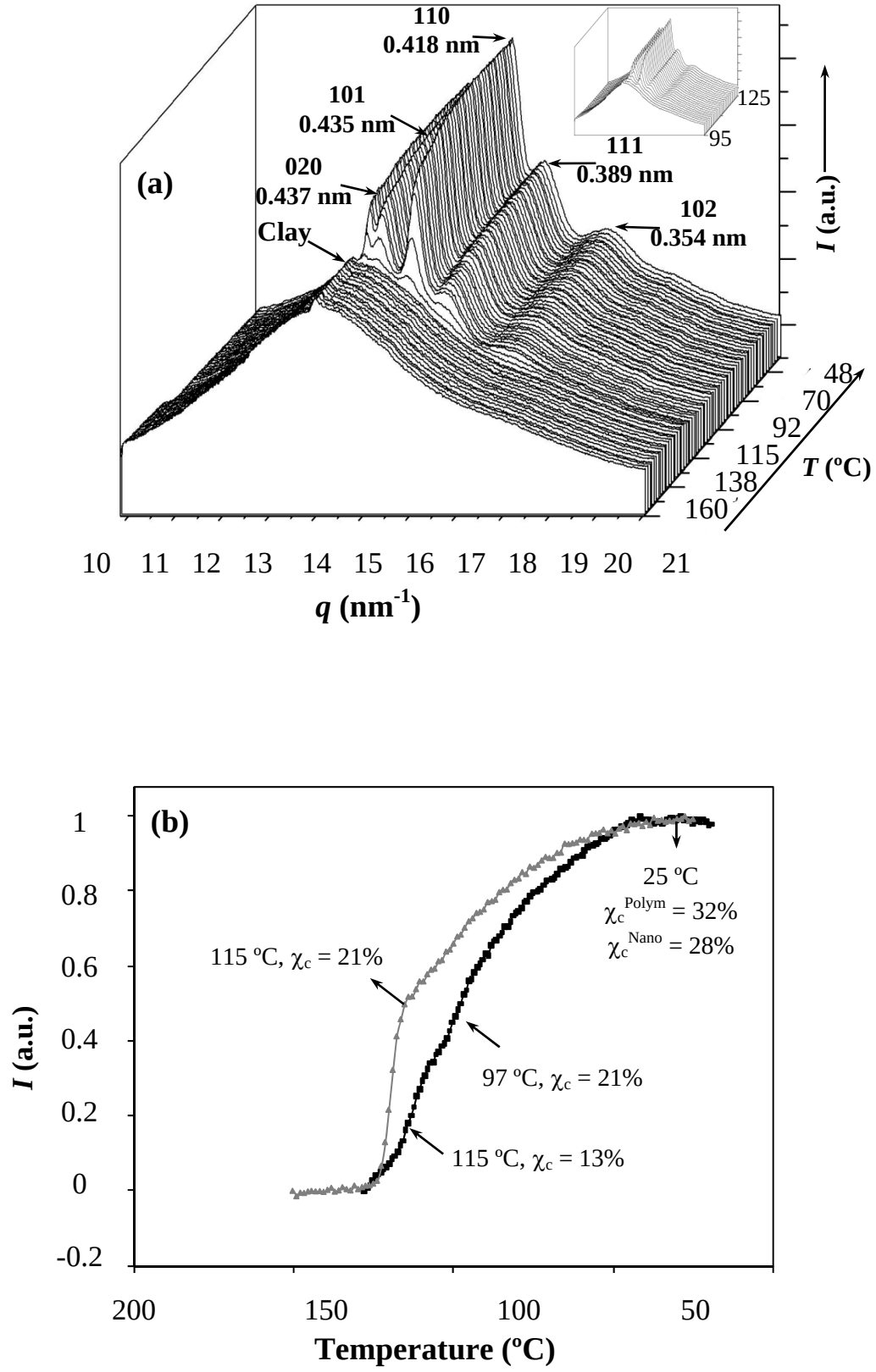

Figure 5.3.6 a) Time-resolved WAXD 3-dimensional profiles of the poly(glc-*alt*-amh)/C25A nanocomposite during the hot non-isothermal crystallization performed at a cooling rate of 3 ºC/min. Inset shows the first frames corresponding to the hot crystallization. b) Plot of the intensity of the main Bragg reflection (110) during the hot crystallization of the neat polymer (■) and the nanocomposite (▲) performed at 3 ºC/min.

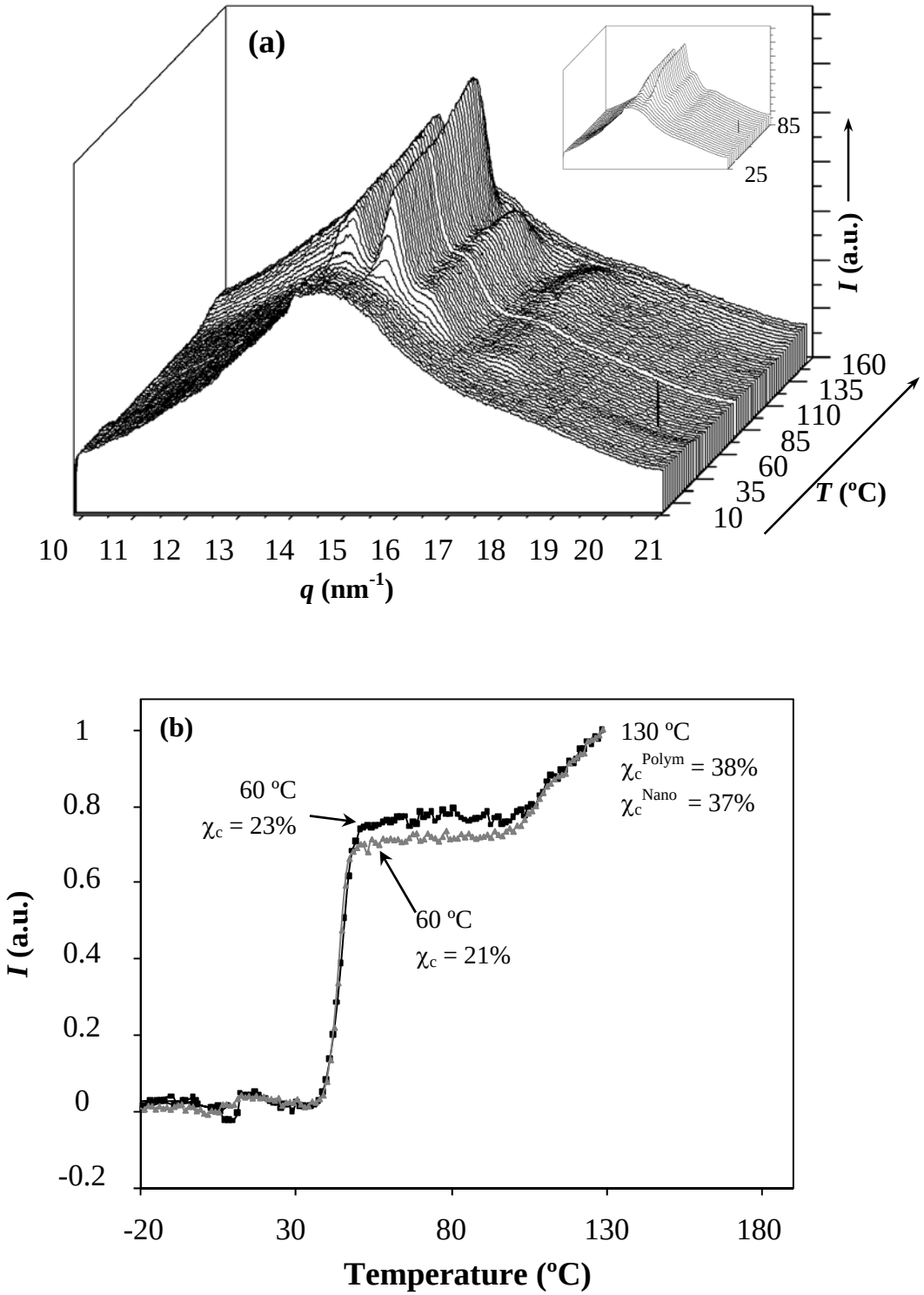

Figure 5.3.7 a) Time-resolved WAXD 3-dimensional profiles of the poly(glc-*alt*-amh)/C25A nanocomposite during the cold non-isothermal crystallization performed at 3 ºC/min. Inset shows the first frames corresponding to the cold crystallization. b) Plot of the intensity of the main Bragg reflection (110) during the cold crystallization of the neat polymer (■) and the nanocomposite (▲) performed at 3 ºC/min.

Changes in the crystalline morphology of poly(glc-*alt*-amh)/C25A nanocomposite and the neat polymer during crystallization from time-resolved SAXS experiments

A weak low angle reflection peak associated with lamellar stacking appeared in both the pristine polymer and nanocomposite samples during the cold and hot crystallization experiments (**Figure 5.3.8**). This peak was detected at the same time (or temperature) as the Bragg reflections in the WAXD patterns, as expected for a characteristic nucleation and crystal growth mechanism. The low intensity of the long spacing peak suggests that electronic differences between amorphous and crystalline phases were small. It should be pointed out that the SAXS peak only had a remarkable intensity at the last stage of the heating runs performed with quenched samples (i.e. after the hot recrystallization process).

SAXS data were analyzed by the normalized one-dimensional correlation function [31], $\gamma(r)$, which corresponds to the Fourier transform of the Lorentz-corrected SAXS profile:

$$\gamma(r) = \int_0^\infty q^2 I(q)\cos(qr)dq \;/\; \int_0^\infty q^2 I(q)dq \qquad (2)$$

SAXS data were collected within a limited angular range only. That is why extrapolations to low and high q values were performed using Vonk's model [32] and Porod's law, respectively.

Figure 5.3.9 illustrates the SAXS profiles obtained for the neat polymer and the nanocomposite at the end of non-isothermal cold and hot crystallization experiments conducted at a cooling/heating rate of 3 ºC/min. The calculated correlation functions for these profiles are shown in **Figure 5.3.10**. These functions are generally analyzed to determine: (1) the long period, L_γ, (i.e. the r value of the first maximum of the correlation function); (2) the amorphous layer thickness, l_a, (i.e. the r value of the intersection of the linear regression in the autocorrelation triangle with the ordinate equal to the first minimum of the correlation function); (3) the crystalline lamellar thickness, l_c, (calculated as $L_\gamma - l_a$); (4) the crystallinity within the lamellar stacks, χ_c^{SAXS} (calculated as l_c / L_γ); and (5) the scattering invariant, Q. Although the thicknesses associated with each phase could not be distinguished [33-35], they were assigned considering that crystallinity within lamellar stacks must always be greater than in the bulk sample deduced from WAXD data (χ_c^{WAXD}). **Table 5.3.1** summarizes the values deduced for the morphological parameters and the degrees of crystallinity attained at representative temperatures for both hot and cold crystallization experiments.

During the cold crystallization processes (**Figure 5.3.11** a and b) the long period decreased mainly because of the decrease on the crystalline lamellar thickness. On the contrary, the amorphous thickness remained practically constant (i.e. 1.7-1.4 nm). The decrease in l_c could be explained assuming a lamellar insertion mechanism which seems more significant for the nanocomposite sample. Note that although the crystalline lamellar thicknesses of both samples at the end of the cold crystallization process were similar (i.e. 6.0 and 5.2 nm at 60 ºC for the nanocomposite and the

neat polymer, respectively), the nanocomposite lamellae were clearly thicker at the initial stages of crystallization (e.g. lc values of 9.1 nm versus 7.2 nm). **Figure 5.3.11** also shows that the lamellar peak appears at a slightly higher temperature for the nanocomposite, in agreement with the calorimetric scans performed at 3 ºC/min.

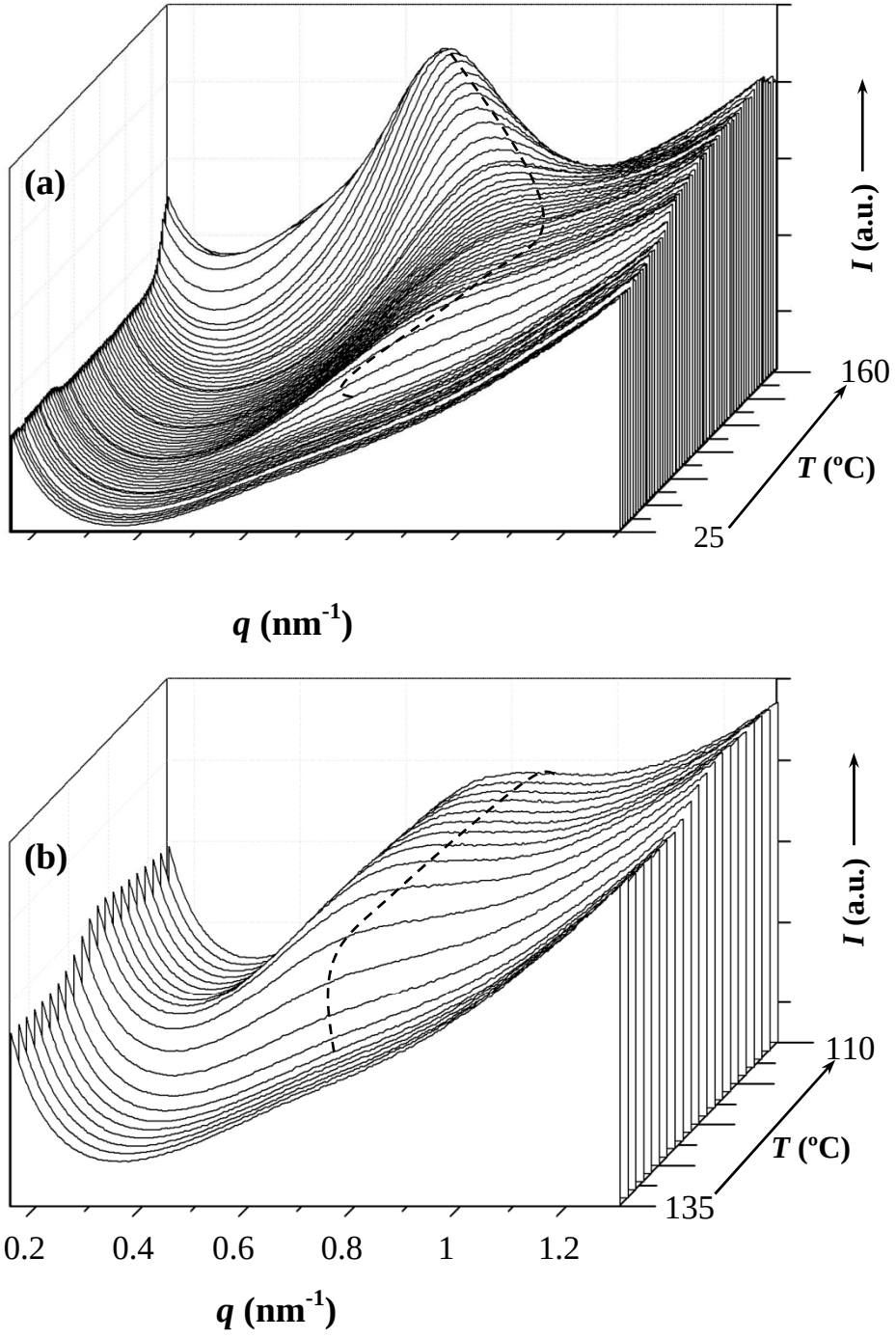

Figure 5.3.8 Time-resolved SAXS three-dimensional profiles of the poly(glc-*alt*-amh)/C25A nanocomposite during the cold (a) and hot (b) non-isothermal crystallizations performed at a heating/cooling rate of 3 ºC/min. SAXS curves after subtraction of the empty sample background and Lorentz correction.

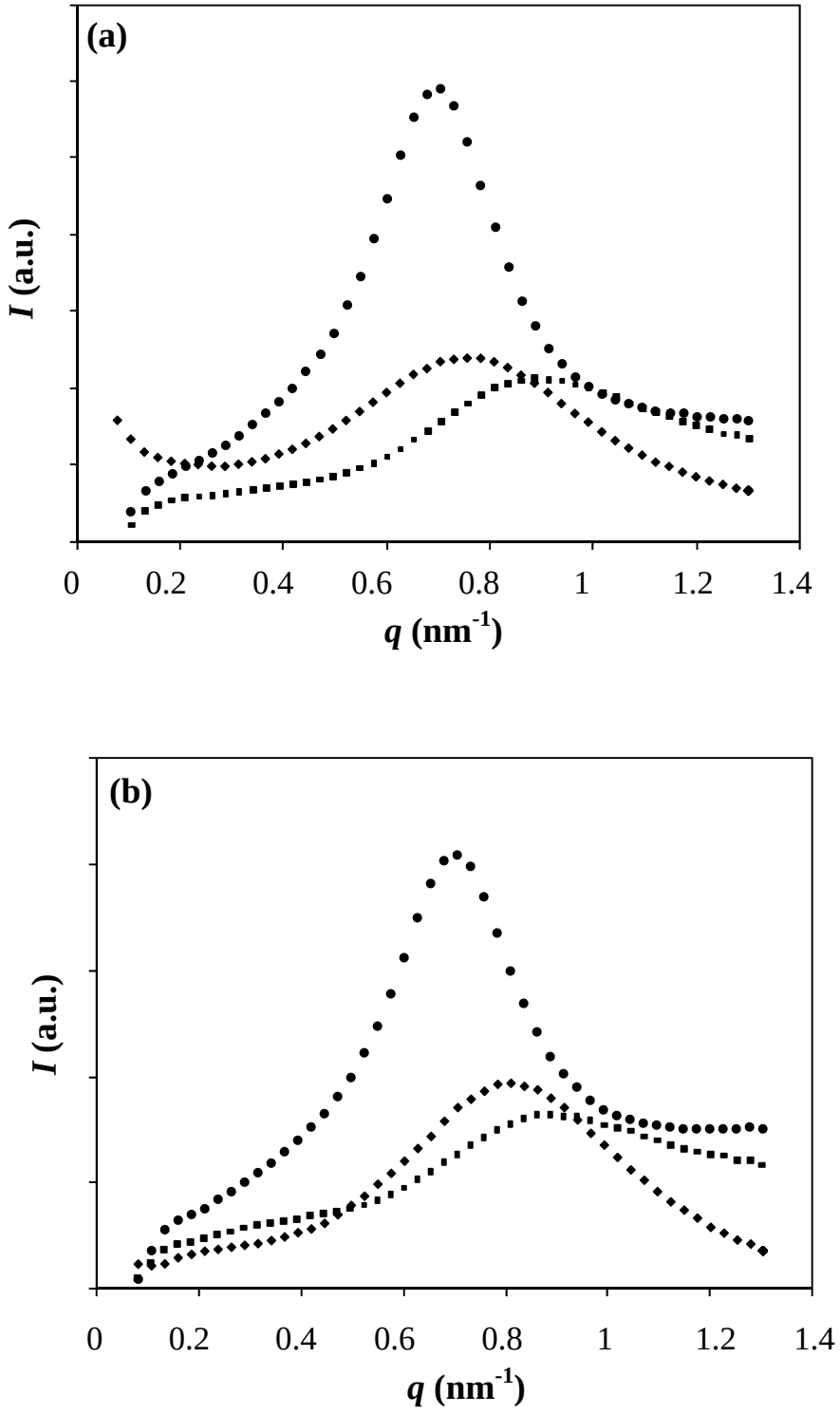

Figure 5.3.9 a) Final SAXS profiles obtained at 60 ºC for cold (■) and 40 ºC for hot (♦) crystallized samples of the neat poly(ester amide) during heating or cooling runs performed at 3 ºC/min. The profile obtained at 130 ºC after a heating run performed at 3 ºC/min (i.e. after completion of the reorganization process) is also shown (●). b) Comparison between correlation functions of the above SAXS profiles.

The long period peak shifted to higher spacings and increased in intensity when temperature was higher than 115 ºC. The maximum values for these spacings were reached at 130 ºC. According to the data in **Table 5.3.1**, the long period increased from 6.6 to 8.7 nm and from 7.5 to 8.8 nm for the neat polymer and the nanocomposite, respectively, during heating runs from 60 to 130 ºC. This suggests a lamellar reorganization that led to thicker lamellae, higher degrees of crystallinity and probably larger electronic density differences between crystalline and amorphous phases. It seems reasonable to think that at temperatures close to fusion the density of the amorphous phase decreased significantly whereas it remained practically constant for the crystalline phase. Crystalline lamellar thicknesses were also greater during the reorganization process, with slightly higher final values for the nanocomposite (i.e. 6.6 nm versus 6.2 nm).

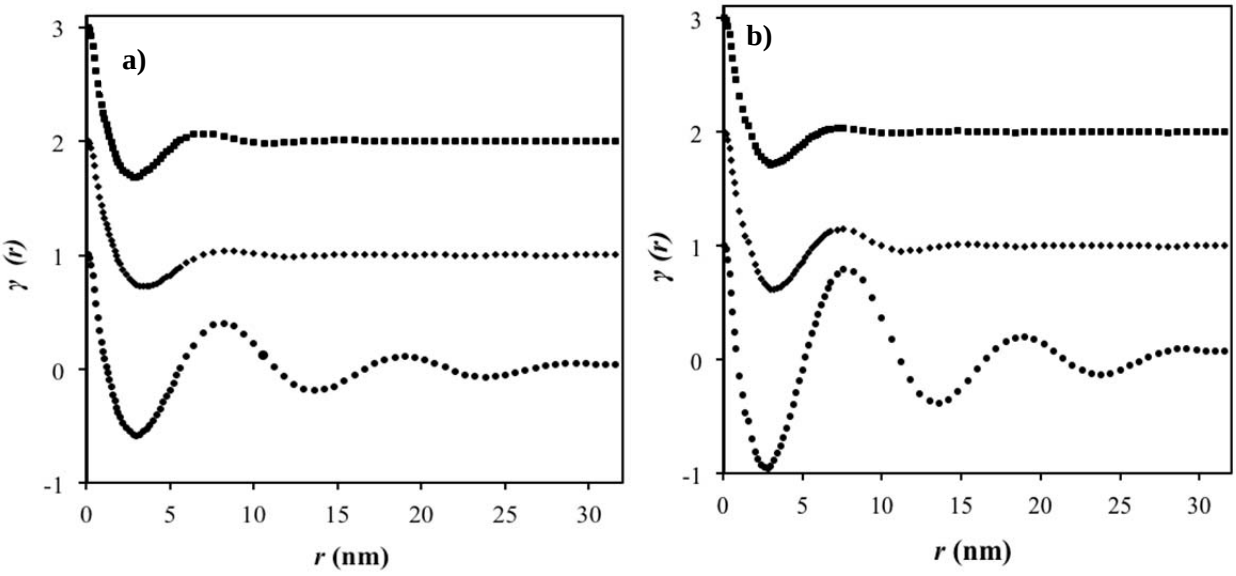

Figure 5.3.10 Correlation functions of final SAXS profiles obtained at 60 ºC for cold (■) and 40 ºC for hot (♦) crystallized samples of the neat poly(ester amide) (a) and the poly(glc-*alt*-amh)/C25A nanocomposite (b) during heating or cooling runs performed at 3 ºC/min. The correlation functions of profiles obtained at 130 ºC after a heating run performed at 3 ºC/min (i.e. after completion of the reorganization process) are also shown (●).

The hot crystallization experiments (**Figure 5.3.11** c and d) showed that the crystalline lamellar thickness at the beginning of crystallization (125 ºC) was greater for the neat polymer (9.1 versus 7.9 nm), suggesting that the presence of clay particles hindered the formation of perfect crystals from the melt state. These values were clearly higher than those found for the reorganized crystals formed at similar temperatures (130 ºC) during the cold crystallization experiments. The lamellar insertion mechanism was again favored in the nanocomposite since the decrease in crystalline lamellar thickness clearly occurred at higher temperatures than in the neat polymer (i.e. thickness started to decrease at 120 and 90 ºC, respectively). However, both samples reached a similar value at 40 ºC (i.e. 6.1 nm). These observations are in agreement with the faster primary crystallization

found for the nanocomposite from WAXD data and indeed from its narrower DSC exothermic peak. Differences in the crystalline lamellar thickness are probably the result of their different crystallization rates, which determine the instant at which the insertion mechanism takes place. In this way, the structure of the nanocomposite sample (exfoliated or intercalated) determines whether the final crystalline lamellar thickness is higher or lower than that observed for the neat polymer [36-38] since the crystallization rate is mainly influenced by the primary nucleation density.

It should be pointed out that the cooling rate at which non-isothermal crystallization was performed also affected the lamellar insertion mechanism. Thus, crystallization occurred in a narrower temperature range when experiments were performed at 20 ºC/min (data not shown), and the decrease in crystalline lamellar thickness was smaller than that observed for the lower rate of 3 ºC/min (**Table 5.3.1**).

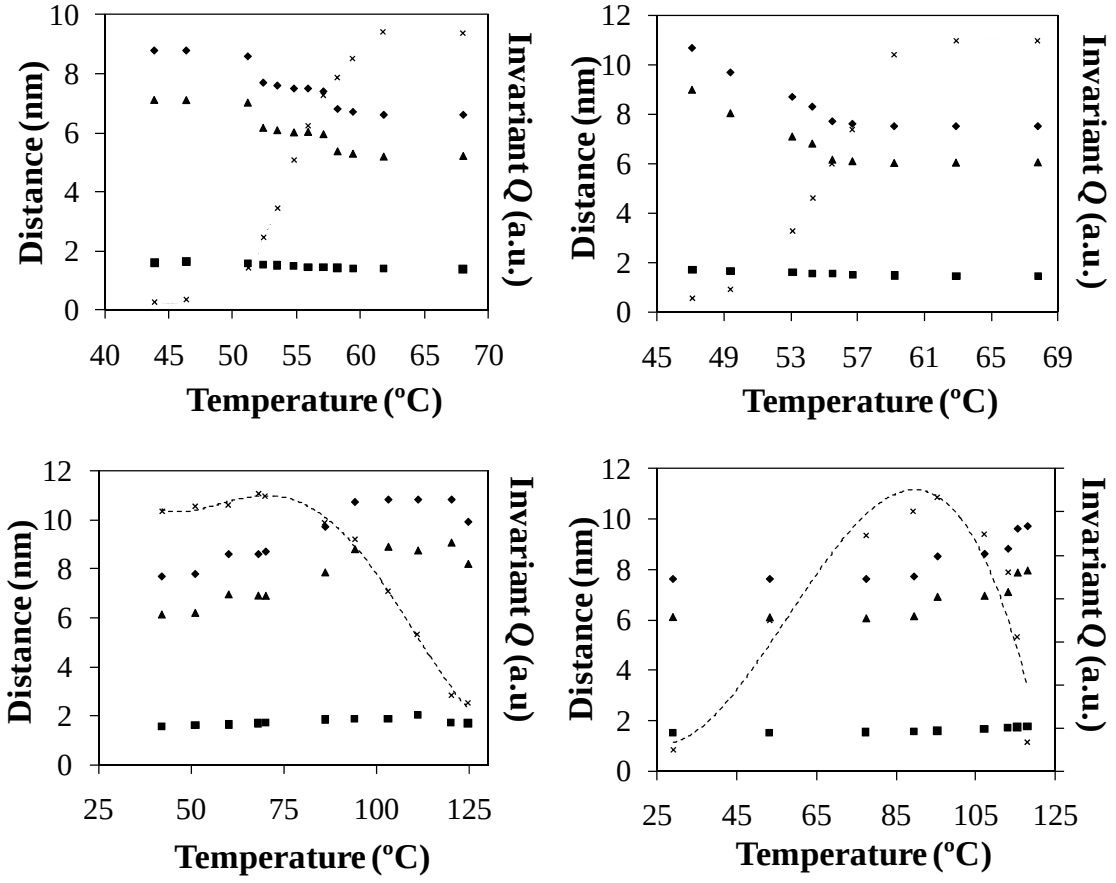

Figure 5.3.11 a) Temperature evolution of L_γ (♦) l_c (▲) l_a (■) main morphological parameters and the invariant Q (x) during non-isothermal cold (a, b) and hot (c, d) crystallizations of the neat polymer (a, c) and poly(glc-*alt*-6HH)/C25A (b, d) at 3 ºC/min.

Table 5.3.1 Morphological parameters and degree of crystallinity for the neat poly(ester amide) and its nanocomposite with Cloisite C25A during hot and cold crystallization processes.

	Neat Polymer					**Nanocomposite**				
	l_γ (nm)	l_c (nm)	l_a (nm)	χ_c^{SAXS} (%)	χ_c^{WAXD} (%)	l_γ (nm)	l_c (nm)	l_a (nm)	χ_c^{SAXS} (%)	χ_c^{WAXD} (%)
Hot Crystallization (125 ºC)[a]	10.8	9.1	1.7	83		9.7	7.9	1.8	81	
Hot Crystallization (40 ºC)[a]	7.7	6.1	1.6	79	32	7.6	6.1	1.5	80	28
Hot Crystallization (40 ºC)[b]	10.5	8.3	2.1	79	30	9.7	8.0	1.6	82	27
Cold Crystallization (45 ºC)[a]	8.8	7.2	1.6	82		10.8	9.1	1.7	84	
Cold Crystallization (60 ºC)[a]	6.6	5.2	1.4	80	23	7.5	6.0	1.5	80	21
Cold Crystallization (90 ºC)[b]	7.6	6.1	1.5	80	22	7.6	6.1	1.5	80	20
Cold crystallization (130 ºC)[a]	8.7	7.5	1.2	86	38	8.8	7.5	1.3	85	37

[a]Processes performed at a rate of 3 ºC/min.

[b]Processes performed at a rate of 20 ºC/min.

The interlamellar amorphous thicknesses of the samples remained practically constant although, as also detected in the cold crystallization experiments, a slight decrease (i.e. from 1.8-1.7 nm to 1.6-1.5 nm) was observed. It is interesting to note that the invariant (Q) decreased at low temperatures. This can only be explained by an increase in the electronic density of the amorphous phase when temperature is lowered, which probably results from the improvement of the strong intermolecular hydrogen bonding interactions. Note also the obvious differences between the neat polymer and the nanocomposite.

Comparison between cold and hot crystallization experiments showed that lamellae were thicker when spherulites were obtained from the glass state due to the reorganization process occurring at high temperatures (for cold crystallized samples) and the insertion mechanism, which was decisive at low temperatures (for hot crystallized samples), that is, when no subsequent thickening process was possible.

L_γ values of the melt reorganized samples (i.e. at the end of the cold crystallization experiments) were clearly higher than the long period determined from twice the value of the first minimum of the correlation function. In this case, the most probable distance between the centers of gravity of two adjacent crystals appeared to be similar to twice the most probable distance between the centers of gravity of a crystal and its adjacent amorphous layer. This suggests a broader distribution of the layer widths of the crystal phase, which was not so clearly detected at the end of the hot crystallization experiments, or even at the end of the cold crystallizations prior to the reorganization process.

5.3.4 Conclusion

Nanocomposites of poly(glc-*alt*-amh) and a 3% content of C25A organomodified clay with an intercalated structure were obtained by the melt mixing technique. Optical microscope studies led to the conclusion that the nucleation rate of the polymer was enhanced by the clay in both hot and cold crystallization experiments. Thus, silicate particles act as effective nucleating agents at low degrees of compatibility, a result that contrasts with previous observations on practically exfoliated structures prepared by in situ polymerization.

The addition of clay particles slightly reduced the radial growth rate, as showed in the hot crystallization experiments where the dimensions of spherulites allowed obtaining accurate measurements. Results also point to a slight increase in the secondary nucleation constant for the nanocomposite sample.

The effect of nanoparticles on the overall crystallization rate is a consequence of the balance of two opposite trends: increase in primary nucleation density and decrease in crystal growth rate, which specifically led to faster crystallization in the hot crystallization experiments.

The degree of crystallinity was always slightly lower for the nanocomposite sample, indicating a disturbing effect of the clay particles on the crystallization processes. It evolved rather differently during the hot crystallization processes, with a sudden increase at the beginning of the process in the case of the nanocomposite that reflects a faster primary crystallization mainly caused by the increase in nucleation density. The poorer nucleation of the neat polymer resulted in a time smearing of the primary and secondary crystallization.

The addition of clay particles was highly influential as it favored a lamellar insertion mechanism and caused a decrease in the average lamellar thickness. Lamellar reorganization occurred at high temperatures, resulting in similar lamellae when the nanocomposite and neat polymer samples crystallized from the glass state.

5.3.5 References

[1] R.A. Gross, B. Kalra, *Science*, **297**, 803 (2002).

[2] G.F. Moore, S.M. Saunders, *Advances in Biodegradable Polymers*. *Rapra Review Reports*, *9*, 16 (1997).

[3] L. Castaldo, F. de Candia, G. Maglio, R. Palumbo, G. Strazza, *J. Appl. Polym. Sci.*, **27**, 1809 (1982).

[4] I. Arvanitoyannis, N. Kawasaki, N. Yamamoto, *Polymer*, **36**, 857 (1995).

[5] N. Paredes, A. Rodríguez-Galán, J. Puiggalí, *J. Polym. Sci. Part A: Polym. Chem.*, **36**, 1271 (1998).

[6] R. Katsavara, V. Beridze, N. Arbuli, D. Kharadze, C.C. Chu, C.Y. Won, *J. Polym. Sci. Part A: Polym. Chem.*, **37**, 391 (1999).

[7] Villuendas, I. Molina, C. Regaño, M. Bueno, A. Martínez de Ilarduya, J. Galbís, S. Muñoz-Guerra, *Macromolecules*, **32**, 8033 (1999).

[8] H.R. Stapert, A.W. Bouwens, P.J. Dijkstra, J. Feijen, *Macromol. Chem. Phys.*, **200**, 1921 (1999).

[9] L. Asín, E. Armelin, J. Montané, A. Rodríguez-Galán, J. Puiggalí, *J. Polym. Sci. Part A: Polym. Chem.*, **39**, 4283 (2001).

[10] M. Vera, A. Almontassir, A. Rodríguez-Galán, J. Puiggalí, *Macromolecules*, **36**, 9784 (2003).

[11] P.A.M. Lips, I.W. Velthoen, P.J. Dijkstra, M. Wessling, J. Feijen, *Polymer*, **46**, 9396 (2005).

[12] E. Grigat, R. Koch, R. Timmermann, *Polym. Degrad. Stab.*, **59**, 223 (1998).

[13] A. Usuki, Y. Kojima, M. Kawasumi, A. Okada, Y. Fukushima, T. Kurauchi, O. Kamigato, *J. Mater. Res*., **8**, 1179 (1993).

[14] M. Kawasumi, *J. Polym. Sci. Part A: Polym. Chem.*, **42**, 819 (2004).

[15] S.T. Lim, Y.H. Hyun, H.J. Choi, *Chem. Mater.*,**14**, 1839 (2002).

[16] S. S. Ray, M. Okamoto, *Prog. Polym. Sci.*, **28**, 1539 (2003).

[17] S. S. Ray, M. Bousmina, *Prog. Mater. Sci.*, **50,** 962 (2005).

[18] M. Vera, A. Rodríguez-Galán, J. Puiggali, *Macromol. Rapid Commun.*, **25**, 812 (2004).

[19] M. Vera, L. Franco, J. Puiggalí, *Macromol. Chem. Phys.*, **205**, 1782 (2004).

[20] L. del Valle, F. Sepulcre, A. Gámez, A. Rodríguez-Galán, J. Puiggali, *Current Trends in Polymer Science*, **12**, 27 (2008).

[21] E. Botines, M.T. Casas, J. Puiggalí, *J. Polym. Sci. Part B: Polym. Phys.*, **45**, 815 (2007).

[22] E. Botines, J. Puiggalí, *Eur. Polym. J.*, **42**, 1595 (2006).

[23] E. Botines, L. Franco, J. Puiggalí, *J. Appl. Polym. Sci.*, **102**, 5545 (2006).

[24] L.T. Morales, L. Franco, M.T. Casas, J. Puiggalí, *J. Polym. Sci. Part A: Polym. Chem.*, **47**, 3616 (2009).

[25] D.R. Rueda, M.C. García-Gutiérrez, A. Nogales, M.J. Capitán, T. Ezquerra, A. Labrador, E. Fraga, D. Beltrán, J. Juanhuix, J.F. Herranz, J. Bordas, Rev. Sci. Instrum., ***77***, Art. No. 033904 Part 1 (2006).

[26] S. S Ray, J. Bandyopadhayay, M. Bousmina, *Eur. Polym. J.*, **44**, 3133 (2008).

[27] P.H. Nam, N. Ninomiya, A. Fujimori, T. Masuko, *Polym. Eng. Sci*., **46**, 39 (2006).

[28] J.I. Lauritzen, J.D. Hoffman, *J. Appl. Phys.*, **44**, 4340 (1973).

[29] T. Suzuki, A.J. Kovacs, *Polym. J.*, **1**, 82 (1970).

[30] S.C. Tjong , S.P, Bao, *J. Polym. Sci. Part B: Polym. Phys.*, **43**, 253 (2004).

[31] C.G. Vonk, G. Kortleve, *Kolloid Z. Z. Polym*., **220**, 19 (1967).

[32] C.G. Vonk, *J. Appl. Cryst.*, **8**, 340 (1975).

[33] B.S. Hsiao, K.H. Gardner, D.Q. Wu, B. Chu, *Polymer*, **34**, 3986 (19939.

[34] K.N. Kruger, H.G. Zachmann, *Macromolecules*, **26**, 5202 (1993).

[35] B.S. Hsiao, Z. Wang, F. Yeh, G. Yan, K.C. Sheth, *Polymer*, **40**, 3515 (1999).

[36] P. Maiti, P.H. Nam, M. Okamoto, T. Kotaka, *Polym. Eng. Sci*., **42**, 1864 (2002).

[37] S. Gestí, M. Zanetti, M. Lazzari, L. Franco, J. Puiggalí, *Eur. Polym. J.*, **45**, 398 (2009).

[38] L.T. Morales, L. Franco, M.T. Casas, J. Puiggalí, *J. Polym. Sci. Part B: Polym. Phys.*, **47**, 3616 (2010).

5.4

Crystallization behavior of clay nanocomposites prepared form a degradable alternating copolyester constituted by glycolic acid and 6-hydroxyhexanoic acid.

An exfoliated nanocomposite was prepared by the film-casting technique from C25A organo-modified clay and a new biodegradable polyester derived from glycolic acid and 6-hydroxyhexanonoic acid. This polyester has a sequential monomer distribution and high crystallinity, allowing a detailed study of its isothermal crystallization. The influence of the clay on the crystallization behavior was investigated by optical microscopy, simultaneous SAXS/WAXD synchrotron radiation and FTIR spectroscopy. Primary nucleation and crystal growth rate decreased significantly with the incorporation of nanoparticles. In addition, the overall crystallization rate of the nanocomposite was logically lower than that of the neat polyester. Bulk crystallizations were modeled from FTIR data with the Avrami equation. The results showed spherulite growth geometry and predetermined (heterogeneous) nucleation for both samples. Morphological studies revealed that both the crystal and the amorphous layer thicknesses were influenced by the presence of silicate layers. The overall percentage of crystallinity and the size of crystalline domains decreased with the addition of the highly miscible organoclay.

5.4.1 Introduction

Biodegradable polymers are regarded as a potential alternative to existing petroleum-based plastics mainly used as commodities since new political regulations tend to promote the use of environmentally friendly materials despite their higher production costs.[1,2] Aliphatic polyesters are currently the main family of degradable polymers due to the presence of a hydrolyzable ester group. However, mechanical and thermal properties are generally not useful for applications such as packaging. Several solutions have been proposed to improve performance properties. Thus, chemical modifications made by adding amide groups or aromatic dicarboxylate units have been considered and, in fact, the resulting polymers have been commercialized (e.g. BAK™, a poly(ester amide) derived from 1,4-butanediol, adipic acid and 6-aminohexanoic acid[3,4], and Ecoflex™, a polyester derived from 1,4-butanediol, adipic acid and terephthalic acid[5,6]).

The properties of materials can also be considerably modified by adding layered silicates into polymer matrices.[7-11] The resulting biodegradable nanocomposites have several advantages generally obtained at low silicate content (5 wt%). Although biodegradable nanocomposites have very good future prospects, the present low level of production and high costs still restrict them for a wide range of applications.

From a structural point of view, there are two main possible arrangements of the clay in the polymer matrix when good interactions can be established. These arrangements are the so called intercalated and exfoliated structures, although it is also usual to find a mixture of both.[12] In the intercalated system the silicate layer stacking is preserved, but the polymer is inserted between the layers. The silicate layers are fully separated and randomly dispersed in the ideal exfoliated system. In this case, the nanostructure effect is more pronounced, and properties can therefore be better enhanced.

Nanoparticles can either increase or decrease the overall crystallization rate of a semicrystalline polymer.[13] This rate depends on two processes: primary nucleation and crystal growth rate. It has been found that nanoparticles can act as a nucleating agent, increasing the bulk crystallization rate, when intercalated structures are formed.[14,15] On the contrary, nucleation density could decrease when the organo-modified clay is highly miscible with the polymer matrix (i.e. exfoliated nanocomposites).[15,16] The effects of nanoparticles on crystal growth are very contradictory.[17-21] For this reason, crystallization behavior is not fully understood. However, interactions between the matrix and nanoreinforcement seem to play a crucial role as a decrease in the growth rate is observed when they become weaker.[15,22] Crystal growth rate is related to two temperature-dependent factors: secondary nucleation and molecular transport, which should be influenced by the presence of nanoparticles.

The aims of this work are to prepare an exfoliated nanocomposite from a new biodegradable copolyester constituted by an alternating distribution of glycolic acid and 6-hydroxyhexanoic acid units, and to study the influence of clay particles on the isothermal crystallization process. Thus, overall crystallization rate, crystal growth rate and change of morphological parameters during crystallization are analyzed for both the pristine and the nanocomposite samples by FTIR spectroscopy, optical microscopy and combined SAXS/WAXD diffraction data.

It should be pointed out that related homopolymers, i.e. polyglycolide and polycaprolactone, and indeed copolymers derived from at least one of the above units are nowadays the samples with the largest number of applications as biodegradable and biocompatible materials.[23] The new semicrystalline copolyester (hereafter named poly(glc-*alt*-6HH)) can be easily synthesized by a method involving a polycondensation reaction with formation of metal halide salts as the driving force (**Scheme 5.4.1**).[24] Several studies involving its chemical and physical characterization have been conducted[25], its biocompatibility[26] has been evaluated and its application as a drug delivery system in the form of microspheres has been investigated.[27]

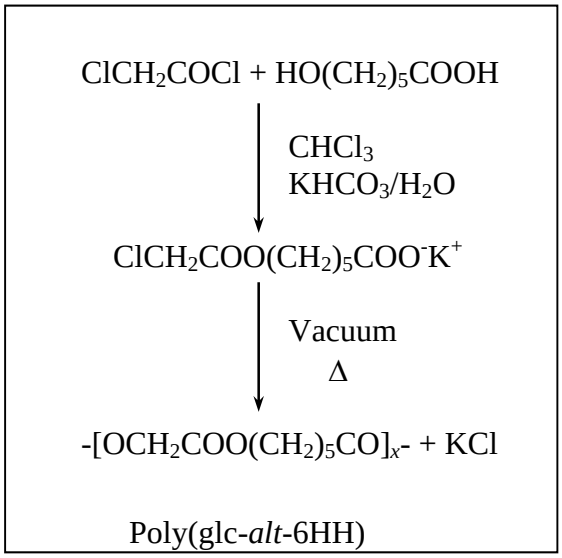

Scheme 5.4.1

5.4.2 Experimental section

Materials

Poly(glc-*alt*-6HH) was synthesized with an 80% yield by thermal polyesterification of the potassium salt of the 6-(2-chloroacetate)hexanoic acid[24] (**Scheme 5.4.1**). The intrinsic viscosity measured in dichloroacetic acid at 25ºC was 0.80 dL/g. The weight average molecular weight and polidispersity index, estimated by GPC, were 28,600 g/mol and 2.07, respectively.

Dimethyl hydrogenated-tallow 2-ethylhexyl ammonium montmorillonite (Cloisite 25A, Southern Clay Products, 2MHTEX) was used as received. The chemical structure of the specific surfactant of the organo-modified layered phyllosilicate is shown in **Scheme 5.4.2**.

CLOISITE

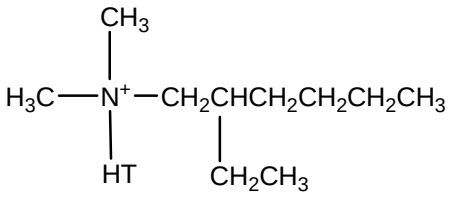

HT: hydrogenated tallow; T: tallow

(~65% C18, ~30% C16, ~5% C14)

Scheme 5.4.2 chemical structure of the organo-modified layered phyllosilicate Cloisite 25A

Preparation of nanocomposite

The nanocomposite was prepared by the solution-intercalation film-casting technique. 100 mg of the polymer was dissolved in 10 mL of chloroform and stirred for 30 min. A clay dispersion (< 0.1 wt %) was prepared in a separate beaker of chloroform and sonicated for 120 min with a Bransonic 220 sonicator. Next, the solution and the dispersion were mixed and stirred together. The amount of organo-modified montmorillonite loading was fixed at 3%. The mixture was then cast on a glass surface and the solvent was evaporated in a vacuum oven at 40 ºC. Optically clear nanocomposite films with thicknesses ranging from 20 to 35 μm were obtained.

Measurements

Intrinsic viscosity was determined using a Cannon-Ubbelhode microviscometer and a dichloroacetic acid solution at 25 ± 0.1 ºC. The molecular weight was estimated by size exclusion chromatography (SEC) using a liquid chromatograph (Shimadzu, model LC-8A) equipped with an Empower computer program (Waters). A PL HFIP gel column (Polymer Lab) and a refractive index detector (Shimadzu RID-10A) were employed. The polymer was dissolved and eluted in hexafluoroisopropanol at a flow rate of 0.5 mL/min (injected volume 100 μL, sample concentration 1.5 mg/mL). The number and weight average molecular weights were calculated using polymethyl methacrylate standards.

Interlayer spacing of the clay was studied by wide angle X-ray scattering (WAXD) using a Siemens D-500 diffractometer (Karlsruhe, Germany) with Cu K_α radiation (λ = 0.1542 nm).

Thermal degradation was determined at a heating rate of 20 ºC/min with around 5 mg samples in a Q50 thermogravimetric analyzer of TA Instruments and under a flow of dry nitrogen.

The structure and distribution of Cloisite were observed with a Philips TECNAI 10 transmission electron microscope (TEM) at an accelerating voltage of 100 kV. TEM specimens were prepared by embedding in a low viscosity modified Spurr epoxy resin and curing at 40°C for a few days and then at 60 °C for 6 h. Ultrathin sections (less than 100 nm) were cut at room temperature using a Sorvall Porter-Blum microtome equipped with a diamond knife. Finally, the sections were collected in a trough filled with water and lifted onto carbon coated copper grids.

The spherulite growth rate was determined by optical microscopy using a Zeiss Axioskop 40 Pol light polarizing microscope equipped with a Linkam temperature control system configured by a THMS 600 heating and freezing stage connected to an LNP 94 liquid nitrogen cooling system. Spherulites formed from homogeneous melt-crystallized thin films obtained by melting 1 mg of the polymer mixture on microscope slides. Next, small sections of these films were pressed or smeared between two cover slides and inserted in the hot stage. The thickness of the squeezed samples was in all cases close to 10 μm. Samples were kept at 100 ºC (more than 30 ºC above the polymer melting point of 69 ºC) for 5 minutes to eliminate sample history effects, and then quickly cooled to the selected crystallization temperature. The radius of the growing spherulites was monitored during crystallization by taking micrographs with a Zeiss AxiosCam MRC5 digital camera at appropriate time intervals. A first-order red tint plate was employed to determine the sign of spherulite birefringence under crossed polarizers.

Simultaneous time-resolved SAXS/WAXD experiments were carried out at the CRG beamline (BM16) of the European Synchrotron Radiation Facility of Grenoble. The beam was monochromatized to a wavelength of 0.098 nm. The capillary with the sample was held on a Linkam hot stage with temperature control within ± 0.1 ºC. SAXS and WAXD profiles were acquired simultaneously during crystallization experiments in time frames of 12 s. Two linear position-sensitive detectors were used [28]: the SAXS detector was calibrated with different orders of diffraction from silver behenate whereas the WAXD detector was calibrated with diffractions of a standard of an alumina (Al_2O_3) sample. The diffraction profiles were normalized to the beam intensity and corrected considering the empty sample background. Deconvolution of WAXD peaks was performed with the PeakFit v4 program by Jandel Scientific Software assuming Gaussian peak profiles. The correlation function and the corresponding parameters were calculated with the CORFUNC program[29] provided by the Collaborative Computational Project 13 for Fibre Diffraction / Non-Crystalline Diffraction, CCP13.

Infrared absorption spectra were recorded with a Fourier Transform FTIR 4100 Jasco spectrometer in a 4000-550 cm^{-1} range. A Specac Golden Gate Heated Diamond ATR Top Plate

which can be used at up to 200 ºC and a Series 4000 High Stability Temperature Controler were also employed.

5.4.3 Results and discussion

- **Dispersion structure of the C25A clay in the composite with Poly(glc-*alt*-6HH)**

The nanocomposite structure was analyzed by X-ray diffraction and transmission electron microscopy. **Figure 5.4.1** shows that the characteristic (001) phyllosilicate diffraction peak (1.93 nm) practically disappeared for poly(glc-*alt*-6HH)/C25A at a 3% clay concentration. The absence of the characteristic interlayer silicate diffraction peak may be indicative of an exfoliated structure. However, this result is also compatible with a preferred orientation of clay particles parallel to the film surface, and indeed with an intercalated structure with a broad interlayer distribution.

a)

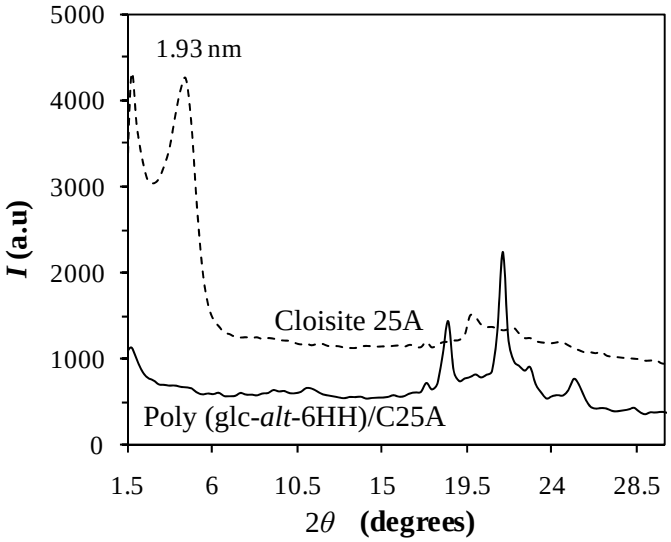

b)

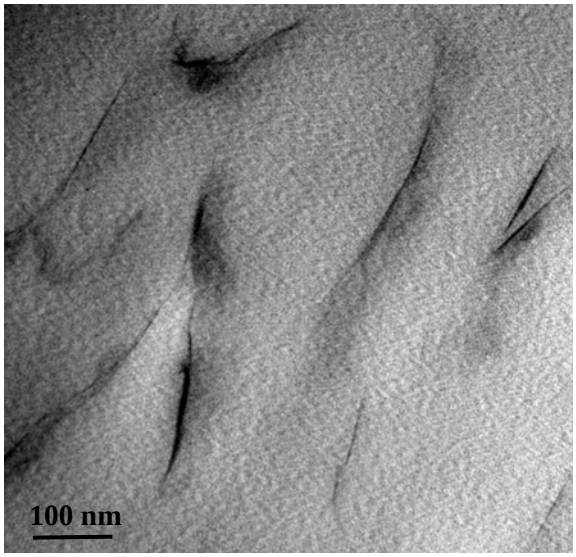

Figure 5.4.1 a) X-ray diffraction patterns of the poly(glc-*alt*-6HH)/C25A nanocomposite and the neat clay. b) Transmission electron micrograph showing the morphology of the poly(glc-*alt*-6HH)/C25A nanocomposite with a Cloisite concentration of 3%.

Direct observation of morphology and phase distribution by transmission electron microscopy of ultrathin sections of the C25A specimen revealed that an exfoliated structure was obtained (**Figure 5.4.1** b). This delamination of the layered silicate points to a high degree of miscibility between the polymer and the organo-modified clay.

Thermal stability

Figure 5.4.2 shows the thermogravimetric traces of the neat polyester and its nanocomposite with 3% of C25A. It is clear that C25A slightly improves thermal stability at the beginning of the degradation process which practically occurs in a single step. Thus, the nanocomposite reached a 10% weight loss at a temperature 10 ºC higher than the corresponding temperature of the neat polyester. In contrast, degradation of the nanocomposite was accelerated in the final stages of the process since a constant residual weight (3%) was attained when temperature reached 470 ºC, whereas at this temperature the neat polyester had a greater residual weight (7%) which progressively diminished. Note that at 560 ºC the residual weight was again greater for the nanocomposite due to its silicate content. It is assumed that, in the early stages of decomposition, clay particles may act as a heat barrier which enhances the thermal stability of the system and shifts the decomposition to higher temperatures. However, new explanations have been given in terms of a nanoconfinement that enhances intermolecular interactions, increases the energy barrier to molecular motion and decreases chemical reactivity. It has been suggested that exfoliated structures may be more efficient in confining and stabilizing polymer matrices.[30]

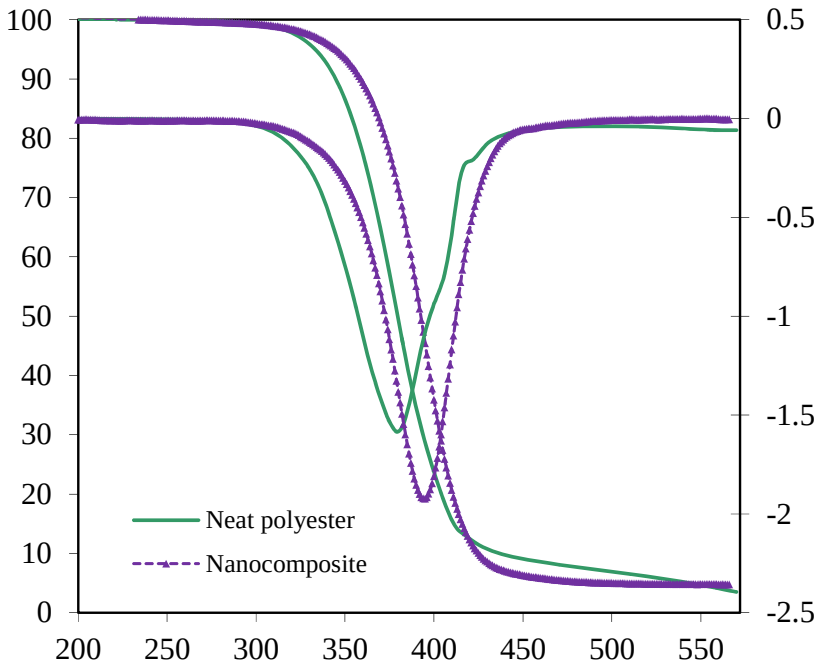

Figure 5.4.2 TGA and DTG curves of neat poly(glc-*alt*-6HH) and its nanocomposite with 3% of C25A under a nitrogen atmosphere.

- **Calorimetric data of the poly(glc-*alt*-6HH)/C25A nanocomposite**

Figure 5.4.3 a plots the DSC isothermal crystallization curves of the poly(glc-*alt*-6HH)/C25A nanocomposite at some representative temperatures. A clear exothermic peak, which becomes broader when temperature is increased, always appears. For comparative purposes, a DSC trace corresponding to the neat polyester[25] shows that, in this case, the overall crystallization rate was faster.

DSC heating traces of the isothermally crystallized nanocomposite samples are shown in b. As explained in the previous calorimetric study on the neat polyester,[25] a double melting peak could be clearly detected in the samples crystallized at the lower temperatures (42-48 ºC). The first peak was interpreted as the melting of the as-crystallized lamellae, whereas the second peak, which appeared at a constant temperature, was attributed to the melting of reorganized crystals, presumably crystallized during scanning. The increased crystallization temperature (T_c) led to thicker lamellae, and therefore to a higher melting temperature for the as–crystallized lamellae and a lower ratio of the reorganized crystals.

The method developed by Hoffman and Weeks[31] (i.e., extrapolation of the plot of T_m versus T_c to $T_m = T_c$) was used to determine the theoretical equilibrium melting temperature (**Figure 5.4.3** c). A value close to 77 ºC was estimated using the first melting peak temperature. This value was identical to that determined for the neat polyester, as can be seen in the plot which also includes the experimental data obtained with poly(glc-*alt*-6HH).

DSC heating scans of isothermally crystallized samples (not shown) revealed that the neat polyester and the poly(glc-*alt*-6HH)/C25A nanocomposite had a similar glass transition temperature well below room temperature (-36 ºC). Literature data suggest that all possibilities (increase, decrease and no variation of T_g) can occur between a pristine polymer and its nanocomposites.[32,33] Furthermore, changes in the glass transition temperature cannot be well correlated with the (intercalated or exfoliated) clay structure. [30]

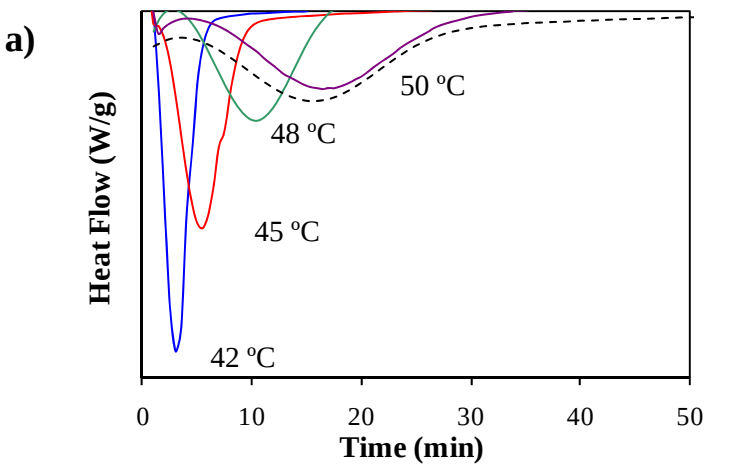
a)
Heat Flow (W/g)
50 ºC
48 ºC
45 ºC
42 ºC
0
10
20
30
40
50
Time (min)

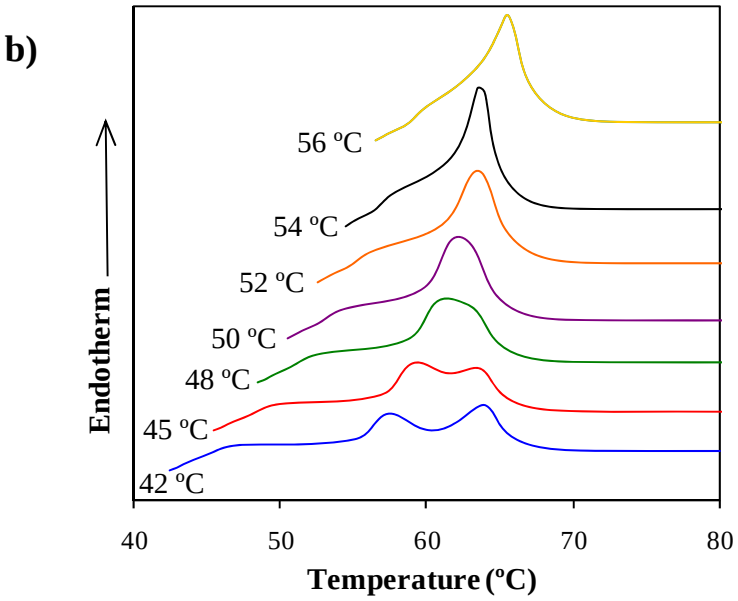
b)
Endotherm
56 ºC
54 ºC
52 ºC
50 ºC
48 ºC
45 ºC
42 ºC
40
50
60
70
80
Temperature (ºC)

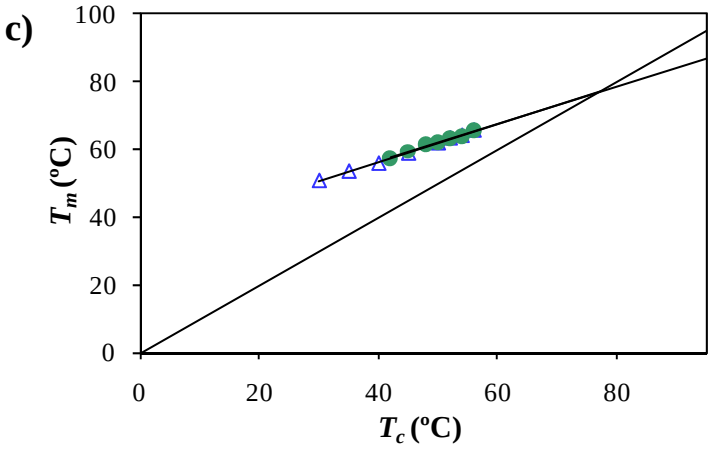
c)
100
80
60
40
20
0
T_m (ºC)
0
20
40
60
80
T_c (ºC)

Optical microscopy studies

The spherulites of the neat polyester and its C25A nanocomposite have a negative birefringence, as demonstrated by the position of the blue and yellow arms in the optical micrographs shown in **Figure 5.4.4**. A fibrilar texture was characteristic for the polyester in the studied temperature range. However, in the case of the nanocomposite, zones of zero birefringence were also detected (inset of **Figure 5.4.4** b), suggesting a twisting of lamellae.

The spherulite radial growth rates (G) of the neat poly(glc-*alt*-6HH) sample and its C25A nanocomposite were determined by observing the evolution of the spherulite radius versus time. Data for crystallization temperatures of 50, 52, 54 and 56 ºC (**Figure 5.4.5** a) showed that, at a given temperature, the nanocomposite sample always had a lower crystal growth rate, as summarized in **Table 5.4.1**. Differences were significantly reduced when the crystallization temperature was lowered.

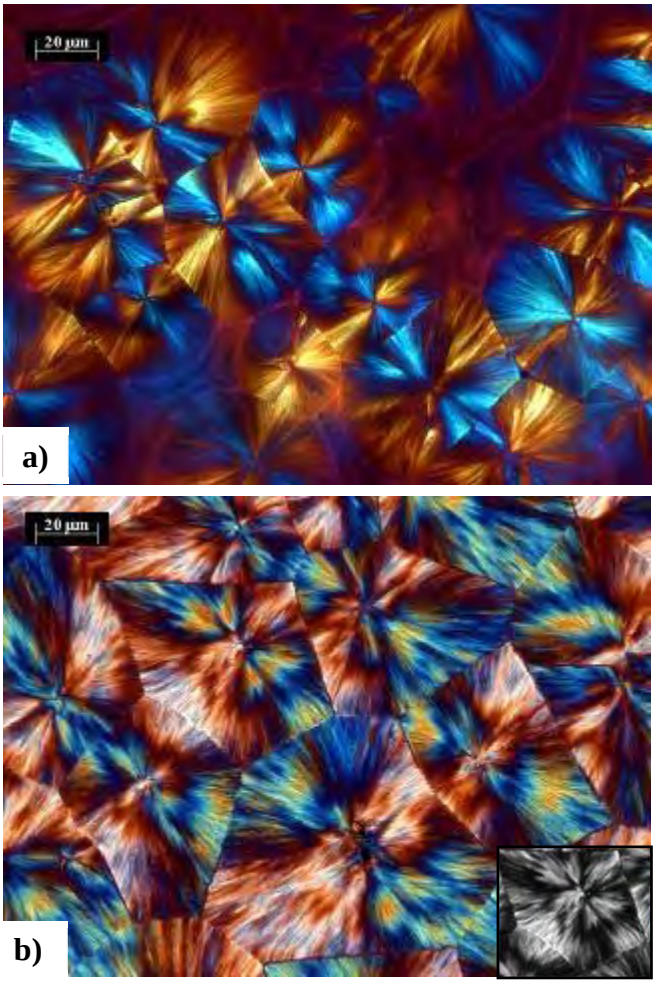

Figure 5.4.4 Optical micrographs taken at the end of isothermal crystallization at 54 ºC of the neat polyester (a) and its nanocomposite with 3% of C25A (b). Spherulites have the same negative birefringence in both samples, as demonstrated by the position of the blue and yellow arms. Zero birefringence zones can be clearly observed in the black and white micrograph shown in the inset of b).

Table 5.4.1 Growth rates of the neat poly(glc-*alt*-6HH) and poly(glc-*alt* 6HH)/C25A samples at different crystallization temperatures.

	***G* (μm/min)**	
***T*$_c$ (ºC)**	**Neat Polyester**	**Nanocomposite**
50	0.83	0.82
52	0.61	0.59
54	0.44	0.39
56	0.26	0.22

It is worth pointing out that the linear increase in the spherulite radius implies that the growth rate is independent of spherulite size and suggests that clay particles must not be excluded during spherulite growth as non crystallizable particles would build up on the crystallization growth front and hinder the transport of crystallizable species from the melt to the growing edge. In this case, a deviation from the linear tendency of spherulite growth should be observed.[15,34]

Nucleation density was also higher for the neat polyester, as deduced from the number of spherulites measured in the field of view of the optical microscope (e.g. 900 versus 525 nucleii/mm^2 at 50 ºC). This difference decreased with increasing the crystallization temperature (**Figure 5.4.5** b). **Figure 5.4.4** a and b show optical micrographs obtained at the end of the crystallization process. Spherulites of the nanocomposite sample are observed to become bigger when impingement occurs as a result of decreased nucleation density. For the same reason, crystallization induction time increased in the case of the nanocomposite (data not shown). The number of spherulites remained practically constant during crystallization of both samples, pointing to an athermal nucleation process.

Dispersed clays clearly influenced the overall crystallization kinetics since both primary nucleation and crystal growth rate led to a deceleration of the crystallization process. Similar observations of their effect on primary nucleation were reported for nanocomposites of poly(butylene succinate-*co*-adipate) with organically modified synthetic fluorine mica with a practically exfoliated structure.[16] Results contrast with the increase in primary nucleation usually observed when the clay shows an intercalated structure.[13] It has been suggested that a homogeneous dispersion of silicate platelets may hinder local lamellar crystallization since they act as obstacles for the mobility and flexibility of polymer chains to fold and join the crystallization growth front.

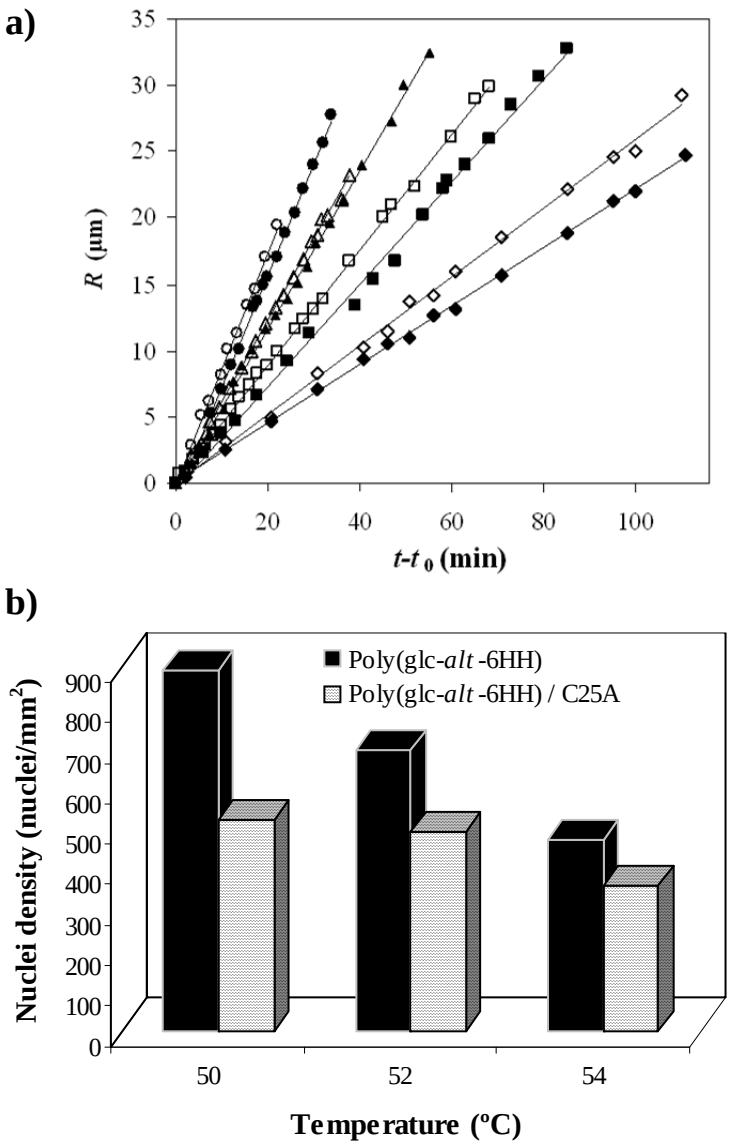

Figure 5.4.5. a) Plot of the spherulite radii of the neat polyester (empty symbols) and its nanocomposite with 3% of C25A (full symbols) versus crystallization time for isothermal hot crystallization temperatures of 50 ºC (○), 52 ºC (Δ), 54 ºC (□) and 56 ºC (◊). b) Comparison of the density of nuclei between the neat polyester and its C25A nanocomposite at three crystallization temperatures.

Spherulite growth rate could be studied with the Lauritzen and Hoffman analysis[35], which considers the influence of two independent processes, i.e. secondary nucleation and molecular transport:

$$G = G_0 \exp[-U^*/(R(T_c-T_\infty))] \exp[-K_g/(T_c(\Delta T) f)] \qquad (5.4.1)$$

where G_0 is a constant pre-exponential factor, U^* represents the activation energy characteristic of the transport of crystallizing segments across the liquid-crystal interface, R is the gas constant, K_g is the secondary nucleation constant, T_∞ is a hypothetical temperature below which motion ceases, T_c is the crystallization temperature, ΔT is the degree of supercooling measured

as $T_m^0 - T_c$ and f is a correction factor accounting for the variation in the bulk melting enthalpy per unit volume with temperature ($f = 2\ T_c / (T_m^0 + T_c)$).

When isothermal crystallization is investigated far above the glass transition temperature, the exact values of U^* and T_∞ hardly affect the temperature dependence of the radial growth rate i.e. the first exponential term of equation 5.4.1), and standard values, such as those reported by Suzuki and Kovacs[36] (U^* = 1500 cal/mol and $T_\infty = T_c - 30$ K), can be employed.

Thus, **Figure 5.4.6** shows the typical Lauritzen-Hoffman (LH) plot for the neat polyester and its C25A nanocomposite. Experimental data for both samples fit well with single linear plots, the correlation coefficient (r^2) being greater than 0.99. Crystallizations were performed within a very narrow temperature range (6 ºC), and consequently a single crystallization regime should be expected. Secondary nucleation constants of 0.50 10^5 K^2 and 0.55 10^5 K^2 were determined from the slopes of these linear plots, where the higher value corresponds to the nanocomposite. Thus, the presence of clay particles seems to have an influence on secondary nucleation, making the activation of effective nuclei on the surface of growing crystals more difficult. The effect of clay particles on the secondary nucleation process is not well understood, although works based on LH analyses have stated that differences in K_g values can be found between a neat polymer and its nanocomposites.

Clay particles may be expected to hinder molecular motion and increase the activation energy of the transport term. However, as explained above, crystallization experiments were conducted at temperatures at which the influence of this term should be minimal. In any case, in **Figure 5.4.6** it can be seen that further increase of the nucleation parameter (from 0.55 10^5 K^2 to 0.59 10^5 K^2) was found when a higher U^* parameter was considered for the nanocomposite sample (e.g. 2000 instead of 1500 cal/mol).

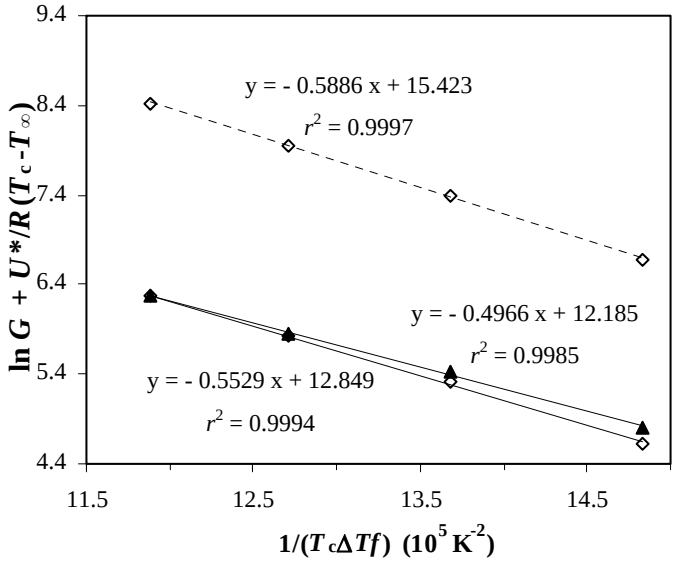

Figure 5.4.6 Lauritzen and Hoffman plots obtained from the spherulite growth rates determined for the neat polyester (▲, solid line) and its C25A nanocomposite (◊, solid line) at different isothermal crystallization temperatures and considering a transport energy parameter of 1500 cal/mol. An LH plot is also shown for the nanocomposite considering a transport energy value of 2000 cal/mol (◊, dotted line).

Crystalline morphology and isothermal crystallization data of poly(glc-*alt*-6HH)/C25A from SAXS/WAXD data

Figure 5.4.7 shows representative time-resolved SAXS and WAXD profiles of poly(glc-*alt*-6HH)/C25A obtained during isothermal crystallization at 54 ºC. A SAXS long period peak is clearly seen at a value of the scattering vector, q = [4π/λ] sin (θ), close to 0.047 $Å^{-1}$ after subtraction of the empty sample background observed near the beam stop. This long period peak can be attributed to the lamellar structure of spherulites and begins to appear at a time value which decreases with decreasing crystallization temperature. Subsequently, the peak intensity increases significantly over time until reaching a plateau value. The initial WAXD profiles show an amorphous halo whose intensity decreases with crystallization, as well as small peaks with constant intensity corresponding to the (*hk*0) clay reflections. During crystallization new Bragg reflections appear. The most intense and significant peaks correspond to the $(11\bar{1})$, (110), (020), (021) and ((022) + (111)) reflections of the polymer structure defined by an orthorhombic unit cell having a = 0.665 nm, b = 0.804 nm and c = 2.15 nm.[25] The intensities of these reflections increase significantly at the beginning of crystallization until reaching their maximum values after a short time interval. For each studied crystallization temperature, the SAXS long period peak and the crystal diffraction peaks appear simultaneously.

SAXS data were analyzed considering the normalized one-dimensional correlation function,[37] $\gamma(r)$, which corresponds to the Fourier transform of the Lorentz-corrected SAXS profile:

$$\gamma(r) = \int_0^\infty q^2 I(q)\cos(qr)dq \;/\; \int_0^\infty q^2 I(q)dq \qquad (5.4.2)$$

Data were collected only within a limited angular range. Therefore, extrapolations to low and high q values were performed using Vonk's model[38] and Porod's law, respectively.

Figure 5.4.8 a shows the final SAXS profiles of poly(glc-*alt*-6HH)/C25A isothermally crystallized within the 48-54 ºC temperature range, whereas the corresponding calculated correlation functions are plotted in **Figure 5.4.8** b. Analysis of the correlation functions allows the determination of the main geometrical parameters of the lamellar structure, assuming a simplified two-phase model: a) long period, L_γ, which corresponds to the r value of the first maximum of the correlation function; b) amorphous layer thickness, l_a, which is assigned to the r value for the intersection of the LRAT (linear regression in the autocorrelation triangle) with the ordinate equal to the first minimum of the correlation function, and c) crystalline lamellar thickness, l_c, calculated as $L_\gamma - l_a$. Crystallinity within the lamellar stacks, X_c^{SAXS}, can be easily calculated as l_c / L_γ.

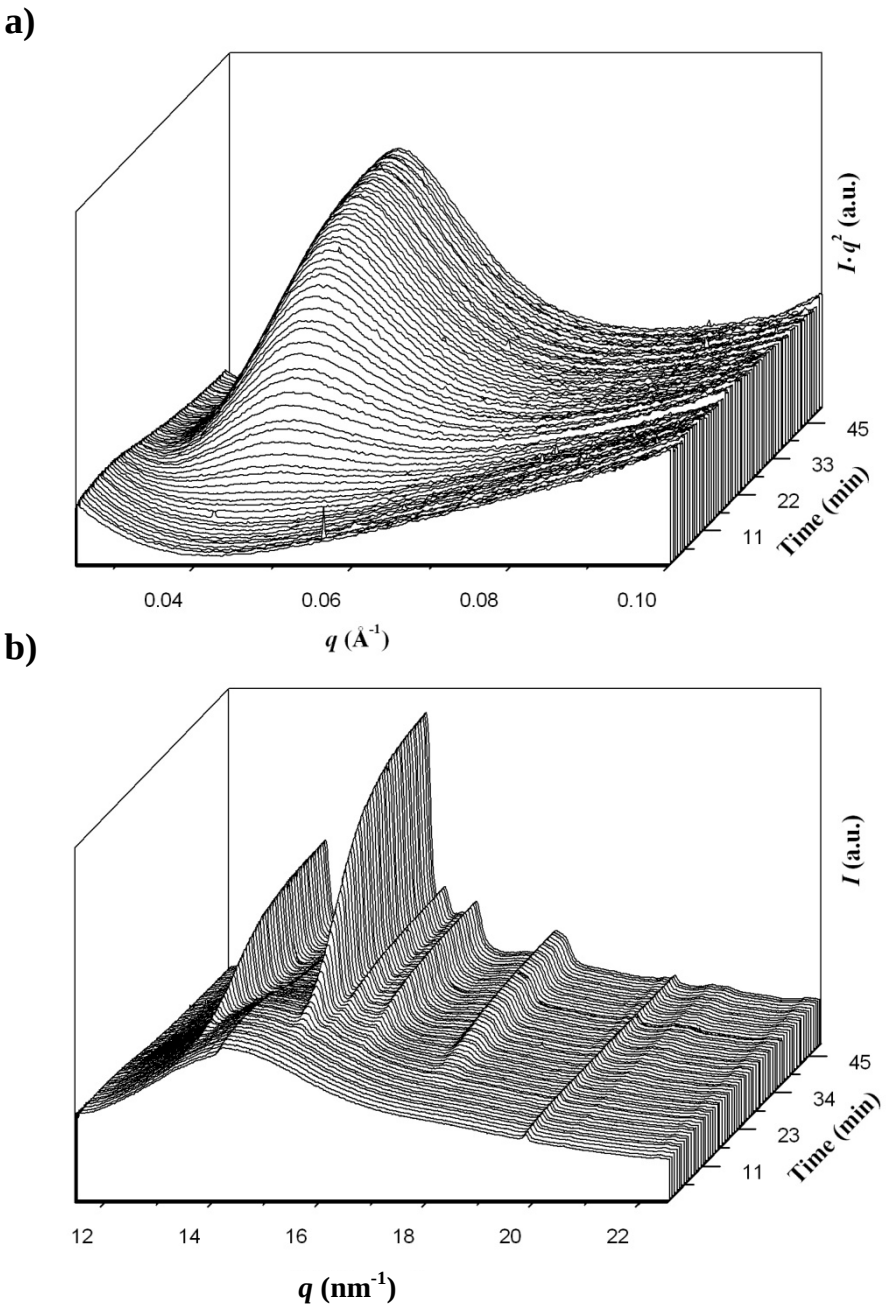

Figure 5.4.7 Time-resolved SAXS (a) and WAXD (b) 3-dimensional profiles of the poly(glc-*alt*-6HH)/C25A nanocomposite during isothermal crystallization at 54 ºC. SAXS curves are shown after subtraction of the empty sample background and Lorentz correction.

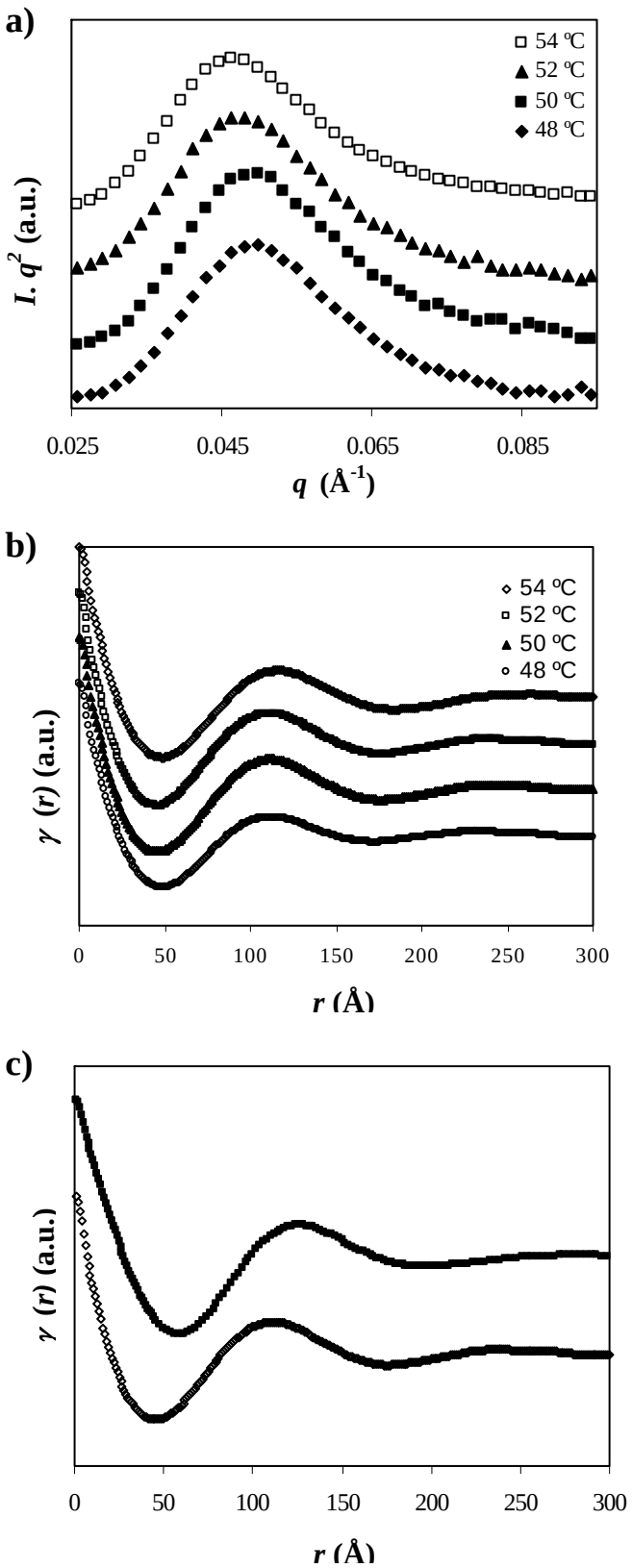

Figure 5.4.8 Final SAXS profiles (a) and corresponding correlation functions (b) at different crystallization temperatures for the poly(glc-*alt*-6HH)/C25A nanocomposite. c) Correlation functions at the end of crystallization at 50 ºC of the neat polyester (■) and its nanocomposite (◊).

The evolution of the morphological parameters of the nanocomposite during crystallization at a representative temperature of 54 ºC is displayed in **Figure 5.4.9** a. During primary crystallization, both the average long period, L_γ, and average lamellar thickness, l_c, decreased significantly, whereas they remained practically constant during secondary crystallization. The initial decrease in L_γ and l_c during primary crystallization is consistent with the formation of new crystals at a rate for which the thickening of existing lamellae is comparatively negligible. The new secondary lamellae are inserted within the loosely stacked bundles of the primary lamellae and lead to denser stacking and a decrease in L_γ. The interlamellar amorphous layer thickness, l_a, was practically constant during crystallization although a slight increase was observed at the beginning of primary crystallization. The new inserted lamellae seem to be subjected to spatial restrictions, resulting in the formation of thinner defective crystals which account for a slight increase in l_a values.

Similar trends have been described previously for neat polyester crystallization.[25] However, it is worth pointing out that the pristine sample has a significantly thicker amorphous layer whereas its lamellar thickness is slightly lower as shown in **Figure 5.4.9** b.
Figure 5.4.8 c compares also the correlation function at the end of the isothermal crystallization at 50 ºC for the two samples.

It must be noted that the difference in the lamellar morphology of the neat polyester and that of its nanocomposite lies in the amorphous layer (**Figure 5.4.9** b), which is clearly larger in the former. Higher primary nucleation and crystal growth rate may lead to more imperfect lamellar folding surfaces.

A similar slight increase in lamellar crystal thickness caused by the addition of clay particles has been described previously in the morphological study of polypropylene/clay nanocomposites and interpreted as a consequence of the insertion of some silicate layers into the inter-lamellar region.[39] Nevertheless, an opposite behavior was detected in polyoctamethylene suberate, where clay particles had an intercalated structure with variable interlayer spacing.[40] At present, literature data indicate that this question is not clear. It is therefore crucial to obtain information to reach a better understanding over the influence of clay particles on lamellar morphology.
For the nanocomposite sample L_γ was slightly higher than the long period determined from twice the value of the first minimum of the correlation function (e.g. values of 113 and 90 Å were respectively determined for the crystallization at 50 ºC). Thus, the most probable distance between the centers of gravity of two adjacent crystals is larger than twice the most probable distance between the centers of gravity of a crystal and its adjacent amorphous layer. This suggests a broader distribution of layer widths of the major component, which in this case

corresponds to the crystal phase. On the contrary, good agreement was found for the pristine polyester (e.g. both measures correspond to 120 Å for the crystallization at 50 ºC).

The geometrical parameters determined for both samples are summarized in **Table 5.4.2**, together with the crystallinity calculated within the lamellar stacks, X_c^{SAXS}. Crystallinity remained practically constant for a given sample in the studied crystallization interval, but it is interesting to note that this value was significantly higher for the nanocomposite (70 versus 80%).

Figure 5.4.9 a also shows the time evolution of the scattering invariant of the C25A nanocomposite during isothermal crystallization at 50 ºC. The evolution reveals a typical behavior where invariant *Q* exhibits a sigmoidal increase with time. After the induction time, t_1, the SAXS profile starts to show a peak whose intensity increases continuously at a rapid rate. Primary crystallization occurs between t_1 and the time at which secondary crystallization starts, t_2. In the case of the neat polymer, this time is slightly shorter for a given crystallization temperature (e.g. 1100 and 600 s were determined for crystallization at 50 ºC of the nanocomposite and the neat polyester), as expected for a higher crystallization rate.

Table 5.4.2. Morphological parameters and degree of crystallinity determined from SAXS measurements during isothermal crystallization of the neat polyester and its nanocomposite with the C25A clay.

Temperature (ºC)	Neat Polyester[a]				Nanocomposite			
	L_γ (Å)	l_c (Å)	l_a (Å)	X_c^{SAXS}	L_γ (Å)	l_c (Å)	l_a (Å)	X_c^{SAXS}
35	110	78	32	0.71				
40	115	79	36	0.68				
45	117	80	37	0.68				
48					111	89	22	0.80
50	120	83	37	0.69	113	91	22	0.80
52					115	93	22	0.81
54					117	94	23	0.80
55	125	85	40	0.68				

[a] Data from reference 28

The evolution of crystallinity of samples was estimated by WAXD. Thus, the integrated intensity for each crystal reflection and the amorphous background were measured for the time-resolved spectra obtained during isothermal crystallization. A Gaussian-Lorentzian peak riding on a baseline was used to fit the amorphous background. All the other crystal reflection peaks were also fitted with Gaussian-Lorentzian functions (**Figure 5.4.10** a). The division of the total intensities of the crystalline reflections I_c by the overall intensity I_T gave a measure of the mass fraction of the crystalline phase in the sample. This value, X_c^{WAXD}, was termed as apparent mass

crystallinity since, owing to possible distortions in the crystal lattice and thermal disorder, the measured value of I_c might underestimate the true value of crystallinity.

The time evolution of WAXD crystallinity at the isothermal crystallization temperature of 50 ºC is displayed in **Figure 5.4.10** b for the neat polyester and its nanocomposite. It is clear that the overall crystallization proceeded faster in the neat polyester and also that a higher degree of crystallinity was attained in this sample (45% versus 33%). These absolute crystallinities did not change significantly (from 45 to 47% and from 33 to 35%) with crystallization temperature in the studied range of 45-55 ºC for the neat polyester and 48-54 ºC for the nanocomposite sample. There was also good agreement between the evolution of the SAXS invariant, *Q*, and the degree of crystallinity evaluated by *WAXD* for both samples.

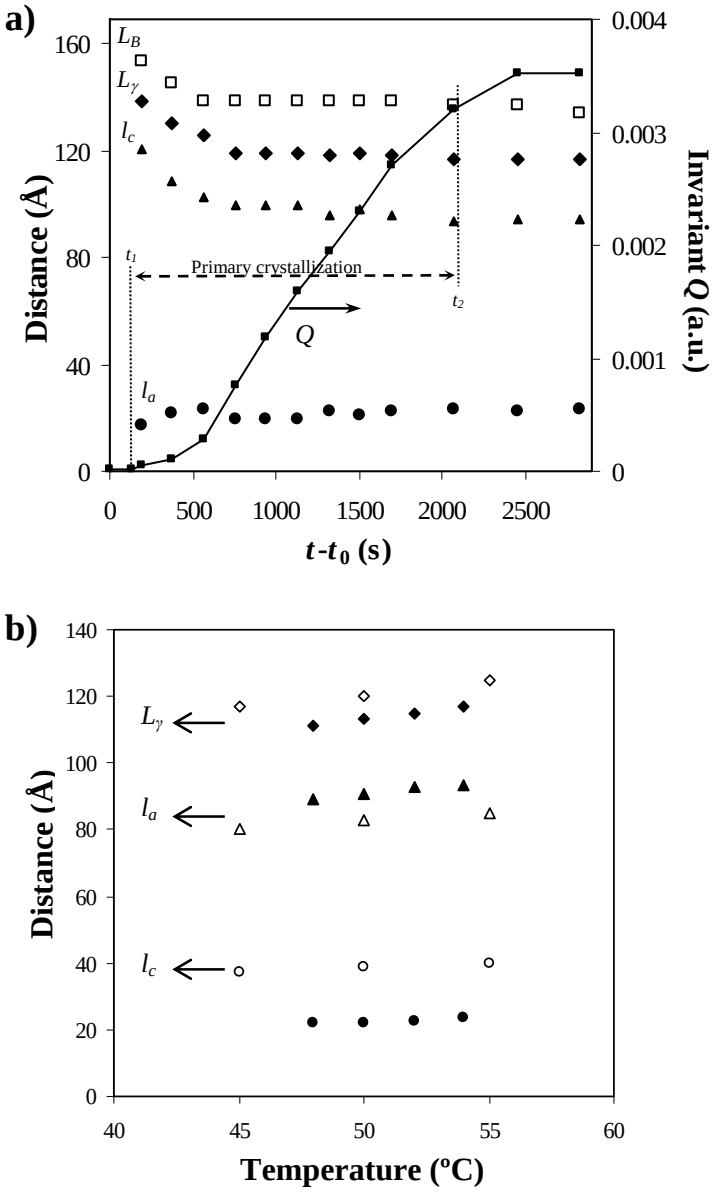

Figure 5.4.9 a) Time evolution of main morphological parameters and the invariant during isothermal crystallization at 54 ºC of poly(glc-*alt*-6HH)/C25A. b) Final lamellar spacings at various crystallization temperatures for the neat polyester (empty symbols) and its nanocomposite (full symbols).

Combinated SAXS and WAXD data can be used to verify the assignment of l_a and l_c thicknesses, which cannot be distinguished from the analysis of the correlation function.[41-43] Thus, the ratio between X_c^{WAXD} and X_c^{SAXS} is an estimate of the volume-filling fraction of the lamellar stacks, X_S. Ratios of 0.58 and 0.39 were determined for the neat polyester and the nanocomposite at the end of crystallization, respectively. Note that the opposite assignment of the amorphous and crystalline layer thicknesses should render an unrealistic ratio greater than one. The determined ratios point to the existence of amorphous domains between lamellar stacks of the studied samples, which appear less significant for the neat polyester.

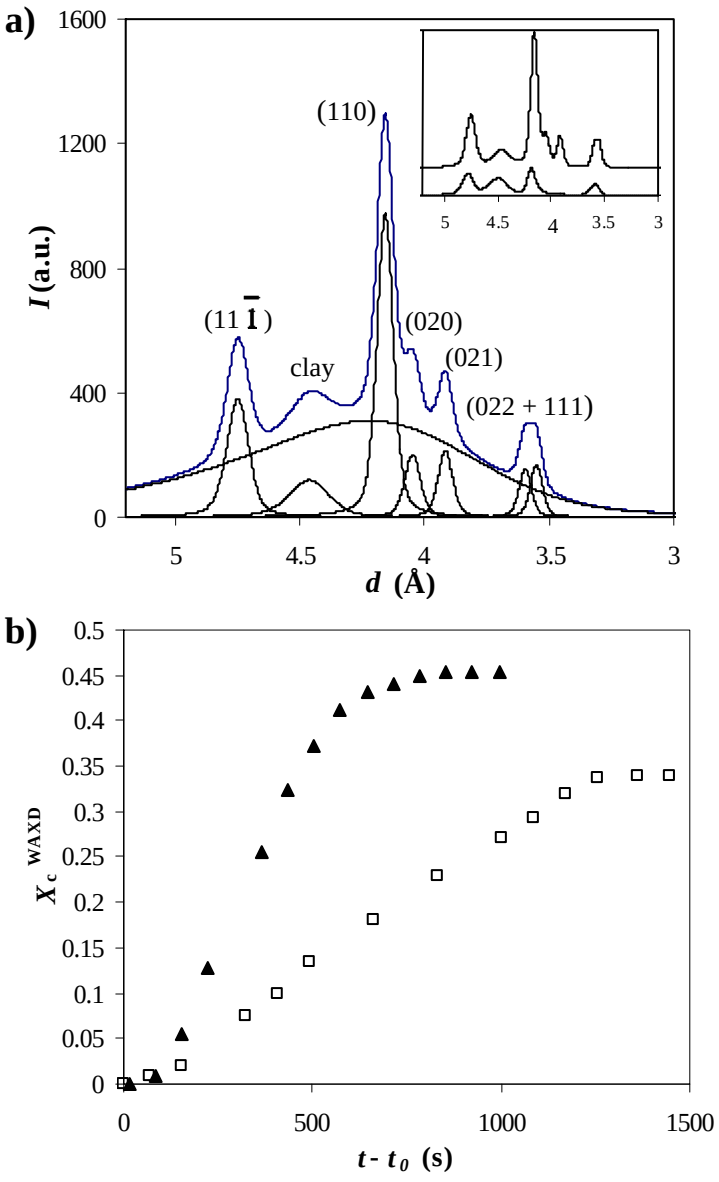

Figure 5.4.10 a) Deconvolution of the WAXD profile corresponding to the end of isothermal crystallization at 50ºC of the nanocomposite. Inset shows the profiles obtained after elimination of the amorphous halo in the early (850 s) and final (2900 s) stages of this crystallization. b) Evolution of crystallinity determined from WAXD data during isothermal crystallization at 50ºC of the neat polyester (▲) and its nanocomposite (□).

Isothermal crystallization kinetics of poly(glc-*alt*-6HH) and its C25A nanocomposite from FTIR analyses

FTIR is highly sensitive to molecular conformation and packing density, hence its usefulness in polymer crystallization studies. Characteristic bands can be correlated to the crystalline and amorphous phases of the bulk and typically remain distinguishable over the course of crystallization. Isothermal studies are preferred to avoid shape susceptibility and intensity of FTIR bands with temperature.

Figure 5.4.11 compares the absorption infrared spectra (1050-1000 cm^{-1}) of the neat polyester in the molten state and at the end of an isothermal crystallization performed at 50 ºC. It is clear that different bands in this region can be assigned to the crystalline (1420, 1234 and 1222 cm^{-1}) or the amorphous phase (1282 and 1196 cm^{-1}) since their absorptions increase or decrease, respectively, during the crystallization process. The continuous evolution of the absorption bands is shown in **Figure 5.4.12** for a representative example corresponding to the isothermal crystallization at 50 ºC of the neat polyester. The opposite behavior (not shown) is logically observed during a heating run of a semicrystalline sample. **Figure 5.4.13**a shows that the five selected bands exhibit a similar behavior for a given sample and crystallization temperature. Note that in all cases absorption values started and stopped changing at the same crystallization time and that the maximum absorption change was also detected at a similar time. Thus, it seems feasible to perform a crystallization kinetic analysis by considering the evolution of these absorption bands.

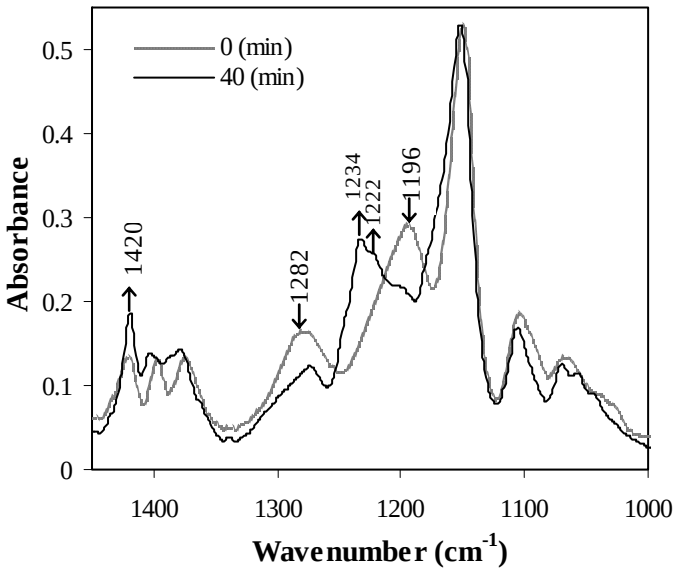

Figure 5.4.11 Absorption FTIR spectra (1500-1000 cm^{-1}) of the neat polyester at the beginning and the end of isothermal crystallization at 50ºC.

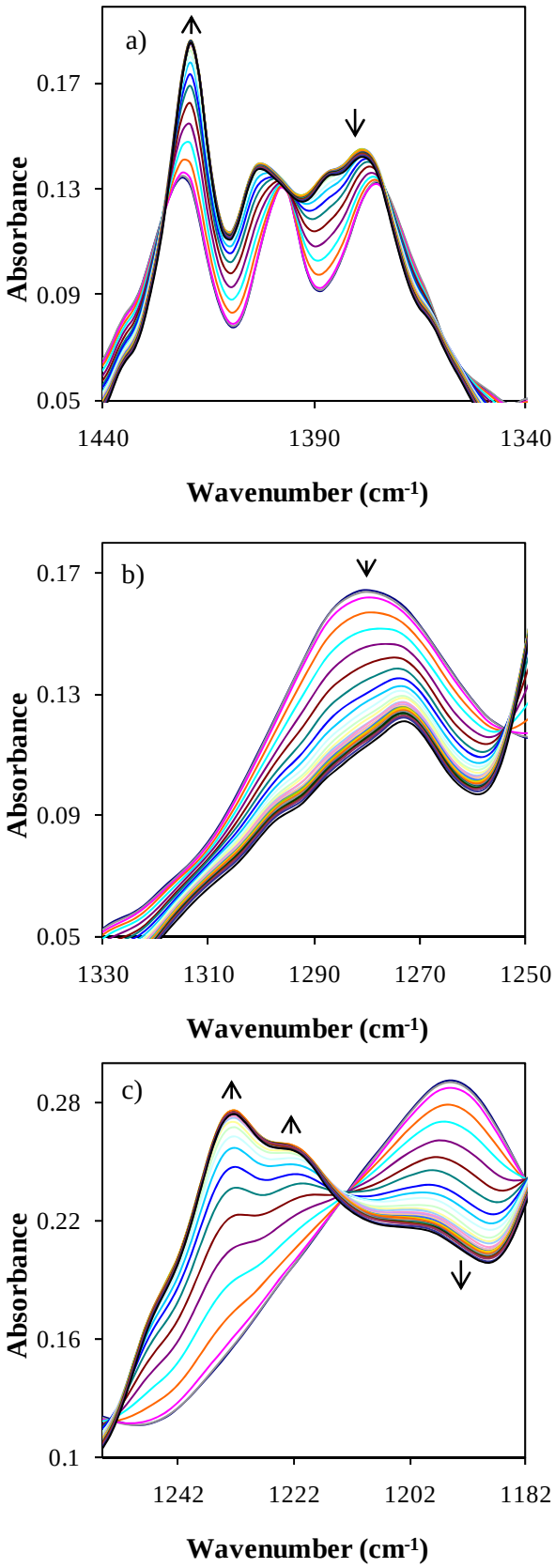

Figure 5.4.12 Changes in the infrared absorption bands at 1420 cm^{-1} (a), 1282 cm^{-1} (b) and 1234, 1222 and 1196 cm^{-1} (c) of the neat polyester during isothermal crystallization at 50ºC.

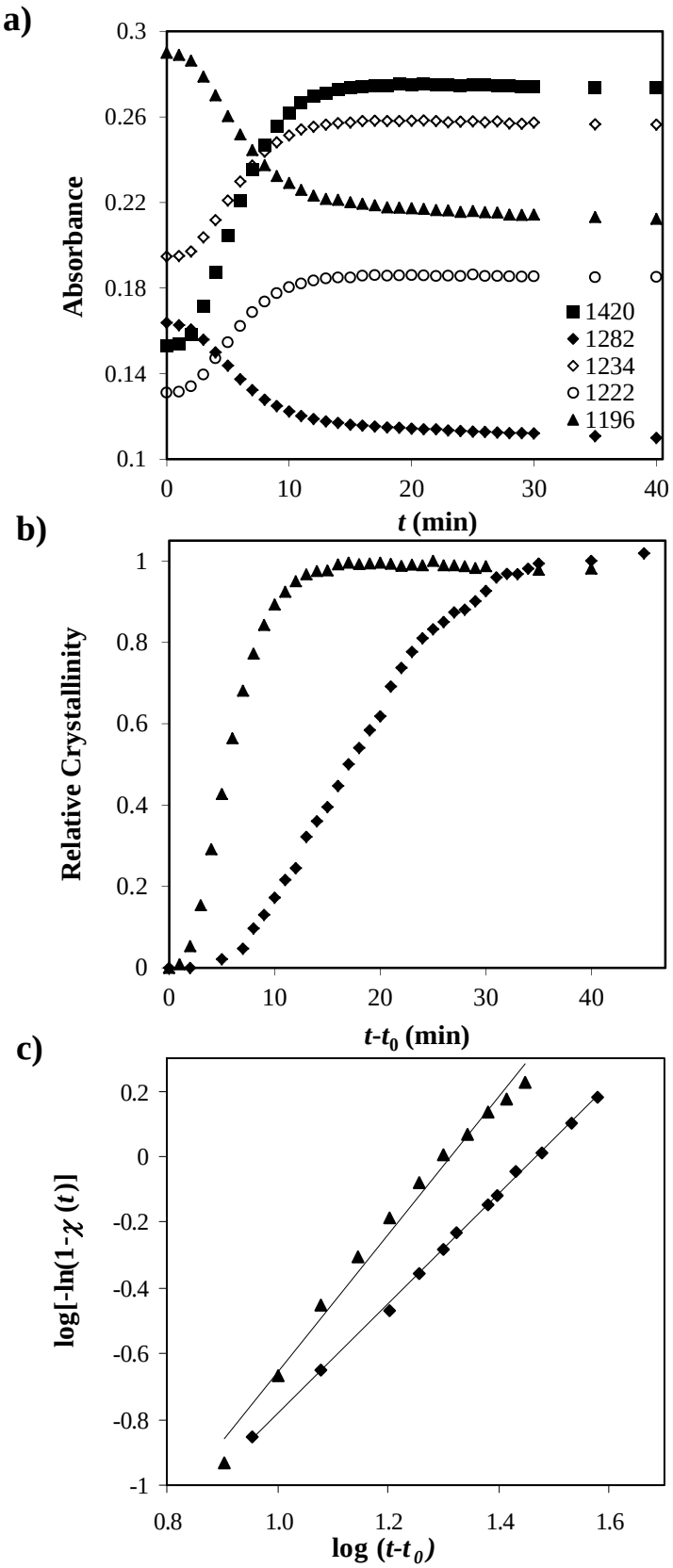

Figure 5.4.13 a) Time evolution of the absorption of selected infrared bands for isothermal crystallization at 50ºC of the neat polyester. Characteristic bands of the amorphous (1282 and 1196 cm^{-1}) and crystalline phases (1420, 1234 and 1222 cm^{-1}) were chosen. b) Time evolution of relative crystallinity deduced from FTIR data (1420 cm^{-1} band) for isothermal crystallization at 50ºC of the neat polyester (▲) and its nanocomposite (♦). c) Avrami plot considering FTIR data (1420 cm^{-1} band) for isothermal crystallization at 50ºC of the neat polyester (▲) and its nanocomposite (♦).

A relative degree of crystallinity, $\chi(t)$, can be defined and measured for any characteristic absorption band associated with the crystalline (equation 5.4.2) or the amorphous phase (equation 5.4.3):

$$\chi(t) = (A_t - A_0) / (A_\infty - A_0) \quad (5.4.2)$$

$$\chi(t) = (A_t - A_\infty) / (A_0 - A_\infty) \quad (5.4.3)$$

where A_t is the absorption measured at a crystallization time t, and A_0 and A_∞ are the initial and final absorptions of the considered band. **Figure 5.4.13** b compares the evolution of crystallinity, evaluated through absorption measurements of the band at 1420 cm^{-1} for the neat polyester and the nanocomposite at a crystallization temperature of 50 ºC. It is again clear that crystallization of the neat polyester proceeds faster.

Kinetic crystallization data were analyzed by the Avrami equation[44-46] for primary crystallization, i.e.:

$$1 - \chi(t) = \exp[-Z(t-t_0)^n] \quad (5.4.4)$$

where Z is the temperature-dependent rate constant and n the Avrami exponent, whose value varies according to the crystallization mechanism. This mechanism is composed of two steps: nucleation, which can be either homogeneous or heterogeneous depending on how nuclei are formed, and crystal growth geometry.

A normalized rate constant, $k = Z^{1/n}$, is usually evaluated for comparison purposes since its dimension ($time^{-1}$) is independent of the Avrami exponent value.

Plots of log $\{-\ln[1-\chi(t)]\}$ against log $(t - t_0)$ for a given sample and crystallization temperature give straight lines (**Figure 5.4.13** c) with slopes corresponding to the Avrami exponents and intercepts at log $(t - t_0) = 0$ equal to log Z. The results were practically independent of the absorption band considered, as can be seen in **Table 5.4.3**.

Avrami exponents of both samples were practically constant in the studied range of crystallization temperatures. Furthermore, the exponents did not change significantly with the addition of nanoparticles, suggesting that crystal growth nucleation and dimensionality remained unaffected. The average value of 2.16-2.12 suggests a predetermined (heterogeneous) nucleation with spherical growth geometry, the ideal of n for such a situation being 3. The alternative interpretation of $n = 3$, i.e. sporadic (homogeneous) nucleation and disk-like growth geometry, was discarded since this is expected to occur at large supercoolings and for thin films. Optical microscopy observations indicated a spherulite growth and an athermal nucleation, in full agreement with the given interpretation of the Avrami exponent. It should also be noted that the Avrami exponent reflects the geometry of spherulites during growth and can be affected by numerous factors. Several explanations have been provided to justify such a fractional Avrami exponent (e.g. truncation effects between spherulites).

Figure 5.4.14 shows that a good correlation between the overall crystallization rate and the reciprocal of the crystallization half time, $\tau_{1/2,}$ is found for the neat polyester and its nanocomposite. These time values, summarized in **Table 5.4.2** for all experiments, can be easily estimated from the conversion curves. Note that they were measured without using kinetic equations; hence, the indicated fit demonstrates the goodness of the Avrami analysis.

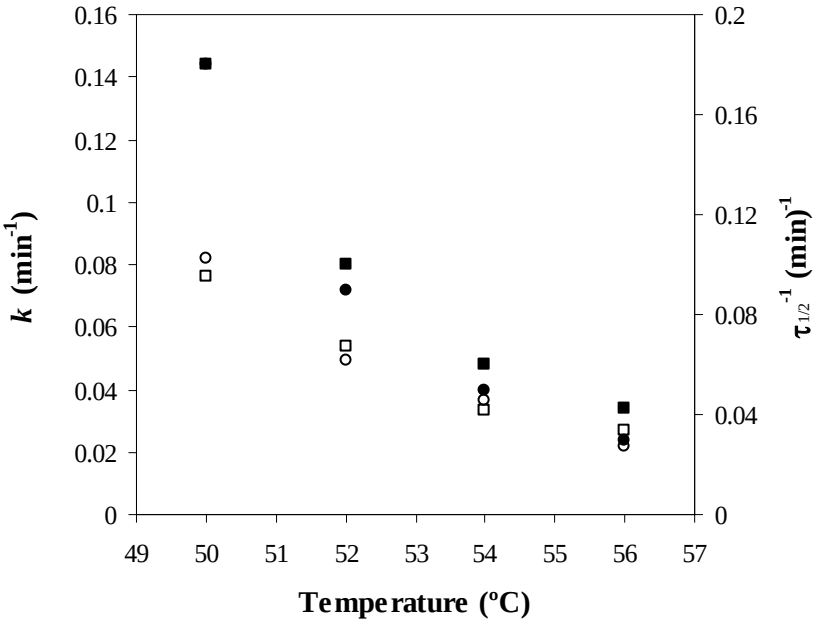

Figure 5.4.14 Comparison between the overall crystallization rate (□) and the reciprocal of the crystallization half time (○) determined at different isothermal crystallization temperatures for the neat polyester (full symbols) and its nanocomposite (empty symbols).

Table 5.4.3 . Kinetic parameters derived from the FTIR analysis of the isothermal hot crystallization of the neat poly(glc-*alt*-6HH) sample and its nanocomposite with the C25A clay.

Temperature (ºC)	Parameter	Neat Polyester					Nanocomposite				
		Wavenumber (cm^{-1})					Wavenumber (cm^{-1})				
		1420	**1234**	**1222**	**1196**	**Average**	**1420**	**1234**	**1222**	**1196**	**Average**
50	*n*	2.38	2.33	2.79	1.71	2.30	2.53	2.54	2.52	1.75	2.34
	$\tau_{1/2}$ (min)	5.54	5.60	6.14	5.54	5.70	12.02	11.86	11.32	12.02	11.81
	k (min^{-1})	0.15	0.14	0.15	0.13	0.14	0.074	0.074	0.076	0.078	0.076
52	*n*	2.38	2.36	2.39	2.27	2.35	2.37	2.38	2.66	1.83	2.31
	$\tau_{1/2}$ (min)	10.74	11.02	10.821	11.56	11.04	15.57	16.53	16.51	16.13	16.18
	k (min^{-1})	0.075	0.074	0.074	0.071	0.073	0.053	0.058	0.056	0.049	0.054
54	*n*	2.09	2.07	2.13	2.06	2.09	1.66	1.65	1.66	1.54	1.62
	$\tau_{1/2}$ (min)	16.53	16.67	15.94	16.98	16.53	21.77	21.39	21.18	23.83	22.04
	k (min^{-1})	0.049	0.048	0.050	0.047	0.0485	0.033	0.034	0.034	0.030	0.033
56	*n*	1.74	2.05	1.80	2.41	2.00	2.10	2.56	2.17	1.97	2.20
	$\tau_{1/2}$ (min)	30.58	31.58	30.20	37.51	32.47	36.85	36.52	36.25	37.80	36.86
	k (min^{-1})	0.033	0.034	0.040	0.028	0.034	0.027	0.026	0.029	0.024	0.027

5.4.4 Conclusions

Nanocomposites of C25A organo-modified clay and a new biodegradable polyester characterized by an alternating distribution of glycolic acid and 6-hydroxyhexanoic acid units were prepared by the solvent-casting technique. X-ray and TEM observations revealed full dispersion of silicate layers and suggested high miscibility between the polymer matrix and the clay. Thermogravimetric analyses showed that the addition of clay particles had a small stabilization effect at the beginning of the degradation process, which is currently interpreted as a consequence of polymer chain nanoconfinement.

The semicrystalline character of the new polyester allowed the study of the influence of clay particles on crystallization kinetics and crystal morphology. Thus, incorporation of C25A decelerated the mechanism of primary nucleation and crystal growth of poly(glc-*alt*-6HH), a trend commonly observed when high homogeneous dispersion of silicate layers occurs. A slight increase in the secondary nucleation constant was also inferred for the nanocomposite by considering the Lauritzen and Hoffman treatment.

FTIR and WAXD data obtained during isothermal crystallization were consistent and indicated a decrease in the overall crystallization rate when silicate layers were added. Optical microscopy revealed differences in spherulite morphology between the neat polyester and its nanocomposite. Furthermore, SAXS data showed significant changes in the morphology of constitutive lamellae since a dramatic decrease in amorphous layer thickness was observed for the nanocomposite. Despite this feature, the degree of crystallinity was higher for the neat polyester, suggesting an increase of the amorphous domains between lamellar stacks when the miscible silicate layers were added to the polymer matrix.

5.4.5 References

[1] Gross, R. A.; Kalra, B. Science 2002, 297, 803-807.

[2] Moore, G. F.; Saunders, S. M. In Advances in Biodegradable Polymers; Rapra Review Reports, 1997, vol 9, no. 2.

[3] Bayer, A. G. Anwendungstechnische Information ATI 968 d, e.

[4] Grigat, E.; Koch, R.; Timmermann, R. Polym Degrad Stab 1998, 59, 223-226.

[5] Yamamoto, M.; Witt, U.; Skupin, G.; Beimborn, D.; Muller, R. J. In Biopolymers; Steinbüchel, A.; Doi, Y., Eds.; Weinheim: Wiley-VCH; Weinheim, 2002; Vol. 4, Chapter 3, p. 299.

[6] Witt, U.; Yamamoto, M.; Seeliger, U.; Muller, R. J.; Warzelhan, V. Angew Chem Int Ed 1999, 38, 1438-1442.

[7] Usuki, A.; Kojima, Y.; Kawasumi, M.; Okada, A.; Fukushima, Y.; Kurauchi, T.; Kamigato, O. J Mater Res 1993, 8, 1179-1184.

[8] Yano, K.; Usuki, A.; Okada, A.; Kurauchi, T.; Kamigaito, O. J Polym Sci, Part A: Polym Chem 1993, 31, 2493-2498.

[9] Kojima, Y.; Usuki, A.; Kawasumi, M.; Okada, A.; Fukushima, Y.; Kurauchi, T.; Kamigaito, O. J Mater Res 1993, 8, 1185-1189.

[10] Kojima, Y.; Usuki, A.; Kawasumi, M.; Okada, A.; Kurauchi, T.; Kamigaito, O. Mater Life 1993, 5, 13-18.

[11] Kawasumi, M. J Polym Sci Part A: Polym Chem 2004, 42, 819-824.

[12] Giannelis, E. P. Adv Mater 1996, 8, 29-35.

[13] Jog, J. P. Mater Sci Tech 2006, 22, 797-804.

[14] Nam, J. Y.; Sinha Ray, S.; Okamoto, M. Macromolecules 2003, 36, 7126-7131.

[15] Krikorian, V.; Pochan, D. J. Macromolecules 2004, 37, 6480-6491.

[16] Sinha Ray, S.; Bousmina, M. Macromol Chem Phys 2006, 207, 1207-1219.

[17] Kennedy, M.; Brown, G.; Stpierre, L. Polym Eng Sci 1990, 30, 769-775.

[18] Nitta, K.; Asuka, K.; Boping, L.; Terano, M. Polymer 2006, 47, 6457-6463.

[19] Somwangthanaroj, A.; Lee, E. C.; Solomon, M. J. Macromolecules 2003, 36, 2333-2342.

[20] Nowackia, R.; Monasseb, B.; Piorkowskaa, E.; Galeskia, A.; Haudinb, J. M. Polymer 2004, 45, 4877-4892.

[21] Burke, M.; Young, R.; Standford, J. Polym Bull 1993, 30, 361-368.

[22] Wang, K.; Wu, J.; Zeng, H. Eur Polym J 2003, 39, 1647-1652.

[23] Middleton, J. C.; Tipton, A. J. Med Plast Biomater 1998, 5, 30-39.

[24] Martínez-Palau, M.; Franco, L.; Puiggalí, J. Macromol Chem Phys 2008, 209, 393-403.

[25] Martínez-Palau, M.; Franco, L.; Puiggalí, J. *Polymer* 2007, 48, 6018-6028.

[26] del Valle, L.; Martínez-Palau, M.; Gámez, A.; Sepulcro, F.; Puiggalí, J. Curr Trends Polymer Sci 2008, 12, 33-41.

[27] Martínez-Palau, M.; Franco, L.; Puiggalí, J. J Appl Polym Sci 2008, 110, 2127-2138.

[28] Rueda, D. R.; García-Gutiérrez, M. C.; Nogales, A.; Capitán, M. J.; Ezquerra, T. A.; Labrador, A.; et al. Rev Sci Instrum 2006, 77, Art. No. 033904 Part 1.

[29] http://www.ccp13.ac.uk/software/program/corfunc/corfunc.htm.

[30] Chen, K.; Wilkie, C. A.; Vyazovkin, S. J Phys Chem 2007, 111, 12685-12692.

[31] Hoffmann, J. D.; Weeks, J. J. J Chem Phys 1962, 37, 1723-1741.

[32] Bandi, S.; Schiraldi, D. A. Macromolecules 2006, 39, 6537-6545.
[33] Lee, Y. H.; Bur, A. J.; Roth, S. C.; Start, P. R. Macromolecules 2005, 38, 3828-3837.
[34] Schultz, J. M. Polymer 1991, 32, 3268-3283.
[35] Lauritzen, J. I.; Hoffman, J. D. J Appl Phys 1973, 44, 4340-4352.
[36] Suzuki, T.; Kovacs, A. J. Polym J 1970, 1, 82-100.
[37] Vonk, C. G.; Kortleve, G. Kolloid Z Z Polym 1967, 220, 19-24.
[38] Vonk, C. G. J Appl Cryst 1975, 8, 340-342.
[39] Maiti, P.; Nam, P. H.; Okamoto, M.; Kotaka, T. Polym Eng Sci 2002, 42, 1864-1871.
[40] Gestí, S.; Zanetti, M.; Lazzari, M.; Franco, L.; Puiggalí, J. Eur Polym J 2009, 45, 398-409.
[41] Hsiao, B. S.; Gardner, K. H.; Wu, D. Q.; Chu, B. Polymer 1993, 34, 3986-3995.
[42] Krueger, K. N.; Zachmann, H. G. Macromolecules 1993, 26, 5202-5208.
[43] Hsiao, B. S.; Wang, Z.; Yeh, F.; Yan, G.; Sheth, K. C. Polymer 1999, 40, 3515-3523.
[44] Avrami, M. J Chem Phys 1939, 7, 1103-1112.
[45] Avrami, M. J Chem Phys 1940, 8, 212-224.
[46] Avrami, M. J Chem Phys 1941, 9, 177-184.

5.5

Thermal stability on clay nanocomposites prepared from a degradable poly(ester amide) constituted by glycolic acid and 6-aminohexanoic acid.

An intercalated nanocomposite of the organically modified montmorillonite Cloisite C25A and a degradable poly(ester amide) based on glycolic acid and 6-aminohexanoic acid units was prepared using a twin-screw co-rotating extruder. The non-isothermal degradation kinetics was investigated by thermogravimetric analysis (TG and DTG) in the temperature range 50-600 ºC at five heating rates (2, 5, 10, 20 and 40 ºC/min) and compared with the neat polymer. Significant differences were found since the nanocomposite showed three degradation steps instead of the two decomposition processes detected in the pristine sample. The onset mass loss temperature decreased in the nanocomposite due to the presence of the organo-modifier compound, but the presence of the silicate layers significantly decreased the degradation rate at the last stages of decomposition. Kinetic analysis was performed using the Kissinger method and the isoconversional (Kissinger-Akahira-Sunose, Flynn-Wall-Ozawa and Friedman) methods. The true kinetic triplets (E, A, f(α)) were determined for the two first two steps of degradation through the Coats-Redfern and the Invariant Kinetic Parameters methods. The results clearly indicated that the presence of the organo-modified clay modified the mechanisms of degradation.

5.5.1 Introduction

Development of new biodegradable polymers is a subject of great interest due to their applications as both commodity and speciality materials[1,2]. The increasing demand of such materials and even the strict requirements needed to fulfil determined user specifications have conducted to the study of new families and also to the modification of properties by preparation of nanocomposites.

Poly(ester amide)s are considered a promising family of biodegradable polymers since can combine a degradable character caused by the existence of hydrolizable ester groups (-COO-) with relatively good thermal and mechanical properties afforded by the strong intermolecular hydrogen bond interactions established between their amide groups (-NHCO-)[3,6]. A synthetic route based on the formation of metal halide salts as the driving force of a thermal polycondensation reaction was recently proposed and successfully applied to prepare alternating copolymers of glycolic acid and ω-amino acids[7,8] such as the 6-aminohexanoic acid derivative (hereafter named poly(glc-*alt*-amh)). Different studies have been performed to understand its crystalline structure[9], crystallization behavior[10] and thermal degradation mechanism[11] as well as to demonstrate its biocompatibility[12].

It has also been demonstrated that exfoliated and intercalated nanocomposites based on a poly(glc-*alt*-amh) matrix and the C25A organo-modified clay can be well prepared by the *in situ* polymerization[13] and the melt intercalation techniques[14] , respectively. Incorporation of the layered silicate had a clear influence on properties (e.g. crystallization behaviour) depending on the final structure of the nanocomposite[13,14]. Thus, nucleation was hindered and enhanced in exfoliated and intercalated structures, respectively.

In the present work, we specifically studied the influence of the C25A organo-modified clay on the thermal degradation mechanism of poly(glc-*alt*-amh). We have selected the intercalated nanocomposite prepared by the melt mixing technique, which has the advantage of using a polymer sample with a predefined molecular weight. Thermal degradation has been evaluated under non-isothermal conditions applying different kinetic methods (differential and integral) and the obtained kinetic parameters compared with those previously deduced for the pristine polymer sample[11].

In general, it is assumed that layered silicates may act as a barrier towards degradation products ablation[15,16]. Thus, the addition of clay may enhance the performance of the char formed by acting as a mass transport barrier to the volatile products generated during decomposition. However, it is not clear if the clay may produce a reverse effect during the last stages of

degradation since it has been claimed that silica layers may also act as a thermal insulator and be a heat source that accelerates the decomposition process[17]. Alternatively, it has also been postulated that thermal stabilization is caused by a nanoconfinement effect of the clay that enhances intermolecular interactions, increases the energy barrier to molecular motion and decreases chemical reactivity[18]. Thermal behaviour of nanocomposites may be also affected by the stability of the organo-modifier compound used to favour the interaction between clay particles and polymer chains. In this way, the initial degradation temperatures of nanocomposites may linearly decrease with the amount of the organo-modifier compound[19].

5.5.2 Experimental section

- **Materials**

Poly(glc-*alt*-amh) was synthesized with an 80% yield by thermal polyesterification of the sodium salt of the N-chloroacetyl-6-aminohexanoic acid[7,8]. The polymer used in this work had an intrinsic viscosity of 0.92 dL/g (dichloroacetic acid at 25 ºC), a polydispersity index of 2.10 and a M_n molecular weight of 50,100 g/mol (from GPC analysis).

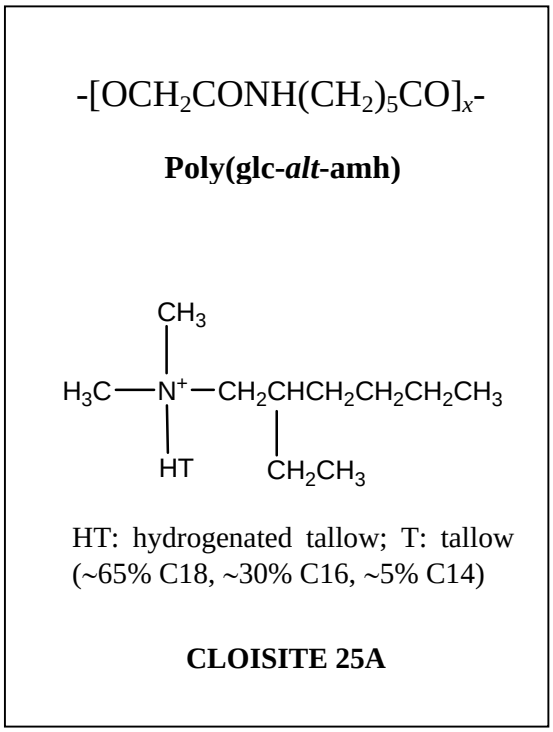

Scheme 5.5.1

Dimethyl hydrogenated-tallow 2-ethylhexyl ammonium montmorillonite (Cloisite 25A, Southern Clay Products, 2MHTEX) was used as received. The chemical structures of the specific surfactant of the organo-modified layered phyllosilicate and the polymer are shown in **Scheme 5.5.1**.

- Scheme 5.5.1**Preparation of nanocomposite**

Nanocomposites containing 3% of C25A clay particles were prepared by melt mixing in two steps using a co-rotating tightly intermeshed twin-screw extruder (DSM Xplore 5ml microcompounder). All materials were dried under vacuum prior to mixing. The processing temperature, screw rotation and cycle time were 190 ºC, 100 rpm and 3 minutes, respectively.

- **Measurements**

The structure and distribution of Cloisite were observed with a Philips TECNAI 10 transmission electron microscope (TEM) at an accelerating voltage of 100 kV. TEM specimens were prepared by embedding the film in a low viscosity modified Spurr epoxy resin and curing at 40°C for a few days and then at 60 °C for 6 h. Ultrathin sections (less than 100 nm) were cut at room temperature using a Sorvall Porter-Blum microtome equipped with a diamond knife. Finally, the sections were collected in a trough filled with water and lifted onto carbon coated copper grids. Interlayer spacing of the clay was studied by wide angle X-ray scattering (WAXD) using a Siemens D-500 diffractometer (Karlsruhe, Germany) with Cu K_α radiation (λ = 0.1542 nm).

Thermal degradation was determined at heating rates of 2, 5, 10 20 and 40 ºC/min with around 5 mg samples in a Q50 thermogravimetric analyzer of TA Instruments and under a flow of dry nitrogen. The analysis was performed in the temperature range from 50 to 600 ºC. Deconvolution of the derivative thermogravimetric analysis (DTG) curve was performed with the PeakFit v4 program by Jandel Scientific Software, using an asymmetric function known as “asymmetric double sigmoidal”

5.5.3 Results and discussion

- **Dispersion structure of the C25A clay in the composite with poly(glc-*alt*-amh)**

Direct observation of the morphology and phase distribution of ultrathin sections of poly(glc-*alt*-amh) / C25A specimens by transmission electron microscopy clearly showed that an intercalated structure was predominant (**Figure 5.5.1**). In this way, X-ray diffraction profiles of the nanocomposite sample revealed also the existence of a low angle reflection associated to the stacking of silicate layers. The measured spacing was close to 2.68 nm, a higher value than that observed in the profile of the C25A clay (1.97 nm). Thus, polymer chains in the nanocomposite sample were intercalated in the galleries of the dispersed clay and increased the interlayer spacing.

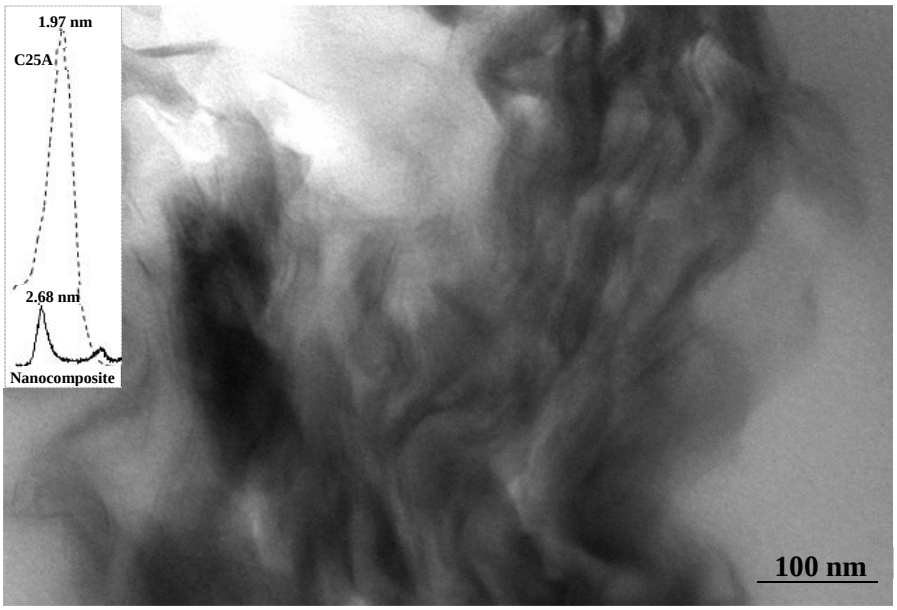

Figure 5.5.1 Transmission electron micrograph showing the morphology of the poly(glc-*alt*-amh)/C25A nanocomposite with a Cloisite concentration of 3%. Inset shows the diffraction peak associated to the interlayer spacing observed in the C25A organo-modified clay (dashed line) and the nanocomposite sample (solid line).

Thermal stability of the poly(glc-*alt*-amh)/C25A nanocomposite

Thermogravimetric scans showed clear differences between the neat polymer and its nanocomposite with the C25A organo-modified clay (**Figure 5.5.2** a). In this way, the nanocomposite showed a lower onset degradation temperature for all the assayed heating rates (**Table 5.5.1**), probably due to the lower stability of the organo-modifier compound, and in general a shift of its degradation curve to lower temperatures. However, curves approached to each other at the last stages of degradation suggesting that the neat polymer decomposition at high temperature proceeded faster than in the nanocomposite. Both samples reached a constant weight percentage, the remaining residue was logically greater for the nanocomposite (13% versus to 9%) due its clay content.

The degree of degradation or conversion, α, at a given temperature (**Figure 5.5.2** b) was calculated as:

$$\alpha = \frac{W_0 - W}{W_0 - W_\infty} \qquad (5.5.1)$$

where W_0, W and W_∞ were the initial weight, the weight at the considered temperature and the final weight at the end of the degradation process, respectively.

a)

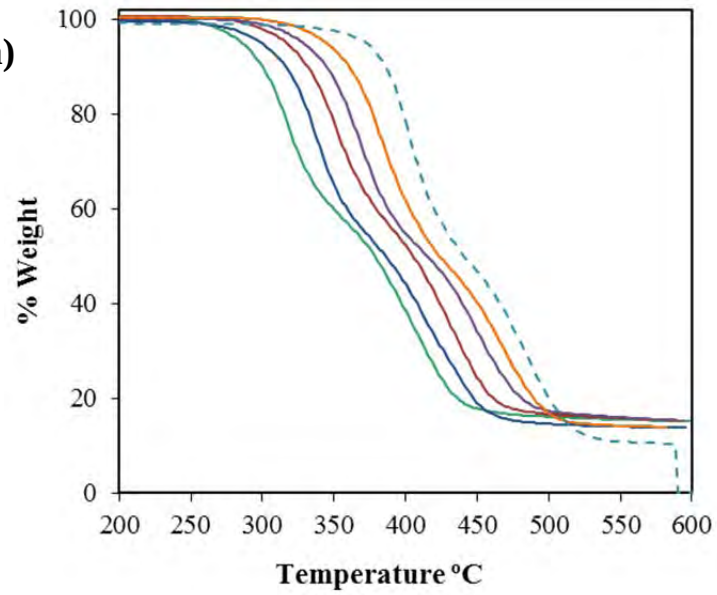
100
80
60
40
20
0
% Weight
200
250
300
350
400
450
500
550
600
Temperature °C

b)

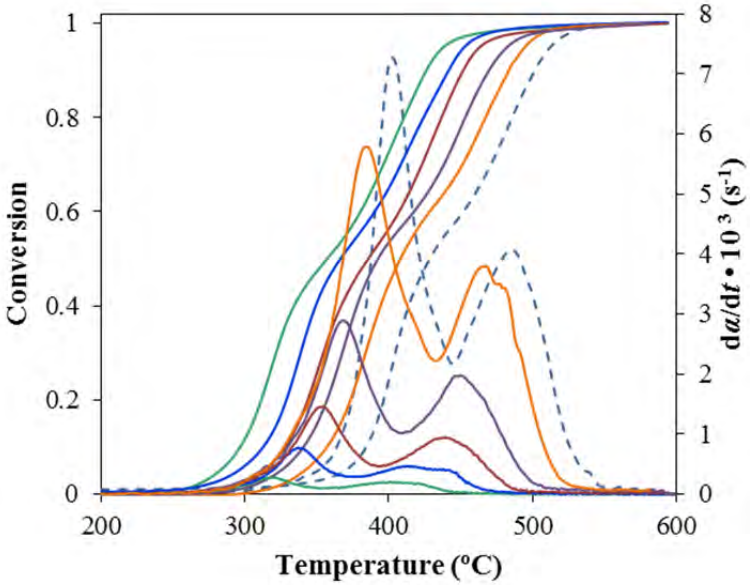
1
0.8
0.6
0.4
0.2
0
Conversion
8
7
6
5
4
3
2
1
0
dα/dt • 10 3 (s-1)
200
300
400
500
600
Temperature (°C)

Figure 5.5.2 b plots the degree of conversion versus temperature (TG curve) of the nanocomposite sample at all the assayed heating rates together with the corresponding derivative curves (DTG). For the sake of completeness, curves of the neat polymer are also shown for a representative heating rate (40 ºC/min). The characteristic TG and DTG temperatures for the nanocomposite and the neat polymer sample are summarized in **Table 5.5.1**.

Table 5.5.1 Thermogravimetric data of the nanocomposite and pristine samples.

Sample	β (ºC/min)	T_{onset} (ºC)	$T_{20\%}$ (ºC)	$T_{50\%}$ (ºC)	$T_{70\%}$ (ºC)	T_{max}(ºC)
Poly(glc-*alt*-amh)[a]	2	207	319	359	411	326/412
	5	220	339	370	423	345/434
	10	232	56	388	433	357/442
	20	240	375	408	451	382/460
	40	260	397	429	471	404/485
Poly(glc-*alt*-amh)/C25A	2	194	314	378	414	315/387/415
	5	215	332	386	426	333/400/363
	10	223	348	404	440	349/420/447
	20	227	362	414	456	
	40	249	378	424	470	379/455/480

[a]From reference 11.

Both samples showed a clear first degradation step which approximately corresponded to a conversion of 0.45-0.50. This step can be mainly associated to the decomposition of the glycolic acid residues as it was previously determined from the study of a series of copolymers derived from different ω-amino acids and consequently with different weight percentages of glycolic acid units [11]. Thermogravimetric traces clearly indicated that this process always ended at lower temperatures for the nanocomposite than for the pristine sample.

DTG curves showed a second degradation step for the neat polymer which was associated to the decomposition of the rich ω-amino acid fraction [11]. This process appeared rather more complicated in the nanocomposite sample since at least two DTG additional peaks were detected at a temperature that increased with the heating rate. Thus, incorporation of clay particles had a remarkable influence on the degradation process which took consequently place according to three differentiated steps. These clear differences between the decomposition of the pristine and the nanocomposite samples demonstrate that the degradation mechanism changed when the organo-modified clay was added and justify undertaking a more detailed kinetic analysis.

Each degradation step of the nanocomposite was then analyzed by mathematical deconvolution of the DTG curves as previously performed with the neat polymer [11]. **Figure 5.5.3** shows the

separation in three and two peaks of the DTG curves obtained at a representative heating rate of 5 ºC/min for the nanocomposite and the pristine polymer, respectively. In all cases, the sum of the separated curves reproduced quite well the experimental signal.

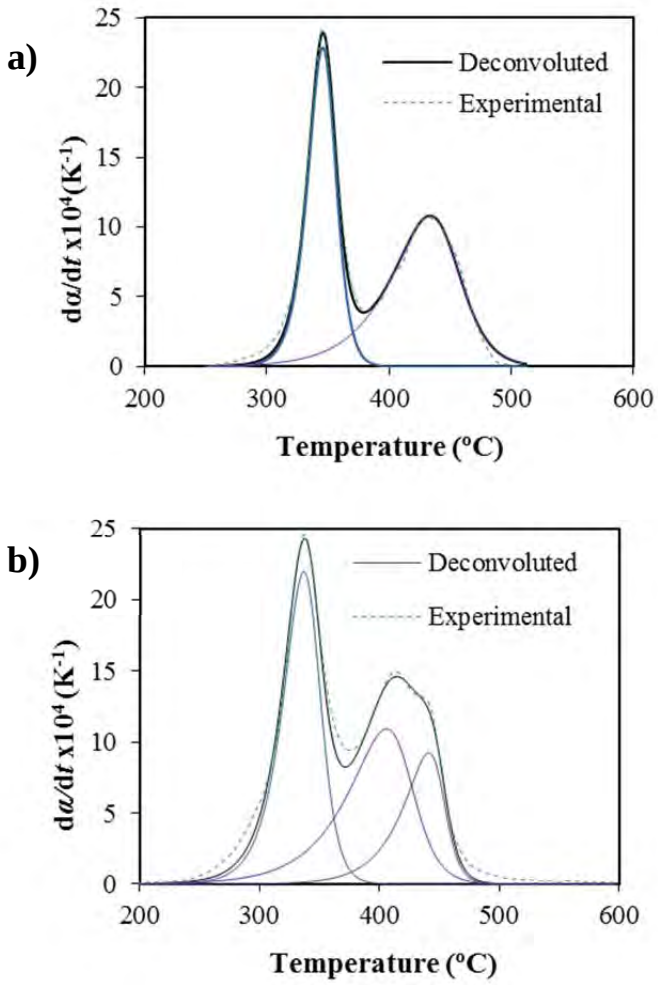

Figure 5.5.3 Deconvolution of DTG curves corresponding to the thermal decomposition of the pristine (a) and the nanocomposite (b) samples at 5 ºC/min.

Evaluation of the activation energy for the thermal degradation of the poly(glc-*alt*-amh)/C25A nanocomposite

According to non-isothermal kinetic theory, thermal degradation of a sample can be expressed by the following function:

$$\frac{d\alpha}{dT} = \frac{1}{\beta} A \exp\left(-\frac{E}{RT}\right) f(\alpha) \qquad (5.5.2)$$

where β is the heating rate, T is the absolute temperature, R the gas constant, $f(\alpha)$ the differential conversion function, and A and E the preexponential and the activation energy for the studied decomposition reaction step.

Activation energies for the three degradation steps were determined by using the Kissinger method[20], and advanced isoconversional methods such as Kissinger-Akahira-Sunose (KAS)[20,21] , Friedman[22,23] and Flynn-Wall-Ozawa (FWO)[24,25] which have the advantage that don't need the knowledge of the exact thermodegradation mechanism. Integral (KAS and FWO) and differential (Friedman) isoconversional methods make use of the isoconversional principle which states that at a constant extent of conversion the reaction rate is a function only of the temperature.

The Kissinger method [20] gives the associated activation energy, E, only at the maximum of the DTG curve for each degradation step and is based on the equation:

$$\ln\frac{\beta}{T_{max}^2} = \ln\frac{AR}{E} + \ln\left[n(1-\alpha_{max})^{n-1}\right] - \frac{E}{RT_{max}} \qquad (5.5.3)$$

where β is the heating rate, T_{max} is the temperature at the maximum reaction rates, α_{max} is the conversion at this T_{max} temperature, n is the reaction order and A the frequency factor. From a plot of $\ln(\beta/T_{max}^2)$ versus $1/T_{max}$ and fitting the data to a straight line (**Figure 5.5.4** a and **Figure 5.5.5** a), the activation energy was calculated from the slopes for each degradation step as summarized in **¡Error! No se encuentra el origen de la referencia.** A good linearity was always observed with correlation coefficients of 0.9999, 0.9968 and 0.9832 for the first, second and third degradation step, respectively.

It should be pointed out that Kissinger is not an isoconversional method since the peak temperature is obtained at different heating rates, and the extent of conversion related to the peak is known to change with the heating rate[26,27]. Moreover, the determined activation energy may loss sense if it varies throughout the degradation process.

In order to calculate the activation energy during the whole process, the KAS method[20,21] was applied. This is based on the integration of equation 5.5.2, which after a subsequent reordering leads to the expression.

$$\ln\frac{\beta}{T^2} = \ln\left[\frac{AR}{g(\alpha)E}\right] - \frac{E}{RT} \qquad (5.5.4)$$

where $g(\alpha)$ is the integral conversion function (i.e. $g(\alpha) = \int_0^{\alpha} \frac{d\alpha}{f(\alpha)}$).

Table 5.5.2 Activation energies of the nanocomposite and pristine samples determined by isoconversional methods.

Sample	**Step**[a]	***E*** **(kJ/mol) Kissinger**[b]	***E*****(kJ/mol) KAS**[c]	***E*****(kJ/mol) Friedman**[c]	***E*** **(kJ/mol) FWO**[c]
Poly(glc-*alt*-amh)[d]	1	118	116	120	120
	2	176	179	185	181
Poly(glc-*alt*-amh)/C25A	1	127	111	133	124
	2	146	139	159	157
	3	168	150	168	161

[a] The different steps of degradation are referred to 1, 2 and 3 in increasing order of temperature.
[b] Calculated at the temperature corresponding to the maximum of each step in the DTG curve.
[c] Summarized energies correspond to mean values obtained from different degrees of conversion (from 0.1 to 0.95).
[d] From reference 11.

For each degree of conversion and degradation process the activation energy was obtained from the slope of the linear representation of $\ln(\beta/T^2)$ versus $1000/T$. A good linearity was obtained with correlation coefficients not less than 0.97, 0.98 and 0.95 for the first, second and third degradation step, respectively. In each case the worst coefficient were found for the lowest conversion degree (0.1), whereas at a conversion of 0.95 the coefficient was in the three cases higher than 0.99. As shown in **Figure 5.5.4** b (step 1) and **Figure 5.5.5** b (steps 2 and 3). Activation energies slightly increased with the conversion degree (**Figure 5.5.6**) and also when degradation progressed from step 1 to step 3. Average values are summarized in **Table 5.5.2**.

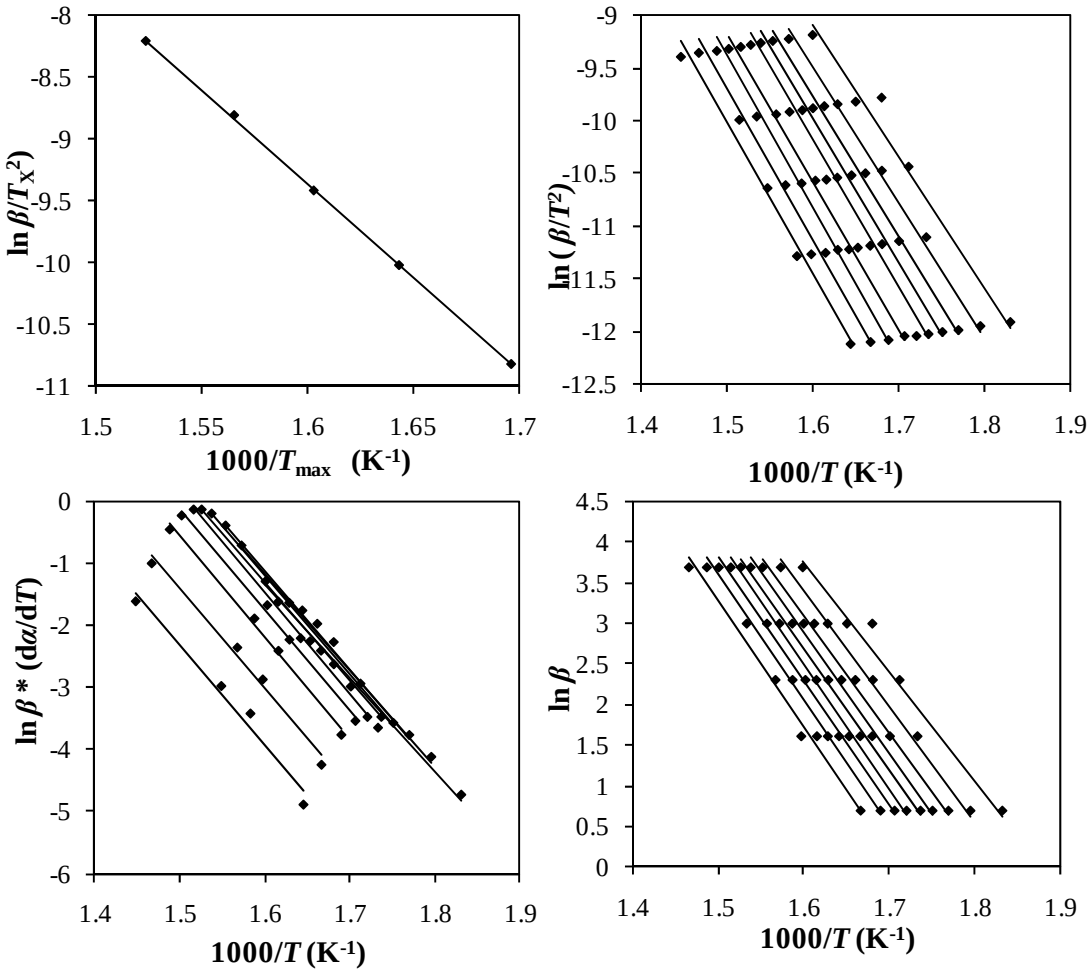

Figure 5.5.4 Kissinger (a), Kas (b), Friedman (c) and FWO (d) plots for the first thermal decomposition step of the poly(glc-*alt*-amh)/C25A nanocomposite sample. From left to right lines correspond to conversion ranging from 0.1 to 0.9 in steps of 0.1 and the conversion of 0.95.

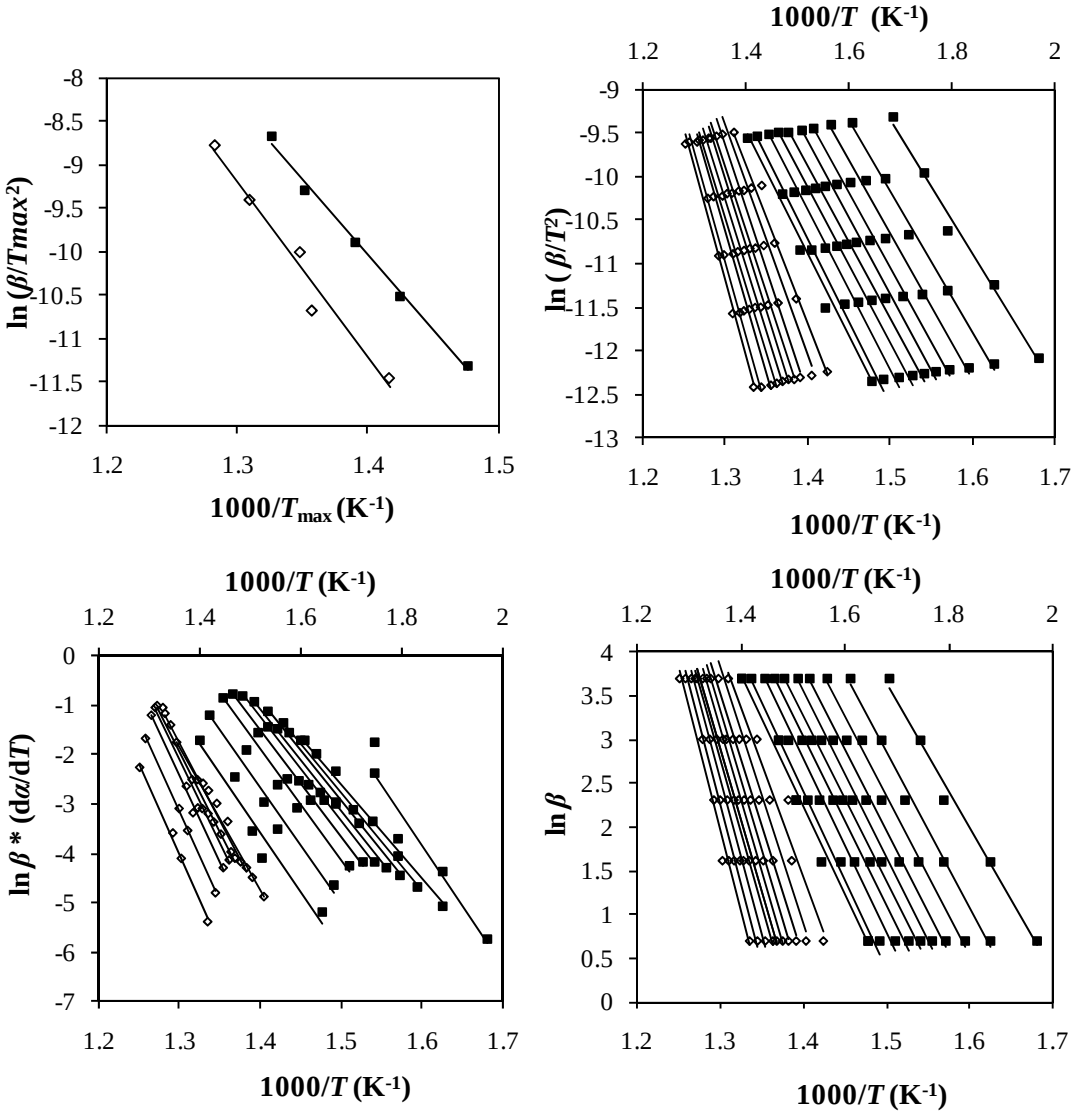

Figure 5.5.5 Kissinger (a), Kas (b), Friedman (c) and FWO (d) plots for the second (♦)and the third (◊) thermal decomposition steps of the poly(glc-*alt*-amh)/C25A nanocomposite sample. From left to right lines correspond to conversion ranging from 0.1 to 0.9 in steps of 0.1 and the conversion of 0.95.

The Friedman method [22,23] (equation 5.5.5) derives from the logarithmic form of the rate equation 5.5.2 and enables also to get the values of activation energies over a wide range of conversions by plotting $\ln(\beta\, d\alpha/dT)$ versus $1000/T$ from thermograms recorded at several heating rates.

$$\ln\left[\beta\frac{d\alpha}{dT}\right] = \ln A + n\ln(1-\alpha) - \frac{E}{RT} \qquad (5.5.5)$$

Figure 5.5.4 c (first degradation step) and **Figure 5.5.5** c (second and third degradation steps) show straight lines whose slopes allowed the evaluation of activation energies (**Table 5.5.2** for average values).

A good linearity was obtained for each conversion with correlation coefficients not less than 0.98, 0.95 and 0.98 for the first, second and third degradation step, respectively.
Finally, the integral Flynn-Wall-Ozawa method[24,25], based on equation 5.5.6, allows also determining the activation energies for each degradation step and conversion degree.

$$\ln\beta = \ln\frac{0.0048AE}{g(\alpha)R} - 1.0516\frac{E}{RT} \qquad (5.5.6)$$

Activation energies (**Table 5.5.2** for average values) were in this case calculated from the linear plots of $\ln\beta$ versus $1000/T$ (**Figure 5.5.4** d and **Figure 5.5.5** d).

Table 5.5.2summarizes the values of the activation energies calculated for the poly(glc-*alt*-amh)/C25A nanocomposite by using the four indicated methods. For the sake of completeness previous results determined for the neat polymer are also included[11]. **Figure 5.5.6** plots also the variation of the activation energy deduced from the Friedman method with the conversion for the three degradation steps. Activation energy was practically constant for the first degradation step and shows a slightly greater fluctuation for the second one, which had an overlapping with the other two steps and particularly with the third one (at higher conversions). Activation energy progressively increased with the conversion degree for the last degradation step as also found in the KAS analysis. Average values of the activation energy for the three considered steps are summarized in **Table 5.5.2.** It can be observed that these average values were close to the single activation energy determined by the Kissinger plot, and higher than the average activation energies determined by the KAS method. Differential isoconversional methods, like Friedman, are recommended over integral when discrepancies exists[21, 22, 23]. Thus, we obtained energies of 130, 153 and 168 kJ/mol by averaging Kissinger and Friedman data for the first, second and third degradation steps, respectively.

The first degradation step had the lowest activation energy for both the neat polymer and the nanocomposite sample. The incorporation of clay particles slightly increased this activation energy. It can also be emphasized that the second stage of degradation of the neat polymer had an activation energy considerably higher than those determined in either the second or the third degradation steps of the nanocomposite sample.

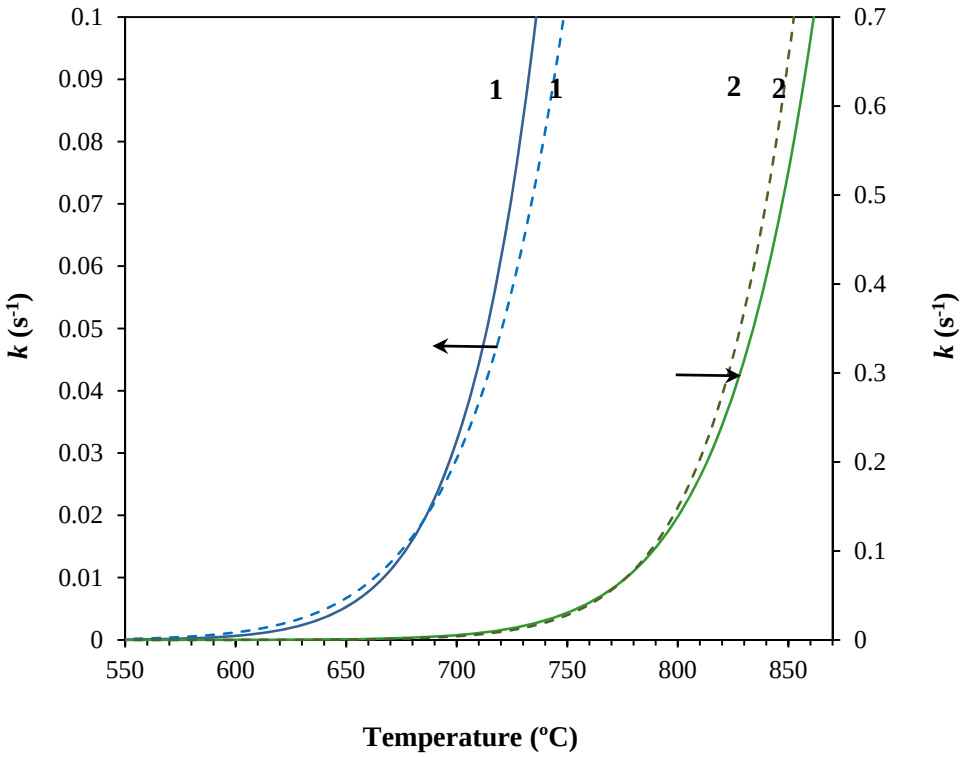

Figure 5.5.6 Dependence of the kinetic rate constant, *k*, on temperature for the different degradation steps (1, 2 and 3) of the pristine (dashed lines) and the poly(glc-*alt*-amh)/C25A nanocomposite (solid lines) sample.

Thermal degradation mechanisms of the poly(glc-*alt*-amh)/C25A nanocomposite

The Coats-Redfern method[28] was chosen in order to determine the thermal degradation mechanism involved in the three different degradation steps of the nanocomposite. Conventional $g(\alpha)$ functions[29,30] were considered and for each one, the activation energy was calculated according to equation 5.5.7, which was derived considering an asymptotic approximation ($2RT/E$ <<1).

$$\ln\frac{g(\alpha)}{T^2} = \ln\left(\frac{AR}{\beta E}\right) - \frac{E}{RT} \qquad (5.5.7)$$

The Coats-Redfern equation was derived assuming that the activation energy was independent of the conversion degree, a feature that seems true for the first step of degradation and even can be considered for the second degradation step at intermediate conversion degrees.
The slope of the linear plot of ln $g(\alpha)/T^2$ versus $1/T$ allowed the activation energy to be determined for each possible model and the model to be selected by considering the agreement with the previously calculated activation energy (**Table 5.5.2**) and the achievement of a good regression coefficient. This methodology enables to determine also the frequency factor from the intercept at the origin. The complete kinetic triplet (E, A and $f(\alpha)$) defines the variation of the degree of conversion with the temperature (equation 5.5.2).

In general, calculations performed at the different heating rates showed a rather similar activation energy values for each degradation step (**Table 5.5.3**), although a great fluctuation was found for some specific model.

Different degradation mechanisms have been deduced for the nanocomposite and the neat polymer samples, even for the common first decomposition step. Thus, the pristine polymer followed a sigmoidal A_2 mechanism[11], whereas the sigmoidal $A_{3/2}$ model, the decelerative R_2 mechanism or the autocatalytic (n = 1.5; m = 0.5) mechanism should be considered for the nanocomposite since their E values were close to those determined by the Kissinger and the isoconversional methods. Note that these methods gave an average activation energy of 124 kJ/mol which was within the energy range calculated for the autocatalytic model (from 100 to 130 kJ/mol), or slightly above or below the corresponding ranges determined for the $A_{3/2}$ (from 101 to 116 kJ/mol) or the R_2 (from 136 to 142 kJ/mol) models, respectively. Discrimination between these three mechanisms should be discussed later.

The last stage of degradation of the poly(glc-*alt*-amh) sample followed an autocatalytic (n = 1.9; m = 0.1) mechanism. This decomposition process was split in other two when cay particles were added, being only possible as above indicated to analyse the mechanism for one of these two processes. Thus, a first order (F_1) mechanism could be associated to the second degradation step of the nanocomposite. It should be pointed out that, in this case, the experimental activation energy 153 kJ/mol was in agreement with only one model and consequently discrimination with other mechanisms was clear.

Table 5.5.4 summarizes the final kinetic parameters deduced for the nanocomposite at the heating rates of 2 ºC/min and 40 ºC/min. For the sake of completeness previous reported data on the neat polymer are also given.

In summary, degradation of glycolic acid units (first step) took place according to an autocatalytic model, whereas a first order model described the beginning of the degradation process that involved the ω-amino acid units.
Note that clay particles should have a great influence at the beginning of degradation due to decomposition of the organo-modifier and also at the end of the process (third step) due to the increasing ratio of silicate layers as the polymer decomposes.

In fact, the variation of the activation energy in the third step suggests a complex mechanism, which also agrees with the presence of shoulders in the corresponding DTG curve (see arrow in **Figure 5.5.2**). It is well reported that clay particles had a remarkable influence on the last stages of degradation although different explanations have been postulated. In general, it is assumed that layered silicates may act as a barrier towards degradation products ablation[27,28]. Thus, the addition of clay may enhance the performance of the char formed acting as a mass transport barrier to the volatile products generated during decomposition. Alternatively, it has also been postulated that thermal stabilization is caused by a nanoconfinement effect of the clay that enhances intermolecular interactions, increases the energy barrier to molecular motion and decreases chemical reactivity[29].

The thermogravimetric trace of the C25A organo-modified clay (**Figure 5.5.2**) showed that a degradation with a 30% weight loss occurred between 290 and 340 ºC (DTG peak at 306 ºC), an observation that demonstrates the low thermal stability of the clay. Furthermore, it is known that the thermal behaviour of nanocomposites may be affected by the stability of the organo-modifier compound used to favour the interaction between clay particles and polymer chains [30.] Decomposition products may influence the degradation mechanism of poly(glc-*alt*-amh), which on the other hand was demonstrated to be highly dependent on the copolymer composition since significant differences were previously found between the 6-aminohexanoic and the 11-aminoundecanoic derivatives[11].

Table 5.5.3 Activation energies of poly(glc-alt-amh)/C25A obtained by the Coats-Redfern method at 2 ºC/min and 40 ºC/min

	First Step				Second Step				Third Step			
	2 ºC/min		40 ºC/min		2 ºC/min		40 ºC/min		2 ºC/min		40 ºC/min	
	E **(kJ/mol)**	***r***	***E*** **(kJ/mol)**	***r***	***E*** **(kJ/mol)**	***r***	***E*** **(kJ/mol)**	***r***	***E*** **(kJ/mol)**	***r***	***E*** **(kJ/mol)**	***r***
$A_{3/2}$	101.31	0.9993	115.58	0.9988	95.43	0.9996	98.70	0.9908	135.29	0.9999	177.49	0.9994
A_2	73.58	0.9992	83.95	0.9987	68.82	0.9995	71.04	0.99	98.60	0.9999	129.92	0.9994
A_3	45.73	0.9991	52.31	0.9985	20.69	0.9878	20.69	0.9757	20.69	0.9878	20.69	0.9757
A_4	32.42	0.9989	36.50	0.9983	28.91	0.9994	29.55	0.9851	43.56	0.9999	58.58	0.9993
D_1	243.23	0.9882	232.84	0.9905	169.71	0.9949	217.63	0.9993	268.97	0.9964	502.09	0.9923
D_2	276.44	0.9936	281.01	0.9946	217.49	0.9982	257.14	1	324.24	0.9983	546.33	0.9966
D_3	294.18	0.9972	317.94	0.9973	257.21	0.9998	279.07	0.9995	368.83	0.9995	572.73	0.9992
D_4	275.97	0.9947	286.18	0.9954	223.36	0.9989	256.71	1	331.65	0.9988	547.14	0.9976
R_2	135.59	0.9952	141.85	0.9957	110.74	0.9992	125.35	0.999	165.03	0.9990	270.77	0.9981
R_3	142.27	0.9970	153.49	0.9971	123.08	0.9998	133.58	0.9995	178.67	0.9995	280.20	0.9920
F_1	156.79	0.9993	178.84	0.9989	150.73	0.9996	151.17	0.998	208.31	0.9999	300.30	0.9997
power	54.06	0.9846	49.99	0.9871	41.77	0.9992	45.68	0.9991	55.37	0.9922	116.28	0.9908
***n*=2**	209.60	0.9959	270.45	0.9996	197.97	0.9965	210.24	0.9908	325.31	0.9980	370.49	0.9887
***n*=1.5 *m*=0.5**	99.98	0.9956	129.76	0.9995	93.55	0.9962	99.17	0.9897	156.90	0.9979	179.08	0.9880
***n*=1.5**	181.51	0.9994	222.20	0.1000	167.36	0.9982	178.75	0.9949	261.92	0.9995	333.57	0.9964
***n*=1.9 *m*=0.1**	187.68	0.9959	242.31	0.9996	177.09	0.9965	188.02	0.9906	291.63	0.9980	332.20	0.9918
***n*=3**	274.29	0.9834	382.59	0.9969	267.91	0.9928	281.99	0.9817	473.82	0.9940	453.99	0.9709

Invariant activation parameters for the thermal decomposition of the poly(glc-*alt*-amh)/C25A nanocomposite

Kinetic parameters can also be evaluated using the IKP (invariant kinetic parameters) method[31,32]. According to this procedure, the values of the activation parameters, obtained from various forms of $f(\alpha)$, are correlated through an apparent compensation effect:

$$\ln A = \alpha^* + \beta^* E \qquad (5.5.8)$$

where α^* and β^* are constants (the compensation effect parameters).

In order to apply this method, the values of $\ln A_i$ versus E_i at each heating rate (β_i) were plotted. These parameters were obtained using the Coats-Redfern methodology for the different kinetic models studied. The plot allowed the α^*_i and β^*_i constants to be determined from the intersection at the origin and the slope, respectively. Furthermore, the straight lines $\ln A_i$ versus E_i for each heating rate should intersect at a point which corresponds to the true values of A and E. These are called the invariant activation parameters (A_{inv}, E_{inv}). Certain variations of the experimental conditions actually determine a region of intersection in the $\ln A$, E space. For this reason, the evaluation of the invariant activation parameters is performed using the following relation:

$$\ln A_{inv} = \alpha^*_i + \beta^*_i E_{inv} \qquad (5.5.9)$$

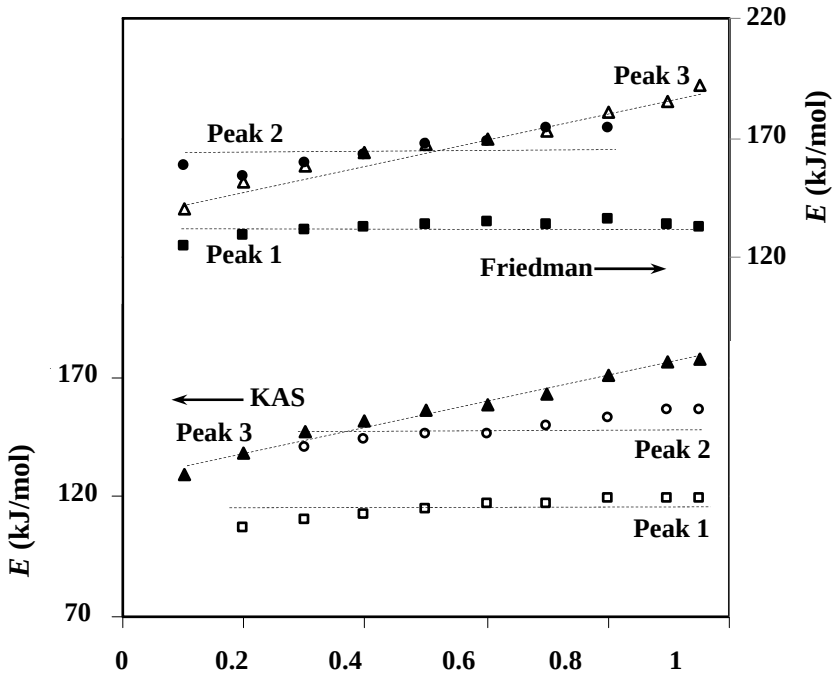

Figure 5.5.7 Plots of the activation energy, calculated with the KAS [15, 16] and Friedman [17,18] methods for the first (squares), second (circles) and third (triangles) degradation steps of the poly(glc-*alt*-amh)/25A nanocomposite sample.

Thus, a plot α^*_i versus β^*_i is actually a straight line whose parameters allow evaluation of the invariant activation parameters.

The IKP method can be well applied if the activation energy does not depend on the degree of conversion, which must be checked by isoconversional methods. The first degradation step of poly(glc-*alt*-amh)/C25A nanocomposite is clearly characterized by a practically constant activation energy as shown in **Figure 5.5.7** from data derived from the KAS method, small variations being only detected at low conversion degrees. **Figure 5.5.8** a shows the compensation relationship for this degradation step where correlation coefficients $r^2 > 0.99$ were derived for all studied heating rates. Plot of **Figure 5.5.8** b shows also a straight line that demonstrates a supercorrelation relation for this degradation step (correlation foefficient of 0.9975). Furthermore, its slope indicates a E_{inv} value (**Table 5.5.4**) that is in good agreement with the derived one from the isoconversional methods (i.e. 133 kJ/mol respect to 111-133 kJ/mol).

Despite a higher variation of the activation energy with temperature was observed for the second and third degradation steps, the IKP method was also attempted. Final values for the A_{inv} and E_{inv} invariant parameters are summarized in **Table 5.5.4** It can be pointed out that a relative good agreement was again found between the invariant activation energies and the values deduced from isoconversional methods (i.e. 154 kJ/mol respect to 139-159 kJ/mol and 166 kJ/mol respect to 150-168 kJ/mol for the second and third degradation steps, respectively). In this way, the IKP methodology conducted to the same degradation mechanisms deduced in the previous section.

Table 5.5.4 Kinetic parameters associated with the different degradation steps of poly(glc-alt-amh)/C25 nanocomposite and the neat polymer

	Neat polymer[a]		**Nanocomposite**	
	Step 1	**Step 2**	**Step 1**	**Step 2**
***E* (kJ/mol)**	111	167	100[b]-130[c]	151[b]-151[c]
ln *A* (min^{-1})	19.64	27.31	18.53[b]-24.41[c]	24.83[b]-25.28[c]
Model	A_2	$n = 1.9$; $m = 0.1$	$n = 1.5$; $m = 0.5$	F_1
***f*(α)**	$2(1-\alpha)[-\ln(1-\alpha)]^{1/2}$	$(2\alpha)^{-1}$	$\alpha^{0.5}(1-\alpha)^{1.5}$	$(1-\alpha)$
***g*(α)**	$[-\ln(1-\alpha)]^{1/2}$	α^2	$[(1-\alpha)/\alpha]^{-0.9}(0.5)^{-1}$	$-\ln(1-\alpha)$
E_{inv} (kJ/mol)	118	169	133	154
ln A_{inv} (min^{-1})	21.03	26.52	24.13	25.11

[a] From reference 11. *E* and ln *A* were determined for a heating rate of 2 ºC/min.
[b]Values calculated for a heating rate of 2 ºC/min.
[c]Values calculated for a heating rate of 40 ºC/min.

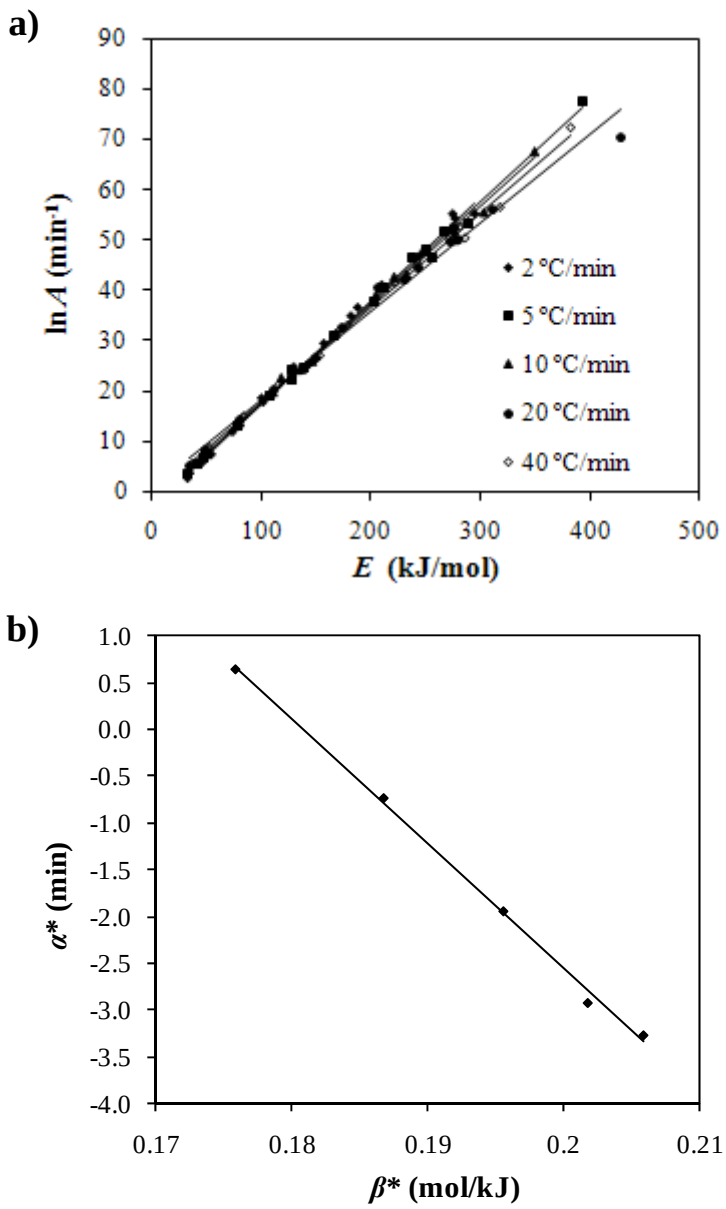

Figure 5.5.8 The compensation (a) and the correlation (b) relationships for the first degradation step of the poly(glc-*alt*-amh)/C25A nanocomposite sample.

Modeling of degradation kinetics

dα/dT data were calculated for each heating rate and degradation step using the equation 5.5.2 and the kinetic parameters (E, A and f(α)) deduced from the Coats and Redfern method. The simulated DTG curve for a given heating rate was thus determined by addition of the three calculated profiles which were properly scaled to fit the experimental curve. Final dependences of the degree of conversion with temperature were obtained by integration of the simulated DTG curves. Calculations were performed using the autocatalytic (n = 1.5; m = 0.5), R_2 and $A_{3/2}$ models previously postulated for the first degradation step and models F_1 and autocatalytic (n = 1.5; m = 0.5) for the second and third step, respectively. **Figure 5.5.9** compares the

experimental and the simulated TG curves for a representative heating rate. Results indicated that the best agreement was obtained when the autocatalytic (n = 1.5; m = 0.5) model was considered for the first step and consequently the other two proposed mechanisms could be clearly discarded. As shown in **Figure 5.5.8**, the fitting to experimental data is good for almost all whole area, with slight divergences in the regions corresponding to the lowest and the highest weight loss. A similar procedure was performed to choose the autocatalytic model over the R_2 model for the third degradation step.

Finally, the invariant values of the activation energies and the pre-exponential factors allowed us to calculate the rate constant, *k*, of the different non-isothermal degradation steps for the nanocomposite and the neat polymer samples. **Figure 5.5.6** compares the temperature dependence of the rate constant for the two studied samples and the different degradation steps.

Although for the first degradation step the nanocomposite showed higher activation energy than the neat polymer, it is clear that its pre-exponential factor was also higher (**Table 5.5.4**). In this way, degradation can proceed faster in the nanocomposite during the first stage of thermal decomposition. It has been claimed that an increase on the activation energy cannot be rationalized in terms of the formation of a surface silicate barrier

On the other hand, the high pre-exponential factor calculated for the second degradation step of the neat polymer justified its higher degradation rate during the last stages of decomposition despite the activation energies of the two samples were quite similar (i.e. 167 kJ/mol for the neat polymer and 151 kJ/mol and 165 kJ/mol for the nanocomposite).

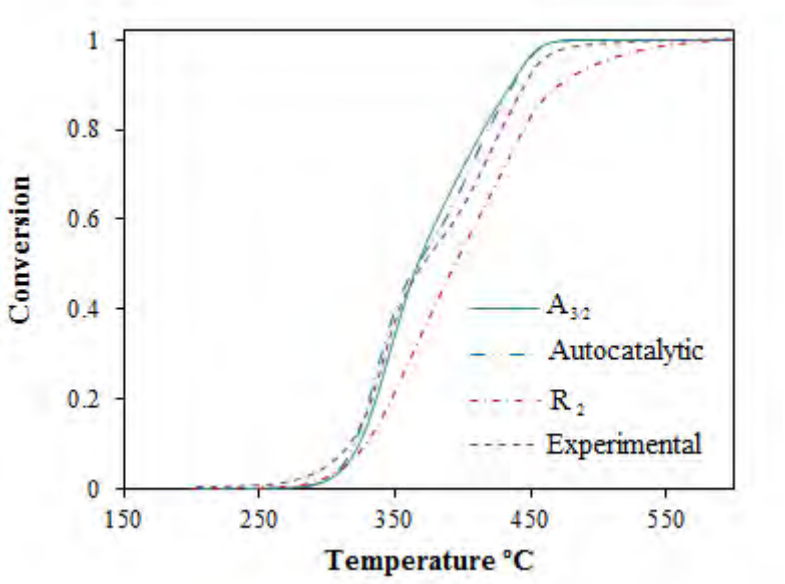

Figure 5.5.9 Comparison between experimental (- - -) and simulated TG curves for the poly(glc-*alt*-amh)/C25A nanocomposite sample at representative heating rate of 5 ºC/min. Curves were calculated considering the autocatalytic, $A_{3/2}$ and R_2 models for the first degradation step.

5.5.4 Conclusion

Thermal decomposition in a nitrogen atmosphere of the alternating biodegradable poly(ester amide) constituted by glycolic acid and 6-aminohexanoic acid units was significantly changed by the incorporation of a small percentage (3 wt %) of the C25A organo-modified clay, which rendered an intercalated structure when the sample was prepared by the melt-mixing technique. The polymer showed a first degradation step, which mainly involved the decomposition of glycolic acid units, and which proceeded faster when the clay was added. The low stability of the organo-modifier compound had a determinant role and contributed to modify the degradation mechanism associated to this step. Results derived from isoconversional analyses, and the Coats-Redfern and IKP methods were highly consistent and allowed postulating an autocatalytic mechanism when simulated degradation data were compared with the experimental curves.

Last stages of degradation proceeded slowly for the nanocomposite, which furthermore showed a complex degradation process due to existence of two additional decomposition mechanisms. Thus, the second degradation step observed in the pristine sample was split due to the influence of clay particles which probably enhanced the performance of the char formed. The pre-exponential factor of the last degradation step of the pristine sample was higher than the calculated value for the nanocomposite suggesting that motion of reactive groups was hindered by the presence of silicate layers.

5.5.5 References

[1] R. A. Gross, B. Kalra, Science 297 (2002) 803.
[2] G. F. Moore, S. M. Saunders, In Advances in Biodegradable Polymers; Rapra Review Reports 9 (1997) 2.
[3] I. Arvanitoyannis, N. Kawasaki, N. Yamamoto, Polymer 36 (1995) 857.
[4] N. Paredes, A. Rodríguez-Galán, J. Puiggalí, J. Polym. Sci. Part A: Polym. Chem. 36 (1998) 1271.
[5] R. Katsavara, V. Beridze, N. Arbuli, D. Kharadze, C. C. Chu, C. Y. Won, J. Polym. Sci. Part A: Polym. Chem. 37 (1999) 391.
[6] H. R. Stapert, A. W. Bouwens, P. J. Dijkstra, J. Feijen, Macromol. Chem. Phys. 200 (1999) 1921.
[7] M. Vera, A. Rodríguez-Galán, J. Puiggalí, Macromol. Rapid Commun. 25 (2004) 812.
[8] M. Vera, A. L. Franco, J. Puiggalí, Macromol. Chem. Phys. 205 (2004) 1782.
[9] E. Botines, M. T. Casas, J. Puiggalí, J. Polym. Sci. Part B: Polym. Phys. 45 (2007) 815.
[10] E. Botines, J. Puiggalí, Eur. Polym. J. 42 (2006) 1595.
[11] E. Botines, L. Franco, J. Puiggalí, J. Appl. Polym. Sci. 102 (2006) 5545.
[12] L. del Valle, F. Sepulcre, A. Gámez, A. Rodríguez-Galán, J. Puiggalí, Current Trends in Polymer Science 12 (2008) 27.
[13] L. T. Morales, L. Franco, M. T. Casas, J. Puiggalí, J. Polym. Sci. Part A: Polym. Chem. 47 (2009) 3616.
[14] L. T. Morales, L. Franco, M. T. Casas, J. Puiggalí. Polym. Eng. Sci., submitted.
[15] B. N. Jang, C. A.Wilkie, Polymer 46 (2005) 2933.
[16] X. Yuan, C. Li, G. Guan, Y. Xiao, D. Zhang, Polym. Degrad. Stab. 93 (2008) 466.
[17] S. Sinha Ray, M. Bousmina, Prog. Mater. Sci. 50 (2005) 962.
[18] K. Chen, C. A.Wilkie, S.Vyazovkin, J. Phys. Chem. B 111 (2007) 12685.
[19] J. H. Chang, Y. Uk.An, G.S. Sur, J. Polym. Sci. Part B: Polym. Phys. 41 (2003) 94.
[20] H. E. Kissinger, Anal. Chem. 29 (1957) 1702.
[21] T. Akahira, T. Sunose, Res. Report Chiba Inst. Technol. 16 (1971) 22.
[22] H. J. Friedman, Polym. Sci. Part C 6 (1964) 183.
[23] H. L. Friedman, J. Polym. Lett. 4 (1966) 323.
[24] T. Ozawa, Bull. Chem. Soc. Jpn. 38 (1965) 1881.
[25] J. H. Flynn, L. A. Wall, J. Polym. Sci. Polym. Lett. 4 (1966) 323.
[26] N. Sbirrazzuoli, Y. Girault, L. Elégant, Thermochim. Acta 25 (1997) 293.
[27] S. Vyazovkin, N. Sbirrazzuoli, Macromol. Rapid Commun. 27 (2006) 1515.
[28] A. W. Coats, J. P. Redfern, Nature 201 (1964) 68.
[29] A. B. Phadnis, Thermochimica Acta 62 (1983) 361.
[30] S. Vyazovkin, D. J Dollimore, Chem. Inform. Comput. Sci. 36 (1996) 42.
[31] A. I. Lesnikovich, S. V. Levchik, J. Therm. Anal. 27 (1983) 89.
[32] A. I. Lesnikovich, S. V.Levchik, J. Therm. Anal. 30 (1985) 677.

6

CONCLUSIONS

- **Structural transitions**
  - Nylons 56, 65 and 47 have similar structures when crystallized directly from synthesis. The molecular arrangement is characterized by a monoclinic unit cell (form I) that can be interpreted in terms of a peculiar packing where hydrogen bonds are established along two directions and where neighboring chains are shifted along their chain axis direction.
  - Although a similar structure was postulated at room temperature for the studied even-odd and odd-even nylons.
  - On heating, nylons 65 and 47 first showed a transition towards a less compact structure (form II) characterized by the presence of two close equatorial reflections (0.422 and 0.401 nm) and subsequently underwent a second transition where the two indicated reflections progressively merged into a single one.
  - On heating, nylon 56 showed only a transition towards a pseudohexagonal packing, although an additional rearrangement of amide groups was detected at some degrees before fusion.
  - Nylons 65, 47 and 56 crystallized from the melt according to the Brill high temperature structure.
    - In the case of nylons 65 and 47, the structure first reverted to form II on cooling, showing a hysteresis effect and then this form II underwent a partial transition to the low temperature structure
    - Nylon 56 did not show a Brill transition during the cooling process alghough a progressive, minor crystallization into the low temperature structure also took place.

- **Spherulitic morphology**
  - Nylon 56 crystallized on cooling into fibrillar spherulites with optical properties that were depended on the crystallization temperature and differed from those found in nylons having conventional sheet structures. During crystallization thinner lamellae inserted into the loosely stacked bundles of primary lamellae and the interlamellar amorphous regions became more compact
  - Nylon 65 crystallization from the melt gives rise to spherulites constituted by lamellae of different thicknesses, which accounts for the multiple melting peaks observed in the calorimetric heating runs. During crystallization thinner lamellae insert into the loosely stacked bundles of primary lamellae and the interlamellar amorphous regions become more compact. Spherulites with different textures (ringed or fibrilar) and birefringences

can be obtained by varying the crystallization conditions. Negative spherulites form in the low temperature region, indicating a molecular arrangement different from that found in conventional even-even nylons, whose low temperature spherulites show a positive birefringence.

- Nylon 47 showed spherulites with different textures and birefringences depending on the crystallization temperature. Negative spherulites formed in the low temperature region, indicating a molecular arrangement different from that found in conventional even-even nylons that gave rise to spherulites with a positive birefringence. Spherulites obtained at low supercoolings were mainly constituted by flat micro-crystals that showed reversible optical properties with temperature. This peculiar behaviour may be a consequence of the postulated structure with two hydrogen bonding directions since small changes on the torsional angles of the odd diamide units could induce a variation on the angle between the two hydrogen boding directions and on the birefringence sign of the crystalline micro-domains.

FTIR

- Nylon 65 absorption bands observed in the room temperature infrared spectra suggests that this polyamide has a structure related to conventional α/β forms despite its different hydrogen-bonding scheme. Spectra are sensitive to the structural changes; specifically the temperature evolution of the amide A band allows the form I to form II transition to be detected.

Nanocomposites

- Nanocomposites with intercalated and exfoliated structures could be obtained from nylon 47 and the C25A and C30B organomodified clays. The final structure mainly depended on the preparation method. Specifically, melt mixing favoured the exfoliated distribution whereas intercalated structures were obtained by solution intercalation. Incorporation of clay particles influenced the overall crystallization rate under both isothermal and non-isothermal conditions. In all cases, clay particles decelerated the crystal growth process and had a strong influence on the primary nucleation which could be enhanced or disfavoured when intercalated or exfoliated structures were respectively achieved.

Poly (glycolic acid-6-hydrohexanoic acid)

The solvent casting technique was appropriate to prepare nanocomposites with an exfoliated structure from the C25A organo-modified clay and a new biodegradable polyester characterized by an alternating distribution of glycolic acid and 6-hydroxyhexanoic acid units. The nanocomposite had interesting characteristic to remark:

- **Thermal analysis**

  Thermogravimetric analyses showed that the addition of clay particles had a small stabilization effect at the beginning of the degradation process, which is currently interpreted as a consequence of polymer chain nanoconfinement.

- **Crystallization**

  The semicrystalline character of the new polyester allowed the study of the influence of clay particles on crystallization kinetics and crystal morphology. Thus, incorporation of C25A decelerated the mechanism of primary nucleation and crystal growth of the neat polyester, a trend commonly observed when high homogeneous dispersion of silicate layers occurs. A slight increase in the secondary nucleation constant was also inferred for the nanocomposite by considering the Lauritzen and Hoffman treatment.

  FTIR and WAXD data obtained during isothermal crystallization were consistent and indicated a decrease in the overall crystallization rate when silicate layers were added.

- **Morphology**

  Optical microscopy revealed differences in spherulite morphology between the neat polyester and its nanocomposite. Furthermore, SAXS data showed significant changes in the morphology of constitutive lamellae since a dramatic decrease in amorphous layer thickness was observed for the nanocomposite. Despite this feature, the degree of crystallinity was higher for the neat polyester, suggesting an increase of the amorphous domains between lamellar stacks when the miscible silicate layers were added to the polymer matrix.

Poly(glycolic acid-alt-6-aminohexanoic acid)

- **Nanocomposite preparation and structure.**

  - The C25A organo-modified montmorillonite has proved to be effective for the preparation of nanocomposites of the degradable alternating poly(ester amide) constituted by glycolic acid and 6-aminohexanoic acid units by the in situ polymerization technique.
  - The in situ polymerization of sodium chloroacetylaminohexanoate in presence of C20A or C30B organo-modified clays rendered intercalated silicate structures, as determined by X-ray diffraction and transmission electron microscopy.
  - Nanocomposites prepared by the melt mixing technique using a 3% content of C25A organo-modified clay and the selected poly(ester amide) rendered an intercalated structure.

- **Polymerization kinetics**

  - Polymerization kinetics of sodium chloroacetylaminohexanoate was strongly influenced by the presence of organo-modified montmorillonites under both nonisothermal and isothermal conditions. The reaction process was rather complicated when polymerization temperatures lower than 145 ºC were selected since polymer crystallization occurred before the polymerization reaction was finished. WAXD profiles revealed changes in the monomer structure and the range where the reaction proceeded in a liquefied state.
    - FTIR and WAXD experiments were appropriate techniques to evaluate the in situ polymerization kinetics and in particular the estimation of the activation energy and the pre-exponential factor. This factor was found to decrease when nanocomposites had an exfoliated structure probably as a consequence of a decrease of the chain mobility and the frequency at which reactive groups were close enough to facilitate the condensation reaction. Nanocomposites with intercalated structures showed also a decrease of the pre-exponential factor but also in the activation energy, which in this case suggest a favoured condensation process caused by the nanoconfinement of monomers in the silicate galleries.

- **Crystallization**

  - The nanocomposite with an exfoliated structure prepared by *in-situ* polymerization thechnique, crystallized at lower rate that the neat polymer since both nucleation density and crystal growth rate were lower. On the contrary the nanocomposite having an

intercalated structure (i.e. prepared by the melt mixing technique) had an enhanced nucleation rate hot and cold crystallization experiments. Thus, silicate particles act as effective nucleating agents at low degrees of compatibility, a result that contrasts with the that obtained with the practically exfoliated structure prepared by *in situ* polymerization.

- The addition of clay particles slightly reduced the radial growth rate, as showed in the hot crystallization experiments where the dimensions of spherulites allowed obtaining accurate measurements. Results also point to a slight increase in the secondary nucleation constant for the nanocomposite sample.
- The effect of nanoparticles on the overall crystallization rate of intercalated structures is a consequence of the balance of two opposite trends: increase in primary nucleation density and decrease in crystal growth rate, which specifically led to faster crystallization in the hot crystallization experiments.
- The degree of crystallinity was always slightly lower for nanocomposite samples respect to the neat polymer, indicating a disturbing effect of the clay particles on the crystallization processes. It evolved rather differently during the hot crystallization processes, with a sudden increase at the beginning of the process in the case of the nanocomposite that reflects a faster primary crystallization mainly caused by the increase in nucleation density. The poorer nucleation of the neat polymer resulted in a time smearing of the primary and secondary crystallization.
- The addition of clay particles was highly influential in the crystal morphology since it favoured a lamellar insertion mechanism and caused a decrease in the average lamellar thickness. Lamellar reorganization occurred at high temperatures, resulting in similar lamellae when the nanocomposite and the neat polymer samples crystallized from the glass state.

Thermal Analysis

- Incorporation of C25 clay particles decreased the thermal stability of the poly(ester amide), probably due to the presence of the organo-modifier compound. Nevertheless, the melting temperature was clearly lower than the temperature at which decomposition started and consequently samples are able to be melt processed.
- The incorporation of a small percentage (3 wt %) of the C25A organo-modified clay to the poly(ester amide) had a significant influence on the thermal decomposition process:
  - The first degradation step, which mainly involved the decomposition of glycolic acid units, proceeded faster when the clay was added. The low stability of the organo-modifier compound had a determinant role and contributed to modify the degradation mechanism associated to this step. Thus, results derived from

isoconversional analyses, and the Coats-Redfern and IKP methods were highly consistent and allowed postulating an autocatalytic mechanism instead of the sigmoidal type A_2 mechanism determined for the neat polymer.

- Last stages of degradation proceeded slowly for the nanocomposite, which furthermore showed a complex degradation process due to existence of two additional decomposition mechanisms. Thus, the second degradation step observed in the pristine sample was split due to the influence of clay particles which probably enhanced the performance of the char formed.

The pre-exponential factor of the last degradation step of the pristine sample was higher than the calculated value for the nanocomposite suggesting that motion of reactive groups was hindered by the presence of silicate layers.

Appendix A

ALIPHATIC POLYESTER AND POLY(ESTER AMIDE) CLAY NANOCOMPOSITES BY IN-SITU POLYMERIZATION*

A.1. Introduction. Biodegradable polymers and their nanocomposites

In recent years interest in biodegradable polymers has grown because of their sustainability and specialized applications mainly in the biomedical field. These polymers are becoming crucial for different industrial sectors like agriculture, automotive industry, medicine and packaging, which require the use of environmentally friendly materials and, in some specific cases, biocompatible polymers. Specifically, polymers susceptible to being employed in packaging seem to be receiving more attention since it is estimated that more than 40% of plastics are used in this area.

Biodegradable polymers can be classified into three categories according to their origin: a) Synthetic polymers, particularly aliphatic polyesters, such as poly(L-lactide) (PLA) [1-3], poly(ε-caprolactone) (PCL) [4-6], poly(*p*-dioxanone) (PPDO) [7-9] and poly(butylene succinate) (PBS) [10-12], b) polyesters produced by microorganisms, which mainly correspond to different poly(hydroxyalkanoate)s (e.g. poly(β-hydroxybutyrate) and poly(3-hydroxybutyrate-*co*-3-hydroxyvalerate)) and c) polymers derived from natural resources (e.g. starch, cellulose, chitin, chitosan, lignin and proteins).

* *The work described in this section appeared in : Morales-Gámez, L. Rodríguez-Galán, Alfonso Franco, L.; Puiggalí, J. In In-situ Synthesis of Polymer Nanocomposites Polymer Nano-, Micro and Macrocomposites (Volume 2); Mittel, V., Ed. Wiley-VCH, Weinheim, 2011; pp. 367-384.*

Despite the large investment in biodegradable polymers, it is clear that they are still far for becoming ideal substitutes of conventional synthetic polymers applied as commodities. In general, the main limitations are their high manufacturing costs and disadvantageous physical properties (e.g. poor mechanical and thermal properties, high hydrophilicity and poor processability). Therefore, it seems very necessary to modify their chemical nature and/or enhance their performance by nanotechnology. In the first case, the incorporation of amide groups into a polyester chain is an interesting option as poly(ester amide)s (PEAs) should establish strong intermolecular interactions that may improve properties and maintain degradability [13,14]. In the second case, the incorporation of nanoscale particles into a polymer matrix should provide polymer/nanoparticle composites with enhanced properties. Although several preparation methodologies have been developed, in-situ polymerization in the presence of layered silicates appears more appropriate to render exfoliated structures, which should have a greater impact on properties than intercalated structures [15].

This chapter reviews the state of art in the preparation of nanocomposites based on biodegradable aliphatic polyesters and poly(ester amide)s by in-situ polymerization.

A.2. Aliphatic polyester clay nanocomposites by in-situ polymerization

2.1. Poly(ε-caprolactone) based nanocomposites

The in-situ polymerization technique has received much attention since the successful preparation of exfoliated nanocomposite structures from polyamides [16-18] by promoting polymerization from initiators located on the clay surfaces.

Early works on in-situ polymerization of ε-caprolactone were carried out by Giannelis *et al*. [19]. A composite consisting of poly(ε-capro1actone) intercalated silicate particles embedded in the same polymer matrix was synthesized by heating Cr^{3+}-fluorohectorite (a synthetic mica type of silicate) to 100 ºC in the presence of an excess of ε-caprolactone.

Intercalation of the monomer was revealed by powder XRD, which showed an increase in the silicate *d* spacing from 1.28 to 1.46 nm, in consistency with a perpendicular orientation of the ε-caprolactone ring to the silicate layers. XRD patterns after polymerization indicated a reduction in the silicate spacing from 1.46 to 1.37 nm, which suggested a dimensional change accompanying polymerization. Thus, the opening of the lactone ring in the monomer gave rise to a monolayer of fully collapsed poly(ε-capro1actone) chains (**Figure A.1**).

The polymer matrix was isolated and found to be indistinguishable (except for chain end groups) from the bulk polymer obtained by metal-alkoxide initiated polymerization. The polymerization reaction was postulated to proceed through cleavage of the acyl-oxygen bond catalyzed by the interlayer Cr3+ ions. The intercalated polymer was strongly adsorbed onto the silicate layers and showed no melting transition.

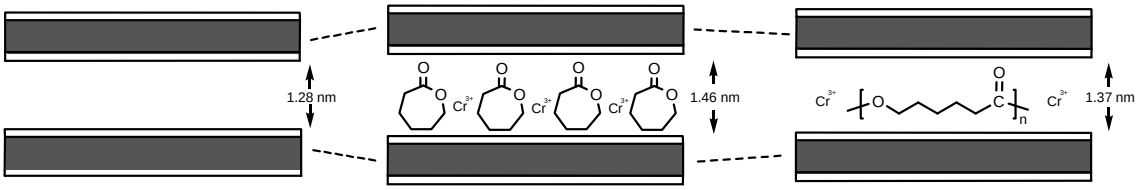

Figure A.1 Changes in the silicate spacing as a consequence of monomer intercalation and subsequent polymerization.

Giannelis *et al.* [20] also reported the preparation of nanocomposites by reacting protonated 12-aminolauric acid-exchanged montmorillonite with ε-caprolactone monomer. The monomer ring was initially intercalated in the gaps between the aminolauric acid chains so that no gallery expansion was detected in the X-ray diffraction patterns. During heating of this mixture at 170 ºC, the organic acid groups initiated ring-opening polymerization of the heterocyclic monomer by nucleophilic attack on the ε-caprolactone carbonyl. Diffraction patterns of powdered composite samples showed no discernable (001) reflections due to the organo-modified clay, suggesting that individual silicate layers were dispersed in the polymer matrix. It was also determined that water permeability through composite films containing modest amounts of silicate was dramatically reduced (e.g. by nearly an order of magnitude at only 4.8 *v* %) due to dispersion of impermeable high aspect ratio silicate layers in the polymer matrix.

The high average grafting density (with the areal grafting density x unperturbed radius of gyration >> 1) of the obtained nanocomposites made these systems excellent models to understand the static conformations and dynamics of polymer brushes, which is a focus of intense theoretical, experimental and simulation interest. Similarities in the rheological response of end-tethered nanocomposites and block copolymers and smectic liquid crystals were demonstrated. The rheology of these end-tethered silicate nanocomposites was investigated using linear viscoelastic measurements in oscillatory shear with small strain amplitudes [21]. It was found that the storage and loss moduli increased at all frequencies with increasing silicate loading. However, their power law dependence on the terminal zone was different from that observed in homopolymers and decreased with increasing silicate loading. At low frequencies the rheological response became almost invariant with frequency, which suggested a solid-like response. Interestingly, the system exhibited a nonterminal rheological behavior and had molecular weights which suggested a marginal entanglement. This was in close agreement with claims concerning lamellar block copolymers and smectic liquid crystals according to which the presence of entanglements was not required to observe nonterminal behavior.

The in-situ polymerization technique has recently been applied for the preparation of PCL/layered aluminosilicate nanocomposites. Tin(II) octoate and dibutyltin(IV) dimethoxide

were reported as appropriated transesterification catalysts to promote the polymerization of ε-caprolactone in the presence of organo-modified clays [22-25]. Montmorillonites with surfaces modified by ammonium cations bearing hydroxyl groups (e.g. bis(2-hydroxyethyl)methyl (hydrogenated tallow alkyl) ammonium) were found to be highly efficient in initiating the polymerization and ‘‘grafting’’ the PCL chains onto the layered silicate surface. Lactone polymerization was postulated to be initiated by all the hydroxyl functions available at the clay surface after activation into either tin(II) or Al(III) alkoxide active species. Hybrid nanocomposites were accordingly generated through covalent grafting of every polyester chain onto the filler surface. Surface-grafted polycaprolactone (PCL) chains were untied and isolated by ionic exchange reaction with LiCl in THF solution and molar masses were measured by size exclusion chromatography. The PCL molecular weight and the extent of clay exfoliation could be controlled and readily tuned by the content of hydroxyl groups available at the clay surface [25]. Another interesting conclusion was that the initiation reaction by aluminum trialkoxide active species yielded grafted PCL chains characterized by a very narrow molecular weight distribution (M_w/M_n~1.2).

Transport properties of water and dichloromethane vapors and mechanical properties were investigated for PCL chains grafted by in-situ polymerization onto clay modified by ammonium salts bearing hydroxyl groups. The clay content was fixed at 3 wt % in inorganics whereas the hydroxyl functionality ranged between 25 and 100%, always leading to clay delamination [26]. The increase in polymer chain grafting density resulted in a better exfoliation of the clays, limiting for example the diffusion of permeant water molecules. In the same way, the diffusion parameters of dichloromethane exhibited a decreasing value on increasing the hydroxyl content in the nanocomposites. Mechanical and dynamic mechanical analyses showed improvement in the nanocomposite elastic modulus in a wide temperature range. Interestingly, for the higher hydroxyl contents (50, 75, and 100%), the modulus could be measured up to 120 °C (i.e. a much higher temperature than the melting temperature of pure PCL).

A surfactant mixture that contained varying proportions of hydroxyl-substituted alkylammonium and unsubstituted alkylammonium cations to exchange the initial Na^+ counterions of the natural montmorillonite was employed to have a tunable amount of hydroxyl functions at the surface of the clays. As previously indicated, those functions were then derivatized into aluminium alkoxides in order to initiate the ring-opening polymerization of ε-caprolactone directly from the clay surface, which was swollen in an organic solvent. Atomic force microscopy measurements on the resulting polymer-grafted nanoplatelets demonstrated the strong dependence of the coating of individual clay particles on the composition of the surfactant mixture used for the cationic exchange [27]. This allowed the generation of a range of morphologies varying from polymer islands distributed over the clay surface to homogeneous

polymer layers thoroughly coating the platelets (**Figure A.2**). Direct visualization of the polymer grafted onto the clay platelets gave relevant information on the structure of the obtained nanohybrid materials. First, the grafting density increased drastically as the proportion of OH-substituted alkylammonium cations used to organo-modify the clay was raised. Second, the polymer deposit was not simply a continuous film growing in thickness with increased OH content. Instead, separate polymer islands formed in the low-OH-content systems, probably as a result of a phase separation process between the ammonium ions induced by the polymerization reaction. Homogeneous coverage and subsequent thickening only took place from 50% OH content. When this situation was achieved, adjacent platelets became fully independent of each other since they were fully covered by the polymer and exfoliation was greatly favored.

Bulk polymerizations of ε-caprolactone were also conducted at 170 ºC in the presence of catalytic traces of water and 10, 30 and 50 wt% of hydrated synthetic montmorillonite SOMASIF ME100 without additional catalysts [28]. ^{1}H NMR and GPC analyses suggested that the montmorillonite present in the system induced both significantly higher lactone hydrolysis and polymer chain growth rates. All systems gave rise to low molecular weights (M_w = 5360–22,432), which seemed to indicate a hindrance effect in diffusion caused by increasing amounts of silicate in the system. Wide-angle X-ray diffraction data revealed that within the interlamellar regions of silicate, ε-caprolactone was arranged in weakly ordered bimolecular pseudo-layers. It is worth noting that the interlayer spacings of montmorillonite in the nanocomposites were slightly smaller than for silicate dispersed in ε-caprolactone. Such results were attibuted to an unfavorable polymerization of ε-caprolactone in the interlayer region of the silicate (i.e. chains remained small and unable to open the clay layers to give rise a delaminated structure). The comparison between measured values of gallery height and calculated dimensions of the poly(ε-caprolactone) chain indicated that polymer chains were flatly arranged on each side of the silicate platelet, creating pseudo-bilayers inside the montmorillonite gallery.

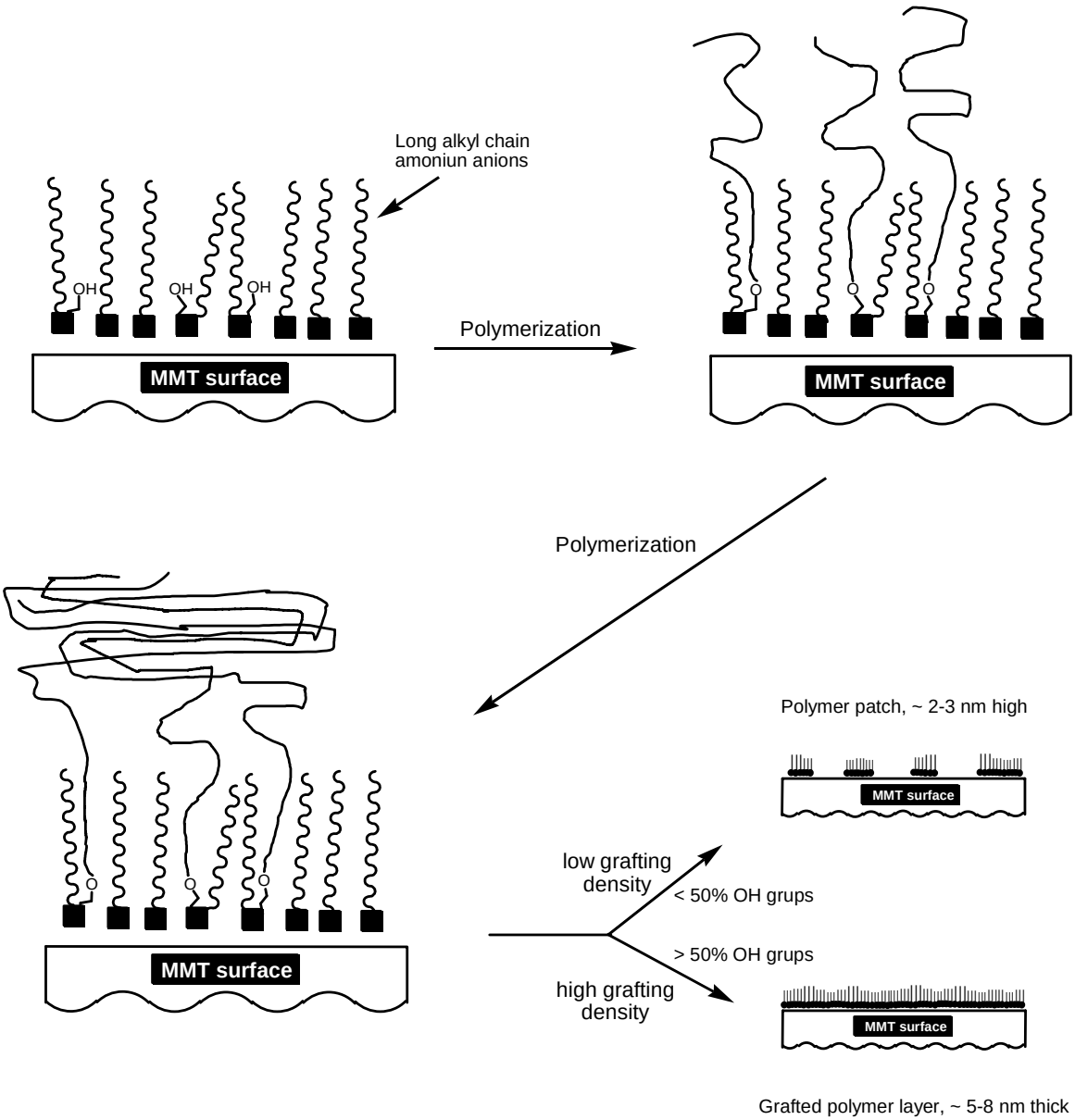

Figure A.2 Scheme of the polymer surface grafting onto individual clay platelets and concomitant phase separation, as explained in detail in reference [26].

Comprehension of the nanocomposite structure and interactions at the polymer/nanofiller interface is crucial in controlling nanocomposite properties. In all cases, nanocomposites are characterized by the presence of a polymer layer at the interface with the inorganic surface whose properties clearly differ from those of the bulk polymer. Pucciariello *et al.* [29] conducted a detailed surface analysis of poly(ε-caprolactone)-montmorillonite clay nanocomposites obtained by in-situ polymerization. The organophilic clay was prepared by treating the natural montmorillonite with a solution of protonated 12-aminolauric acid. In-situ polymerization of ε-caprolactone was performed under a nitrogen atmosphere at room

temperature for 2 h and then at 170 °C for 48 h. The organo-modified montmorillonite concentration was close to 18% as this was previously determined as the maximum content at which the silicate was exfoliated [30,31]. The X-ray photoelectron spectroscopy (XPS) technique gave information on atom concentrations in the surface layer, the valence state of these atoms and the bonding of their nearest neighbors. Spectroscopic data indicated a great polarization of Si-O and Al-O bonds in the organo-modified montmorillonite, which was attributed to the electron-attracting and electron-donor effects of the NH_3^+ and COOH groups of the aminolauric ion, which efficiently coordinated the partially negatively charged oxygens and the partially positively charged silicons (aluminums) of the clay (**Figure A.3** a). XPS data of the nanocomposite revealed lower binding energies of Si-O and Al-O bonds, and consequently a reduced ionicity of such bonds with respect to the organophilic clay. Thus, the presence of the polymer limited the polarizing effect of the aminolauric cation because of the electron-donor/electron-attracting effects of the ester group oxygens (**Figure A.3** b).

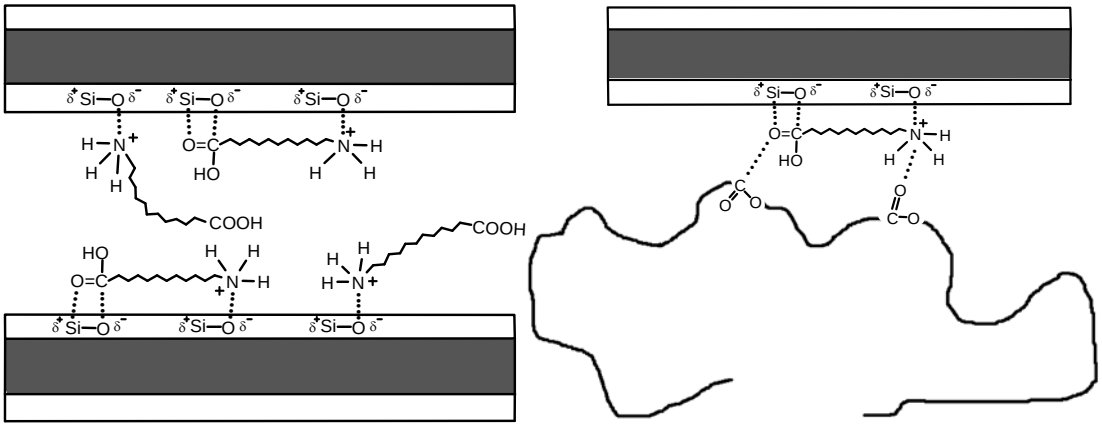

Figure A.3 Schemes explained in detail in Ref. [30] showing: a) Coordination of the aminolauric cation $HOCO-(CH_2)_{11}-NH_3^+$ to the clay. b) Model of the interactions occurring in the polymer-alkylammonium cation-clay system.

Poly(ε-caprolactone) was studied as a polymer biodegradable matrix which adds potential to the use of derived nanocomposites as biodegradable packaging materials. The synthesis of a series of montmorillonite-PCL nanocomposites in which the content of the inorganic material was varied regularly from 0 to 44 wt.-% was performed to find some basic structure/property correlations of the multiphase nanocomposites and investigate the permeability to organic (e.g. dichloromethane) and inorganic (e.g. water) solvents of the multiphase polymers [32]. In-situ polymerization was carried out at 85 ºC using a montmorillonite modified with protonated 12-aminolauric acid. Permeability to water and dichloromethane was found to decrease significantly with increasing clay content. In particular, the water permeability behavior was largely dominated by the diffusion parameter. The diffusion path of the polar molecules of

water was assumed to be slowed down with respect to dichloromethane vapor because of not only the physical barrier of the clay layers but also the hydrophilic character of the platelets. Barrier properties associated with the biodegradability of poly(ε-caprolactone) play an important role in enhancing interest in these nanocomposites as biodegradable packaging materials.

PCL is thermodynamically miscible with many other polymers (e.g. PVC or SAN copolymer) and can be used as an environmentally decomposable additive that facilitates plastic degradation [33]. A study was recently undertaken to dissolve PCL-clay systems prepared by in-situ polymerization in a SAN matrix and evaluate the structure and mechanical properties of these ternary nanocomposites [34]. The in-situ polymerization was performed at 170 ºC using a commercial montmorillonite modified with hexadecyltrimethylammonium bromide. Clay content was of 10, 30 or 50 wt.% since nanocomposites were then used as masterbatches to obtain SAN/(PCL/clay) ternary blends containing 0.66–5.65 wt.% of the organo-modified clay. Blends of PCL nanocomposites with SAN copolymer gave rise to intercalated and semi-exfoliated structures, as deduced from XRD and TEM techniques. The increase of clay in the system led to higher values of Young's modulus. Thus, compared to unmodified SAN the addition of only 0.66 wt.% resulted in approximately a 10% increase in stiffness modulus while at 5.65 wt.% a 40% increase was obtained.

Supercritical CO_2 has been studied as an alternative polymerization medium (e.g. for ring-opening polymerization of lactones [35,36]) for more conventional organic solvents due to its well known advantages [37]. Thus, it is environmentally friendly, non toxic, non flammable and economical since its critical parameters are relatively easily obtained. Furthermore, its fluid/solvent properties can be tuned by small changes in temperature.

Preparation of nanocomposites by redispersion of masterbatches of exfoliated PCL-nanocomposites into polymers miscible with PCL, such as the styrene/acrylonitrile copolymer [34], showed encouraging results but also drawbacks, e.g. difficulty in recovering the aggregated bulk masterbatch and need to purify it before use. Detrembleur *et al.* [38] proposed an alternative method based on the preparation of PCL/clay masterbatches by in-situ intercalative polymerization in supercritical carbon dioxide. The specific properties of this solvent allowed in-situ polymerization at high clay content without viscosity problems. This is never the case for bulk polymerization processes, where clay loading is usually limited to 30 wt %. Furthermore, the product obtained after depressurization was an easily recoverable fine powder and supercritical CO_2 was able to extract the residual monomer during depressurization, directly providing a ready-to-use dry powder. The ring-opening polymerization of ε-caprolactone in supercritical carbon dioxide occurred as a dispersion polymerization since only the monomer was soluble in this medium under typical supercritical conditions [39]. Catalysts

like $Sn(Oct)_2$ were preferably used as they should have low sensitivity to the carbonation reaction and protic impurities. Polymerizations of ε-caprolactone were carried out in supercritical CO_2 (85 ºC, 28 MPa) using the natural montmorillonite and the clay organo-modified with a non-functional (Cloisite 20A) or a functional (Cloisite 30B) quaternary ammonium salt. In all cases, nanocomposites were qualified as ‘‘pre-exfoliated’’ masterbatches since true exfoliation could not be reached at high clay contents. Redispersion of organo-modified clay/polymer masterbatches into chlorinated polyethylene was proved to be more efficient in terms of quality of clay delamination than direct blending of commercial clay.

Starch, a natural polymer constituted by linear α-glucan amylose and highly branched amylopectin, is considered one of the most promising candidates to be used as environmentally friendly materials. It has an attractive combination of availability, price and performance, but its mechanical properties are poorer than those of synthetic polymers mainly due to its hydrophilic nature, which makes it sensitive to moisture content. For this reason, starch has been modified by blending with synthetic polymers such as poly(ε-caprolactone) and even with layered silicates [40,41]. Nazami *et al.* [42] have recently prepared starch-*g*-polycaprolactone by in-situ ring-opening polymerization of ε-caprolactone in the presence of starch, $Sn(Oct)_2$ and an organo-modified montmorillonite (i.e. Cloisite 15A) at reaction temperatures between 100-150 ºC. Results suggested a slight improvement in thermal stability but intercalation of the copolymer into clay galleries was less effective than the solution intercalation method.

2.2. Polylactide based nanocomposites

Polylactide (PLA) is a well-known green polymer which receives great attention from the polymer industry since it can be produced from renewable resources (e.g. corn starch and other carbohydrate-rich substances like maize, sugar or wheat) and is biodegradable and compostable. These advantages make PLA an attractive alternative to classical commodity polymers (e.g. in the production of loose-fill packaging, compost bags, food packaging and disposable tableware). However, several properties need to be improved to widen its range of applications. For example, PLA is too brittle and permeable to gases to render optimal application performances, especially for packaging purposes. Despite this, PLA is currently one of the most widely used speciality polymers in the biomedical field (e.g. for sutures, stents, dialysis media, drug delivery devices and even for tissue engineering).

The introduction of a few percent of nanofillers, such as layered aluminosilicate clays, has been extensively considered to enhance PLA properties. However, the greatest improvement is usually achieved when nanoparticles are fully and uniformly delaminated (exfoliated) in the polymer matrix, a challenge that cannot be fully met by direct melt blending of the clay as this usually leads to intercalated nanocomposites [43,44]. The use of in-situ polymerization

techniques appears fully justified since the monomer can penetrate and then polymerize inside the clay sheets, enhancing the delamination efficiency.

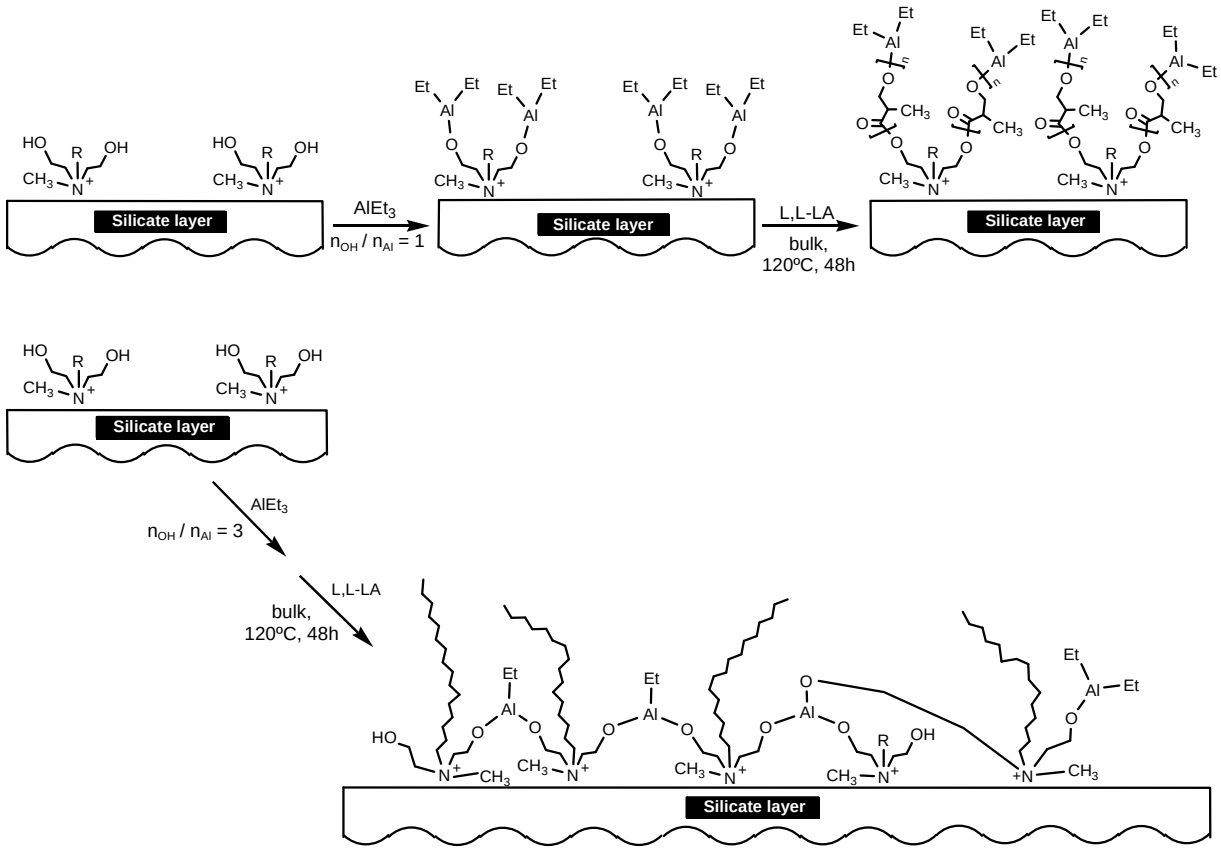

Figure A.4 a) Scheme of the L,L-lactide in-situ polymerization performed from Cloisite 30B using triethylaluminium ($AlEt_3$) as the initiator (R stands for tallow alkyl chain). b) Scheme of a mixture of aluminium mono-, di-, and tri-alkoxides produced by addition of $AlEt_3$ onto Cloisite 30B in a $n_{OH}/n_{Al} = 3$ molar ratio.

In-situ ring-opening polymerization of the lactide monomer in the presence of clay has been extensively studied [45,46]. For instance, PLA/MMT nanocomposites were prepared in bulk with catalysts such as tin(II) octoate ($Sn(Oct)_2$) or triethylaluminum in the presence of montmorillonite clays (e.g. Cloisites 25A and 30B) organo-modified with an ammonium salt functionalized or not with hydroxyl groups. When Cloisite 30B was used, polymerization was co-initiated by a molar equivalent of $AlEt_3$ or $Sn(Oct)_2$ with respect to the hydroxyl groups borne by the ammonium cations of the filler, which was added before the L,L-lactide monomer. The presence of hydroxyl groups was found to be critical because these led to aluminium alkoxide or tin alkoxide active species (**Figure A.4**and Equation A.1), which acted as initiators and led to polylactide chains grafted onto the clay surface.

$$Sn\,(Oct)_2 + n\,OH \longrightarrow Sn(Oct)_{2-n}(OR)_n + n\,OctH \qquad (A.1)$$

The molar ratio between hydroxyl groups and aluminium cations was crucial in promoting a controlled polymerization. Thus, a defect of aluminium cations should lead to more efficient aluminium trialkoxides but this was not the case when polymerizations were performed from lactide rings [46]. It was claimed that the probability to form a large amount of trialkoxide species from the anchored hydroxyl groups was rather low, and most probably a mixture of aluminium mono-, di-, and tri-alkoxides was formed (**Figure 6.4** b). This distribution was responsible for the observed low monomer conversion, loss of polymerization control and bimodality of the molecular weight distribution.

The grafted chains pushed the lamellar sheets apart from each other and led to the achievement of an excellent degree of clay exfoliation, which for example leads to improved thermal stability compared to unfilled PLA and even intercalated counterparts. Moreover, while the T_g and T_m of the PLA matrix were not influenced by the nanofiller, the degree of crystallinity of the polyester in the exfoliated structure was significantly higher than in the intercalated nanocomposite [45].

The grafting reaction was confirmed by the impossibility of dissolving the so-produced PLA chains in good solvents like toluene, THF or $CHCl_3$. In fact, a specific cationic exchange reaction with LiCl was required to recover the PLA chains, suggesting that polyester chains were attached to the ammonium cations localized in close vicinity and in electrostatic interaction with the montmorillonite surface. Interestingly, polymerization conditions (e.g. bulk with 3 wt% of Cloisite) allowed the synthesis of PLA grafts with a number average molecular weight close to 14,000 g/mol and a relatively narrow distribution for such a heterogeneous initiation process (i.e. polydispersity index was close to 1.5).

Dubois *et al*. [46] also used in-situ polymerization to prepare a PLA-MMT masterbatch and confirmed that its dilution with the neat PLA during melt processing was an effective technique for improving clay dispersion.

It is well known that brittleness is a strong limitation for the application of PLA. The use of plasticizing agents is a usual procedure that may allow PLA to fulfil mechanical requirements. Considerable efforts have been made to improve PLA brittleness to make it competitive with low-cost flexible commodity polymers (e.g. polyethylene and polypropylene). Several types of compounds such as citrate ester, poly(ethylene glycol) (PEG), glucose monoesters, partial fatty acid esters, oligomeric lactic acid and glycerol have been studied as plasticizers for PLA [47-49]. However, the addition of a plasticizer generally reduces strength and modulus. Moreover, despite the increase of deformation, PLA-based materials having a good balance of stiffness and high deformation are still required for wide applications. For this reason, the possibility of preparing nanocomposites based on the PLA matrix and adding a plasticizer compound has been considered, specifically, the preparation of nanocomposites by melt blending a PLLA matrix, a plasticizer like poly(ethylene glycol) and a nanofiller.

Nevertheless, PEG tends to diffuse out of the material and accumulates at the nanocomposite surface, leading to structural matrix changes upon ageing [50]. Thus, in-situ polymerization of L,L-lactide in the presence of both dihydroxylated PEG (M_w =1 000) and Cloisite 30B has been studied as an interesting alternative since it leads to nanocomposites based on a triblock copolymer matrix where the central polyethylene block affords flexibility and is not susceptible to diffusing out of the material [45]. Results showed that intensive clay platelet destructuration was achieved independent of the PEG weight ratio. The plasticizing effect of the PEG sequence (entrapped in the triblock copolymer) was highlighted by the significant T_g decrease of the nanocomposite (e.g. from 60 to 12 ºC at 16.2 wt.-% content in PEG). Moreover, the thermal degradation of the resulting nanocomposites was dependent on the relative content in PEG blocks and decreased as the polyether level increased within the triblock copolymer.

Polylactide/vermiculite nanocomposites were also prepared by in-situ intercalative polymerization of L,L-lactide in the presence of vermiculite clay particles (VMT) that were treated with an alkylammonium surfactant in order to decrease their highly hydrophilic character and favor diffusion of the cyclic monomer into the clay interlayer spaces [51]. XRD suggested that exfoliated structures were attained and TEM observations revealed that VMT layers were exfoliated and dispersed uniformly in the polylactide matrix. TGA indicated a slight improvement in thermal stability (i.e. the onset temperature increased from 279 to 314 ºC when 5% of organo-modified clay was added). Dynamo-mechanical analyses showed an increase in storage and loss moduli caused by the reinforcing effect of the nanoscale VMT layers, as well as a slight increase of T_g with increasing the clay content.

Nanocomposites based on anionic clays or layered double hydroxides (LDHs) have also been widely studied. These clays are comprised of positively charged layers with anions and water molecules in the interlayer region. Compounds were defined with the general formula $(Mg_{1-x}Al_x(OH)_2)^{x+}(A^-)_x\ nH_2O$, in which A^- represents an interlamellar anion (e.g. carbonate) [52]. Although LDHs occur naturally, they are usually synthesized under controlled conditions in order to obtain materials with a known, homogeneous composition [53]. LDH platelets have a high aspect ratio, tuneable layer charge density and can be prepared by low-cost processes. The potential suitability of organo-LDHs for intercalation of hydrophobic polymers, the potentially greater susceptibility to complete exfoliation than that of cationic clays and the catalytic activity for polymerization of lactides in the interlayer are also worth mentioning [54,55].

Taviot-Gueho and Leroux [56] suggested in-situ polymerization as an appropriate method for preparing polymer-LDH compounds because of the more confined interlayer spacing compared to a typical unmodified montmorillonite clay (0.78 nm versus 1.26 nm). The high charge density in LDHs and their dense packing favor the insertion of small molecules such as the lactide

dimer over the insertion of long PLA chains. This should lead to an effective dispersion of LDH platelets in the growing polymer matrix. Efforts have also focused on the insertion of new organic anionic species in LDH interlayers to enhance/modify hydrophobicity of LDHs [56,57].

Plackett *et al*. [58] studied in-situ polymerization of the lactide dimmer in the presence of LDHs modified with carbonate (LDH-CO_3) or laurate units LDH (LDH-C_{12}). LDH-CO_3 was synthesized by a conventional co-precipitation method [59] whereas LDH-C_{12} was prepared using the reconstruction method. In this procedure the previously synthesized LDH-CO_3 was calcined to form a mixed metal oxide (MMO) and then dispersed into an ethanol/water solution containing sodium laureate. This process involved fast rehydration of the layered structure, followed by a slower anion exchange reaction, giving rise to the so-called "memory effect" mechanism [60]. X-ray diffraction, scanning electron microscopy and transmission electron microscopy revealed that exfoliated nanocomposites were obtained when using LDH-C_{12} but that LDH-CO_3 gave a partly phase-separated morphology (**Figure A.5**).

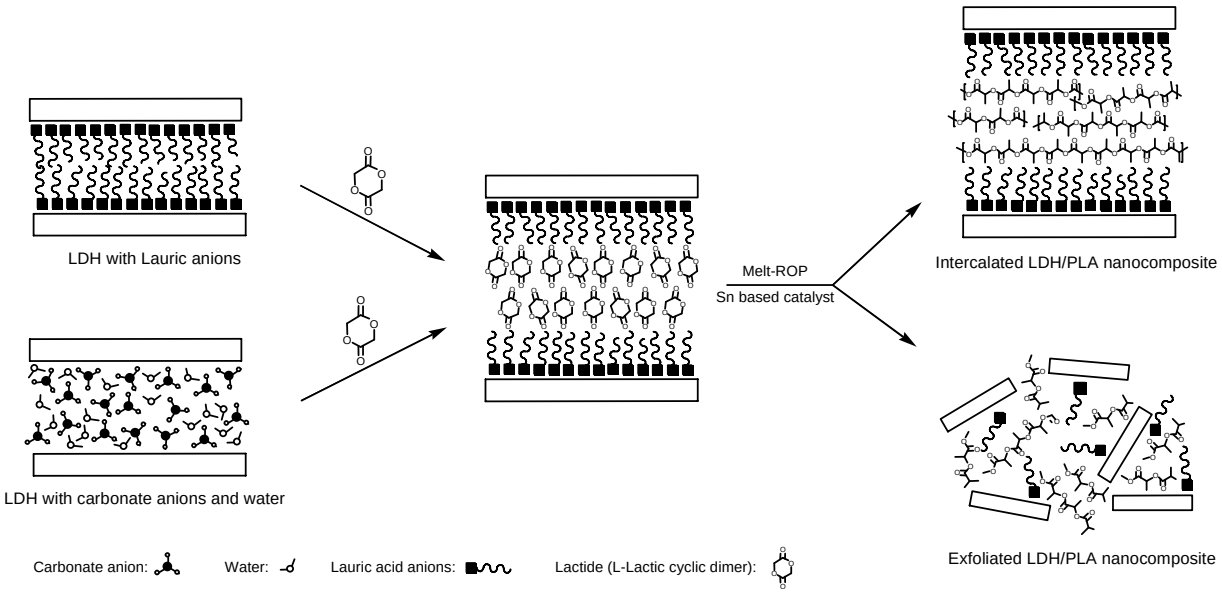

Figure A.5 Ring opening polymerization of lactide rings in the presence of layered double hydroxides modified with carbonate or laurate units.

Thermogravimetric analysis showed that PLA-LDH combinations exhibited higher degradation onset temperatures than unfilled PLA. Differential scanning calorimetry indicated that both crystallinity and temperature of crystallization increased on adding LDH-C_{12} or LDH-CO_3, suggesting that these additives have a nucleating effect. Although in-situ polymerization of lactide in the presence of 1-5% LDH-C_{12} could be a promising method for producing nanocomposites with an exfoliated structure, the molecular weight was significantly reduced when compared with the polymer synthesized in the absence of LDHs. Since this phenomenon

also occurred when $Mg(OH)_2$ was used instead of LDH, a chain-termination mechanism via LDH surface hydroxyl groups and/or metal-catalyzed degradation was proposed.

From an industrial point of view, the melt-intercalation technique is usually preferred to in-situ polymerization because it is simpler and uses already existing technologies. In this sense, methods that combine the efficiency of the in-situ polymerization approach and the practicability of the melt-intercalation technique are currently being applied. Thus, a highly filled polymer/clay masterbatch was first synthesized using an appropriate solvent and then dispersed into the commercial polymer by melt blending.

Detrembleur *et al*. [61] used supercritical carbon dioxide as a polymerization medium for in-situ polymerization of D,L-lactide in the presence of different organo-modified clays (e.g. C20A and C30B). Polymerizations were performed at 85 ºC and 240 bar where the lactide monomer was partially soluble whereas the formed polymer precipitated. The polymerization kinetic rate was observed to decrease with increasing the clay amount due to significant hindrance of the clay. A slightly higher conversion was observed in the C30B-based systems since its hydroxyl groups acted efficiently as polymerization initiators. Studies carried out at low clay levels (3 wt%) demonstrated that final structures were also strongly influenced by the nature of the organo-modifier compound since intercalated or exfoliated nanocomposites were obtained using C20A and C30B, respectively. Nanocomposites were also successfully obtained with clay levels as high as 35-50% and were then useful as masterbatches to be mixed with the commercial PLA matrix. In this way, well-delaminated nanocomposites with 3 wt% of Cloisite 30B were attained, as deduced from TEM and XRD analysis. The nanocomposites showed significant improvement in both stiffness (up to 20%) and toughness (e.g. from 5.1 to 6.0 kJ/m^2) compared with the unfilled matrix.

2.3. Poly(butylen succinate) based nanocomposites

Poly(butylene succinate) (PBS) is currently one of the most commonly applied biodegradable polyesters of the poly(alkylene dicarboxylate) family. It is commercialized by Showa Highpolymer as BIONOLLE and is usually copolymerized and blended to improve mechanical properties and biodegradability [62-65]. However, these methods (i.e. copolymerization and blending) often cause problems that affect crystallinity and melting point since the incorporation of a second component results in imperfect packing and/or isomorphism, and adversely affects the temperature range over which the resulting materials can be used [66,67]. Preparation of nanocomposites appears as a promising alternative method to the production of commercial PBS-based polymers. In this case, the aggregation trend of inorganic materials caused by strong hydrophilic interactions should be avoided.

Kim et al. [68] prepared nanocomposites by in-situ polymerization of 1,4-butane diol and succinic acid in the presence of Closite 25A or a twice functionalized organoclay (TFC) using titanium(IV) butoxide as a catalyst. TFC was prepared by reaction of C25A with a silane coupling agent that gave rise to epoxy functional groups. These were expected to enhance the chemical bonding of TFC layers with PBS end groups, and consequently lead to better dispersion and exfoliation of the clay layers in the PBS matrix. Furthermore, the thermal stability of PBS/TFC was clearly improved, which was attributed to the increased interaction between the inorganic components and the polymer. Lower thermal stability and an intercalated structure were characteristic of PBS/C25A nanocomposites.

Nanocomposites based on the PBS matrix were prepared by two-step polymerization consisting of direct esterification and polycondensation from succinic acid, 1,4-butanediol, titanium tetrabutoxide and fumed silica [69]. The first step was carried out at 190 ºC over 2 h and the second under vacuum at 240 ºC for 3-5 h. Solid-state ^{29}Si NMR and FTIR analysis indicated that silanol-bonded carbonyl groups were established within PBS/silica nanocomposite materials. Rheological effects inherent to the silica filler were evaluated and showed that despite high shear force, PBS/silica nanocomposites maintained a relatively high melt viscosity attributable to a network structure resulting from covalent bonding between silica and the polymer chain. Greatly improved mechanical properties were attained with only addition of 3.5 wt % of silica. Thus, an increase in both tensile strength (from 26.3 to 38.6 MPa) and elongation (from 56% to 515%) at break compared with parent PBS was reported. PBS/silica nanocomposites showed composition dependency on biodegradation ascribable to reduced crystallinity and preferential microbial attack.

Im *et al*. [70] treated Closite 30B with the coupling agent 1,6-diisocyanatohexane (HDI) to form covalent bonds between silanol groups on the clay side and between a silanol group and the hydroxyl group of the organo-modifier in the silicate layer (**Figure 6.6**). In this way, it was possible to increase both basal spacing and the favorable interaction between clay and PBS. Nanocomposites were prepared by two-step *in-situ* polymerization, as previously indicated. It was found that, at the same level of clay content, these nanocomposites showed a higher degree of exfoliation, as well as improvement in all mechanical properties, including tensile strength, storage modulus, and elongation at breaks compared with PBS and C30B nanocomposites.

Dubois *et al.* [71] demonstrated that the enhancement of *in-situ* transesterification reactions was a highly effective method to improve organo-clay dispersion and exfoliation in a polyester matrix. Thus, Bionolle/Cloisite 30B nanocomposites were prepared by melt intercalation with addition of dibutyltin dilaurate ($(Bu)_2Sn(Lau)_2$) as a catalyst. Polyester chains were covalently linked to the organo-modifier as a result of effective transesterification reactions occurring between the polymer chains and the hydroxyl groups of the organoclay. As a consequence of

this process, clay exfoliation was enhanced and stiffness of the final compound clearly increased (i.e. Young's modulus showed an increase of 60% compared with the neat polyester).

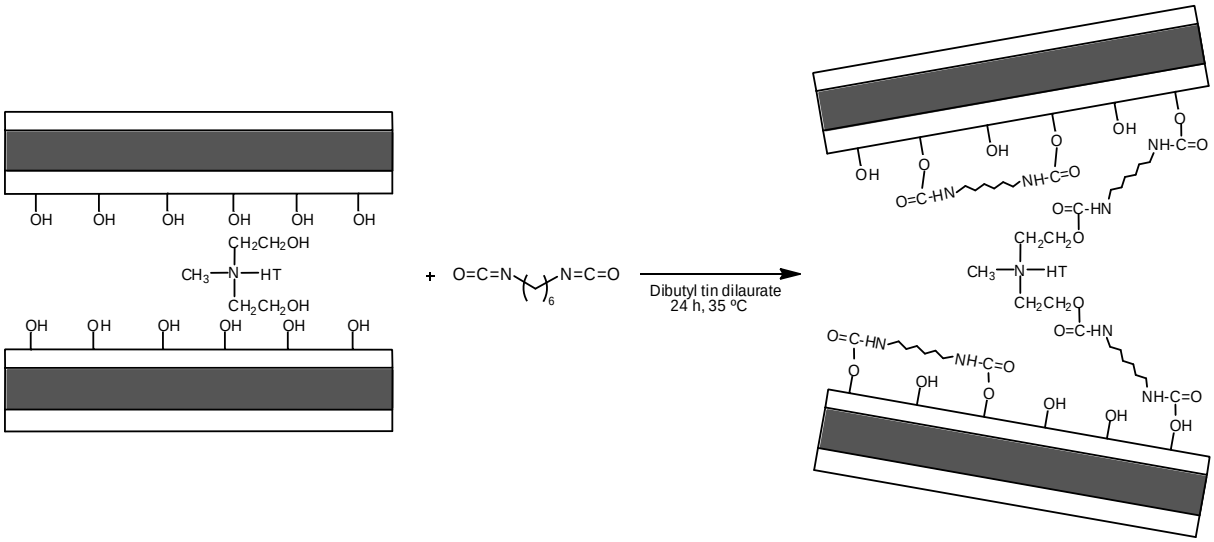

Figure A.6 Formation of covalent bonds between HDI and the silanol and hydroxyl groups in an organo-modified montmorillonite as explained in Ref. [70].

2.4. Poly(*p*-dioxanone) based nanocomposites

Poly(*p*-dioxanone) (PPDO) is a biodegradable polymer of great interest for applications in the biomedical field (e.g. bioabsorbable surgical sutures, bone fixation devices and drug delivery systems) due its outstanding mechanical properties, for instance high tensile strength and excellent flexibility [72]. This polymer has also been applied as a drug delivery system and has great potential for general use in systems such as films, molded products, laminates, foams, non-woven materials, adhesives and coatings [73]. However, PPDO has some unfavorable characteristics (e.g. high hydrophobicity, low crystallization rate and low melt strength), which may limit its application and processing. Modifications based on the preparation of nanocomposites now appear as an ideal method to improve physical properties and avoid some of the above limitations. In this line, Wang *et al.* [74] studied the *in-situ* ring-opening polymerization of PPDO with organo-modified montmorillonites (natural sodium montmorillonite, montmorillonite modified by octadecyltrimethyl ammonium chloride, and montmorillonite modified by hydroxyethylhexadecyldimethyl ammonium bromine) in the presence of triethylaluminum. Reactions were performed for approximately 20 h at 50 ºC. Interestingly, montmorillonites accelerated the polymerization reaction and led to a viscosity-average molecular weight of PPDO of 44,900 g/mol in only 0.5 h. Furthermore, a nucleating effect of montmorillonites was clearly observed and the crystallization temperature of PPDO increased by approximately 18 ºC. All three montmorillonites improved the thermal stability of

PPDO and increased its glass-transition and melting temperature. In addition, the melt strength of the PPDO/MMT nanocomposites increased dramatically when compared with that of the neat PPDO [73]. These results suggested that biodegradable PPDO/MMT thin films could be prepared by blowing process since low crystallization rate and low melt strength limitations can be overcame.

A.3. Poly(ester amide)s clay nanocomposites by in-situ polymerization

Poly(ester amide)s (PEAs) are a new class of polymers that combine the good degradability of polyesters with the high thermal stability, high modulus and high tensile strength of polyamides, which makes it possible to obtain good material and processing properties while maintaining degradability. PEAs are also highly attractive since their properties can be tuned due to the large variety of monomers that can be used (e.g. α-amino acids, α,ω-aminoalcohols, carbohydrates…). Thus, polymers can be synthesized with variable ester/amide ratio, variable aliphatic/aromatic ratio, variable hydrophilicity (e.g. incorporating poly(ethylene oxide) blocks or changing the length of polymethylene sequences), variable stereochemistry and variable monomer distribution. Thermoplastic elastomers, and amorphous and semicrystalline materials can be obtained from segmented, random and ordered microstructures, respectively. PEAs are now being considered for use as biodegradable matrices in nanocomposite preparation, although few works focus on the in-situ polymerization method.

Nanocomposites of organo-modified montmorillonites (C20A, C25A and C30B) and a biodegradable PEA were obtained by in-situ polycondensation of sodium chloroacetylaminohexanoate [75]. This synthesis was based on a thermal polycondensation reaction where the formation of a metal halide salt became the driving force of the process [76,77].

$$ClCH_2CONH(CH_2)_{n-1}COO^- Na^+ \longrightarrow [OCH_2CONH(CH_2)_{n-1}CO]_x^- + x\ Na^+Cl \qquad (A.2)$$

The great simplicity of this method raises interest in this family of polymers characterized by a semicrystalline character due to the regular distribution of the two units involved, which contrasts with the more amorphous nature of copolymers prepared by ring-opening polymerization. Exfoliated or intercalated structures were attained depending on the organo-modifier (i.e. the most dispersed structure was obtained by addition of Cloisite A). Polymerization kinetics was strongly influenced by the presence of organo-modified montmorillonites under both non isothermal and isothermal conditions. Both FTIR and WAXD experiments were used to study the polymerization process following the time evolution of the

1742 cm^{-1} absorption band of the ester group or the diffraction intensity of characteristic NaCl reflections (**Figure A.7** a), respectively. The temperature dependence of the polymerization kinetic constant allowed inferring that kinetic differences between the polymerization of the neat monomer and its mixture with C25A could be attributed to the preexponential frequency factor (**Figure A.7** b). In this way, clay particles seemed to reduce chain mobility and the frequency at which reactive groups were close enough to facilitate the condensation reaction. The thermal stability and crystallization behavior of the neat polymer and its nanocomposites were significantly different. In general, exfoliated structures decreased both primary nucleation and crystal growth rate whereas intercalated structures increased the density of primary nuclei. These nanocomposites were also prepared by the melt mixing technique, which rendered intercalated structures with a higher overall crystallization rate [78].

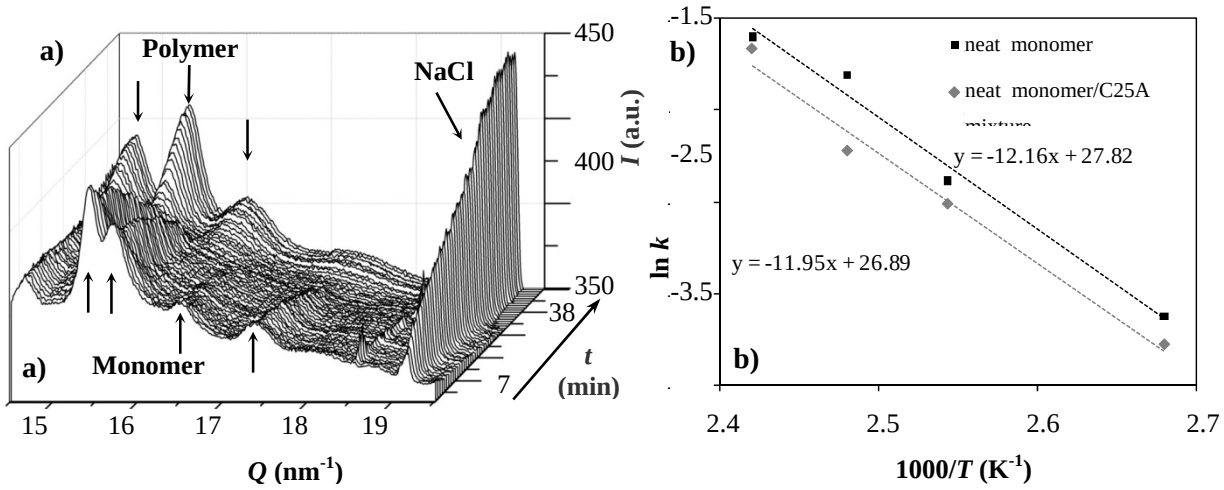

A.4. Conclusions

The increasing demand for biodegradable materials in the world market is leading to the development of products with better properties than those of existing materials. Efforts mainly focus on the synthesis of new biodegradable polymers with potential applications as both commodity and specialty materials. In this sense, poly(ester amide)s can be considered a modification of conventional biodegradable polyesters that may provide enhanced properties. Incorporation of nanoparticles into biodegradable polymer matrices is another effective approach to improve the properties of pristine polymers remarkably. There is now a considerably body of literature concerning the preparation of nanocomposites from the more usual biodegradable polyesters (e.g. poly(ε-caprolactone), polylactide, poly(butylen succinate) and poly(*p*-dioxanone) and silicate clays by *in-situ* polymerization. In general, this results in polymers grafted onto the silicate layers, favoring a subsequent exfoliation. Thus, in-situ polymerization seems to be more appropriate than other methodologies (i.e. melt or solution intercalation) that usually render intercalated structures. Despite the increasing interest in developing new biodegradable polymers, few works deal with the preparation of nanocomposites based on poly(ester amide)s matrices. Thus, this may be a very promising topic for future research.

A.5. References

[1] Perepelkin, K.E. (2002) Chemistry and technology of chemical fibers. Poly(lactide) fibers:fabrication, properties, use, prospects, a review. *Fibre. Chem.*, **34** (2), 85-100.

[2] Agrawal, A.K., Bhalla, R. (2003) Advances in the Production of Poly(Lactic Acid) Fibers. A Review . J. Macromol. Sci. -Polym. Rev., C43 (4), 479-503.

[3] Lee, J.H., Park, T.J., Park, H.S., Lee, D.S., Lee, Y.K., Yoon, S.C., Nam, J.D. (2003) Thermal and mechanical characteristics of poly(l-lactic acid) nanocomposite scaffold. Biomaterials, 24 (16), 2773-2778.

[4] Kai, W.H., Hua, L., Zhao, L., Inoue, Y. (2006) Synthesis of Novel Star Shaped Poly(ε-caprolactone) Utilizing Fullerene as the Molecular Core. Macromol. Rapid. Commun., 27 (19), 1702-1706.

[5] Li, H.Y., Debuigne, A., Jerome, R., Lecomte, P. (2006) Synthesis of Macrocyclic Poly(ε-caprolactone) by Intramolecular Cross-Linking of Unsaturated End Groups of Chains Precyclic by the Initiation. Angew. Chem. Int. Ed., 45 (14), 2264-2267.

[6] Luong-Van, E., Grondahl, L., Chua, K.N., Leong, K.W., Nurcombe, V., Cool, S.M. (2006) Controlled release of heparin from poly(ε-caprolactone) electrospun fibers. Biomaterials, 27 (9), 2042-2050.

[7] Sabino, M.A., Feijoo, J.L., Muller, A.J. (2000) Crystallisation and morphology of poly(p-dioxanone). Macromol. Chem. Phys., 201 (18), 2687-2698.

[8] Pezzin, A.P.T., van Ekenstein, G.O.R., Duek, E.A.R. (2001) Melt behaviour, crystallinity and morphology of poly(p-dioxanone). Polymer, 42 (19), 8303-8306.

[9] Yang, K.K., Wang, X.L., Wang, Y.Z. (2002) Poly(p-Dioxanone) and its copolymers. J. Macromol. Sci.-Polym. Rev., C42 (3), 373-398.

[10] Kim, J., Shin, T.K., Choi, H.J., Jhon, M.S. (1999) Miscibility of biodegradable synthetic aliphatic polyester and poly(epichlorohydrin) blends. Polymer, 40 (24), 6873-6876.

[11] Carroccio, S., Rizzarelli, P., Puglisi, C., Montaudo, G. (2004) MALDI Investigation of Photooxidation in Aliphatic Polyesters: Poly(butylene succinate). Macromolecules, 37 (17), 6576-6586.

[12] Dong, T., Shin, K.M., Zhu, B., Inoue, Y. (2006) Nucleation and Crystallization Behavior of Poly(butylene succinate) Induced by Its α-Cyclodextrin Inclusion Complex: Effect of Stoichiometry, Macromolecules, 39 (6), 2427-2428.

[13] Okada, M. (2002) Chemical Synthesis of Biodegradable Polymers. Prog. Polym. Sci., 27 (1), 87-133.

[14] Lips, P.A.M.; Dijkstra, P.J. (2005) Biodegradable Polymers for Industrials Applications, CRC Press, Boca Raton, Ch. 5, 109-139.

[15] Ray, S.S, Okamoto, M. (2003) Polymer/layered silicate nanocomposites: a review from preparation to processing. Prog. Polym. Sci., 28 (11), 1539–1641.

[16] Usuki, A, Kojima, K., Kawasumi, M., Okada, A., Fukushima, Y., Kurauchi, T., Kamigaito, O. (1993) Synthesis of nylon 6-clay hybrid. J. Mater. Res., 8 (5), 1179-1184.

[17] Yano, K., Usuki, A., Okada, A., Kurauchi, T., Kamigaito, O. (1993) Synthesis and properties of polyimide–clay hybrid. J. Polym. Sci. Part A: Polym. Chem., 31 (10), 2493-2498.

[18] Kojima, Y., Kukumori, K., Usuki, A., Okada, A., Kurauchi, T. (1993) Gas permeabilities in rubber-clay hybrid. J. Mater. Sci. Lett., 12 (12), 889-890.

[19] Messersmith, P.B., Giannelis, E.P. (1993) Polymer-Layered Silicate Nanocomposites: In Situ Intercalative Polymerization of α-Caprolactone in Layered Silicates. Chem. Mater., 5 (8), 1064-1066.

[20] Messersmith, P.B., Giannelis, E.P. (1995) Synthesis and Barrier Properties of Poly(-Capro1actone)-Layered Silicate Nanocomposites. J. Polym. Sci: Part A: Polym. Chem., 33 (7), 1047-1057.

[21] Krishnamoorti, R., Giannelis, E.P. (1997) Rheology of End-Tethered Polymer Layered Silicate Nanocomposites. Macromolecules, 30 (14), 4097-4102.

[22] Lepoittevin, B., Panstoustier, N., Alexandre, M., Calberg, C., Jérôme, R., Dubois, Ph. (2002) Layered Silicate/Polyester Nanohybrids by Controlled Ring-Opening Polymerization. Macromol. Symp. 183 (1), 95–102.

[23] Kubies, D., Pantoustier, N., Dubois, Ph., Rulmont, A., Jérôme, R. (2002) Controlled Ring-Opening Polymerization of ε-Caprolactone in the Presence of Layered Silicates and Formation of Nanocomposites. Macromolecules, 35 (9), 3318-3320.

[24] Lepoittevin, B., Pantoustier, N., Devalckenaere, M., Alexandre, M., Calberg, C., Jérôme, R., Dubois, Ph. (2002) Poly(ε-caprolactone)/Clay Nanocomposites by in-Situ Intercalative Polymerization Catalyzed by Dibutyltin Dimethoxide. Macromolecules, 35 (22), 8385-8390.

[25] Lepoittevin, B., Panstoustier, N., Alexandre, M., Calberg, C., Jérôme, R., Dubois, Ph. (2002) Polyester layered silicate nanohybrids by controlled grafting polymerization. J. Mater. Chem., 12 (12), 3528-3532.

[26] Gorrasi, G., Tortora, M.S., Vittoria, V., Pollet, E., Alexandre, M., Dubois, Ph. (2004) Physical Properties of Poly(ε-caprolactone) Layered Silicate Nanocomposites Prepared by Controlled Grafting Polymerization. J. Polym. Sci.: Part B: Polym. Phys., 42 (8), 1466–1475.

[27] Viville, P., Lazzaroni, R., Pollet, E., Alexandre, M., Dubois, Ph. (2004) Controlled Polymer Grafting on Single Clay Nanoplatelets. J. Am. Chem. Soc., 126 (29), 9007-9012.

[28] Kiersnowski, A., Dabrowski, P., Budde, H., Kressler, J., Pigłowski, J. (2004) Synthesis and structure of poly(-caprolactone)/synthetic montmorillonite nano-intercalates. European Polymer Journal, 40 (11), 2591–2598.

[29] Pucciariello, R., Villani, V., Langerame, F., Gorrasi, G., Vittoria, V. (2004) Interfacial Effects in Organophilic Montmorillonite–Poly(α-caprolactone) Nanocomposites. J. Polym. Sci.: Part B: Polym. Phys., 42 (21), 3907–3919.

[30] Gorrasi, G., Tortora, M., Vittoria, V., Pollet, E., Lepoittevin, B., Alexandre, M., Dubois, P. (2003) Vapor barrier properties of polycaprolactone montmorillonite nanocomposites: effect of clay dispersion. Polymer, 44 (8), 2271-2279.

[31] Pucciariello, R., Villani, V., Belviso, S., Gorrasi, G., Tortora, M., Vittoria, V. J. (2004) Phase behavior of modifired montmorillonite-poly(ε-caprolactone) nanocomposites. J. Polym. Sci. Part B: Polym. Phys., 42(7), 1321-1332.

[32] Tortora, M., Vittoria, V., Galli, G., Ritrovati, S., Chiellini, E. (2002) Transport Properties of Modified Montmorillonite-Poly(ε-caprolactone) Nanocomposites. Macromol. Mater. Eng., 287 (4), 243-249.

[33] Eastmond, G.C. (1999) Poly(ε−caprolactone) Blends . Adv Polym Sci., 149, 59-223.

[34] Kiersnowski, A., Piglowski, J. (2004) Polymer-layered silicate nanocomposites based on poly(ε-caprolactone). Eur. Polym. J., 40 (6), 1199–1207.

[35] Stassin, F., Halleux, O., Jérôme, R. (2001) Ring-opening polymerization of ε−caprolactone in supercritical carbon dioxide. Macromolecules, 34 (22), 775–781.

[36] Bratton, D., Brown, M., Howdle, S.M. (2002) Suspension polymerization of L-lactide in supercritical carbon dioxide in the presence of a triblock copolymer stabilizer. Macromolecules, 36 (16), 5908–5911.

[37] Wells, S.L., DeSimone, J.M. (2001) CO2 technology platform: an important tool for environmental problem solving. Angew. Chem. Int. Ed., 40 (3), 518–527.

[38] Urbanczyk, L., Calberg, C., Stassin, F., Alexandre, M., Jérôme, R., Jérôme, C., Detrembleur, C. (2008) Synthesis of PCL/clay masterbatches in supercritical carbon dioxide. Polymer, 49 (18), 3979–3986.

[39] Stassin, F., Jérôme, R. (2001) Ring-opening polymerization of epsilon-caprolactone in supercritical carbon dioxide. Macromolecules, 34 (4), 775–781.

[40] Avella, M., Vlieger, J.J.D., Errico, M.E., Fischer, S., Vacca, P., Volpe, M.G. (2005). Biodegradable starch/clay nanocomposite films for food packaging applications. *Food Chem.*, **93** (3), 467–474.

[41] Pandey, J.K., Kumar, A.P., Misra, M., Mohanty, A.K., Drzal, L.T., Singh, R.P. (2005) Recent advances in biodegradable nanocomposites. *J. Nanosci. Nanotechnol.*, **5** (4), 497–525.

[42] Namazi, H., Mosadegh, M., Dadkhah, A. (2009) New intercalated layer silicate nanocomposites based on synthesized starch-*g*-PCL prepared via solution intercalation and in situ polymerization methods: As a comparative study. *Carbohyd. Polym*., **75** (4), 665–669.

[43] Ray, S.S, Maiti, P., Okamoto, M., Yamada, K., Ueda, K. (2002) New polylactide/layered silicate nanocomposites. 1. Preparation, characterization, and properties. *Macromolecules*, **35** (8), 3104–3110.

[44] Ray, S.S, Okamoto, K., Yamada, K., Okamoto, M. (2002) Novel porous ceramic material via burning of polylactide/layered silicate nanocomposite. *Nano. Lett.* **2** (4), 423–425.

[45] Paul, M.A., Alexandre, M., Degée, P., Calberg, C., Jérôme, R., Dubois, P. (2003) Exfoliated polylactide/clay nanocomposites by in situ coordination-insertion polymerization. *Macromol. Rapid. Commun.* **24** (6), 66–561.

[46] Paul, M.A., Delcourt, C., Alexandre, M., Degée, P., Monteverde, F., Rulmont, A., Dubois, P. (2005) (Plasticized) polylactide/(organo-)clay nanocomposites by in situ intercalative polymerization. *Macromol. Chem. Phys*., **206** (4), 484–498.

[47] Jacobsen, S.; Fritz, H.G. (1999) Plasticizing polylactide - The effect of different plasticizers on the mechanical properties. *Polym. Eng. Sci*., **39** (7), 1303-1310.

[48] Martin, O.; Ave´rous, L. (2001) Poly(lactic acid): plasticization and properties of biodegradable multiphase systems. *Polymer*, **42** (14), 6209-6219.

[49]. Baiardo, M., Frisoni, G., Scandola, M., Rimelen, M., Lips, D., Ruffieux, K., Wintermantel, E. (2003) Thermal and mechanical properties of plasticized poly(L-lactic acid). J. Appl. Polym. Sci., 90 (7), 1731-1738.

[50] Hu, Y., Rogunova, M., Topolkaraev, V., Hiltner, A., Baer, E. (2003) Aging of poly(lactide)/poly(ethylene glycol) blends. Part 1. Poly(lactide) with low stereoregularity. *Polymer*, **44** (19), 5701-5710.

[51] Zhang, J.H., Zhuang, W., Zhang, Q., Liu, B., Wang, W., Hu, B.X., Shen, J. (2007) Novel polylactide/vermiculite nanocomposites by in situ intercalative polymerization. I. preparation, characterization, and properties. *Polym. Composite.*, **28** (4), 545-550.

[52] Saber, O., Tagaya, H. (2008) Preparation and intercalation reactions of nano-structural materials, Zn-Al-Ti LDH. *Mater. Chem. Phys.*, **108** (2-3), 449-455.

[53] Pluta, M. (2004) Morphology and properties of polylactide modified by thermal treatment, filling with layered silicates and plasticization. *Polymer*, **45** (24), 8239-8251.

[54] Li, L., Ma, R.Z., Ebina, Y., Iyi, N., Sasaki, T. (2005) Positively charged nanosheets derived via total delamination of layered double hydroxides. *Chem. Mat.*, **17** (17), 4386-4391.

[55] Zammarano, M., Bellayer, S., Gilman, J.W., Franceschi, M., Beyer, F.L., Harris, R.H., Meriani, S. (2006) Delamination of organo-modified layered double hydroxides in polyamide 6 by melt processing. *Polyme*r, **47** (2), 652-662.

[56] Sabbar, E.M., Roy, M.E., Leroux, F. (2006) Probing the interaction between di- and trifunctionalized carboxy-phosphonic acid and LDH layer structure. *J. Phys. Chem. Solids*, **67** (11), 2419-2429.

[57] Jaubertie, C., Holgado, M.J., San Roman, M.S., Rives, V. (2006) Structural characterization and delamination of lactate-intercalated Zn, Al- layered double hydroxides. *Chem. Mater*, **18** (13), 3114-3121.

[58] Katiyar, V., Gerds, N., Koch, C.B., Risbo, J., Hansen, H.C.B., Plackett, D. (2010) Poly L-lactide-layered double hydroxide nanocomposites via in situ polymerization of L-lactide. *Polym. Degrad. Stabil*., **95** (12), 2563-2573.

[59] Miyata, S. (1975) The syntheses of hydrotalcite-like compounds and their structures and physicochemical properties 1. systems Mg^{2+}-Al^{3+}-NO^{-3}, Mg^{2+} -Al^{3+}-Cl^{-} ,Mg^{2+}-Al^{3+}-ClO^{-4}, Ni^{2+}-Al^{3+}-Cl^{-} and Zn^{2+}-Al^{3+}-Cl^{-}. *Clays Clay Miner*., **23**(5), 369-375.

[60] Cavani, F., Clause, O., Trifiro, F., Vaccari, A. (1991) Anionic clays with hydrotalcite-like structure as precursors of hydrogenation catalysts. *Adv. Catal. Des.* 186-190.

[61] Urbanczyk, L., Ngoundjo, F., Alexandre, M., Jérôme, C., Detrembleur, C., Calberg, C. (2009) Synthesis of polylactide/clay nanocomposites by in situ intercalative polymerization in supercritical carbon dioxide. *Eur. Polym. J*., **45** (3), 643–648.

[62] Fujimaki, T. (1998) Processability and properties of aliphatic polyesters, 'BIONOLLE', synthesized by polycondensation reaction. *Polym. Degrad. Stabil.*, **59** (1-3), 209-214.

[63] Yoo, Y.T., Lee, B.J., Han, S.I., Im, S.S., Kim, D.K. (2003) Physical properties and biodegradation of poly(butylene adipate) ionomers. *Polym. Degrad. Stabil.*, **79** (2), 257-264.

[64] Han, S.I., Kang, S.W., Kim, B.S., Im, S.S. (2005) A novel polymeric ionomer as a potential biomaterial: crystallization behavior, degradation, and in-vitro cellular interactions. *Adv. Funct. Mater*., **15** (3), 367-374.

[65] Han, S.I., Yoo, Y., Kim, D.K., Im, S,S. (2004) Biodegradable aliphatic polyester ionomers. *Macromol. Biosci*., **4** (3), 199-207.

[66] Takiyama, E., Fujimaki, T. (1992) Characteristics of biodegradable aliphatic polymer e bionolle. *Plastics*, **43**, 87.

[67] Abe, H., Doi, Y., Hori, Y., Hagiwara, T. (1998) Physical properties and enzymatic degradability of copolymers of (R)-3-hydroxybutyric acid and (S,S)- lactide. *Polymer*, **39** (1), 59-67.

[68] Kim, H.S., Chen, G.X., Jin, H.J., Yoon, J.S. (2008) *In situ* copolymerization of butylene succinate with twice functionalized organoclay: Thermal stability. *Colloid Surface A*, **313-314**, 56-59.

[69] Han, S., Lim, J.S., Kim, D.K., Kim, M.N., Im, S.S. (2008) In situ polymerized poly(butylene succinate)/silica nanocomposites: Physical properties and biodegradation. *Polym. Degrad. Stabil.*, **93** (5), 889-895.

[70] Hwang, S., Yoo, E.S., Im, S.S. (2009) Effect of the urethane group on treated clay surfaces for high-performance poly(butylene succinate)/montmorillonite nanocomposites. *Polym. Degrad. Stabil.*, **94** (12), 2163–2169.

[71] Pollet, E., Delcourt, C., Alexandre, M., Dubois, Ph. (2006) Transesterification catalysts to improve clay exfoliation in synthetic biodegradable polyester nanocomposites. *Eur. Polym. J.*, **42** (6), 1330–1341.

[72] Yang, K.K., Wang, X.L., Wang, Y.Z. (2002) Poly(p-Dioxanone) and its copolymers. J. Macromol. Sci. Part C Polym. Rev., 42 (3), 373-398.

[73] Yang, K.K., Wang, X.L., Wang, Y.Z. (2007) Progress in Nanocomposite of Biodegradable Polymer. J. Ind. Eng. Chem., 13 (4), 485-500.

[74] Huang, F.Y., Wang, Y.Z., Wang, X.L., Yang, K.K., Zhou, Q., Huang, F.Y. (2005) Preparation and characterization of a novel biodegradable poly(p-dioxanone)/montmorillonite nanocomposite. J. Polym. Sci. Polym. Chem., 43 (11), 2298-2303.

[75] Morales, L; Franco, L; Casas, MT; Puiggalí, J. (2009) Poly(ester amide)/Clay Nanocomposites Prepared by In Situ Polymerization of the Sodium Salt of N-Chloroacetyl-6-Aminohexanoic Acid. J. Polym. Sci. Part A: Polym. Chem., 47 (14), 3616-3629.

[76] Epple, M.; Kirschnick, H. (1996) The Thermally Induced Solid-State Polymerization Reaction in Halogenoacetates. Chem. Ber., 129 (9), 1123-1129.

[77] Herzberg, O.; Epple, M. (2001) Formation of Polyesters by Thermally Induced Polymerization Reactions of Molecular Solids. Eur. J. Inorg. Chem., 2001 (6), 1395-1406.

[78] Morales, L; Franco, L; Casas, MT; Puiggalí, J. (in press) Crystallization studies on a clay nanocomposite prepared from a degradable poly(ester amide) constituted by glycolic acid and 6-aminohexanoic acid. Polym. Eng. Sci., 2010, in press.